High-concentration nanofluids prepared from functionalised silica nanoparticles: synthesis optimisation and investigation of rheological properties

by

Christopher Lee Hassam

Thesis
Submitted to Flinders University
for the degree of

Doctor of Philosophy
College of Science and Engineering
19/02/19

Declaration

'I certify that this thesis does not incorporate without acknowledgment any material previously submitted for a degree or diploma in any university; and that to the best of my knowledge and belief it does not contain any material previously published or written by another person except where due reference is made in the text.';

Christopher Hassam

on 20/09/18

Acknowledgements

I would like to offer my sincerest gratitude to my supervisors who have helped, guided and supported me throughout my PhD. First, Professor David Lewis, whose guidance and advice has helped shape my scientific and professional development. To Dr Jonathan Campbell whose expertise, particularly with equipment, has been instrumental. Dr Takashi Nakanishi for his help and support during my time at NIMS and beyond.

I would also like to extend my thanks to my research groups past and present, at Flinders University and at NIMS, for your conversation, advice and friendship. I would also like to the Australian Government for the provision of an Australian Postgraduate Award, and NIMS for the opportunity and financial support to conduct a part of my research in Japan, via the Flinders University-NIMS International Cooperative Graduate Program.

I would like to acknowledge my friends with particular thanks to Sean, Kimmi, Tommi, Réka and Aga, for your friendship, conversation and humour. Also to Bloky, Bec, Jon, Oskar and Mangos, who have livened up the office and labs, and made Flinders a more interesting and enjoyable place.

To my family, my parents, grandparents, siblings and everyone else, you can stop asking when I will be finished. I cannot thank you enough for your support over the years. A particular thankyou to my grandparents, Val and Don, for supporting me and remaining excited about what I had been doing.

Finally, to Cedric, for your patience with how long this has been "nearly finished".

Summary

The rheological properties of nanofluids – dispersions of nanoparticles in a solvent – are highly dependent on the interaction between the particles, particularly at high nanoparticle concentration. To understand how these inter-particle interactions impact the rheological properties, the particles must have both well-controlled surface functionality, as well as high surface coverage of functional groups. Silica nanoparticles are a convenient substrate for such dispersions, owing to their general thermal stability and easily modifiable chemistry, however, conventional modification techniques of silica nanoparticles often result in undesirably low surface coverage.

This thesis reports the preparation and characterisation of high concentration nanofluids prepared from silica nanoparticles, bearing quantifiable and high surface functional densities of organic moieties. An optimised method of producing gram-scale quantities of silica nanoparticles from (3-mercaptopropyl)trimethoxysilane (3-MPTMS), with narrow size dispersity is presented. These particles are characterised for diameter and surface area, and a new method of quantifying the dispersity of diameter and shape is proposed.

High degrees of functionalisation were achieved with undec-10-enoic acid (6.5 groups·nm^{-2}), 10-undecen-1-ol (13.5 groups·nm^{-2}), 11-Br-1-undecene (8.5 groups·nm^{-2}), as well as sodium 4-vinylbenzenestyrenesulfonate (1.3 groups·nm^{-2}) based on established methods of determining the attachment density using thermogravimetric analysis (TGA) and attenuated total reflectance infrared spectroscopy (ATR-FTIR). Data analysis from TGA has been extended to provide a new general approach to analysing the data using peak fitting.

All systems studied showed shear thinning behaviour; however, for some systems this was only evident at high concentration. Systems with poor aqueous interaction showed shear thinning behaviour with shear rate at all concentrations prepared. Purchased samples of LUDOX AS40 were found to show shear thinning behaviour only at concentrations greater than 40 %w/w, while synthesised TEOS particles only showed shear thinning behaviour

Undec-10-enoic acid functionalised silica nanoparticles (COOH-SiNPs) were chosen to determine pH effects on the dispersion rheological properties of high solids solutions. As the pH is decreased, particularly below the pKa of undec-10-enoic acid, aggregation occurs at lower concentration, as monitored by dynamic light scattering (DLS) and zeta potential

measurements. At pH 13, it was found that the concentration of the nanofluid could be increased to 49 %w/w with only minimal impact on the rheological properties of the dispersion: high pH values allowed dispersions to be produced that showed Newtonian behaviour across shear rates spanning four orders of magnitude. The effect of aggregation was further investigated by sonication of COOH-SiNPs at neutral pH and monitoring the effect on the rheological properties of the dispersions with time post-sonication. The effect of pH after drying was also investigated on the particles by means of TGA, and it was found the thermal stability of the particles was greater when dried from a high pH dispersion.

To further investigate the role of aggregation with correlation to the particle surface properties, rheological investigations of nanofluids prepared from nanoparticles functionalised with both hydrophilic and hydrophobic groups, as well as unfunctionalised SH-SiNPs are compared, and the effect of concentration on these samples were investigated. When unfunctionalised, SH-SiNPs at high concentration produced severe shear thinning effects, resulting in unstable dispersions. Attachment of hydrophobic moieties such as 11-bromo-1-undecene (Br-SiNPs) or 1-undecene (U-SiNPs) resulted in even greater aggregation, preventing particles from forming dispersions at any concentration. It was also found that particles functionalised with 10-undecen-1-ol (OH-SiNPs) showed poor aqueous stability, despite the presence of a polar terminal functional group.

The SH-SiNPs functionalised with sodium 4-vinylbenzenestyrenesulfonate (StS-SiNPs) were found to produce hydrophilic particles that could form high concentration dispersions, which exhibited light scattering effects producing bright blue colouration and opalescence under directed light. The samples showed shear thinning behaviour that was modelled using the Cross equation. Behaviour characteristic of viscoelastic solids was noted at concentrations greater than 40 %w/w. High concentration solutions of these particles showed rheopexy when analysed by sequential increasing and decreasing shear rate measurements.

Further applications and extensions of this work are proposed in which the microstructure of a high concentration nanofluid of StS-SINPs is investigated while undergoing shear deformation. Further work is also possible through the attachment of moieties that show a switchable effect based on pH, light or other mechanism, and how this is affected by the high density of functionalisation achievable.

Table of contents

List of figures

List of tables

List of abbreviations

AIBN	azobisisobutyronitrile
ATR	attenuated total reflection/reflectance
ATR-FTIR	attenuated total reflectance Fourier transform infrared (spectroscopy)
BET	Brunauer-Emmett-Teller (theory)
Br-SiNP(s)	11-bromo-1-undecene functionalised silica nanoparticle(s)
COOH-SiNP(s)	undec-10-enoic acid functionalised silica nanoparticle(s)
COONa-SiNP(s)	undec-10-enoic acid functionalised silica nanoparticle(s), sodium salt
DLS	dynamic light scattering
DLVO	Derjaguin-Landau-Verwey-Overbeek (theory)
EDXS	energy-dispersive X-ray spectroscopy
FTIR	Fourier transform infrared (spectroscopy)
IUPAC	International Union of Pure and Applied Chemistry
NIBS	non-invasive backscatter system
OH-SiNP(s)	10-undecen-1-ol functionalised silica nanoparticle(s)
PDI	polydispersity index
PTFE	poly(tetrafluoroethylene)
SEM	scanning electron microscopy
SH-SiNP(s)	propyl-thiol terminated silica nanoparticle(s)
SiNP(s)	silica nanoparticle(s)
STA	simultaneous thermal analyser
StS-SiNP(s)	sodium 4-vinylbenzenestyrenesulfonate functionalised silica nanoparticle(s)
TGA	thermogravimetric analysis
U-SiNP(s)	1-undecene functionalised silica nanoparticle(s)

List of symbols

$[\eta]$	Intrinsic viscosity
A	Area
a	Semi major axis
α_c	Cross rate constant
B	Amplitude
C	BET constant
c	Semi minor axis
D	Fractal dimension
Đ	Dispersity
D_{SS}	Surface-surface distance
d_p	Particle diameter
d_S	Mean surface diameter
Δ	Heat
Δr	Difference between sphere and inner sphere radii
ΔV	Difference between sphere and inner sphere volumes
δ	Debye length
δ	Bending vibrational mode
e	Charge of electron
ϵ_0	Permittivity of free space
ϵ_r	Permittivity of solvent
η	Viscosity
η_s	Viscosity of base fluid

η_0	Zero shear viscosity
η_∞	Infinite shear viscosity
η_{eff}	Effective viscosity
F	Shear force
$f(r)$	Probability function of normal distribution around r
ϕ	Volume fraction of particles/spheres
ϕ_{a}	Agglomerate internal volume fraction
ϕ_{c}	Critical packing fraction
ϕ_{eff}	Effective volume fraction
ϕ_{F}	Freezing volume fraction
ϕ_{FCC}	Face-centred cubic packing fraction
ϕ_{G}	Glassy transition point
ϕ_{m}	Maximum packing fraction
ϕ_{M}	Melting volume fraction
ϕ_{RCP}	Random close packing volume fraction
$\dot{\gamma}$	Shear rate
$\dot{\gamma}_{\text{c}}$	Critical shear rate
hν	UV light (Planck constant and frequency of light)
I	Intensity of scattered light
K	Consistency index
k_{B}	Boltzmann's constant
κ^{-1}	Debye-Hückel screening length
λ	Wavelength

λ_c	Relaxation constant
MM_{moiety}	Molar mass of moiety
$MM_{SH-SiNPs}$	Molar mass of repeating $SiO_{1.5}C_3H_7S$ unit
m	Cross model flow index
$m_{SH-SiNPs}$	Mass of SH-SiNPs
m_{moiety}	Mass of moiety
m_p	Mass of particles
μ	Mean particle radius
N	Length subject to condition $0 \leq N < r$
N_{Av}	Avogadro's constant
n	Flow index
n_p	Number of particles
n_0	Number of ions per unit volume of each type in bulk solution
ν	Stretching vibrational mode
$p/p°$	Relative pressure
R_{agg}	Radius of gyration of agglomerate
R^2	Coefficient of determination
r	Particle radius
r_i	Inner sphere radius
r'	Effective particle radius
ρ	Particle density
SA	Surface area of particles
SSA	Specific surface area

$SSA(r)$	Specific surface area of sphere of radius, r
SSA_{avg}	Weighted average of particle specific surface area
$SSA_{dist}(r)$	Specific surface area of distribution of spheres with mean radius r
σ	Standard deviation
$\sigma_i(r)$	Probability of particle with radius r existing from standard deviation
T	Absolute temperature
T_{max}	Temperature at maximum rate of mass loss
τ	Stress
τ_c	Critical shear stress
τ_0	Yield stress
V_A	Attractive van der Waals interaction potential
V_{inner}	Inner sphere volume
$V_{particle}$	Volume of spherical particle
V_R	Repulsive electrostatic interaction potential
V_T	Total interaction potential
w_{moiety}	Mass fraction of moiety
w_1	Width factor in asymmetric double sigmoidal function
w_2	Low temperature width factor in asymmetric double sigmoidal function
w_3	High temperature width factor in asymmetric double sigmoidal function
x_c	Centre
x_i	Probability of particle of radius $r + i$ existing
Z_{av}	Z-average particle diameter
z_i	Valence of ions

1   Introduction

1.1 Motivation

Nanofluids have been a subject of intense research owing to their potential for favourable properties for heat-transfer fluid applications, drilling fluids, and production and processing of nanoceramics. There are, however, few publications regarding the properties of highly concentrated nanofluids that dedicate significant attention to the success or degree of surface modification commonly applied to particles, with the surface functionalisation often showing poor attachment densities, or not being investigated. This thesis focusses on the synthesis and resulting rheological properties achievable by high concentration aqueous nanofluids when functionalised with undec-10-enoic acid groups, 11-bromo-1-undecene, 10-undecene-1-ol groups, and sodium 4-vinylbenzenestyrenesulfonate.

Aims

- To prepare high concentration nanofluids and to investigate their rheological properties with an aim towards tuning these properties based on the surface functional chemistry of the nanoparticles within them.

- For generating high concentration solutions, the aims for the synthesis are:

  o To optimise and upscale a synthetic method for the production of thiol-terminal silica nanoparticles (SH-SiNPs), allowing for large-scale synthesis of nanoparticles with good control over particle diameter, narrow particle dispersity, predictable specific surface area, and with known, quantifiable, and easily reacted surface groups.

  o Create a more accurate method for surface-functional density characterisation of nanoparticles with attached undec-10-enoic acid, 11-bromo-1-undecene, 10-undecene-1-ol and sodium 4-vinylbenzenestyrenesulfonate.

- In the investigation of the nanofluid properties, the aims are:

  o Investigate and measure the effect of pH on the aggregation of undec-10-enoic acid functionalised nanoparticles, and the rheological properties of high-concentration dispersions of these particles.

  o To investigate the effect of concentration of nanoparticles in standard solutions of nanoparticles, and compare these to the rheological properties of functionalised nanoparticles bearing hydrophobic and hydrophilic moieties.

1.2 Nanotechnology and nanoscale properties

Nanotechnology is a method, approach and body of knowledge concerned with the synthesis, manipulation, control, and application of nanomaterials in the fabrication of novel materials or devices. Nanomaterials are characterised by their mesoscopic properties, exhibiting unique and novel properties that cannot be achieved in bulk materials. Quantum effects on the nanoscale can give these materials unique and exceptional properties, and nanotechnology seeks to allow these properties to be exploited, creating new materials and products. The properties capable of being manipulated in such a manner include, but are not limited to: viscosity [1-3], conductivity (both thermal [4-6] and electrical [7, 8]), reactivity [9], catalytic activity [10-12] and colour [13].

The ability to manipulate these properties is enabled by the unique effects that are present on the nanoscale, which are either eliminated or reduced to the point of insignificance when scaled up to a macroscale, or bulk size. Gold is one of the best-known examples, showing the difference between bulk and nanoscale effects. Bulk gold is relatively chemically inert; it does not tarnish or corrode, resisting reaction with most acids and bases. However, gold nanoparticles have been studied extensively for their useful properties, such as catalytic activity [10, 14, 15].

In this example, the catalytic activity has been attributed to the presence of the under-coordinated surface sites on the catalyst, which increases with decreasing particle size [10]. Indeed, it has been found that the catalytic activity of gold nanoparticles is increased with decreasing particle size. Once the gold is above a certain threshold of size, however, the catalytic activity drops off, and the gold exhibits the inert nature of bulk gold [16].

This disappearance of the quantum properties of nanoparticles leads to the definition of a nanoparticle, which is given by the International Union of Pure and Applied Chemistry (IUPAC) as being a particle between 1-100 nm (if a tube or fibre is being considered, having at least 2 dimensions in the 1-100 nm range) [17, 18]. However, it should be noted that certain properties, including transparency and dispersion stability among others, show interesting "nanoscale" properties at greater length scales than 100 nm. It is therefore considered acceptable, when these properties are investigated, to extend the nanoparticle designation to sub-500 nm scale particles [17].

1.3 Nanofluids

Nanofluids are colloidal liquid suspensions of nanoparticles, with concentrations typically ranging between 0.01-5 % [1–3]. The nanoparticles used can include powders of ceramics [19], metal oxides [20-22], carbides [23] and nitrides [24, 25], carbon nanotubes [26] and metals [3], which can be suspended in organic, aqueous or ionic liquid media.

One area in which nanofluids have garnered attention is in the production of nanoceramics. Nanoceramics can be produced from nanofluids, where having a pourable source of nanoparticles simplifies the manufacturing process [27-29]. For production of ceramics from nanofluids, high concentration fluids that have controllable viscosity and resistance to sedimentation are desirable [28]. In producing nanofluids containing yttrium oxide in ethanol Żyła *et al*. found that solutions of greater than 10 %w/w showed non-Newtonian behaviour, as well as unexpected behaviour, which was attributed to sedimentation of the nanofluid [30]. Generally, however, research interest into nanofluids stems from the anomalously large enhancement of one, or more, base fluid properties compared with a dispersion of an equal quantity of larger particles [31, 32].

Since the term was coined by Choi and Eastman [33], nanofluids have seen attention for using them as heat-transfer fluids, due to their apparent, anomalously high increase in thermal conductivity [31, 32]. Different mechanisms have been proposed for the origin of the anomalous enhancement, such as formation of a semi-solid layer of solvent at the particle-fluid interface, increased heat transfer due to the greater surface area-to-volume ratio of the nanoparticles, and increased mobility of nanoparticles compared to an equivalent mass of macro scale particles [34-36].

Significant and widespread disagreement exists in published works however, regarding the replicability and consistency of the purported property enhancements [21, 37-39]. Some groups report significant enhancements with minute quantities of nanoparticles, with the enhancement outstripping the expected values due to simple mixing theory, while other groups report no significant deviation from standard models [34]. Even with the same solid particles and solvents, such as alumina nanoparticles in water different results have been found: some finding no or less significant enhancement [22, 40, 41], but others finding significant, anomalously high enhancement [42-44]. Such disagreement can be partially attributed to the inconsistency between groups found with respect to particle size and preparation conditions, with few groups measuring identical systems [45]. It is commonly agreed, however, that the

desirable properties of nanofluids are enhanced with increasing nanoparticle concentration [5, 37, 38, 46].

Further improving nanofluid properties by a continued increase in concentration is, however, not viable. In addition to increases in the desirable properties, a number of undesirable properties may also change with concentration. Solution viscosity can dramatically increase with increasing concentration [21, 39, 47], and significant deviations from Newtonian behaviour are common [48, 49], even at lower concentrations. Increased viscosity of a solution can reduce its usability, requiring greater mechanical energy to pour or pump the fluid, which can eliminate their benefit over conventional fluids. Non-Newtonian behaviour, such as the introduction of yield stresses, or shear thickening behaviour at high shear rates, must also be accounted for during processing of particle solutions, necessitating an understanding and control over the fluid behaviour over a wide range of shear rates [50, 51].

Solution stability is also of significant concern, particularly for high concentration solutions. Poor stability in solution leads to particle aggregation, resulting in large viscosity increases, and reduction of the desired properties [52]. This has been proposed as a potential reason for the discrepancy in the measured properties of nanofluids in solution. Should dispersion stability be unaccounted for in nanofluid research, it is plausible that the larger effective particles being measured by a number of groups would therefore show no effective enhancement compared with a dispersion of conventional particles.

1.3.1 Fluid-solid mixtures

Mixtures of fluids (gaseous or liquid) and solid particles are a broad category. When particles are suspended in a liquid, and their diameter is below approximately 1000 nm, the suspension can be called a colloid [53]. Larger particles also form suspensions, however these are usually unstable and short lived [54].

When considering fluid-solid mixtures, it is important to define the terms being used for clarity. Imprecision in terminology is present in nanofluid and colloidal research, based on differing definitions between groups. In this work, a dispersion is defined as sample or system in which there is more than one phase, with at least one phase separated into fine, separated domains, dispersed through a continuous phase [55].

When the dispersed phase is made of solid nanoparticles (sometimes called the primary units), these can form larger dispersed units, defined by their interaction. When the particles are

strongly bound together in an irreversible large structure, such as by sintering of ceramic particles, the larger unit is referred to as an aggregate [56]. When the particles are loosely bound into a larger structure that can be broken into primary units by the application of force or some other means, the larger unit is referred to as an agglomerate [56].

When a particle is suspended in solution, its movements are determined by its size, surface chemistry (including surface charge) and relative density in solution. Heavy, dense particles of large size and negligible particle-solvent interaction will naturally sediment out over time, with the rate of sedimentation being dependent on those properties. Smaller particles, and in particular nanoparticles, can remain suspended through Brownian motion [53, 57].

Brownian motion is the movement of particles in solution based on the impact of atoms and molecules in the solution [58]. Based on the relatively tiny forces this causes on the particles, only particles small enough for this force to be significant can be suspended in this manner. Thus, smaller particles are capable of remaining suspended over extended periods.

Surface chemistry also influences suspension stability [2, 27, 59]. Forces acting on the particle surface can ultimately favour either particle-fluid interaction, or particle-particle interaction. The particle-fluid interaction can further favour either particle-solvent interaction, or particle-gas interaction [60-62]. If the particle-solvent interaction is dominant, the suspension can be expected to exist as a colloidal state, with the particles homogeneously suspended throughout the solution. If the interparticle interaction is dominant, the particles can be expected to aggregate in solution. These aggregates can be expected to act as larger particles, reducing the effect of Brownian motion [63]. Thus, it would be expected for these aggregates to coalesce and to sediment from solution.

Even in cases where the particle-solvent interaction promotes a stable dispersion, other factors, such as the concentration of the mixture can play a significant role. Increased concentration of particles in solution can have both favourable and unfavourable effects on dispersion stability. Too great a concentration of particles in solution may overcome the stabilisation method used, resulting in particle aggregation and sedimentation. Alternatively, an increased concentration can result in greater solution stability, by increasing solution viscosity [64]. The higher the viscosity, the greater the opposition force towards settling of the particles, resulting in greater stability of the particles in solution.

However, increasing the concentration cannot continue infinitely. The particles have a defined volume, and eventually the maximum concentration can theoretically be reached, with particles

existing in as small a fraction of fluid as possible, and the "dispersion" showing solid-like properties, tending towards infinite viscosity [4].

1.3.2 Colloidal stability

Nanofluids are a type of colloid in which the dispersed medium is nanoparticulate. Nanoparticles characteristically possess a large surface area, which is inherently unstable. Aggregation is a method by which this surface area can be decreased, and so in the absence of a stabilising force, particles in solution tend towards forming large aggregates. Stabilisation methods, therefore, are repulsive forces between particles preventing their aggregation and allowing them to remain dispersed as single particles [65].

Classical Derjaguin-Landau-Verwey-Overbeek (DLVO) theory is a commonly applied theory in colloidal science for estimating the interaction potential between particles [62]. Effectively it represents the total interparticle interactions as a sum of the attractive van der Waals interactions and repulsive electrostatic interactions (Equation 1.1). If the electrostatic repulsion is less than the van der Waals attraction, the particles aggregate and the colloid is unstable [65].

$$V_{\mathrm{T}} = V_{\mathrm{A}} + V_{\mathrm{R}}$$

Equation 1.1

$Where$:

$V_{\mathrm{T}} = total\ interaction\ potential$

$V_{\mathrm{A}} = attractive\ van\ der\ Waals\ interaction\ potential$

$V_{\mathrm{R}} = repulsive\ electrostatic\ interaction\ potential$

It has been found that for colloidal solutions with smaller diameter dispersed phases, and in particular, for nanoparticles, classical DLVO theory does not adequately explain or reflect the stability of prepared solutions [61, 66]. Additional forces not considered in classical DLVO theory have been introduced as a method of bringing the theory more in line with the experimental observations. These include terms for steric stabilisation of the particles, hydrogen bonding effects, hydrophobic interactions, as well as structural, shape and curvature effects [66]. Inclusion of these factors in analyses in the literature is inconsistent and debated [61].

Considering DLVO theory, it can therefore be considered that stabilisation of a colloid can be achieved either through increasing the electrostatic repulsion, or through introduction of an

additional repulsive force. Broadly, colloids can be stabilised by electrostatic stabilisation, steric stabilisation or both (sometimes called electrosteric stabilisation).

1.3.2.1 Electrostatic stabilisation

Electrostatic stabilisation of nanoparticles in solution is achieved by induction of a dipole layer at their surface [2, 67-69]. Assuming a single species of particle in solution, each particle will have the same dipole [70]. The overall effect is a repulsive double layer forming around each particle [62, 71]. The source of the charge at the surface varies depending on the materials and methods used. Causes include adsorption of ions or charged species on the surface, dissociation of charged species on the surface, ion substitution and, surface electron accumulation or depletion [72].

Electrostatic stabilisation however has a number of issues that prevent it from being applicable to all nanofluids. First and most limiting, to be effective electrostatic stabilisation is most easily achieved in aqueous conditions. Non-aqueous solvents can be used for electrostatic stabilisation [73]. Hsu *et al.* found long-range stabilisation of poly(methylmethacrylate) particles in non-polar solutions with reverse micelles [74]. The stabilising effect could not be attributed to the 12-hydroxy-steric acid present on the surface of the colloidal particles; instead, the interparticle repulsion was a measureable and tuneable electrostatic stabilisation. However, overall this is less common than the more universally applicable method of steric stabilisation.

Concentration of the particles as well as the ionic species in solution influences electrostatic stabilisation [75]. Increased concentration of the ionic species results in tighter double layer formation, which reduces their effective diameter, inhibiting their effectiveness [62]. The additional counterions in solution shield the charges between particles, allowing them to approach closer to each other, promoting their aggregation [76]. If the concentration increases too much, the double layer essentially disappears, and the particles aggregate [77].

If particle concentration increases too much, the particles' double layers begin to interfere with each other [78]. This changes the resulting double layers formed, potentially resulting in an unstable dispersion. Further, above a critical concentration, particle interaction is guaranteed geometrically, which can lead to aggregate formation.

If the origin of the charge is a pH responsive group, such as an acid or amine functionality, the charged surface of the particles is often affected by pH, ionising or deionising based on the level in solution. This may be desirable to produce reversibly stable solutions. Additionally, adjustment of the pH of a solution can introduce significant quantities of ions into the solution,

increasing the ionic concentration and thus suppressing the electrical double layers. The nature of the base counterion used also significantly affects the solution stability [79].

Usefully, the particles in the system remain relatively unaltered by this process, such as stabilisation of silica particles by deprotonation of silanol groups. There are also fewer contributions from non-particulate components of the solution, with the addition of polymer for example; the solution properties may be altered by the polymer, rendering the contributions of the particles negligible.

1.3.2.2 Steric stabilisation

Steric stabilisation of colloids is achieved by attaching or grafting macromolecules to colloidal particles [80]. Usually, the macromolecules are polymers with a chain length greater than the distance at which van der Waals interactions occur [76].

In comparison to electrostatic stabilisation, steric stabilisation shows different benefits and drawbacks, which render it suitable for different applications. Steric stabilisation is insensitive to ionic concentration and often pH, as the size of the electrical double layer is effectively irrelevant, allowing non-aqueous and non-polar solutions to be used with minimal difficulty [76]. The main restriction of solvent becomes compatibility with the stabilising polymer. Copolymers are often the favoured agent, as they can be customised based on the particle and solvent system required [81].

Whilst in electrostatic stabilisation the collapse of the double layer will lead to agglomeration, attempting to reintroduce it by diluting will not usually separate the particles without the addition of energy, steric stabilisation can be easily reversible [76]. For sterically stabilised compounds, if an aggregation agent is added to the solution the dispersion can be regained by dilution. It is also for this reason that the particles can spontaneously redisperse after drying, which is rare for aggregated electrostatically stabilised particles.

Difficulties with using steric stabilisation include ensuring the coverage of the particles is uniform: non-uniform coverage of the particles can lead to bridging between particles due to partially adsorbed polymer, resulting in greater aggregation [82]. Additionally, solution properties can be dramatically affected by the presence of polymer. Even small quantities of polymeric material can have large effects on solution properties, and the particles themselves may have only a minor effect on the solution properties exhibited, complicating analysis. Further, if the particles are required to have specific surface geometries or groups the polymer may cover these, rendering the particles unsuited for their application.

1.3.3 Light scattering of dispersed media

Inhomogeneities in a dispersed phase, such as nanoparticles in solution, misted water, emulsions of oil and water, and myriad others, cause incident light to be scattered. Scattering is the change of direction experienced by light when it encounters such an inhomogeneity. Elastic light scattering, in which the incident light does not experience a wavelength change, can be classified according to the scale of the scattering body (such as a particle).

When the particle diameter (d_p) is significantly smaller than the wavelength of the scattered light ($d_\mathrm{p} \ll \lambda$) with $d_\mathrm{p} < \frac{\lambda}{10}$ usually taken as the upper limit, the light scattering is explained by Rayleigh scattering. When undergoing Rayleigh scattering, light is incident upon a small sphere (or equivalent sphere), and the electromagnetic radiation causes an oscillation in the electronic cloud of the sample, which quickly emits light in a random direction. The shape of the scattering centre is less important for Rayleigh scattering, as the dimensions of the particle lead to it being treated as a point scattering source. Further, Rayleigh scattering shows significant wavelength dependence, with the intensity of scattered light varying by $I \sim \lambda^{-4}$.

When the particle diameter is approximately the wavelength of light, ($d_\mathrm{p} \approx \lambda$) Mie scattering describes the process undergone. Mie scattering is the result of scattering from a particle large enough that it cannot be considered a point source, and shows shape dependence, largely applied to spheres, though other shapes are possible with adaptations to the theory. Mie scattering is largely wavelength independent, and so tends to result in a white appearance from materials. The size of the scattering body is important, with forward scattering becoming more favoured with increasing particle diameter. When $d_\mathrm{p} \gg \lambda$, Mie scattering can be approximated by geometric optics.

Both Rayleigh and Mie scattering processes are elastic, with no change to the wavelength of the light before and after scattering. Inelastic processes occur when there is a change in wavelength, and gives rise to a number of effects, including Raman scattering.

Tyndall scattering is an important optical property of many colloids. Tyndall scattering occurs in colloidal solutions, with scattering bodies between 40 and ~1000 nm in diameter, on the order of the wavelength of light, and above the usual range for Rayleigh scattering. The Tyndall effect does show the same $I \sim \lambda^{-4}$ dependence of Rayleigh scattering, resulting in blue light being more strongly scattered. This causes colloidal dispersions that exhibit this property to

appear blue when viewing reflected or scattered light, and to appear orange when viewing transmitted light.

The inhomogeneities in a system consisting of particles can also arise from the spacing between particles in ordered, periodic structures, which is known as Bragg diffraction. Briefly, Bragg diffraction occurs when light is incident upon a periodic structure, and the scattered light emitted from the structure either constructively or destructively interferes, depending on the wavelength and the angle of incidence. One natural example of such a phenomenon is the appearance of colour in precious opal, with opal being effectively a colloidal crystal of silica particles in water [83]. Gao *et al.* (2017) investigated using nanoparticles for the purpose of producing materials that exhibit structural colour [84]. While opalescent solid structures have been produced previously [85-87], they have provided an example of the applicability of using artificial opalescent structures for colouring cotton fabrics.

1.3.4 Preparation of nanofluids

Nanofluids are synthesised by two distinct methods. One is a two-step method, in which nanoparticles are first bought, synthesised, or produced in some manner and then dispersed in the fluid with any aid to the dispersal necessary. The other is a single step method in which the particles are directly synthesised in the base fluid. Each method has distinct advantages and disadvantages [88].

In the two-step method large quantities of standardised particles can be purchased and dispersed in fluid, however, there may be restrictions in the surface groups of the particles able to be chosen. In the single step method, the particles can be synthesised and tuned during synthesis to the desired functionality, however there may be other limitations on the choices of base fluid available.

Preparation of the nanoparticles directly, allows for improved tuning of the base particle properties: the particle size distribution can be controlled and tweaked, meeting the needs of the experimentalist. The base fluids chosen to prepare the nanofluids are just as varied as the solid additives chosen; they include fluids such as water, ethylene glycol and oils, including silicone oils, petroleum-based oils and natural oils like coconut oil [88, 89]. As nanoparticles have exceptionally large surface areas relative to their volume the attractive force between the nanoparticles is sufficient to cause significant agglomeration resulting in the reduction of desirable properties of the nanofluid, unless steps are taken to prevent this.

Stabilisation of nanofluids has been achieved by both steric and electrostatic methods using a wide variety, or combination of, methods. These include addition of surfactants [39, 47, 80, 90, 91], grafted polymer groups [20, 92], oxidation of the surface [93], control of the solution pH [47], coating with thin inorganic layers [48], or small molecular additives [22, 40, 41].

The addition of a surfactant is a useful method for inducing solution stability, as the surfactant can be selected or tailored for the specific particle-solvent combination of interest. They have been applied to a variety of nanoparticles, including metals, ceramics and carbon nanotubes. However, introducing surfactants increases the rheological complexity of the solution, and can increase the nanofluid viscosity, introduce foaming effects, or reduce the desired properties of the fluid [94-96]. Nguyen at al [97] measured a significant hysteresis in the properties of dispersant-stabilised nanofluids when heated above a critical temperature, it was suggested this would correlate well with the degradation or dissociation of dispersant at high temperatures, thus increasing aggregation within the sample and giving the property degradation observed.

Small molecular attachments can avoid these problems, as they do not usually constitute a significant enough portion of the nanoparticles to affect the intrinsic nanoparticle properties. Unfortunately, previous work in which small molecules are used to stabilize nanoparticles in solution has often required extensive particle modification to be performed [98]. Surface functional density of attachments is also rarely commented upon or quantified for small molecules, in comparison to large polymer attachments [99, 100]. Recently, however, more attention has been paid to the critical effect of surface coverage of functional groups. The surface coverage of mercaptoundecenoic acid on gold nanoparticles has been found to be of paramount importance for their application: Ansar *et al.* found that with coverages of 60 %, the particle dispersion properties were insufficient, but with 100 % surface coverage the catalytic ability of the particles were blocked, with an optimal surface coverage determined to be 90 % [14].

1.4 Silica nanoparticles

Silica nanoparticles (SiNPs) were selected to produce the nanofluids used in this work. SiNPs are used conventionally because they have a well-known and controllable surface chemistry, they can be made easily in defined sizes with low size dispersity, and their preparation can be undertaken at large scale without sacrificing the desired particle properties.

Conventionally, SiNPs are prepared by the Stöber method [101]. This method uses concurrent hydrolysis and condensation of tetraethylorthosilicate (TEOS) to produce SiNPs of well-defined sizes, terminated by hydroxyl groups. These particles are then functionalised by condensing a functional group bearing silane onto the surface, resulting in particles with a defined surface functionality [102-105]. Whilst producing particles with defined and controllable size, this method can lead to low surface functional densities of the desired functional group [98]. Alternatively, the TEOS and functional group bearing silane can be co-condensed in the particle growth [106].

An alternative, and simpler method was created by Nakayama and Ishimura [107], in which a single silane precursor, bearing a functional group, is reacted in a one-pot reaction to produce particles of the desired size and functionality. This method was modified by Mangos *et al.* [108], producing on a larger scale, particles of controlled size and functionality.

1.4.1 Growth mechanism

Growth of organosilane monomers into large structures is influenced by the pH, temperature, alkoxide concentration and solvent effects [109]. If the silica structure is formed at low pH (below 7), it results in a porous 3D gel. Under acidic conditions, the oligomers of particles formed are largely uncharged, facilitating their contact, allowing greater connectivity to occur. Under basic conditions, the intermediate silanol group are highly charged, stabilising the particles as they form, allowing them to remain discrete [110]. The size and uniformity of the particles are determined by the specific conditions of formation. Solution pH influences the structure produced as illustrated in Figure 1.1 [111].

With some modifications to the synthesis conditions, alternative silane sources can be used as single silane precursors. Such sources shown to be usable include 3-mercaptopropyltrimethoxysilane (3-MPTMS) [107, 108, 112].This allows for a higher surface functional density of the group of interest, as each condensing silane unit has a functional group present. Regardless of the silane precursor selected, the reaction can be expected to proceed as illustrated in Equation 1.2-Equation 1.4.

$$\text{Si(OR)}_4 \underset{\text{Condensation}}{\overset{\text{Hydrolysis}}{\rightleftharpoons}} \text{Si(OR)}_3\text{OH} + \text{ROH}$$

Equation 1.2

$$2(\text{Si(OR)}_3\text{OH}) \underset{\text{Hydrolysis}}{\overset{\text{Condensation}}{\rightleftharpoons}} (\text{OR})_3\text{SiOSi(OR)}_3 + \text{H}_2\text{O}$$

Equation 1.3

$$\text{Si(OR)}_3\text{OH} + \text{Si(OR)}_4 \underset{\text{Alcoholysis}}{\overset{\text{Condensation}}{\rightleftharpoons}} (\text{OR})_3\text{SiOSi(OR)}_3 + \text{ROH}$$

Equation 1.4
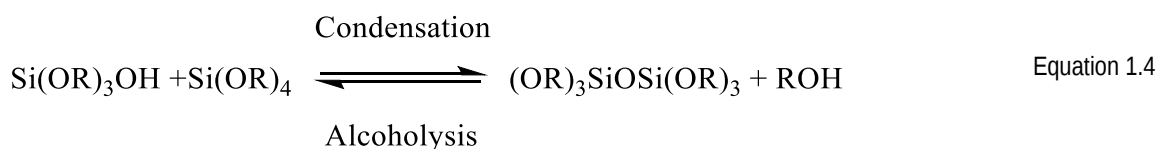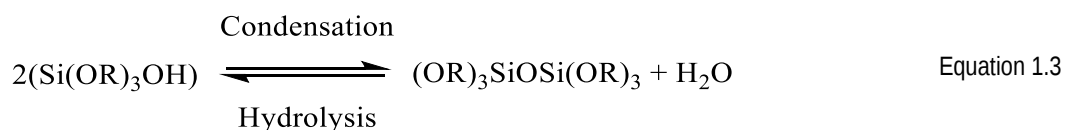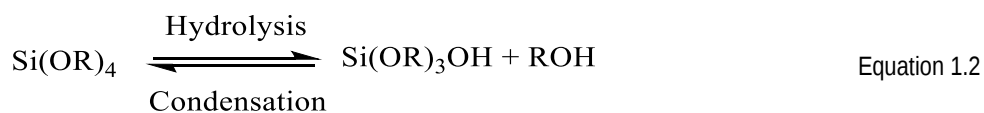
The dimers are then formed into linear, then cyclic trimers, forming the particle precursors through repeated hydrolysis and condensation reactions [111]. The type of structure, size of primary particles and polydispersity of particles are influenced by the solution pH, solvent, monomer ratio and other factors.

Under basic conditions, the condensation reaction is usually considered to progress through the nucleophilic attack of a deprotonated silanol group on an uncharged silanol. Following the condensation further condensation reactions can occur, increasing the size of the particle. As -OSi is a better electron withdrawing group than OH, which in turn is better than OR, this means the more substituted silicon centres are favoured for subsequent reaction, compared to monomers or dimers, resulting in particle growth [113].

The monomer, dimer or larger units are electrostatically stabilised under basic conditions. The pH selected for the Stöber synthesis is usually in the order of pH 11-12. This places it above the pK_{a1} of orthosilicic acid (9.8) but below the pK_{a2} (13.2) [109, 111]. This means that for each silicon unit only one silanol group would be expected to be deprotonated during the reaction. That is, the monomer units would be monovalent, the dimers mono- or divalent (depending on silanol distribution) etc.

14
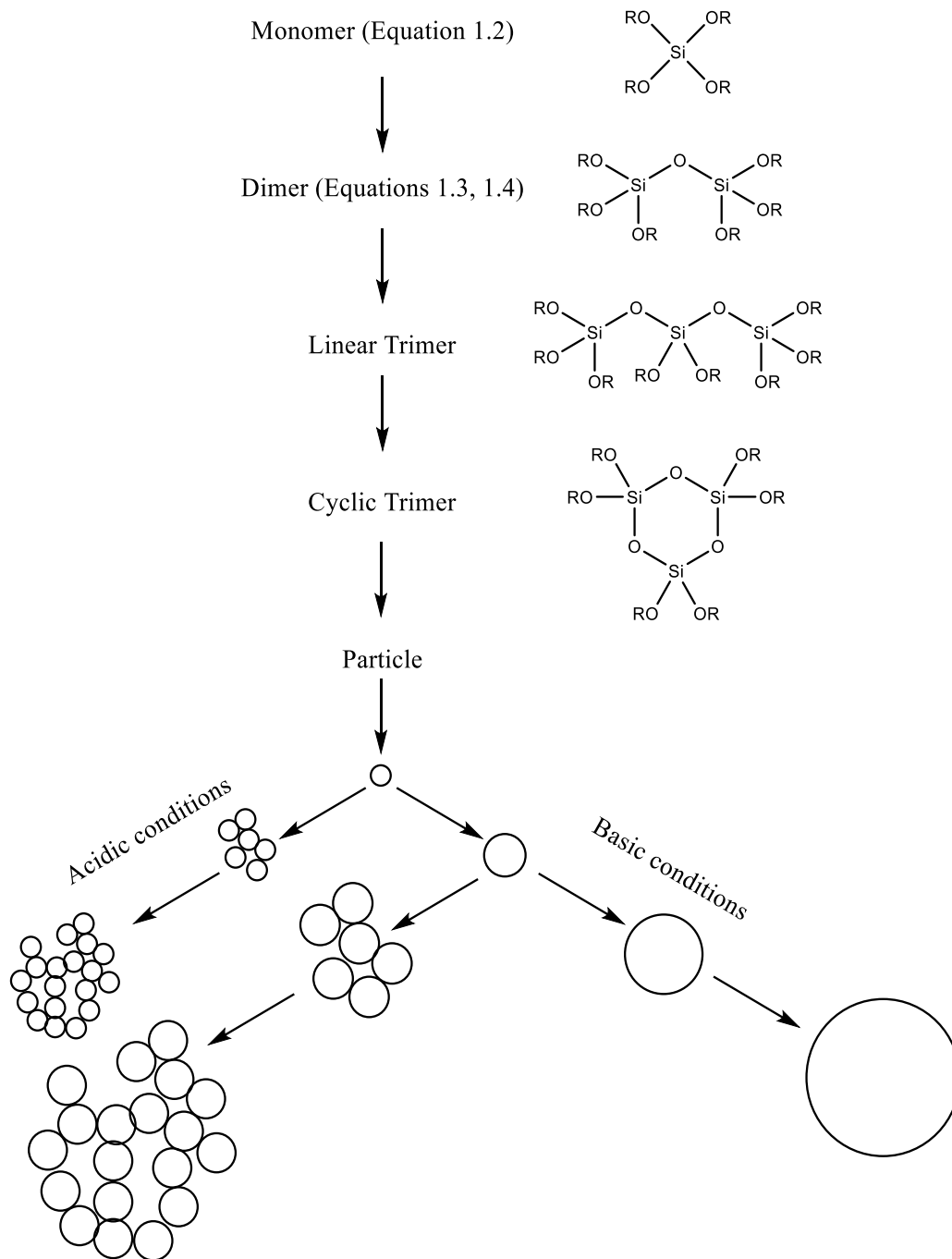
Figure 1.1: Silica structure formation pathways from silane precursors

The units formed are then grown into larger particles. The precise mechanism of this particle growth is well studied in literature, with three major proposed mechanisms: a nucleation-growth model such as the LaMer model, a controlled aggregation model, or a combination of both mechanisms, either concurrently or sequentially [110]. A general representation of these methods is provided in Figure 1.2.
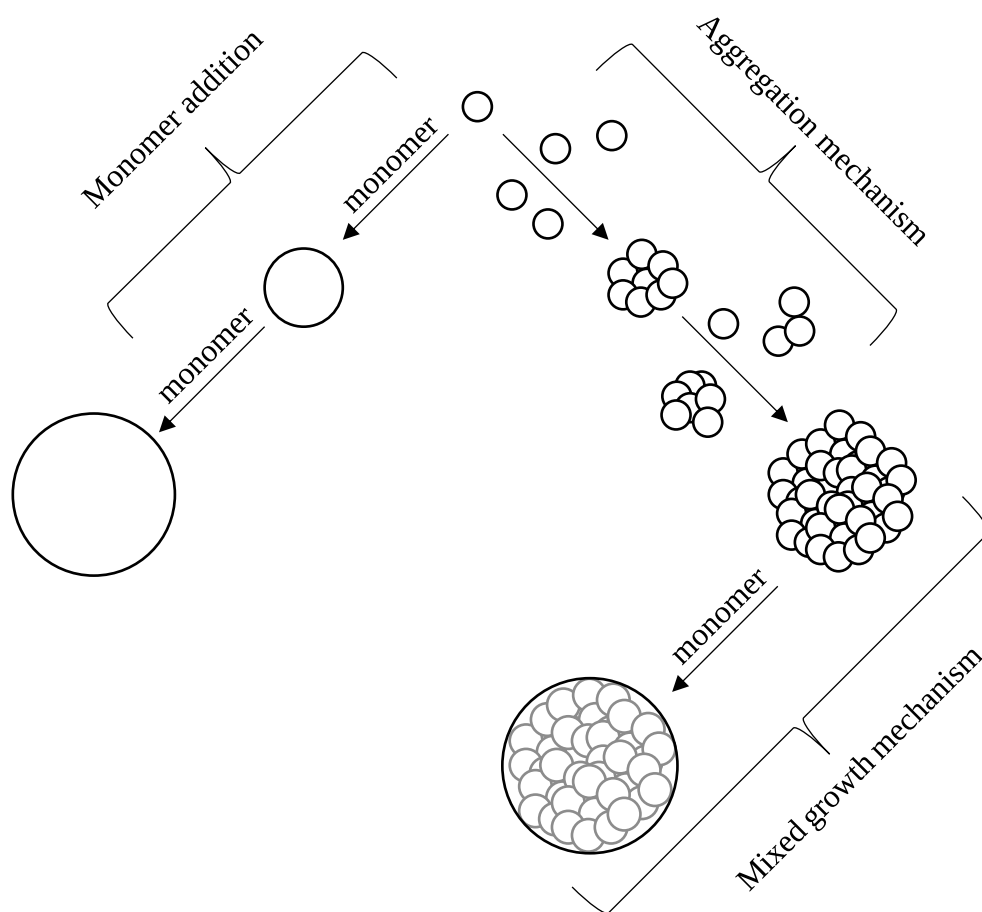
Figure 1.2: General representation of Stöber silica particle growth by monomer addition, aggregation, or mixed mechanisms

LaMer model of particle growth posits the monomer concentration in solution increases to a critical level, at which point nucleation sites form [114]. This reduces the concentration immediately below the critical value, preventing the formation of additional nucleation sites. Under basic conditions, these sites are charge stabilised in solution, preventing their aggregation. The particles then grow through the addition of monomer units to the growing sites, resulting in larger particles [109, 110].

The controlled aggregation mechanism suggests nucleation continues throughout the reaction, forming small primary particle units [115]. These primary particles are small, showing poor colloidal stability and a tendency to aggregate. The aggregates form into larger, more stable particles throughout the reaction.

Mixed models suggest both reactions occur, with the formation of primary, aggregating units as the first stage of the reaction [109]. The primary particles form and aggregate until the monomer concentration in solution falls below the critical nucleation concentration preventing

the formation of new primary particles. Following this, the remaining monomer diffuses onto the particle surface [116]. This forms a smooth layer of silicon over the surface, obscuring the rough features of an aggregated particle. Some researchers have suggested the nucleation continues throughout the second stage of the particle growth, in conjunction with the monomer diffusion [109].

Research into the precise growth mechanism of Stöber silica particles has been undertaken by many researchers across a broad timeframe and considering a wide variety of conditions, as well as requirements for the formed particles [85, 101, 103, 106, 107, 109, 111, 113, 116-119]. This has led to a variety of reaction mechanisms being proposed, each of which may apply under the specific conditions investigated. This suggests that for the optimal growth of different monomers the conditions being used must be tested to enable the production of the best nanoparticles possible.

In this work, 3-MPTMS is used as the precursor to generate silica nanoparticles. Mechanistically the growth of the particles is considered similar to that of the conventional Stöber synthesis using TEOS. MPTMS, however, has different solvent interaction, initial rates of hydrolysis and stability of primary particle nuclei formed in solution. Ishimura and Nakamura [107, 112], as well as Mangos et al. [108] have used 3-MPTMS for particle synthesis and produced solvent conditions useable as a starting point for determining the optimal conditions for particle synthesis using 3-MPTMS as the sole silane precursor. The general reaction is summarised in Figure 1.3.
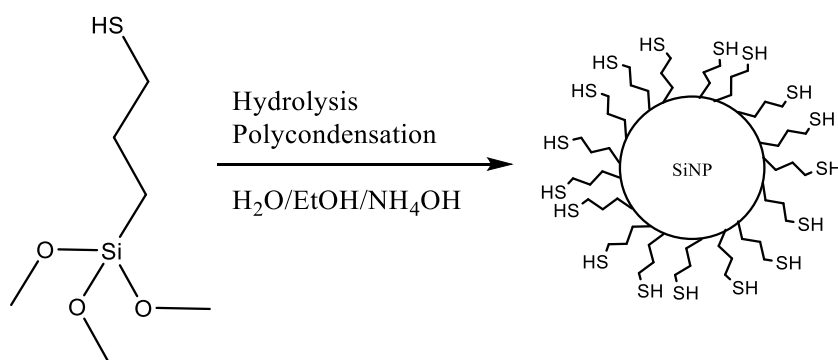
Figure 1.3: Summarised particle synthesis reaction from 3-MPTMS silane precursor via modified Stöber synthesis

1.4.2 Functionalisation of silica nanoparticles

Conventionally, particles prepared from TEOS are subsequently functionalised by silanisation with using a silane group terminated with the desired functional group, and if necessary further

reactions are undertaken from this group. However, it has been found that this can result in poor surface functional group densities, significantly lower than that of the approximately 5 OH groups·nm^{-2} present on the surface of the unreacted TEOS particles group [98, 120-122]. The SH-SiNPs prepared from 3-MPTMS, however, have been found to have great capacity for surface functionalisation [108], possessing a reactive thiol moiety on each silane unit in the particles.

Thiol-ene click chemistry allows for rapid, high-yielding functionalisation of the particle surface with a variety of functional groups. While the level of reactivity varies with the attached moiety, effectively any functional group with an alkene group is a valid target for the reaction [123]. This chemistry was selected due to its proven ability to produce high functional density particles, with a variety of terminal groups available. It has been shown that using this chemistry, particles with surface functional densities approaching the maximum theoretical hydroxyl groups presented on the surface can be obtained [108].

1.4.2.1 Thiol-alkene chemistry

Thiol-alkene chemistry is a well-studied "click" reaction. Click reactions are high yielding, stereoselective, fast, and are thermodynamically driven, making them well suited to the production of functional materials [124, 125]. Further, the product of the reaction, a functional group tethered to the particle via a thioether bond is stable under aqueous conditions.
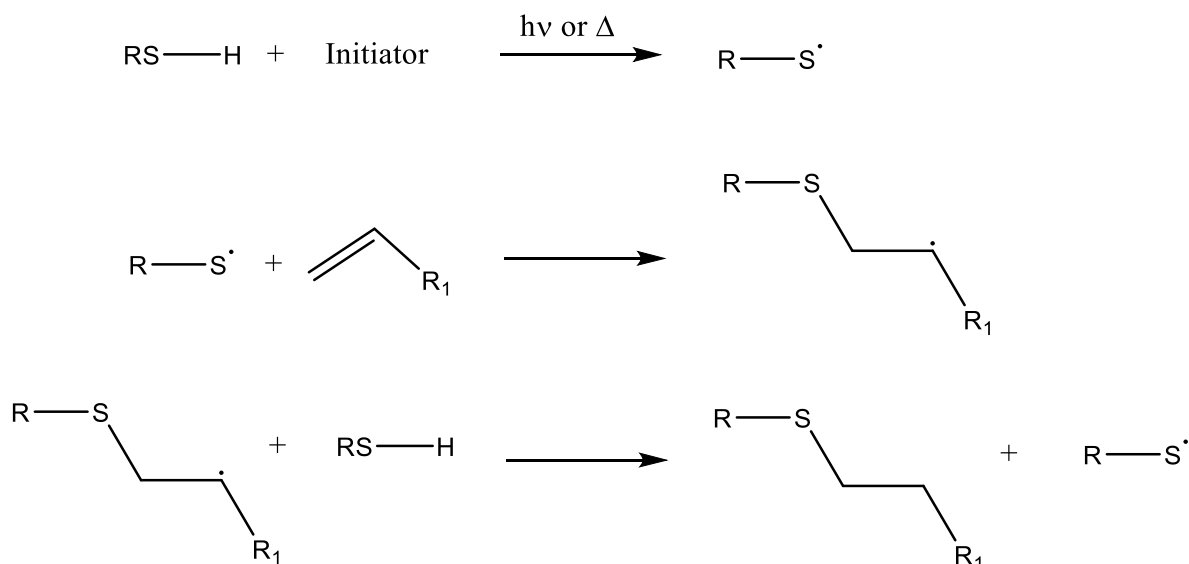
Figure 1.4: Radical initiated thiol-ene click-chemistry reaction schematic

Figure 1.4 displays the thiol-ene reaction. Briefly anti-Markovnikov addition of the thiol compound across the alkene occurs, producing a thiol-ether bond [124, 126]. Different alkene

structures show different degrees of reactivity towards the click reaction [123], however, almost any alkene-group containing molecule is useable.

The particle thus gains a tethered functional group allowing for the introduction of a wide range of moieties on the surface. The addition reaction can be driven either by a radical source (driven by light, heat or both) or by the base or nucleophile catalysed Michael addition.

1.5 Characterisation of silica nanoparticles and nanofluids

The aim of the work is in the understanding and correlation of the properties of the particles, individually and in interaction with each other, and the overall properties of the produced solution. A variety of techniques were selected to help elucidate this relationship. Further, there was interest in the properties of the solutions as their conditions changed. Their pH, ionic strength and concentration were also examined for their effects on solutions prepared.

1.5.1 Nanoparticle sizing

Understanding particle size and size dispersity is critical to understanding the particle properties. Myriad techniques for determination of size and related properties are highly desirable. It has been shown that using a single technique for the measurement of particle size can result in biased measurements, through insufficient sample size of the particles to be measured, to the dispersity or modality of the sample confusing the measured particle size. For this reason, particles were measured using both DLS measurements, and direct particle imaging using scanning electron microscopy (SEM).

1.5.1.1 Dynamic light scattering (DLS)

In DLS measurement, a light is scattered by scattering bodies in a solution and this is used to determine their diameter [127]. Scattering bodies are varied, including particles, polymers, or proteins. Light incident on particles in solution is scattered in all directions (so long as the particles are small, larger particles favour forward scattering). A detector is placed at a specific angle to the sample; in the DLS system used, this angle is 173°. The detector measures the scattered light producing a speckle pattern, bright spots occurring due to constructive interference of scattered light, dark spots due to destructive interference. This results in either constructive or destructive interference. The measurement is repeated for short periods and compared across the time measured [127].
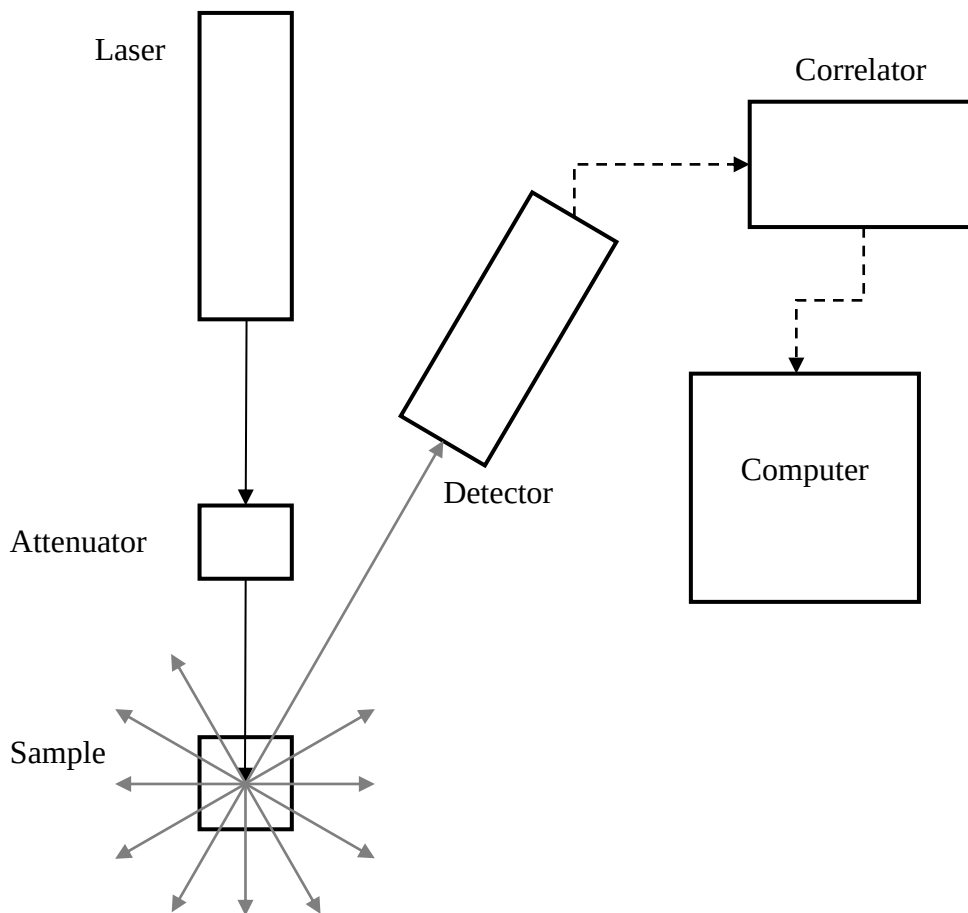
Figure 1.5: Schematic of DLS apparatus in operation

Particles in solution are constantly moving, as they experience Brownian motion [57, 58]. This is movement due to the bombardment of the particles by molecules and atoms within the solution. Smaller particles move faster due to this effect than larger particles. This means that the pattern of destructive and constructive interference will change more rapidly for small particles than larger particles. The correlator compares the signals in the speckle pattern to determine how rapidly the changes to constructive and destructive interference are caused, and thus how rapidly the particles are moving. This is then converted into an apparent diameter of the particle in solution [128].

One important consideration to be made with DLS is that the measured diameter of the particle in solution is always going to be greater than the real diameter of the particle. The particle in solution does not exist in isolation; it is surrounded by a shell of solvent molecules. In water, the size of the particle and its shell is termed the hydrodynamic volume and this is the volume

measured. This volume is variable, based on multiple factors, such as the surface charge of the particles of interest and the ionic strength of the solution.

DLS is also a technique that must be used with some care in the analysis of the data. If the solution being examined is monomodal, the measured value produced by the DLS can be expected to correlate well with other techniques [129]. If, however, the solution is bi- or multi-modal, greater effort must be made to correctly interpret the data [129].

If the particles in solution exist in two different populations, however are similar enough in size to each other (within approximately 1 decade) the separation of the particles may prove impossible, and the sample will be reported as containing a particle with an average size somewhere between the two populations, and a correspondingly high dispersity. If the particles are of greatly different size, it must be remembered that large particles are better light scatterers, and as such may be overrepresented in the data, compared to the real population of the sample. With bi- and multi-modal samples, the Z-average (Z_{av}) measure of particle diameter is inaccurate and should not be used in favour of the peak positions [129].

Measuring the hydrodynamic radius of a sample in solution can provide additional information on the particle state in solution. Aggregates of particles can behave as single large particles in solution, including in measurement by light scattering processes. This results in light scattering techniques being sensitive to the aggregation state of the sample, which gives some information as to the dispersion stability [130]. However, this may also produce artificially high particle areas, or prevent accurate measurement if the particle aggregation is too significant. When using DLS it is therefore always of benefit to use an additional technique for measuring the diameter of the sample of interest [129].

1.5.1.2 Scanning electron microscopy

SEM is a technique for imaging a surface at resolutions unattainable by a conventional light-based microscope. When using SEM, a focussed beam of electrons fired at the surface in a raster pattern. The electrons impact upon the surface and interact in different ways with the surface. By combining the beam position with the results from the detector an image of the surface can be built up. Different information can be gained from the surface by changing which detector is being used for the imaging [131, 132].

When an electron impacts the surface the way it interacts with the surface is dependent on numerous factors, including its energy and the surface composition [132]. For SEM the electrons of interest are backscattered electrons and secondary electrons. Backscattered

electrons are electrons that impact upon the sample and are bounced out. Backscattered electrons are useful for measuring multiphase samples, as they provide better contrast between phases Secondary electrons occur when an electron enters the sample and displaces an electron that is ejected from the sample. This ejected electron is a secondary electron. As this process is only feasible in the upper section of the sample, secondary electrons are most useful for providing topographical and morphological information about the sample.

When the electrons impact the surface they are also capable of producing X-rays characteristic of the atom impacted. This is useable for energy dispersive X-ray spectroscopy (EDXS): the characteristic X-rays from the surface are useable to identify specific elements in the sample [132]. For functionalised nanoparticles, this can provide chemical information indicating the presence or absence of elements that only occur in the reacted sample.

The great advantage of SEM in measuring particle sizes is that the particle diameter is measured directly (with an additional conductive coating of gold or platinum that has a known thickness). Therefore, when enough particles are measured the average diameter can be taken as a direct value for the particle diameter. However, determining particle diameter in this fashion can be time-consuming, requiring measurement of a large number of particles across multiple measurements of a sample. This means that care must be taken during SEM measurements to prevent bias in measurement, such as by preferential measurement of one size range of particles in a multimodal sample.

Unfortunately, SEM is also unable to provide information of the particle in solution. Because SEM samples require drying all information about particle behaviour in solution is lost. Some information is provided by the state in which the particles dry, with differing levels of ordering possible based on the stability of the dispersion; however, this behaviour is also affected by a number of other factors during drying.

1.5.1.3 Surface area determination by BET analysis

Brunauer-Emmett-Teller (BET) analysis of nitrogen sorption measurements of solid surfaces is a widely used method of determining the surface area of a sample of nanoparticles. A large sample of the solid of interest (approximately 100 mg though dependent on the surface area of the material to be measured) is dried and degassed for measurement in a fixed volume. The quantity of the inert gas adsorbed to the surface is measured at multiple relative pressures. By using the known area of the inert gas adsorbing to the surface the specific surface area can be determined, along with sample porosity and an indication of particle size [133].

1.5.2 Characterisation of nanoparticle chemistry

1.5.2.1 Zeta potential

Zeta potential is a technique for the measurement of the electric potential of a particle at the slipping layer that occurs between the particle and the bulk solution [77]. Zeta potential measurement as a technique is useful for providing information on the electrostatic stabilisation expected for a given colloidal solution. Zeta potential does not give an overall indication of stability of a solution, notably steric stabilisation is not measurable by zeta potential at all. However, for samples that are electrostatically stabilised, the zeta potential can provide an estimate as to the dispersion stability, based on the magnitude of the zeta potential measured [134]. Positive and negative zeta potentials both indicate the potential for electrostatic stabilisation, indicating positive or negative surface charge respectively. As each particle in solution experiences the same conditions, their surface charges are the same and thus the particles are stabilised by the repulsive electrostatic forces.

1.5.2.2 ATR-FTIR spectroscopy

Fourier transform infrared (FTIR) spectroscopy is a simple method that provides information on the functional groups within a sample [135]. Infrared light incident upon the sample causes bond vibrations within a sample. Only bond vibrations that result in a change in their dipole moment produce peaks within an FTIR spectrum.

ATR-FTIR spectroscopy is a method of measuring the FTIR spectrum of a sample using a solid (or liquid) sample, requiring no additional preparation [136]. The infrared light is shone into an attenuated total reflectance (ATR) crystal in such a way as to experience total internal reflection at least one time from the internal surface of the crystal in an area in which it is in contact with the sample. This total internal reflection produces an evanescent wave that passes into the sample surface. The beam is measured by a detector as it leaves the crystal. From the absorbencies in spectrum produced, the vibrational modes of the functional groups in the sample can be determined.

1.5.2.3 Thermogravimetric analysis

Thermogravimetric analysis (TGA) is a technique for characterising material samples by heating a known mass of sample under a continuous flow of gas that is used to characterise pyrolysis and decomposition processes of a sample [137-139]. The gas selected is important as it will determine the processes the material may undergo [140]. TGA is useful for identifying material degradation, decomposition, oxidation and reduction, and other thermally initiated

processes. The choice of gas enables or prevents some of these processes from occurring, and the gas can be changed partway through a procedure to characterise the material degradation and degradation products further.

TGA is useful for measuring materials samples as it is able to provide information that, when combined with knowledge of the structure of the material, can provide insight into the material composition. Desorption of volatiles can be measured, and, in certain cases with analysis of the proportionate weight of the sample removed, the stability of various portions of the sample can be indicated [108, 138, 141, 142].

In TGA, the sample is placed into a pre-weighed pan, which is suspended on a precision balance, along with a reference sample. This is in a temperature programmable furnace that is used to heat the samples. A purge gas is used throughout the experiment. This gas can be inert, such as N_2 or argon, when monitoring non-oxidative decomposition of the sample, or oxidative, such air, when removing the organic components from the sample.

1.5.3 Viscosity and rheological measurements

Viscosity is the resistance to flow experienced by a material, based on the internal friction of the flowing units in the material. These flowing units may be molecular, like in a solvent, or made of larger units, such as particles, or combinations of particles and tightly bound surface layers. Colloidal dispersions and nanofluids in particular, have been noted to show increased viscosity compared to their base fluids, which can be attributed to the increase in internal friction due to the dispersed phase.

1.5.3.1 Rheological measurements

Rheological behaviour is an interpretation of the relationship between the stress, which is the force applied to a unit area of a sample, and the strain, which is a dimensionless measure of the amount of deformation experienced by a material [143]. Strain is often noted by the strain rate, in units of s^{-1}. Most commonly, rheological measurements are performed using a shearing deformation, often described using a two-plate model (Figure 1.6). A sample is between two parallel plates, one moving, and the other stationary. The shear force (F) applied to a plate of area (A) gives the shear stress, $\tau = F/A$. Shear rate ($\dot{\gamma}$) is measured by the resultant velocity (usually a rotational speed).
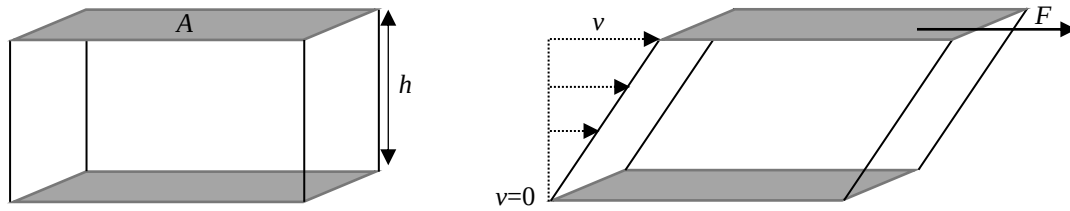
Figure 1.6: Two plate model of shear deformation. A sample of fluid is between two plates of area, *A*, separated by a gap, *h*. A shear force, *F*, applied causes the upper plate moves with velocity, *v*, and the lower plate is stationary.

A sample's viscosity is the ratio of the shear stress to the shear rate, $\eta = \frac{\tau}{\dot{\gamma}}$, and can be thought of as a measure of the sample's resistance to flow [143]. If the viscosity of a sample is constant with applied shear force, the sample is considered Newtonian. Fluids whose viscosity shows dependence on shear rate are non-Newtonian.

Rotational rheometers use different geometries to measure sample viscosity, three common geometries are illustrated in Figure 1.7 [143]. Parallel plate geometries allow for high viscosity samples, such as gels, to be measured relatively easily. They are useful for large-particle dispersions, as the gap size is directly controllable. However, the shear rate across the plates is not uniform and requires correction. The sample volume required varies based on the size of the plate and the gap size, but can be less than 0.5 mL. Cone-and-plate geometries consist of a flat plate, and a truncated cone. The sample gap is fixed, preventing the measurement of large particle dispersions (typically the largest particle should be ten times smaller than the gap size); however they produce a uniform rate of shear across the entire sample, simplifying analysis. Sample size is dependent on the radius and angle of the cone. Double concentric cylinders are useful for low viscosity samples. They show near uniform shear rates throughout the sample and are not prone to ejection of the sample from the geometry at high shear rates. They, however, require large volumes of sample, approximately 10 mL.
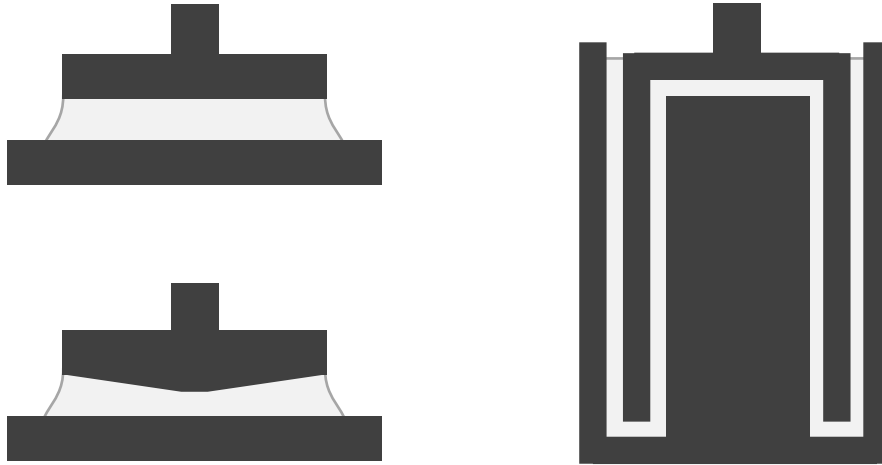
Figure 1.7: Cross-sectional illustrations of parallel-plate, truncated cone-plate, & double concentric cylinder geometries

1.5.3.2 Dispersion viscosity

For dispersions of solid particles, the dispersion viscosity shows significant dependence on interparticle interaction [2, 144-146]. Such interactions are dependent on particle spacing in solution, which in turn is dependent on the volume fraction of the particles. The simplest theories regarding particle spacing in solution assume the particles are uniform non-interacting hard spheres, which do not show an electrical double layer.

In the ideal case of non-interacting particles, the particle separation can be determined mathematically. Frankel and Arivos (1967) modelled the dependence of interparticle separation on the particle volume fraction [147], and this was extended by Hoffman and Kevelam (1999) for arbitrary maximum packing fractions, and for dispersions of polydisperse particles, shown in Equation 1.5 [148]. The separation was modelled relating the separation to the volume fraction and the surface mean diameter (d_S), or the equivalent diameter of a sphere with the same volume:surface area ratio as the particle of interest.

$$D_{SS} = d_S \left(\sqrt[3]{\frac{\phi_m}{\phi}} - 1 \right)$$

Equation 1.5

Where

D_{SS} = surface − surface distance

d_S = mean surface diameter ≡ Sauter mean diameter

ϕ_m = maximum packing fraction

ϕ = volume fraction of particles

The interactions of the particles in the solution are dependent on their volume fraction with a brief summary of different regimes presented in Figure 1.8 [149]. The dilute regime, when particle volume fractions are below approximately 0.05, shows negligible particle interaction, with the interparticle distance sufficiently large as to prevent interaction between particles. The concentrated regime occurs when the particle interaction becomes an important factor in the solution, but while the particles remain uncaged by their neighbours and free to move. For hard spheres when the concentration reaches the glassy transition point ($\phi_G = 0.58$), the particles are confined to cages, referred to as caging, causing an effective increase in viscosity and the development of an apparent yield stress [150, 151]. Lower concentration phase changes for hard spheres are also present at $\phi_F = 0.494 < \phi < 545 = \phi_M$, the freezing and melting volume fractions, during which both liquid and colloidal crystal structures exist, with crystallisation progressing as concentration increases [149]. The packing describes a solid at the random close packing fraction, ($\phi_{RCP} = 0.64$) with a monodisperse, hard-sphere maximum packing fraction at the face-centred cubic packing fraction ($\phi_{FCC} = 0.74$).
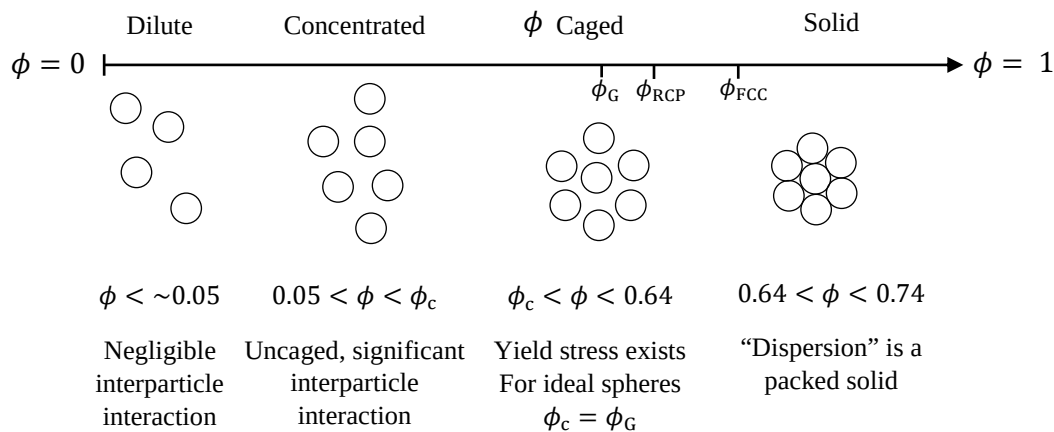
Figure 1.8: Diagram of particles in dispersions at increasing concentrations, adapted from Quemada and Berli (2002) [149].

It is worth noting that the maximum packing fraction is capable of increasing above 0.74 for distributions of spheres, which describes the particles. The increased packing fraction available to particle distributions is a function of the dimensionless standard deviation [152].

The particles are, however, not hard spheres. They may exist as agglomerates, or be stabilised in solution by a steric layer, or an electrical double layer that repels the particles from each other, preventing their aggregation. Equivalently, this can be represented as a bound liquid layer at the particle surface. In the work of Yu & Choi [153] or Avsec and Oblak [154], the length of the bound-liquid layers are used to estimate effective particle volumes in solution

with good agreement found with experimental results of particle thermophysical properties, based on appropriate bound-liquid layer length estimates.

The double layer of the particles can be predicted by the formula [72]:

$$\frac{1}{\kappa} = \left(\frac{\epsilon_r \epsilon_0 k_B T}{2 n_0 z_i^2 e^2}\right)^{\frac{1}{2}}$$

<div align="right">Equation 1.6</div>

Where

$\epsilon_r = permittivity\ of\ solvent\ (for\ water\ at\ 25\ °C\ this\ is\ 78.6\ F.m^{-1})$

$\epsilon_0 = permittivity\ of\ free\ space$

$k_B = Boltzmann's\ constant$

$T = absolute\ temperature$

$n_0 = number\ of\ ions\ per\ unit\ volume\ of\ each\ type\ in\ bulk\ solution$

$z_i = valence\ of\ ions$

$e = electronic\ charge$

$\frac{1}{\kappa} = thickness\ of\ double\ layer$

The consideration of the double layer increases the particles effective radius, which increases the effective volume fraction. This then indicates that a given mass concentration of particles produces a higher volume fraction, which results in a lower onset of non-Newtonian behaviour. However, as the particle concentration increases the double layers around the particles can begin to overlap; this affects their interaction and the subsequent rheological properties of the solutions [78].

Once aggregated in solution the aggregates flow, and unless broken by an appropriate level of shear force the aggregates breakdown into smaller units [63, 155]. Theoretically, at infinite shear rate it would be expected that all interparticle interaction is effectively overcome by shear force, rendering the primary particles as the main component of the solution [156].

This can be used to interpret the rheological properties of the solution. The electric double layer of the particles can be considered as an effective part of the particles, increasing their volume for a given mass concentration. The effective volume can be calculated by the formula:

$$\phi_{\text{eff}} = \phi \left(\frac{r + \delta}{r} \right)^3 = \phi \left(\frac{r'}{r} \right)^3 \qquad \text{Equation 1.7}$$

Where

$$\phi_{\text{eff}} = effective\ volume\ fraction$$
$$r = particle\ radius$$
$$\delta = Debye\ length/stabilising\ layer\ thickness$$
$$r' = effective\ particle\ radius$$

Particle agglomeration also causes an increase in the effective particle size, which is again measurable by DLS to produce an effective particle size. A particle agglomerate with radius of gyration, R_{agg}, and fractal dimension, D, is defined as having n_{p} particles of radius r, by the relationship [157]:

$$n_{\text{p}} = \left(\frac{R_{\text{agg}}}{r} \right)^D \qquad \text{Equation 1.8}$$

The internal volume fraction of this aggregate (ϕ_{a}) is given by:

$$\phi_{\text{a}} = \left(\frac{R_{\text{agg}}}{r} \right)^{D-3} \qquad \text{Equation 1.9}$$

$$\therefore \phi_{\text{eff}} = \phi \left(\frac{R_{\text{agg}}}{r} \right)^{3-D} \qquad \text{Equation 1.10}$$

Figure 1.9 shows a 2D schematic of caged dispersions of particles, showing hard spheres, stabilised particles and agglomerates. It can be seen that the stabilised particles require a significantly lower volume fraction of particles within the same volume of solution for the particles to become caged by their neighbours. The same is true of the agglomerates, and for these it is intuitive that the volume fraction required is dependent on the particle density within the agglomerate structure.
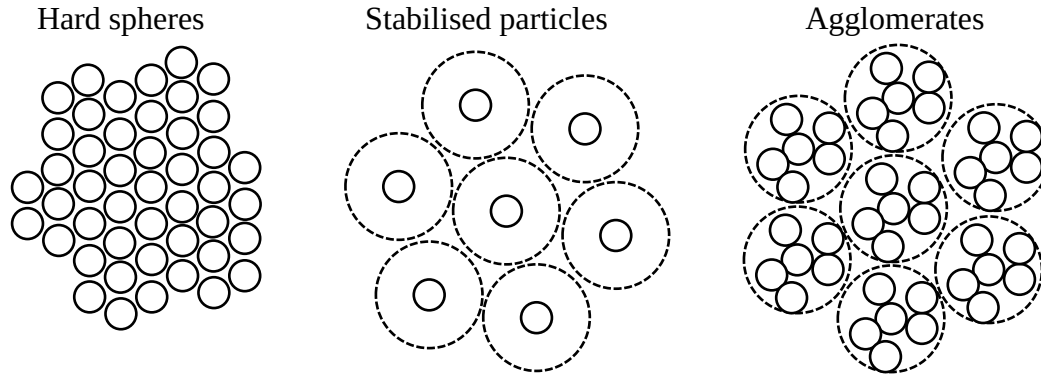
Figure 1.9: Representative 2D diagram of packing of hard spheres, stabilised particles, and agglomerates. Dotted lines indicate effective particle size in solution.

For both of these effects the effective particle volume is noted to change based on the shear rate considered, which is why commonly the two limiting cases of zero shear, and infinite shear are considered and used during rheological modelling [156]. The primary particle size can be determined from SEM measurements, and these can be used in conjunction to determine the effective volume fraction of the particles.

Multiple methods have been proposed for determining the effective viscosity of fluids prepared from nanoparticles. The simplest of these is the Einstein equation, applicable to dilute suspensions of non-interacting spheres [158]. This model, while simple, is not applicable for the nanofluids in this work, all of which are above the dilute limit at which this model applies.

The Ward equation [159], modified by Avsec and Oblak [154] to include the bound-liquid layer around the particles is given by Equation 1.11.

$$\eta = \eta_s \frac{1}{1 - 2.5\phi_{\text{eff}}} = \eta_s(1 + 2.5\phi_{\text{eff}} + (2.5\phi_{\text{eff}})^2 + (2.5\phi_{\text{eff}})^3 + \cdots)$$

Equation 1.11

Where

$$\eta_s = viscosity\ of\ solvent$$

Equation 1.11 has been found to give good agreement for dispersions of spheres for samples where $\phi_{\text{eff}} < 0.35$, however, disagrees with experimental values at greater volume fractions. Some models define a critical volume fraction within the equation, in order to account for unavoidable interparticle interaction at high concentrations.

The Krieger-Dougherty model [160] is a popular model for the viscosity of colloidal dispersions at different volume fractions, given by Equation 1.12.

$$\eta = \eta_s \left(\left(1 - \frac{\phi}{\phi_c} \right)^{-[\eta]\phi_c} \right)$$

Where

$$[\eta] = intrinsic\ viscosity\ ([\eta] = 2.5\ for\ spheres)$$
$$\phi_c = critical\ volume\ fraction$$

Better fits can be achieved with the Krieger-Dougherty equation if, instead of using an intrinsic viscosity of $[\eta] = 2.5$, which is the case for spherical particles, the intrinsic viscosity is instead treated as a fitting parameter [146, 161]. Also requiring consideration is that the volume fraction of interest for the determination of the solution properties is not that of the individual primary particles, but those of the effective particles in solution [63, 156, 162].

Effective particles in solution are the flowing "units" within the solution. In the case of non-interacting hard spheres in solution, these units are the primary particles. When the particles interact, the units change. Particle-solvent interaction results in the formation of a bound layer of liquid and charged particles at the surface of the particle, increasing the effective particle volume at the same mass fraction of particle. Aggregates of multiple particles also form effective particle units in solution, which flow as individual, non-spherical particles until they are broken apart by increasing shear forces [63, 162].

The Quemada model [163] is another popular model for the viscosity of dispersed systems of particles, given by Equation 1.13. It can be seen to be similar in form to the Krieger-Dougherty equation, and in fact, the two are the same if the condition $[\eta]\phi_c = 2$ is met.

$$\eta = \eta_s \left(\left(1 - \left(\frac{\phi}{\phi_c} \right) \right)^{-2} \right)$$

Mendoza *et al.* [156] have proposed an equation containing an explicit crowding term for the particles, which when considering the effective volume of the particles, returns a good estimation of the zero and infinite shear viscosities when fitted to the data. This model is given by:

$$\eta = \eta_s \left(1 - \left(\frac{\phi}{1 - \left(\frac{1 - \phi_c}{\phi_c}\right)\phi} \right) \right)^{-2.5}$$

<div align="right">Equation 1.14</div>

In this work Equation 1.12-Equation 1.14 are used to evaluate the relationship between the apparent viscosities determined at low and high shear rates for different concentration nanofluids, and to determine their critical volume fraction.

1.5.3.3 Rheological behaviour

Rheology is the measurement of the response of matter when a force is applied. This response can be Newtonian or non-Newtonian, generalized curves of these behaviours are displayed in Figure 1.10, represented in both stress-shear rate format (Figure 1.10a) and viscosity-shear rate format (Figure 1.10b). A Newtonian response is such that when a force is applied the same viscous response is exhibited, i.e. the fluid always shows the same viscosity, no matter what shear rate this is measured at.

Non-Newtonian responses can be broken into a number of categories, depending on whether or not the response shows a dependence on time. If the reaction is time-independent, that is, solely dependent on shear rate, the fluids are termed shear thinning or shear thickening, depending on whether the measured viscosity is larger or smaller at higher shear rates. Time independent behaviours may be considered as special cases of the time-dependent viscosity behaviours, as under real conditions there will always be a time delay, however it may be immeasurably small.

If a sample's measured viscosity decreases with an applied shear force, the sample is considered as shear thinning, presuming no measurable time-dependence is present [143, 164, 165]. Shear thickening materials are the opposite, showing an increase in viscosity with applied shear rate. On a stress-shear rate plot, these are determinable by the decreasing or increasing slope of the rheogram, while on a viscosity-shear rate plot the value can be read directly.

a) General flow curves:
- Yield pseudoplastic $(\tau_0 > 0, n < 1)$
- Bingham plastic $(\tau_0 > 0, n = 0)$
- Shear thinning $(\tau_0 = 0, n < 1)$
- Newtonian $(\tau_0 = 0, n = 1)$
- Shear thickening $(\tau_0 = 0, n > 1)$

Axes: τ (Pa) versus $\dot{\gamma}$ (s^{-1})

b) General viscosity curves:
- Yield behaviour
- Bingham plastic
- Yield pseudoplastic
- Zero shear viscosity
- Shear thinning
- Newtonian
- Shear thickening

Axes: η (Pa·s) versus $\dot{\gamma}$ (s^{-1})
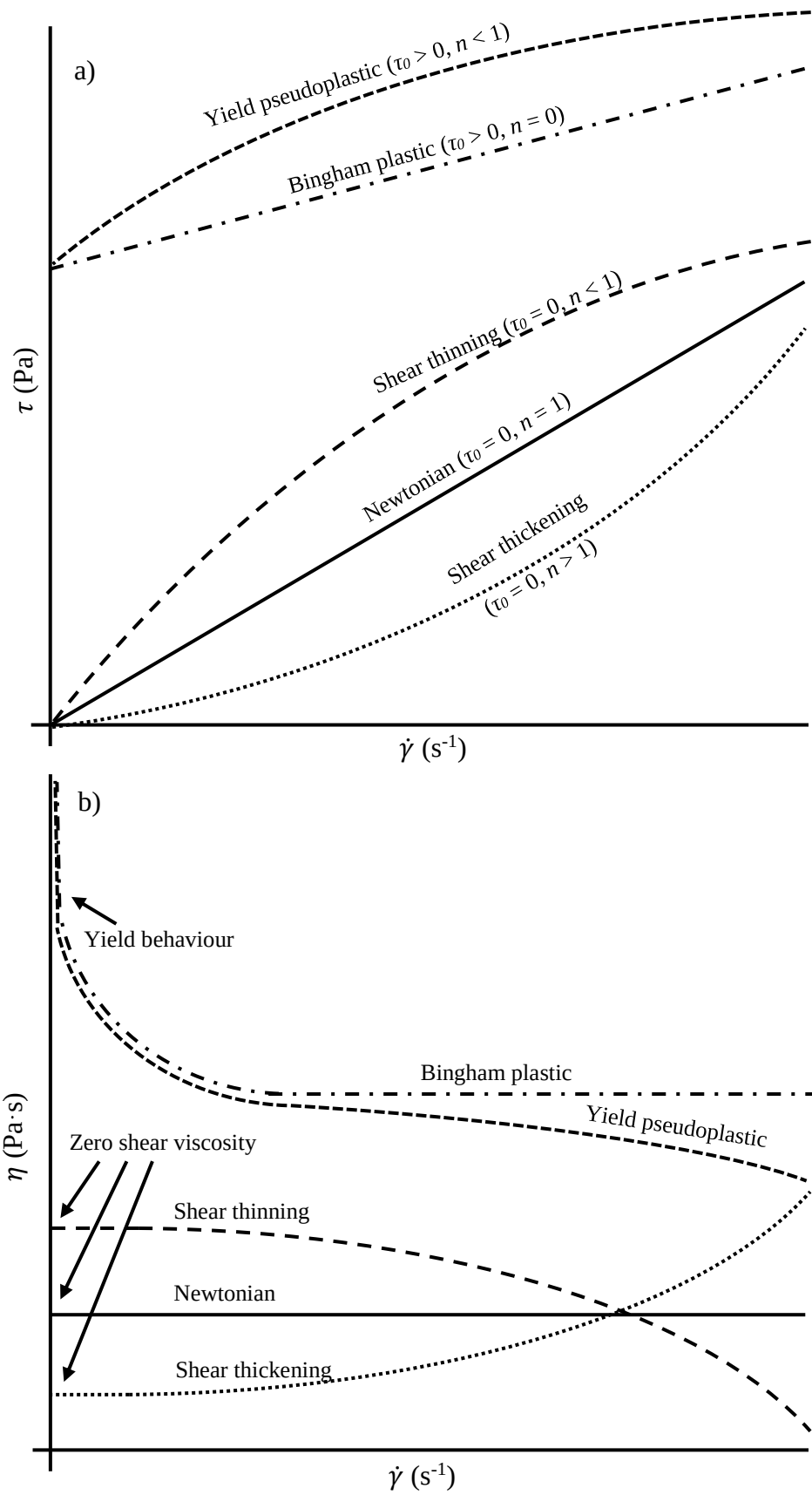
Figure 1.10: a) General flow curves of Newtonian and non-Newtonian fluids, b) general viscosity curves of Newtonian and non-Newtonian fluids

33

As the shear rate applied to a sample approaches zero, two behaviours can be expected. The sample viscosity approaches a specific value, termed the zero-shear viscosity, or the viscosity tends towards infinity, showing yielding behaviour. On a stress-shear rate plot the yield stress can be measured by extrapolating the curve to zero shear, giving the yield stress value. There is a considerable body of literature devoted to the concept of yield stress as a phenomenon concerning its origin, nature and existence [166-168]. However, the concept of yielding at a specific stress range is a highly useful description for many fluid flows [166, 169-171].

If a time-dependency is present, the fluid can be termed thixotropic, anti-thixotropic or rheopectic depending on the response it exhibits. Most commonly, a fluid showing a time-dependent non-Newtonian viscosity will show thixotropy. With an increasing applied shear rate, the measured viscosity decreases and a flow rheogram shows a decreasing slope with increasing shear rate (Figure 1.11). When the shear rate is then decreased, the curve is shifted to higher shear rates compared to the original curve, returning to the original stress value. If the original value is not returned, and instead a lower stress is obtained, the sample has undergone work softening [143, 164, 165].

Less common is anti-thixotropy, which shows the opposite curve (Figure 1.11). When the shear rate is increased the slope of a shear stress-shear rate plot increases, that is the viscosity of the solution increases. When change in shear rate becomes negative, the curve shifts to lower shear rates compared with the original curve. This is indicative of a structure that is formed under high shear rates and is more stable to shear, but is destroyed when at rest. If the original stress value is not returned, the material has undergone work hardening [143, 164, 165].

Rheopectic materials are here defined as materials that show a shear thinning behaviour upon increasing shear, but show a downwards curve, shifted towards lower shear rates compared to the original curve [143, 164, 165]. The shift to lower shear rates indicates the presence of a shear force causes more rapid reconstruction of an internal structure, compared with the situation in which no force is applied. These differences are illustrated with the theoretical curves presented in Figure 1.11.
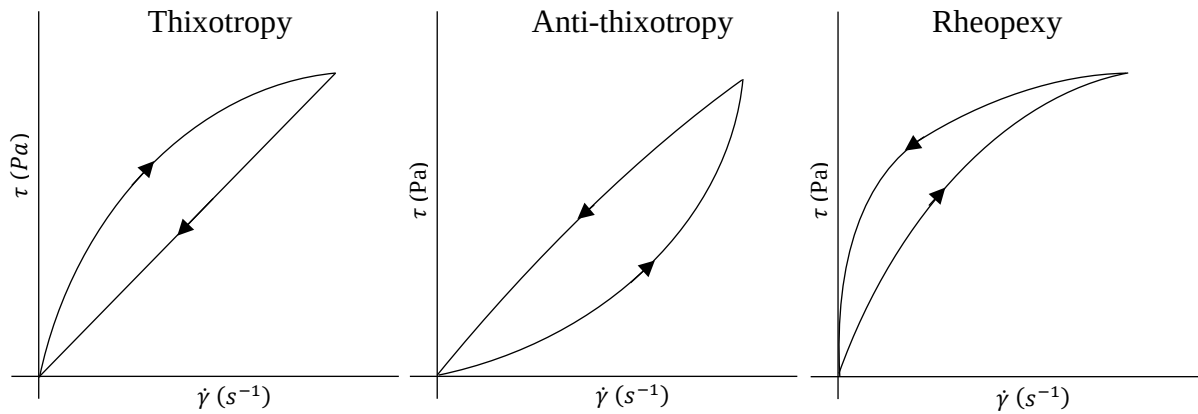
Figure 1.11: Generalised flow rheograms for thixotropy, anti-thixotropy and rheopexy of time-dependent non-Newtonian fluids

Some works use different definitions of anti-thixotropy and rheopexy, considering them as synonymous. The definitions presented here are in accordance with the IUPAC, British Standards Institute, and the National Institute of Standards and Technology [143, 164, 165].

1.5.3.4 Rheological models

Many real fluids will show combinations of different rheological responses at different shear rates. For rheological modelling, generalised Newtonian fluids are often assumed [172]. These idealised fluids show no time-dependent viscosity effects, and thus have no prior shear dependence. Different models of different complexity account for shear rate ranges, generally with the more complex models accounting for a broader range of shear rates. Figure 1.12 shows a generalised Newtonian viscosity curve, and indicates regions of the curve in which specific models are applicable.
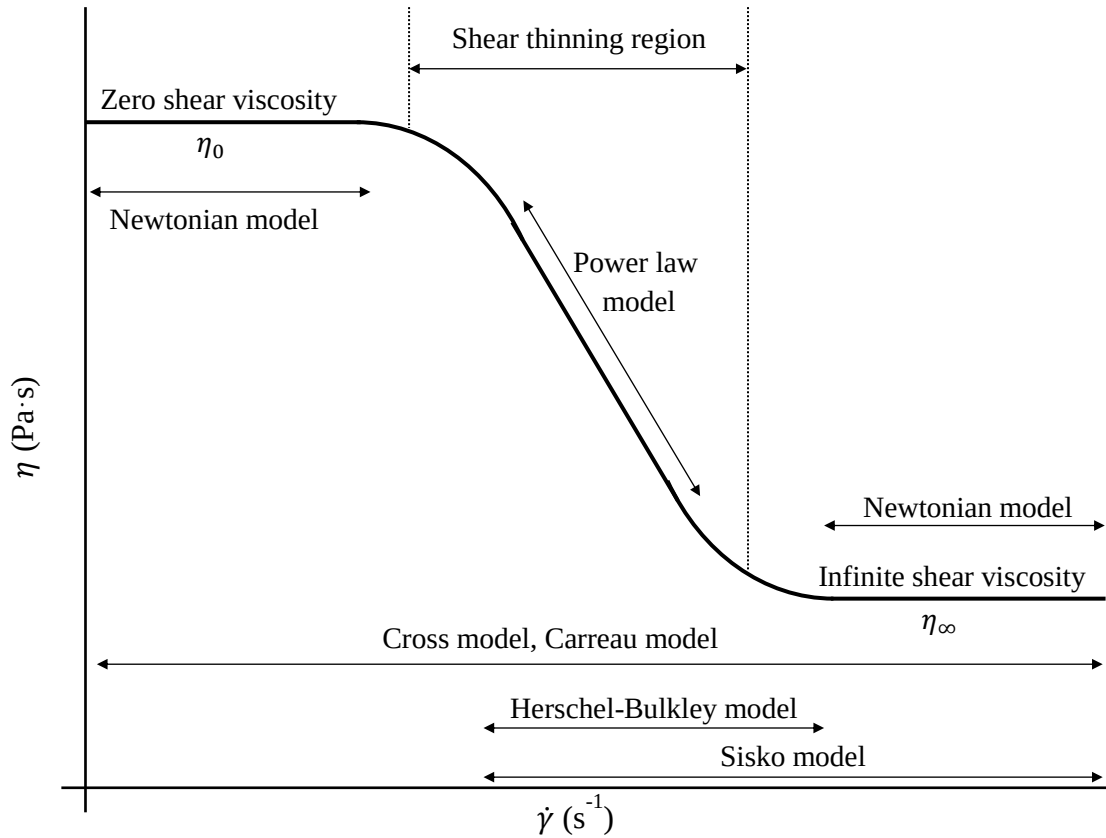
Figure 1.12: Generalised Newtonian fluid representative curve with key sections indicated. Useful ranges for specific rheological models are indicated.

Most rheological models are semi-empirical, rather than theoretically based. This is in part, due to the extreme difficulty in accurately predicting or modelling a complex flowing system, particularly when sample inhomogeneity (such as in the case of suspended particles) is considered. Often only specific sections of the viscosity profile are observable, such as the shear-thinning region. This causes difficulty in fitting the more complex models of rheology to such data, and simpler models may be preferable. A generalised Newtonian fluid model relates shear stress, shear rate and effective viscosity (η_{eff}) by the formula $\tau = \eta_{\mathrm{eff}}(\dot{\gamma})\dot{\gamma}$ [172]. A limited number of commonly used rheological models are presented in Table 1.1, along with the relevant equations, presented in $\eta_{\mathrm{eff}} = f(\dot{\gamma})$ form [173].

Table 1.1: Selected rheological models and equations

Model name	Reference	Model equation ($\eta_{eff}(\dot{\gamma})$)	Equation
Newtonian		$\eta_{\text{eff}} = \eta_0$	Equation 1.15
Power law		$\eta_{\text{eff}} = K\dot{\gamma}^{n-1}$	Equation 1.16
Herschel-Bulkley	[174]	$\eta_{\text{eff}} = K\dot{\gamma}^{n-1} + \tau_0\dot{\gamma}^{-1}$	Equation 1.17
Cross	[175]	$\eta_{\text{eff}} = \eta_\infty + \frac{\eta_0 - \eta_\infty}{1 + (\alpha_c\dot{\gamma})^m}$	Equation 1.18
Carreau	[176]	$\eta_{\text{eff}} = \eta_\infty + (\eta_0 - \eta_\infty)(1 + (\lambda_c\dot{\gamma})^2)^{\frac{n-1}{2}}$	Equation 1.19

Where:

$$\eta_0 = \text{zero-shear viscosity}$$
$$\eta_\infty = \text{infinite-shear viscosity}$$
$$K = \text{consistency index}$$
$$n = \text{flow index}$$
$$m = \text{Cross flow index}$$
$$\alpha_c = \text{Cross rate constant}$$
$$\lambda_c = \text{relaxation constant}$$
$$\tau_0 = \text{yield stress}$$

Newtonian fluids (Equation 1.15) are the simplest to consider, however can only be used to represent the zero- and infinite-shear plateau viscosities.

The power-law model (Equation 1.16) is one of the most common forms, and is used to characterise the behaviour of the shear thinning (or shear thickening) section of the viscosity profile. This model relates the shear rate and shear stress using K, the consistency index, which is dimensionally Pa·s^n, and n, the flow index, a dimensionless constant that describes the dependence of viscosity on the shear rate, describing the flow behaviour as follows:

$$Flow\ behaviour = \begin{cases} Shear\ thinning & n < 1 \\ Newtonian & n = 1 \\ Shear\ thickening & n > 1 \end{cases}$$

This model is limited in that it predicts a single relationship between the shear rate and the effective viscosity measured at all shear rates, leaving it unable to account for any fluid that shows a changing behaviour with shear rate.

In the Herschel-Bulkley model (Equation 1.17) there are three fitting parameters, allowing a wider range the fluid to be modelled. It assumes a yield stress, consistency index, and flow index. If the yield stress is taken as zero, this model simplifies to the power-law model, and to a Newtonian fluid if both the yield stress and flow index are zero.

The Cross (Equation 1.18) and Carreau (Equation 1.19) models are four-parameter models of a generalised Newtonian fluid, and are able to cover the widest range of data. Due to the often-limited range of observable behaviour, fitting of all four parameters can be difficult. Simplifications of the fitting depend on which sections of the data are visible, some work assume the infinite shear viscosity value to be small enough as to show negligible effect on the overall fit if the value is not observable. Other assumptions have been to note that for situations in which the zero-shear viscosity is not visible, mathematically little difference is found when $\eta_0 > 1000\eta_\infty$, and so confining $\eta_0 = 1000\eta_\infty$ serves to allow for easier fitting.

The constants α_c and λ_c are time constants relating to the flow behaviour. In a Cross fluid, $a_c = \dot{\gamma}_c^{-1}$, where $\dot{\gamma}_c$ is the critical shear rate, where $\eta_{\text{eff}}(\dot{\gamma}_c) = \frac{\eta_0 + \eta_\infty}{2}$. This gives an estimate of the shear rate range at which the zero-shear viscosity plateau transitions into the shear thinning range.

The Cross model can also be used to estimate a critical stress value (τ_c), at which point the effective viscosity of the sample experiences dramatic change, given by $\tau_c = \eta_0 \dot{\gamma}_c$. Alternatively the Cross and Carreau models can be modified to directly incorporate a yield stress term [173], however, this then brings the fitting parameters for each equation up to five, consequently increasing the fitting difficulty.

2   Materials, methods, instrumentation

2.1 Overview

This chapter provides information on the chemicals used in these experiments, and the experimental methodologies used. Firstly, the chemical and instrumentation lists were presented. After this, the procedures used in this thesis were detailed, starting with nanoparticle synthesis, then functionalisation, and nanofluid preparation. General procedures and the preparation and handling of standards noted. Finally the analytical methodologies and conditions were given.

2.2 Chemicals and instrumentation

2.2.1 Chemical list

Function	Name	Supplier	Purity/Concentration
Silane	3-mercaptopropyltrimethoxysilane	Sigma-Aldrich	95 %
	tetraethylorthosilicate	Sigma-Aldrich	98 %
Moiety	11-bromo-1-undecene	Sigma-Aldrich	95 %
	undec-10-enoic acid	Sigma-Aldrich	98 %
	11-undecen-1-ol	Sigma-Aldrich	98 %
	1-undecene	TCI	>98 %
	sodium 4-vinylbenzenesulfonate	Sigma-Aldrich	>90 %
Initiator	azobisisobutyronitrile	Merck	>98.0 %
Solvent	Milli-Q® water	Millipore	18.2 MΩ
	ethanol	Sigma-Aldrich	>99.8 %
	propan-2-ol	Chemsupply	>99.5 %
Other	hydrochloric acid	RCI Labscan	32 %
	sodium hydroxide	Sigma-Aldrich	>99.998 %
	sodium chloride	Sigma-Aldrich	>99.0 %
	ammonia	Chemsupply, or TCI	25 % 28 %
Standard	LUDOX® AS-40 silica colloid	Sigma-Aldrich	40 %

2.2.2 Instrument list

Name	Supplier	Category
Malvern Zetasizer ZS	Malvern Panalytical	DLS/Zetasizer
DLS-8000	Otsuka Electronics Co., Ltd	DLS
Inspect FEI F50 SEM	Thermo Fisher Scientific	SEM/EDXS
Thermo Nicolet Nexus 870	Nicolet Instrument Corporation	ATR-FTIR spectrophotometer
Perkin Elmer STA 8000	Perkin Elmer	TGA (STA)
TA Instruments AR 2000	TA Instruments	Rheometer
Physica MCR 301	Anton-Paar	Rheometer
RAMAN-11	Nanophoton	Raman microscope
Tri-Star II 3030	Micromeritics	BET analysis
Quorumtech K757X Sputter coater	Quorum Technologies	Sputter coater
Memmert VO400	Memmert	Vacuum oven
Eppendorf MiniSpin	Eppendorf	Centrifuge

2.3 Particle synthesis

2.3.1 Preparation of thiol functionalised silica nanoparticles

Table 2.1 displays the quantities of reagents used in each particle synthesis, with the Z-average diameter and PDI referenced in each case indicating the diameter of final particles obtained. For each reaction mixture, water and ammonia solution, or, water, ammonia solution and ethanol were combined. To this mixture, 3-MPTMS was added and stirred at a low rate, sufficient to prevent settling of the 3-MPTMS in the mixture. After 1 hour, the stirring rate was increased (550 rpm) to induce vortexation. After 3 days, the resultant solution was gravity filtered using a Whatman filter paper (11 µm pore size) to remove large aggregates.

Table 2.1: Summarised synthesis conditions for SH-SiNPs with measured particle diameters and PDI values

Scale	Water (mL)	Ethanol (mL)	Ammonia, 28% (mL)	MPTMS (mL)	Z-average diameter (nm)	PDI
50	46.4	0	3.6	0.06	106-139	0.036-0.128
50	46.4	0	3.6	0.12	158-276	0.031-0.082
50	46.4	0	3.6	0.18	182	0.015
50	46.4	0	3.6	0.60	296	0.092
50	46.4	0	3.6	0.10	Aggregated	N/A
50	45.4	1	3.6	0.10	123	0.178
50	41.4	5	3.6	0.10	108-132	0.127-0.130
50	41.4	5	3.6	0.12	172	0.158
400	330	40	30	0.96	157	0.030
400	371	0	29	0.91	276	0.055
800	660	80	60	1.9	165	0.023
800	724	0	58	1.8	107	0.025
1000	825	100	75	2.4	164	0.034
2000	1650	200	150	4.8	176	0.048
3000	2475	800	225	7.2	164	0.026

2.3.2 Preparation of silanol functionalised silica nanoparticles

SiNPs were synthesised according to the Stöber process, TEOS (4 mL) was dissolved in ethanol (50 mL) and NH$_4$OH (25 %, 4 mL) added to the mixture. Over a reaction period of two hours the reaction mixture changed from a clear, colourless solution to a white, opaque solution, the Z-average was approximately 170 nm.

2.4 Particle functionalisation

2.4.1 Functionalisation of SH-SiNPs with functional-group bearing alkene

Azobisisobutyronitrile (AIBN) (0.2 mmol, 40 mg) was dissolved in ethanol (99.8 %, 20 mL) and 10-undecenoic acid (3.4 mmol, 0.7 mL), 4-vinylbenzenestyrene sulfonate (0.6 g), 11-undecen-1-ol (3.1 mmol, 0.63 mL), 11-bromo-1-undecene (3.0 mmol, 0.7 mL) or undecene (5 mmol, 0.6 mL) was then added to the aqueous dispersion of SH-SiNPs (250 mL) and heated under reflux. After 2 hours, the solution was returned to room temperature and sodium chloride solution (6 mol·L^{-1}, 20 mL) was added to the solutions of COOH-SiNPs and StS-SiNPs to induce particle aggregation. After the particles collapsed, the sample was filtered under vacuum through a Sartorius Stedim filter (0.45 µm, PTFE).

The resultant solid material was washed with ethanol (200 mL) and water (500 mL). The particles were collected from the filter paper and redispersed in sodium hydroxide solution (0.01 M, 50 mL). The obtained solution was then centrifuged (Eppendorf MiniSpin) (13x10^3 rcf, 4 minutes) and the pellet retained. 3. This process was repeated until the pellet obtained exhibited blue coloration on the edges characteristic of light scattering, at least 3 times.

2.4.2 Particle cleaning

For TEOS-SiNPs, SH-SiNPs, COOH-SiNPs and StS-SiNPs, the solution was centrifuged (14.1x10^3 rcf, 7 minutes) to collect the SiNP pellet. The pellets were redispersed in a mixture of ethanol (12 mL) and Milli-Q water (12 mL) under sonication (15 minutes) in a bath sonicator (Soniclean). The dispersion was then centrifuged (14.1x10^3 rcf, 7 minutes) and the SiNP pellet collected. This procedure was repeated two more times using ethanol (12 mL) and water (12 mL), and then three times using Milli-Q water (24 mL) as the dispersant.

For Br-SiNPs, OH-SiNPs and U-SiNPs, the solution was centrifuged (14.1x10^3 rcf, 7 minutes) to collect the SiNP pellet. The pellets were redispersed in ethanol (24 mL) under sonication (15 minutes) in a bath sonicator. The dispersions were then centrifuged (14.1x10^3 rcf, 7 minutes) and the SiNP pellet collected. This procedure was repeated two more times, and then three times using Milli-Q water (24 mL) as the dispersant.

2.5 Nanofluid preparation

Nanofluids were prepared by dilution of the SiNP pellet recovered from centrifugation. Milli-Q water was used as the diluent; producing dispersions with concentrations between 2 and 49 %w/w. The concentration was determined gravimetrically. Briefly, a known mass and volume of the sample was placed into a pre-dried and weighed vessel. This was then dried in a vacuum oven (Memmert VO400) (1 day, 70 °C, 20 mbar). The residue and vessel were weighed and compared to the mass of the empty vessel. This mass was then used to determine the concentration of the solutions by mass.

For low concentration nanofluids (up to 5 %w/w) prepared from dried particles, known quantities of SiNPs were dispersed in Milli-Q water. The particles were dispersed by sonication (30 minutes) in a bath sonicator, followed by stirring for at least 12 hours. Prior to analysis samples were sonicated (30 minutes) in a bath sonicator. For the nanoparticles of silanol, acid and styrene sulphonate functionality, this was sufficient to create a stable colloidal dispersion of particles. For thiol terminal particles, this produced an unstable dispersion prone to aggregation. For undecene, bromoundecene and undecenol terminal particles, this produced a highly unstable dispersion that sedimented within a period of no greater than 1 hour, or an inhomogeneous dispersion.

2.6 Analytical techniques

2.6.1 Dynamic light scattering

DLS measurements were performed using a Malvern Zetasizer ZS in a non-invasive backscattering (NIBS) configuration. All runs were performed in triplicate in monomodal mode, at 25 °C, in 1 cm path length cuvettes. Attenuator index, path length, number of scans, and mean position were determined automatically in NIBS configuration.

2.6.1.1 Zeta potential measurement

Zeta potential measurements were performed using the Malvern Zetasizer ZS in DTS 1070 folded capillary cells. Samples of 1 mg/mL of the nanoparticles of interest were prepared in sodium chloride solution (10 mM), with pH values measured before and after zeta potential analysis. Solution pH was adjusted by the addition of µL scale quantities of sodium hydroxide (0.01 M or 0.1 M) and hydrochloric acid (0.01 M). To investigate the effect of pH, DLS measurements were taken of the samples under the same conditions.

2.6.2 Thermogravimetric analysis

TGA measurements of the particles were undertaken using a Perkin Elmer STA8000. The particle samples were first dried in a vacuum oven (70 °C, 20 mbar) for at least 24 hours to ensure solvent removal prior to measurement. At least 5 mg of sample was heated at 10 °C·min^{-1} from 30 to 900 °C. The purge gas was nitrogen at a flow rate of 20 mL·min^{-1}. At 900 °C, the purge gas was then changed to air and the sample held at 900 °C for 2 minutes.

2.6.3 Raman spectroscopy

SiNP samples were deposited on glass slides for analysis. Raman spectroscopy was performed using a RAMAN-11, with a laser wavelength of 532 nm. Laser power was adjusted for each sample to avoid sample fluorescence.

2.6.4 Rheology

Rheological measurements were performed using a stress controlled RA 2000 Rheometer (TA Instruments). All samples were measured at 25 °C, with temperature maintained by a Peltier plate system. Shear sweep measurements were taken using a dual-plate system (aluminium, 40 mm diameter) with a gap size of 0.1 mm. Samples were pre-sheared at 100 s^{-1} for 1 minute and allowed to equilibrate for 1 minute prior to measurement. Low viscosity samples were measured using a double concentric cylinder configuration, with outer rotor, inner rotor and stater inner radii of 21.96, 20.38 and 20.00 respectively, with a gap size of 0.5 mm. Up-down rheological measurements of StS-SiNP nanofluids were undertaken using a stainless steel 20 mm diameter cone-and-plate system, with a truncation of 0.017 mm and a cone angle of 0.5°. SH-SiNP shear rate measurements were taken using a Physica MCR301 (Anton-Paar), stress-controlled rotational rheometer, and a stainless steel, 50 mm diameter, 1°, 0.101 mm truncation, cone-and-plate geometry.

2.6.5 BET surface area analysis

Specific surface areas of particles were determined by BET isotherm analysis using a TriStar II 3030 surface area and porosity analyser (Micromeritics Instrument Corporation). Prior to analysis SiNPs were dried in a vacuum oven (70 °C, 20 mbar) overnight, and then at 0.1 mbar at 90 °C for 1 hour.

2.6.6 Scanning electron microscopy

Silicon wafers (University Wafer, P/B, SSP, 100 orientation) were cleaned via sonication in ethanol and then rinsed with ethanol and dried under a stream of N_2 gas. The SiNP solutions were then drop cast onto the wafers and allowed to dry. The samples were then placed in a vacuum oven and dried at 60 °C for at least 1 hour at 20 mbar, to ensure removal of solvent.

Before measurement, the particle samples were coated with a 2 nm platinum film using a Quorumtech K575X Sputter coater. The measurements were made using an Inspect FEI F50 SEM.

2.6.6.1 Energy-dispersive X-ray spectroscopy

Samples for analysis using EDXS were prepared as detailed in Section 2.6.6, however were not coated with a platinum film.

2.6.7 Data analysis

Graphs were prepared using OriginPro 9.0.0 or QtiPlot 1.0.0-rc1. Peak fitting was performed using Fityk 1.3.1, using a weighted least squares Levenberg-Marquadt algorithm. SEM image analysis was performed using ImageJ.

3 Preparation of functionalised nanoparticles

3.1 Overview

In this chapter, a method for producing thiol-terminal silica nanoparticles (SH-SiNPs) was adapted to produce greater quantities of particles, in larger scale reactions. At the same time control over the particle diameter and dispersity was improved upon, and nanoparticle solution stability and suitability for further reaction was maintained.

The synthetic method for producing SH-SiNPs was optimised by changing the reaction volume, concentration and solvent conditions. It was found that by introducing ethanol to the reaction mixture, the precursor solubility was improved such that the reaction could be successfully upscaled. A modified version of the protocol was designed in which solution volumes of up to 3 L were used to produce gram-scale quantities of SH-SiNPs at controllable sizes between 80 and 200 nm, with improved monodispersity compared to previous syntheses of similar particles.

The formula for the specific surface area of smooth spheres was modified to account for the dispersity in particle diameter and non-sphericity of the particles. Excellent agreement was found between the adjusted theoretical values (38.6 and 39.3 $m^2 \cdot g^{-1}$ for spheres and spheroids) and the measured value (39.0 ± 0.7 $m^2 \cdot g^{-1}$). Optical effects of the synthesised nanoparticles were briefly remarked upon.

It is common practice to use TEOS to synthesise SiOH nanoparticles via the Stöber process [27, 84, 107, 118]. It is used as it produces highly monodisperse particles of a defined size, and well understood surface chemistry. Usually, TEOS particles are coated in a functional group-bearing silane, to introduce a reactive surface moiety, which can then be functionalised [103, 177-179]. Whilst this method has been used to produce a wide variety of functionalised particles, it can result in a sharp reduction in the particle surface functionality [98, 177], compared to the theoretical value for silanol surface functional density of 4.9 groups$\cdot$nm^{-2} on TEOS silica particles [180, 181].

As a sole precursor, MPTMS has been used to produce nanoparticles bearing high surface densities of thiol groups [107, 108, 112]. These particles are of interest as they can also be synthesised such that the particles produced are highly monodisperse and show excellent diameter control [108]. Further reactions are also simple, exploiting thiol-ene click chemistry, allowing high surface functional densities to be achieved [108].

Monodisperse particles with diameters between 20-500 nm often produce optical effects [84, 182, 183]. This can be particularly noticeable with particles in solution, producing light scattering effects such as the Tyndall effect (where a beam of light passed through the solution becomes dispersed by the light scattering off particles), or Rayleigh scattering, where light of different wavelengths is preferentially forward or backscattered. The Tyndall effect is useful for determining the stability of a colloidal system, and thus, nanofluids [184].

In this work, TEOS particles were synthesised for use as a standard, for comparison with SH-SiNPs however, they were not used as the substrate particles for further functionalisation. They were used to prepare aqueous nanofluids to compare against fluids prepared from SH-SiNPs and those bearing other functional groups.

SH-SiNPs were synthesised as particle substrates for further functionalisation. These particles have been used before for this purpose, producing high surface functional densities. Particle diameter has been shown to be controllable by silane precursor concentration [107, 108].

This work dealt with high concentration nanofluids, with nanoparticle content of up to 49 %w/w, and with enough volume of nanofluid prepared to ensure accurate rheological analysis. Compared with typical nanofluid investigations, which use small concentrations, typically between 0.1-5 % [8, 88], a large quantity of particles must be prepared, which required modification of the prior methods for generating SH-SiNPs. While increasing the quantity was necessary, it was not able to be at the expense of control of the size, dispersity, stability or further reactivity of the particles.

3.2 Synthesis protocol modifications

To produce large quantities of nanoparticles in a reasonable period, the literature method was modified. Concentration, volume and solvent conditions were investigated for their potential to produce particles more efficiently. Of critical concern was in ensuring that the modifications to the process did not negatively affect the particle yield or polydispersity index (PDI) (or Dispersity, Đ), and that the diameters of the synthesised particles remained under good control.

3.2.1 Effect of silane precursor concentration at low volumes

Previous MPTMS based particle syntheses have been concerned with microgram and milligram quantities in reaction volumes up to 50 mL. It is known from previous work that increasing the concentration of particles in solution results in larger particles, it also increases the rate at which particles form. Whilst still operating in the lower concentration regime (6.1-61 mmol·L^{-1}) of the previously investigated concentrations, the MPTMS was increased to determine the effect on particle size.

Table 3.1: Particle diameters measured by DLS over time with different MPTMS concentration in SH-SiNP synthesis, all samples prepared with water (Milli-Q, 46.4 mL) and ammonia solution (28 %, 3.6 mL). N/A indicates DLS measurement unable to be taken due to instrument limitation.

MPTMS (mmol·L^{-1})	Day 1		Day 2		Day 3		Day 4	
	Z_{av} (nm)	PDI	Z_{av} (nm)	PDI	Z_{av} (nm)	PDI	Z_{av} (nm)	PDI
6.1	N/A	-	265	0.360	155	0.374	139	0.128
							132	0.101
							106	0.036
							124	0.041
12.2	141	0.102	175	0.060	198	0.039	222	0.031
	145	0.051	153	0.032	-	-	158	0.058
	192	0.068	N/A	-	285	0.093	276	0.082
	189	0.058	N/A	-	277	0.104	270	0.055
18.3	171	0.045	180	0.038	N/A	-	182	0.015
61.0	484	0.128	483	0.209	N/A	-	296	0.092

Table 3.1 shows the Z-average diameter and PDI for each sample with time. It was found that all samples measured produced large silica aggregates or amorphous structures. Each sample followed a similar change in appearance, first becoming hazy with a slight blue tinge, before turning translucent and white, and then turning completely opaque and white in colour. The rapidity with which these changes occurred changed depending on the MPTMS concentration in solution. 6.1 mmol·L^{-1} samples turned translucent after two days, and required greater than four days to turn completely opaque. 12.2 mmol·L^{-1} samples became translucent after 1 day and opaque after three days. 18.3 mmol·L^{-1} sample became opaque after one day, while the 61.0 mmol·L^{-1} solution reached opacity after two minutes.

Two apparent patterns were noted for particle growth with changing concentration: either a sample would grow steadily over the reaction period, reach their final diameters and stabilise, or large apparent particles would develop quickly and then reduce in diameter with time. The

former process was indicative of the expected growth mechanism of the particles, and appeared with the syntheses made at 12.2 and 18.3 mmol·L^{-1}. The latter process, found with the 6.1 and 61.0 mmol·L^{-1} concentrations, was potentially explainable by the formation of large amorphous silica structures in solution. During the early stages of reaction, these aggregates were small enough to remain dispersed, however collapse out of solution with time, forming a white precipitate on the base and sides of the reaction vessel.

Multiple syntheses of particles at 6.1 and 12.2 mmol·L^{-1} were done. At these concentrations, particles were unable to be prepared in a repeatable manner, with different average sizes and different levels of polydispersity achieved. Less variation was found with the 6.1 mmol·L^{-1} concentration samples compared to the 12.2 mmol·L^{-1} samples.

Aggregate formation during reaction tended to occur at the early stage of reaction, which had the consequence of reducing the effective concentration of MPTMS in solution. Referring to the figure published in [107] it can be observed that in the concentration range being studied, the particle diameters increase rapidly with increasing concentration of MPTMS, far more so than at higher concentrations. In this region therefore, slight changes in the reagent concentration can have significant effects on the diameters of the particles formed. Thus, increasing reagent concentration would only be a viable method of increasing particle yield if aggregate formation could be eliminated from the synthesis process. Removal of aggregates after the synthesis has concluded has been serviceable in previous work. Aggregate structures, however, represent wasted reagent, and introduce uncertainty in each reaction as to the effective silane concentration, and thus the expected particle diameters, which is unacceptable for large-scale particle synthesis.

3.2.2 Effect of reaction volume on particle synthesis

To overcome the sensitivity of the particle size to MPTMS concentration in low volume systems, larger reaction volumes were evaluated to produce more consistent particle diameters, as well as greater quantities of particles for further modification and use. Three equi-molar reactions at different volumes were prepared. Details of the volumes used and the diameters measured over time are displayed in Table 3.2.

Table 3.2: Reagent and solvent volumes of SH-SiNP syntheses, with Z-average diameters measured over a period of three days for different reaction scales

Reagent volumes (mL)				
Water	Ammonia (28 %)	MPTMS	Z-average diameter (nm)	PDI
46.4	3.6	0.114	187	0.087
371.2	28.8	0.912	276	0.055
724	57.6	1.824	107	0.025

It was found that increasing the scale did not result in a significantly increased yield of particles, nor was a relationship between reaction volume and particle diameter determinable. This was determined to be a result of the inhomogeneity in the reaction conditions. The original method this synthesis was based upon was conducted on the μL scale, which was subsequently expanded up to the mL scale. One of the assumptions made during the synthesis was that the reaction mixture was homogeneous, and that the reagent was capable of dispersing in the solution as a single phase quickly.

At high volumes, the dispersion of the MPTMS was less effective, unable to disperse rapidly enough to ensure a homogeneous solution when high stirring rates were introduced. If high stirring rates were not introduced and the particles formed solely through dispersion, a large aggregate mass was formed on the bottom of the reaction container, and any particles that did grow were irretrievable from the amorphous silica structure. The inhomogeneity observed resulted in the formation of large aggregates in the volumes with high silane concentration. As was observed when attempting to change the concentration directly, this resulted in an unaccountable change in the concentration of the silane reagent in solution. The particle diameters were thus uncontrolled, which rendered simple upscaling an unsuitable method for increasing particle yield.

3.2.3 Effect of solvent conditions on particle synthesis

Elimination of aggregates formation during particle synthesis was identified as the critical limiting factor to produce large-scale reactions with controllable particle diameters. Aggregate formation was largely a result of inhomogeneity in the reaction mixture. The solvent was changed to produce a reaction mixture capable of producing larger scale reactions of nanoparticles without losing control of the diameter or polydispersity of particles.

Table 3.3: Solvent conditions and DLS measured particle diameters for SH-SiNP synthesis. Two samples of each condition were prepared. In all cases 3.6 mL of ammonia solution (28 %) and 100 µL of MPTMS were used.

Reagent volumes (mL)			
Water	Ethanol	Z-average diameter (nm)	PDI
46.4	0	Aggregated	N/A
		Aggregated	N/A
45.4	1	123*	0.178
		Aggregated	N/A
41.4	5	132	0.127
		108	0.130

* After filtration of large aggregates present in samples

To allow the MPTMS to be more effectively dispersed in solution, testing with differing ethanol concentrations was done to determine if good control over particle diameters could be retained with increased reaction volumes. Initial tests were done on a 50 mL scale, with the diameters and results presented in Table 3.3.

Samples prepared without ethanol present showed aggregate formation, when these samples were filtered in preparation for DLS measurement, the concentration of the sample was rendered too low for effective measurement. This indicated that for these cases most of the sample prepared was the large aggregations visible, thus that the particle synthesis was unsuccessful under these conditions.

With 2 % ethanol (1 mL), particles could be formed in measurable concentrations in both samples after 3 days, at smaller diameters than expected. After 4 days, the presence of large aggregates in each sample made measurement difficult. When filtered, one of the samples resulted in particles with an average mean diameter of 123 nm, smaller than expected for the concentration of MPTMS used under the original conditions.

With 10 % ethanol (5 mL), particles formed in each solution with a minimal production of aggregate structures. Similar sizes were attained for each reaction, with PDIs similar to the reactions without the presence of ethanol. This indicated a reduction in the precursor lost to the production of aggregates, which could lead to greater consistency between reactions.

Table 3.4: Reagent and solvent volumes of SH-SiNP syntheses in a 10 % ethanol solution, with Z-average diameters measured over a period of three days for different reaction scales

Reaction volumes (mL)	Z-average diameter (nm)	PDI
40	172	0.158
400	157	0.030
800	165	0.023
1000	164	0.034
2000	176	0.048
3000	164	0.026

The effect of the synthesis volume with 10 % ethanol was investigated to produce large quantities of particles (Table 3.4). The samples all showed similar Z-average diameters and low PDI values. This indicated that the particle diameters remained controlled, and that the formation of aggregates or large particles were minimised. This suggested that the homogeneity of the reaction mixture was no longer an issue even at increased scales, and allowed synthesis of large batches of particles.

Concentration of the MPTMS in 10 % ethanol solutions was investigated for its effect on particle size (Figure 3.1). Like the relationship found by Ishimura and Nakamura [107] and expanded upon by Mangos *et al*. [108] the nanoparticle diameter could be controlled by the MPTMS concentration in solution. It should be noted that the relationship between MPTMS concentration and particle diameter was linear in this case, which was not the case for TEOS.
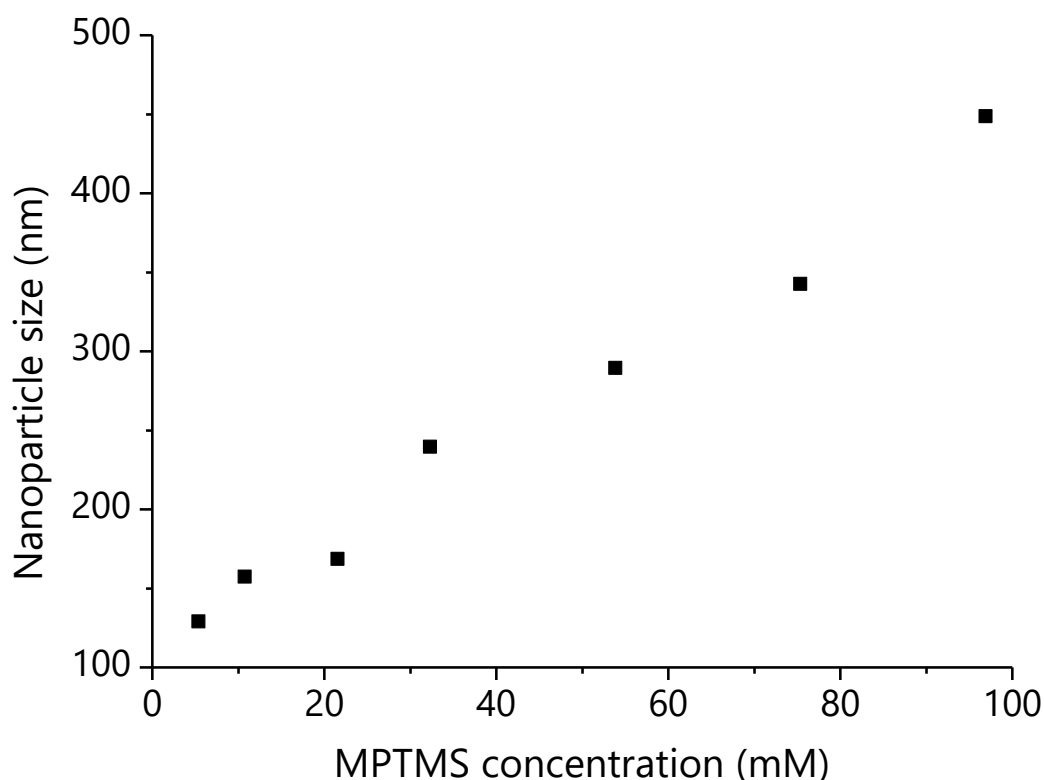
Figure 3.1: Particle diameter as measured by DLS against the concentration of MPTMS in reaction mixture, all reactions 50 mL scale, with 10 % ethanol.

Optimal particle synthesis conditions were determined to be using a solution of 10 % ethanol. This allowed for the use of higher concentrations of silane precursor and higher reaction volumes to be used, and resulted in faster, larger scale productions of nanoparticles without sacrificing their monodispersity or diameter control.

The nanoparticle synthesis method was selected and used as it provides good control over the overall diameter and monodispersity of the particles, whilst allowing further, high-functional density surfaces to be realised. However, batch-to-batch variability remained a concern for analysing the particles.

For most measurements, the concerns of batch-to-batch variability were addressed by synthesising large batches of nanoparticles and functionalising them in multiple ways. This produced a series of silica nanoparticles from the same SH-SiNP stock, with different functional groups, or allowed production of large quantities of identical particles, as desired. This ensured the average diameter of the initial particles remained constant for a given set of measurements, allowing for direct comparison.

Multiple batches of particles were produced, and it was found that slight variations in conditions resulted in particle diameter variations. Changes such as ambient temperature and age of ammonia used in the reaction could result in different particle diameters being formed. This was critical to account for as even small changes in particle radius could result in large differences in particle surface area, and consequently, surface functional density.

3.3 Particle characterisation

Further characterisation of the SH-SiNPs was undertaken using BET porosimetry, TGA using a simultaneous thermal analyser (STA), and observation of their optical properties. BET theory was used to determine the particle surface area, and indicate their porosity (if any) or surface roughness. This was of particularly important when defining surface functional density, as small changes to the roughness of the surface can create large differences in the surface functional density measurable.

STA was used to measure the particle thermal degradation under inert atmosphere. This gave indication of the stability of the particles, and how it differed based on particle size.

The small particle sizes resulted in interesting optical properties due to light scattering. In solution the particles dispersion could be indicated by the Tyndall effect, and when concentrated the particles exhibited structural colouration, though this became less intense as the particles dried.

3.3.1 Particle diameter measurements

For an accurate understanding of the synthesised particles, having a precise measurement of the diameters and variation in diameters of the particles was critical. To this end, two methods were used to measure particle diameter: DLS and SEM. DLS measurements provided information on the hydrodynamic radius of the particles in solution. DLS achieves this through light scattering in a sample, resulting in the measurement of a large number of particles within a short period. The Z-average measurement gives an indication of the average hydrodynamic radius or radii, while the PDI of the measured peaks indicates the sample dispersity. Conversely, SEM provided direct imaging of the particles, giving an indication of the actual diameter of the particles as well as the distribution. SEM was limited to the actual particles that could be seen. Dilute samples were made in an attempt to minimise the formation of larger structures, which caused charging or shadowing effects, however, movement during drying largely prevented the formation of particle monolayers during drop-casting.

SEM images of SH-SiNPs can be seen in Figure 3.2, which shows that the particles were relatively uniform and were able to "pack" in a disordered array. Higher resolution imaging of SH-SiNPs was performed (Figure 3.3). The particles formed appeared largely spherical, with less than a 5 nm difference between axial and equatorial radii.
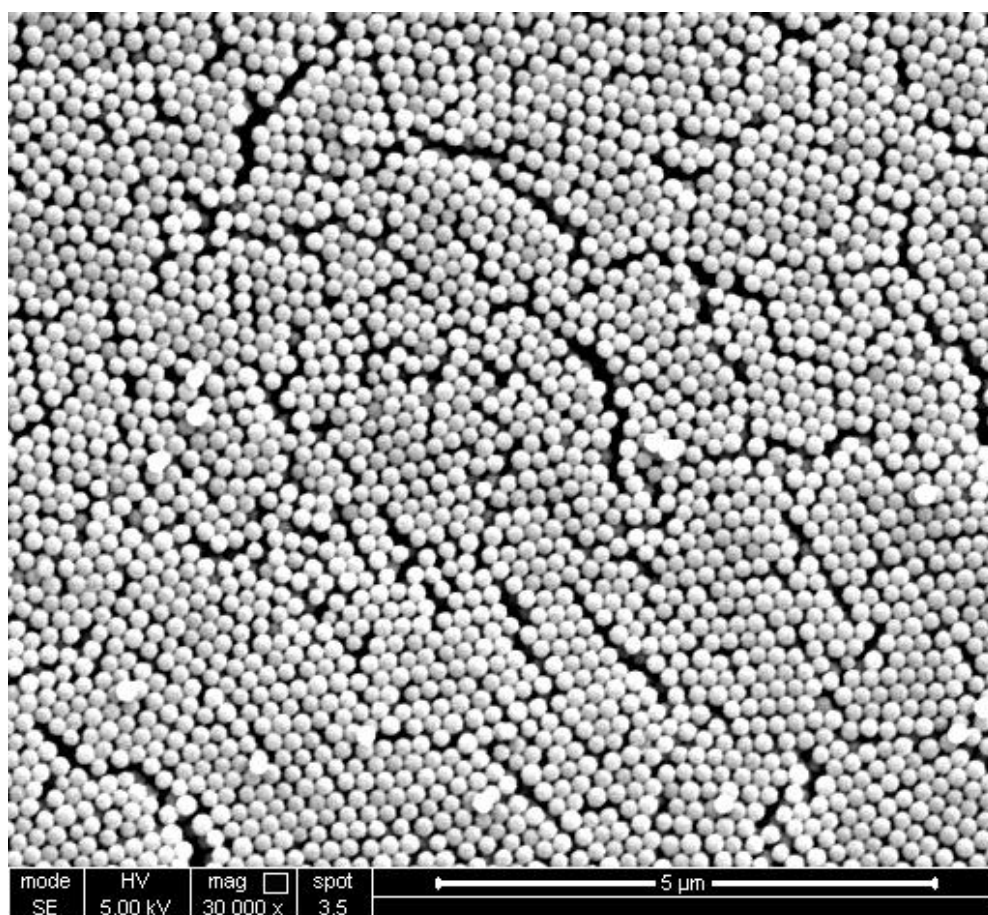
Figure 3.2: SEM images of SH-SiNPs. Samples were prepared by drop-casting nanoparticle solution onto silicon wafer and drying under air. Excess sample removed by compressed air. Samples coated with gold layer (2 nm thickness).

DLS measurements were taken of large and small sized particles to compare their hydrodynamic diameters in solution with their diameters as measured by SEM (Figure 3.4). The particle diameters measured by DLS tended to be similar to, or larger than the values determined by SEM. It was also noted that the standard deviation of particle diameter was not related to the average particle diameter, that is, smaller and larger particles had comparative standard deviations, not proportionate standard deviations.
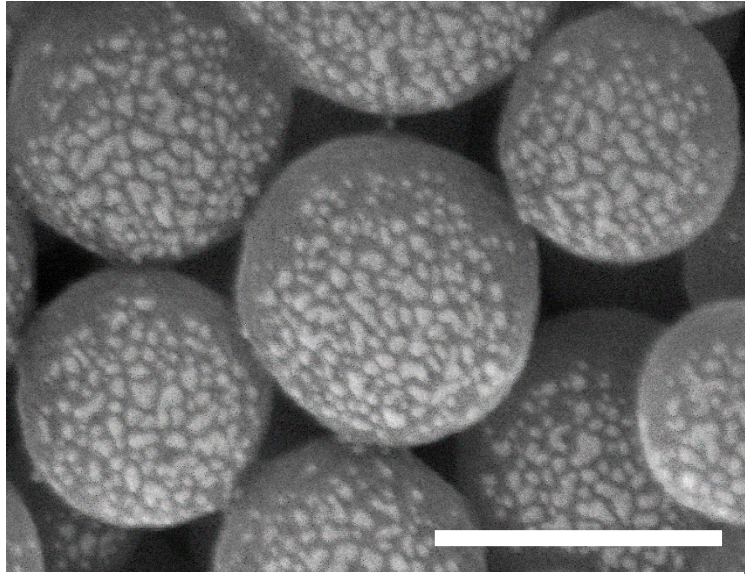
Figure 3.3: High-resolution SEM image of SH-SiNPs, coated with 2 nm gold coating. Scale bar is 200 nm.

Figure 3.4: Particle diameters measured for SH-SiNPs of different size regimes, using SEM and DLS. Error bars are ±1 standard deviation, derived from the PDI values.
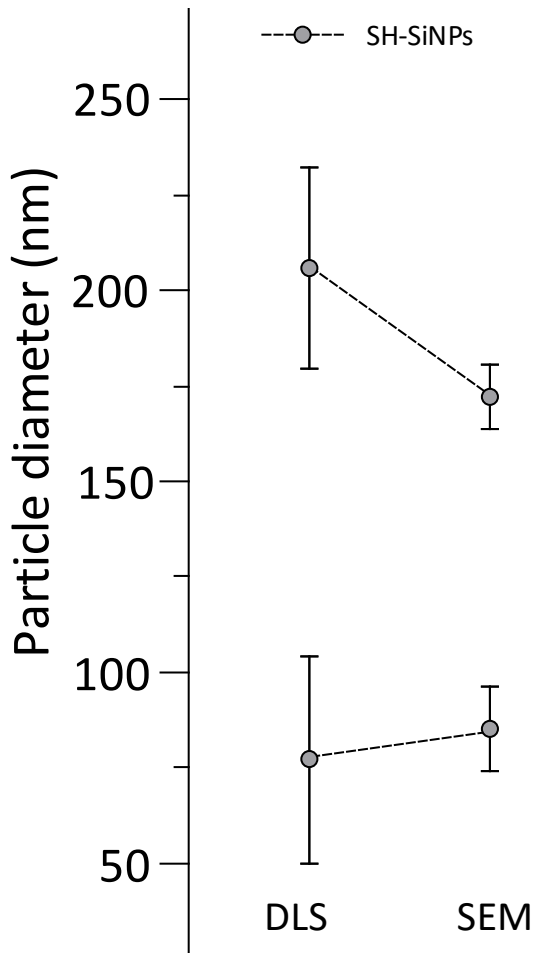
The slightly larger Z-average values were a consequence of a number of factors. In DLS the hydrodynamic radius of particles are measured: that is both the particle itself, and the layer of solvent and ions bound to the surface. Additionally, a "particle" in DLS refers to a scattering object in solution, in nanoparticle samples this could be the primary particle, or it may be a dimer, trimer or larger aggregate of the particles. These will act as scattering objects in solution with much larger radii. This serves to increase the Z-average diameter of the measurement, and increases the PDI of the sample measured.

3.3.2 ATR-FTIR spectroscopic investigation of particles

ATR-FTIR measurements were taken of SH-SiNPs (Figure 3.5). Peak positions are summarised in Table 3.5 for each of the spectra measured. The most intense peak in each spectrum was due to Si-O-Si bond vibration, and all peaks found showed good agreement with expected values from literature [104, 185-188].
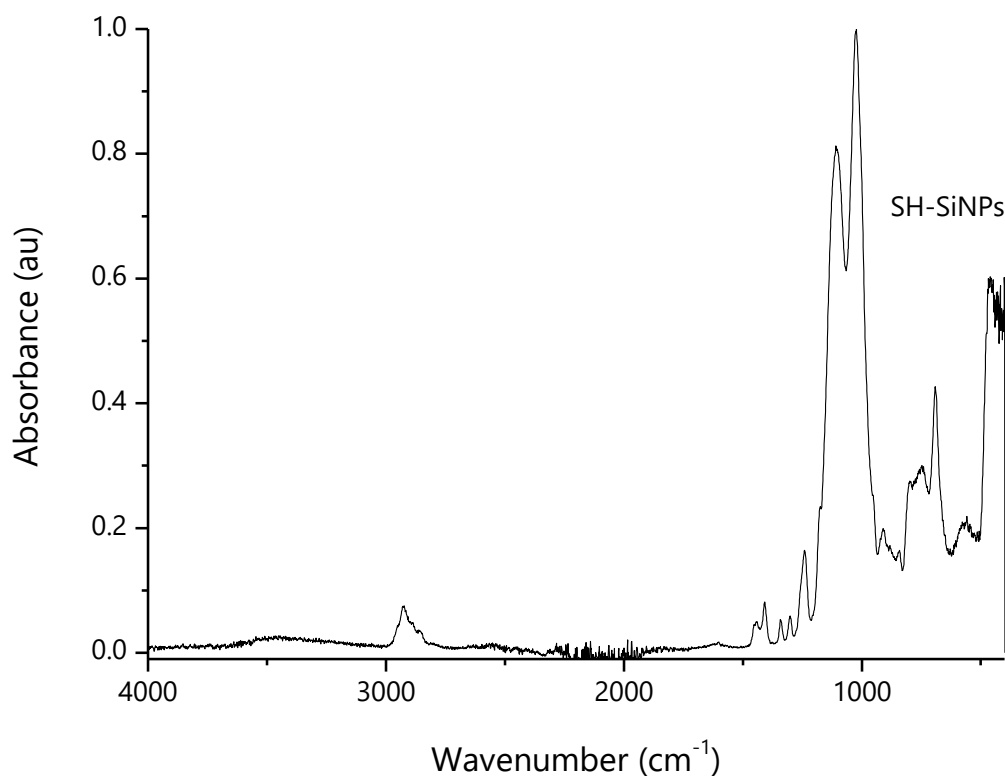
Figure 3.5: ATR-FTIR spectra of SiNPs prepared with MPTMS as the sole silane precursor

Table 3.5: Vibrational modes observed in ATR-FTIR spectra of SH-SiNPs.

Wavenumber (cm^{-1})	Assignment
3500-3000	$\nu(OH)$
2924	$\nu(CH_2)$
2850	$\nu(SH)$
1638	$\delta(OH)$*
1340, 1300	CH_2, CH_3 bend
1240	CH_2 twist
1108, 1025	$\nu(Si-O-Si)$
795	Si-O
696	$\nu(Si-C)$

*Indicates presence of water

The presence or absence of specific vibrational modes can be useful for assessing the completion of the reaction. For the SH-SiNPs, the peaks that would be present due to the

60

methoxy group, in the case of incomplete hydrolysis, were not visible. Unfortunately, the Si-O-C peaks were obscured by the intense Si-O-Si absorption and the –OCH$_3$ vibration was not visible due to the weak peak being obscured by the CH$_2$, CH$_3$ and SH vibrations in the 2800-3000 cm^{-1} range. No peaks appeared to be present at 611, 639 or 821 cm^{-1}, which suggested the absence of symmetric and asymmetric Si-O-C stretching peaks.

Raman spectroscopy was employed for the SH-SiNPs (Figure 3.6) to investigate the presence, or absence of funcitonal groups further. The peaks found are summarised in Table 3.6, and largely consisted of various vibrational modes present due to the propyl group. The peaks found showed good agreement with the literature measurements of MPTMS [189-191]. There were not peaks present at 611, 821 or 1087 cm^{-1}, indicative of the lack of Si-O-C bonds, or at 920 cm^{-1}, which would be characteristic of the CH$_3$ present in methoxy groups. The lack of these peaks in the spectrum suggested complete, or a high degree of hydrolysis had occurred.
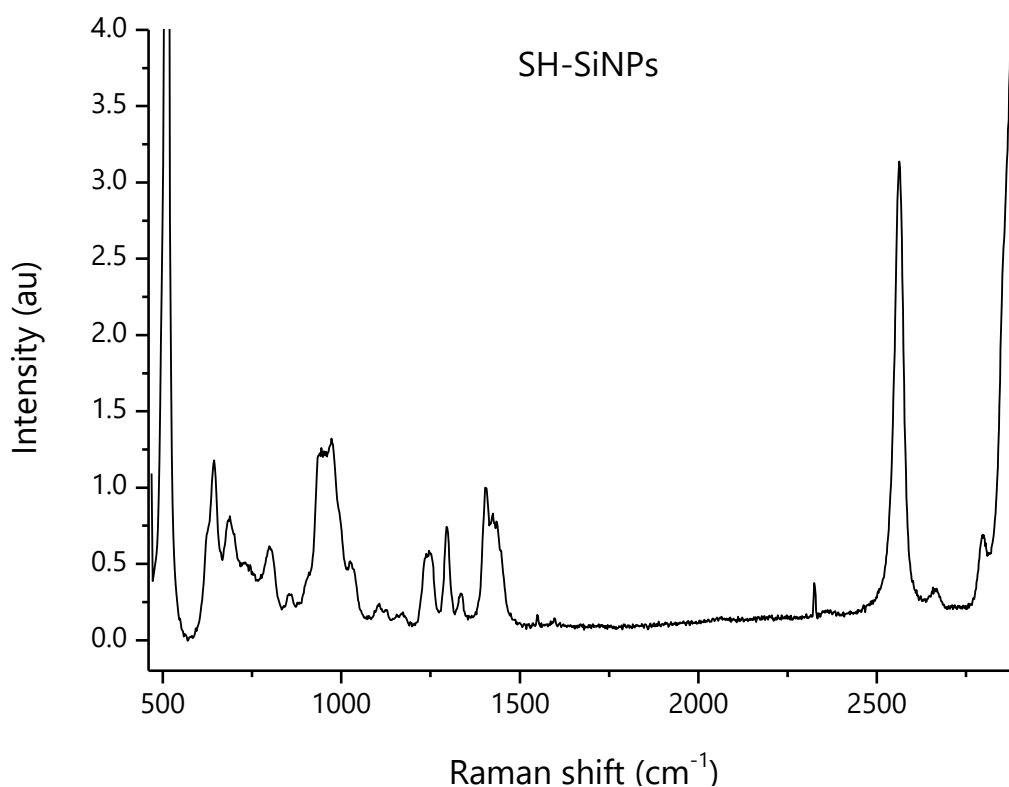
Figure 3.6: Raman spectrum of SH-SiNPs

Table 3.6: Assignments of peaks observed in Raman spectrum of SH-SiNPs

Raman shift (cm^{-1})	Assignment
642	ν(S-C)
687	ν(Si-C), ν(SC)
800	ν(Si-O-Si)
856	⎫
930-980	⎬ CH$_2$
1024	⎭
1107	Si-O-Si
1127	⎫
1170	⎪
1245	⎪
1295	⎬ CH$_2$
1335	alkyl peaks due
1405	to propyl chain
1424	⎪
1436	⎭
2563	ν(SH)
2797	Overtone/combination
2888	ν(CH$_2$)
2911	ν(CH$_2$)

3.3.3 Particle surface area

SH-SiNPs were imaged by SEM and the diameter of the particles measured, 45 particles were measured, each from three images. These values were averaged and the standard deviation measured, giving an average particle diameter of 84±12 nm. Their specific surface area was calculated with the assumption that the particles were smooth spheres, and the surface area was measured by use of a BET isotherm, producing an estimate of the particle surface area. Excellent agreement was found between the theoretical value and the measured value, supporting the statement that the particles are non-porous, as indicated by SEM (Figure 3.3)

3.3.3.1 Geometric calculations of particle specific surface area

A given sample of smooth, uniform, spheres have a theoretical specific surface area given by Equation 3.1, showing proportionality between the specific surface area and the inverse radius of the particles.

$$SSA(r) = \frac{SA}{m_p}$$

$$= \frac{4\pi r^2}{\frac{4}{3}\pi r^3 \rho}$$

$$= \frac{3}{r\rho}$$

Where:

$SSA(r) = specific\ surface\ area\ of\ spheres\ of\ radius, r$

$SA = surface\ area\ of\ particles$

$m_p = mass\ of\ particles$

$= (volume\ of\ particles) \times (density)$

$\rho = particle\ density$

This formula implies that if the particles are monodisperse and smooth the specific surface area will be a straight line with a y-intercept of zero for particles of infinite radius.

Synthesised particles exhibit a small variance around a mean radius. Consider a monomodal sample of particles with mean radius, r, whose radii are normally distributed with standard deviation, σ. The specific surface area of the resulting particle sample will be larger than that of a sample of uniform spheres of radius, r.

This change in the specific surface area can be accounted for using the particle distribution. It is known that for a geometric object with a known distribution related to one property, such as radius, the distribution can be applied to related properties, such as specific surface area [192].

In a normal distribution around a radius, r, the probability of a particle of radius $r + i$ existing, can be represented as a positive number, $\frac{x_i}{2}$, such that $\sum_{i=0}^{N} x_i = 1$. As the normal distribution is symmetric, this means that a particle of radius $r - i$ also has a probability of $\frac{x_i}{2}$ to exist. This explicitly includes the mean radius, which is representable as $r + 0$ and $r - 0$, each assigned the probability $\frac{x_0}{2}$. Thus, the average specific surface area of a particle can be represented as:

$$SSA_{\text{dist}}(r) = \frac{x_0}{2}\left(\frac{3}{\rho}\right)\left(\frac{1}{r+0}+\frac{1}{r-0}\right) + \frac{x_1}{2}\left(\frac{3}{\rho}\right)\left(\frac{1}{r+1}+\frac{1}{r-1}\right) + \frac{x_2}{2}\left(\frac{3}{\rho}\right)\left(\frac{1}{r+2}+\frac{1}{r-2}\right)$$
$$+ \cdots + \frac{x_n}{2}\left(\frac{3}{\rho}\right)\left(\frac{1}{r+N}+\frac{1}{r-N}\right)$$

As both r and N in this equation are both real units of length and are components of a particle radius, this implies the relationship $r > N \geq 0$ is true by definition. Consequently, all terms $\left(\frac{1}{r+N} + \frac{1}{r-N}\right)$ are therefore positive and real for all N.

For perfectly monodisperse particles, the probability $x_0 = 1$ and all other probabilities, $x_i, i > 0$, are zero, in which case the original specific surface area formula (Equation 3.1) is returned. In all other cases, all the probability terms are positive and real. Therefore, the specific surface area of particles with a normally distributed radius ($SSA_{\text{dist}}(r)$), is greater than for a uniform sample of particles, as follows.

$$\text{If:} \quad \frac{1}{2}\left(\frac{1}{r+N} + \frac{1}{r-N}\right) > \frac{1}{r}$$

$$\text{then } SSA_{\text{dist}}(r) > SSA(r)$$

$$\frac{1}{2}\left(\frac{1}{r+N} + \frac{1}{r-N}\right) > \frac{1}{r}$$

$$\frac{(r-N) + (r+N)}{2(r+N)(r-N)} > \frac{1}{r}$$

$$\frac{r}{r^2 - N^2} > \frac{1}{r}$$

$$\frac{r}{r^2 - N^2} - \frac{1}{r} > 0$$

$$\frac{r^2 - (r^2 - N^2)}{r(r^2 - N^2)} > 0$$

$$\frac{N^2}{r^3 - rN^2} > 0$$

Recalling that $r > N$, it is thus true that $r^3 > rN^2$ for all values of r and N, thus $r^3 - rN^2 > 0$.

$$\text{Thus} \quad \frac{N^2}{r^3 - rN^2} > 0$$

$$\frac{1}{2}\left(\frac{1}{r+N} + \frac{1}{r-N}\right) > \frac{1}{r}$$

$$\therefore \; SSA_{\text{dist}}(r) > SSA(r)$$

for any given mean radius, the specific surface area measured will be higher for particles that show a variance in particle radii, than would be measured for uniform particles of the same mean radius. This effect can be accounted for by modification of Equation 3.1.

The specific surface area becomes calculable as a weighted average of the specific surface areas of all particles within the distribution of particles. If the weighting of the particles is not normal, but is still known, this method is still applicable, simply substituting in the known distribution in place of the normal distribution. This would be required for small-radius particles where the standard deviation measured would suggest the presence of particles with an impossible negative radius. Thus, so long as the distribution is known, it can be accounted for by calculating a weighted average of the particle specific surface area. This weighted average is given in Equation 3.2.

$$SSA_{\text{avg}} = \sum_{i=1}^{N} \sigma_i(r) \left(\frac{SA_i(r)}{m_{\text{p}}} \right) \qquad \text{Equation 3.2}$$

Where $\sigma_i(r)$ is the function indicating the probability of a particle of radius r existing.

If the probability density function is known, the specific surface area can be represented in integral form, presented below for the normal distribution.

$$SSA_{\text{avg}} = \int_{r=0}^{\infty} f(r) \left(\frac{SA(r)}{m_{\text{p}}} \right) dr$$

$$SSA_{\text{avg}} = \int_{r=0}^{\infty} \left(\frac{1}{\sqrt{2\pi\sigma^2}} e^{-\frac{(r-\mu)^2}{2\sigma^2}} \right) \left(\frac{3}{r\rho} \right) dr$$

Where

$\sigma = standard\ deviation$

$\mu = mean\ particle\ radius$

For the measured particles of diameter 84±11 nm, Equation 3.2 gives a specific surface area of 38.6 $m^2.g^{-1}$. For reference, a sample of monodisperse spheres of diameter 84 nm would have a theoretical specific surface area of 37.8 $m^2.g^{-1}$.

It was noted from the high-resolution SEM images that the particles showed a slight non-sphericity, so for the general case the particles may be modelled as spheroids. The weight-average specific surface area can be calculated replacing the surface area and volume formulae of spheres with those of spheroids. For simplicity, in this case it is assumed that the standard

deviation of the radii applies equally to the semi-major (*a*) and semi-minor (*c*) axes, that is, that the axial and equatorial radii of all particles within the sample differ by a constant value. For this case:

$$SSA_{\text{avg}} = \sum_{i=1}^{N} \sigma_i(r)\left(\frac{SA_i(r)}{\text{g}}\right)$$

Where $\quad \dfrac{SA(r)}{g} = \dfrac{\left(2\pi a^2 + \dfrac{\pi c^2}{\left(1 - \dfrac{c^2}{a^2}\right)^{\frac{1}{2}}} \ln\left(\dfrac{1 + \left(1 - \dfrac{c^2}{a^2}\right)^{\frac{1}{2}}}{1 - \left(1 - \dfrac{c^2}{a^2}\right)^{\frac{1}{2}}}\right)\right) n}{\dfrac{4\pi}{3} a^2 c \rho n}$ Equation 3.3

With a 2 nm difference between the semi-major and semi-minor axes Equation 3.3 gives a specific surface area of 39.3 $m^2.g^{-1}$, slightly higher than that of the spherical model.

3.3.3.2 BET Isotherm measurement for specific surface area determination

Figure 3.7 displays the BET isotherm measured for the sample of SH-SiNPs with a diameter of 84±11 nm. It was noted that in the expected region of applicability for a BET isotherm, relative pressures 0.05-0.3, the adsorption and desorption traces were the same. A slight hysteresis was noted at higher pressures. The shape of the overall isotherm was indicative of a type IV isotherm, which would indicate mesoporosity of the sample, as well as indicating strong interaction between the adsorbent and adsorbate [133]. The differing factor between the type IV and V isotherms is the value of the C parameter, related to the interaction between the adsorbate and adsorbent. For the SH-SiNPs, this value was C>>1, thus indicating that the inflection point noted below 0.05 p/p^o indicates the formation of the monolayer.

The shape of the hysteresis also provided a key point about the sample. Type IV isotherms usually display a plateau at high pressure, indicating that the sample pores have been filled, whereas the SH-SiNPs did not show a plateau was reached at the maximum pressure. This was indicative that the pore volume in the system was being overestimated, and that the hysteresis loop was instead a result of filling the void volume between particles. The shape of the loop was similar to an H3 loop according to IUPAC classification [193], which is associated with slit like pores, and is often the result of aggregated clay particles [194]. An H1 loop, which

usually shows a plateau at high pressures, is also possible. In this case, the lack of plateau at high pressures would indicate the filling of void volume, rather than defined pores. H1 loops can be obtained in samples of fine powders of nearly uniform spheres [194], which described the particle sample.

The specific surface area calculated from this sample indicated a specific surface area of 39.0 ± 0.7 $m^2 \cdot g^{-1}$, which showed excellent agreement with the values derived from the theoretical calculations: 38.6 $m^2 \cdot g^{-1}$ assuming the particles are spheres, and 39.3 $m^2 \cdot g^{-1}$ assuming spheroidal particles. This agreement indicates that the particles were smooth, with little roughness on the surface to increase surface area from the theoretical value.
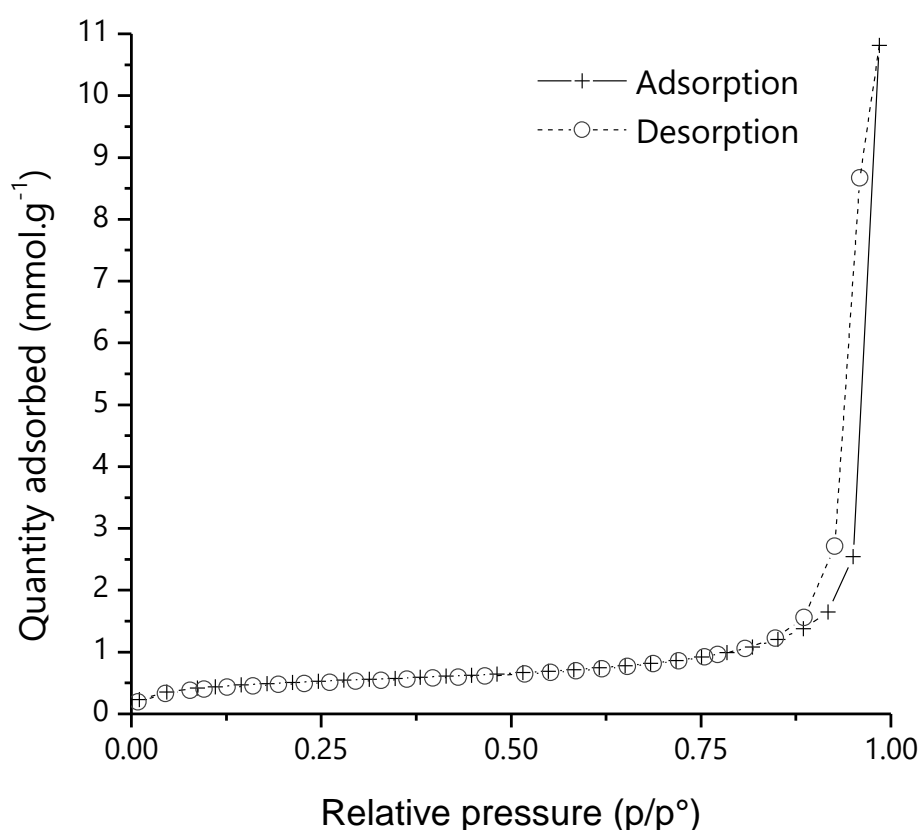
Figure 3.7: Linear plot of BET isotherm of SH-SiNPs with diameter 84±11 nm

3.3.4 Stability and solution dispersability

Stability of nanoparticles under storage is important for their application. Silica particles may form irreversible bonding leading to large aggregates, which collapse out of solution. In TEOS particles, this is usually through the formaion of siloxane bridges across the exposed surface silanes. SH-SiNPs may not show complete condensation, leaving silanol groups able to form interparticle bridges. Another possibility is through formation of disulphide bonds. It is also

desirable that aggregation occurring because of drying is reversible, meaning once dried a dispersion of primary particles is achievable.

For storage tests, nanoparticles were dried under vacuum overnight to ensure complete removal of solvent. It was found that the SiOH SiNPs could be redispersed in water with sonication after this time. The SH-SiNPs were also capable of being redispersed in water, however, large agglomerates were present, as well as the loss of the characteristic light-scattering effect, instead the solutions appeared opaque and white, indicating aggregation. The increased Z-average diameter and variance was likely due to the presence of dimers or larger agglomerates that are unsuccessfully broken apart on redispersion. Greater success was achievable if the particles were first redispersed in ethanol, followed by washing in either water, ethanol or acetonitrile. A sample of SH-SiNPs displayed a Z-average diameter of 176 ± 14 nm before processing, and after drying and redispersion the same sample showed 189 ± 35 nm.

Achieving redispersion with the nanoparticles is important for their application. Functionalisation of the particles requires dispersion in solvents appropriate for further modification. This aggregation may block reactive sites during particle functionalisation, or cause sedimentation of the particles, removing them from the reaction medium and preventing their complete functionalisation. SH-SiNPs were redispersible without significant aggregation, allowing further desired reactions to proceed unhindered. Based on the aggregation that does occur, it was decided for optimised reactivity and dispersability the SH-SiNPs would be not allowed to dry out prior to reaction, to minimise irreversible aggregation effects.

3.3.5 Optical properties

SH-SiNPs prepared in this work showed structural colour during synthesis and processing. In solution, light scattering typical of colloidal solutions was evident, with a blue reflectance and orange transmittance of light. Once cleaned, the particles began to show greater colouration, showing blue colours when wet. Once the samples dried, the colour became white, with a slight blue tinge (Figure 3.8).

Figure 3.8: SH-SiNPs dried in a sample vial showing blue colouration

Particles that were collapsed by salt during the cleaning process lost the light scattering effect in solution, becoming opaque with no transmittance of light. The samples recovered from these formed white solids with no evident colouring, until multiple washing steps (>3) in water had been undertaken. After this, the blue colouration returned. Solution colouration due to the dispersed particles was also affected by the functionality of the particles, discussed further in Section 6.5.

3.4 Conclusions

The previously established method for producing µg scale quantities of SH-SiNPs has been modified to enable multi-litre scale reactions yielding gram quantities of particles, improving yield and monodispersity of particles. Excellent control was retained over the particle diameters, reducing batch-to-batch variability by elimination of the formation of large amorphous agglomerates during reaction.

MPTMS concentration in aqueous solutions was found to increase particle yield, however also resulted in an increase in polydispersity, and formation of large aggregates in solution. The aggregation resulted in increased batch-to-batch variability, rendering this method unsuited for producing larger particle yields.

Increasing reaction volume increased particle yield, however, produced inhomogeneous reaction mixtures due to the limited ability of MPTMS to disperse in water. Pre-hydrolysis of the MPTMS was unable to overcome this limitation. Large aggregate formation became more prevalent at increased volumes, increasing batch-to-batch variability.

Changing the solvent conditions to include 10 % ethanol was found to produce more uniform particles. The control over particle diameter was retained at increased silane concentrations and at increased volumes. This allowed for narrower dispersions of size-controlled particles to be produced in larger yields per reaction. Reaction mixtures remained homogeneous (and thus usable) up to 3 L in scale.

A reproducible method for synthesising large-scale quantities of particles suitable for further reaction via thiol-ene click chemistry was established. Unless otherwise specified, all particle samples used in the following chapters are based on the synthetic protocol laid out in Section 2.1.1.

The theoretical determination of the specific surface area of the SH-SiNPs samples was modified to account for the dispersity in the particles as synthesised, resulting in agreement between the theoretical value (38.6 $m^2 \cdot g^{-1}$) and the value measured by BET (39.0 ± 7 $m^2 \cdot g^{-1}$). This supports that the particles as synthesised are smooth, simplifying further analysis of particle surface functional density.

4 Development of methods for accurate determination of surface functional density of silica nanoparticles

4.1 Overview

Particle surface functionality is one of the most important factors for particle application, affecting their dispersability in solvent, aggregation, and suitability for application or further reaction. In characterising surface functionality, it is important to understand not just the chemical identity of the moieties attached to the surface, but the amount of attachments per unit area. It must also be known whether the surface functionality is chemically bonded to the surface or associated with non-specific physisorption. Further, characterisation must be as independent as possible of batch-to-batch variability; size-based differences must be known and accounted for.

Some methods that have been used to characterise particle surface functionality modifications include ATR-FTIR spectroscopy [108], elemental analysis [177], TGA [108, 177, 195], TGA-Mass Spectrometry and nuclear magnetic resonance [196], or potentiometric titrations [197]. For this work, ATR-FTIR spectroscopy and TGA were used to provide complementary information on the particle functionalities, and to produce independent estimates of the particle surface functional density. Both methods have their limitations. In this chapter, it is described how new approaches to data analysis from these techniques offered new insights into surface density determination.

TGA is a robust method of analysis, capable of giving highly accurate information about the mass of reagent added to the particles. By comparing functionalised and unfunctionalised particles the difference in degradation profiles were compared, which allowed direct quantitation of the amount of sample composed of the adduct.

Kinetic reactions are often modelled by the derivative curve of the conversion. This process was applied to the mass loss of the curve herein. The dTGA curves were fitted with asymmetric double sigmoidal peaks, which are a peak shape suited for analysis of skewed distributions [198]. It is known that Gaussian and Lorentzian line shapes often provide a poor fit of kinetic processes, such as thermal decomposition and pyrolysis, with better fits achievable with asymmetric functions [199].

Reactions are often modelled using sigmoidal functions, such as the Fraser-Suzuki function [199, 200], or an asymmetric double sigmoidal function [137]. These types of functions have been found to fit the derivative thermograms significantly better than more conventionally used Gaussian functions.

The asymmetric double sigmoidal peak function is given by the equation:

$$y = B \frac{1}{1 + e^{-\left(\frac{x - x_c + \frac{w_1}{2}}{w_2}\right)}} \left(1 - \frac{1}{1 + e^{-\left(1 - \frac{x - x_c - \frac{w_1}{2}}{w3}\right)}} \right)$$

Equation 4.1

$Where$

$B = amplitude$

$x_c = centre$

$w_1 = width\ factor$

$w_2 = width\ on\ low\ temperature\ side$

$w_3 = width\ on\ high\ temperature\ side$

The Gaussian function is

$$y = B e^{-\frac{1}{2}\left(\frac{x - x_c}{\sigma}\right)^2}$$

Equation 4.2

An alternate method of constructing the ATR-FTIR calibration curve was proposed allowing for a wider scope of sample analysis. Nanoparticles are too small to cause appreciable scattering of infrared light, and so long as the particles remain in this size regime, the effect of scattering is negligible. Thus, as particle surface area was accurately known, and an appropriate internal reference peak is present, this allows for quantitative measurement of the particle surface functional density [108].

4.2 Surface functional density measurements

Conventionally, the surface functional density is determined by establishing the functional group content of the nanoparticles. Knowing this the functional groups are determined by

$$\sigma = w_{\text{moiety}} \times \frac{N_{Av}}{MM_{\text{moiety}} \cdot SSA}$$

<div align="right">Equation 4.3</div>

Where

$$\sigma = \text{number of surface groups per nm}^2$$

$$N_{Av} = \text{Avogadro's constant}$$

$$w_{\text{moiety}} = \text{mass fraction of moiety}$$

$$= \frac{m_{\text{moiety}}}{m_{\text{moiety}} + m_{\text{SH-SiNPs}}}$$

$$MM_{\text{moiety}} = \text{molar mass of attached moiety}$$

$$m_{\text{moiety}} = \text{mass of attached moiety}$$

$$m_{\text{SH-SiNPs}} = \text{mass of SH} - \text{SiNPs in sample}$$

4.2.1 Geometric estimations

Surface functional density is based on the number of functional (or functionalisable) groups per square nm of surface available. Zhuravlev's constant suggests that 4.6 OH groups·nm^{-2} are available on the surface of amorphous silica [201]. Previous work estimated approximately 4.9 groups·nm^2 were available for functionalisation [108], however this referred to an 8th generation particle simulation: the values were continuing to increase with each generation, and a limitation in computer power prevented further values from being accurately calculated. It was theorised that the underlying MPTMS layers had accessible thiol groups, increasing the functional density achievable for the particles.

A geometric estimate was considered, based on consideration of which sulfur atoms are available for reaction. Assuming the particles are spherical and of uniform density, those sulfur atoms capable of reaction are those in the outermost layer, consisting of those atoms on the outermost surface, as well as those exposed from sub-layers. This produces an effective surface volume that gives a range of the number of surface functional groups available, dependent on the depth of the effective surface selected, as well as the diameter of the particles selected.

The length of the MPTMS molecule used to produce the particle is approximately 0.7 nm [202]. Assuming any functional groups present in the outermost 0.7 nm is potentially available for

reaction; the number of moles available in the "effective surface" can be defined geometrically as follows.

$$\text{Particle radius} = r$$

$$\text{Inner sphere radius} = r_i = r - 0.7 \text{ nm}$$

$$\text{Effective surface} = \left(V_{\text{particle}} - V_{\text{inner}}\right) = \Delta V$$

$$= \frac{4}{3}\pi r^3 - \frac{4}{3}\pi (r_i)^3$$

$$= \frac{4}{3}\pi (r^3 - (r - 0.7)^3) = \frac{4}{3}\pi(\Delta r)$$

$$\text{Surface mass} = \rho \left(\frac{4}{3}\pi \Delta r\right)$$

$$\text{Surface moles} = \frac{\rho \frac{4}{3}\pi \Delta r}{MM_{\text{SH-SiNPs}}}$$

$$\text{Particle surface area} = 4\pi r^2$$

$$\frac{\text{Surface moles}}{\text{Surface area}} = \frac{\rho \frac{4}{3}\pi \Delta r}{4\pi r^2 MM_{\text{SH-SiNPs}}} = \frac{\rho \Delta r}{3 r^2 MM_{\text{SH-SiNPs}}}$$

Where

$$\rho = \text{SH-SiNP } density = 1.9 \text{ g·cm}^{-3}$$

$$V_{\text{particle}} = Volume\ of\ particle\ of\ radius\ r$$

$$V_{\text{inner}} = Volume\ of\ sphere\ of\ radius\ (r - 0.7)$$

$$MM_{\text{SH-SiNPs}} = molar\ mass\ of\ repeating\ unit\ of\ SH - SiNPs$$

$$= SiO_{1.5}C_3H_7S = 127.249 \text{ g·mol}^{-1}$$

Accordingly, the available surface groups in a sample of SH-SiNPs shows a slight dependence on radius; however, between particles with $r = 15$ nm, to $r = 100$ nm the value ranges from 6.01 to 6.25 groups·nm^{-2}. This value is slightly higher than the theoretical estimates made in previous works. Due to this relatively small change with radius, the variation of particle radii within a sample has a negligible effect on the theoretical surface groups available for reaction.

4.2.2 Surface attachment density determination – TGA

The surface area of the particles was known, as described in Section 3.4.3. Independently determining the quantity of functional groups attached to the surface allowed for the quantification of the surface functional density of the particles, which was compared with the

geometric estimate and results from previous works. TGA analysis of the particles allowed for the determination of the organic content of the particle samples, enabling it to be used to determine the quantity of the organic moiety attached to the particle surface. Further, TGA can differentiate between physisorbed and chemisorbed bonds if the attached molecule is sufficiently volatile, which is not possible using ATR-FTIR spectroscopy. In this work, the attached functional groups were volatile at a low enough temperature as to be easily distinguished in the TGA measurements.

Figure 4.1 shows that for undec-10-enoic acid a clear distinction was visible between the functionalised particles and those with undec-10-enoic acid present but not reacted. A large mass loss was evident starting at 100°C, due to the unreacted undec-10-enoic acid. The mass loss occured significantly below the boiling point of undec-10-enoic acid, 275°C, as the vessel used for TGA measurement was open, which allowed volatilisation at lower temperatures
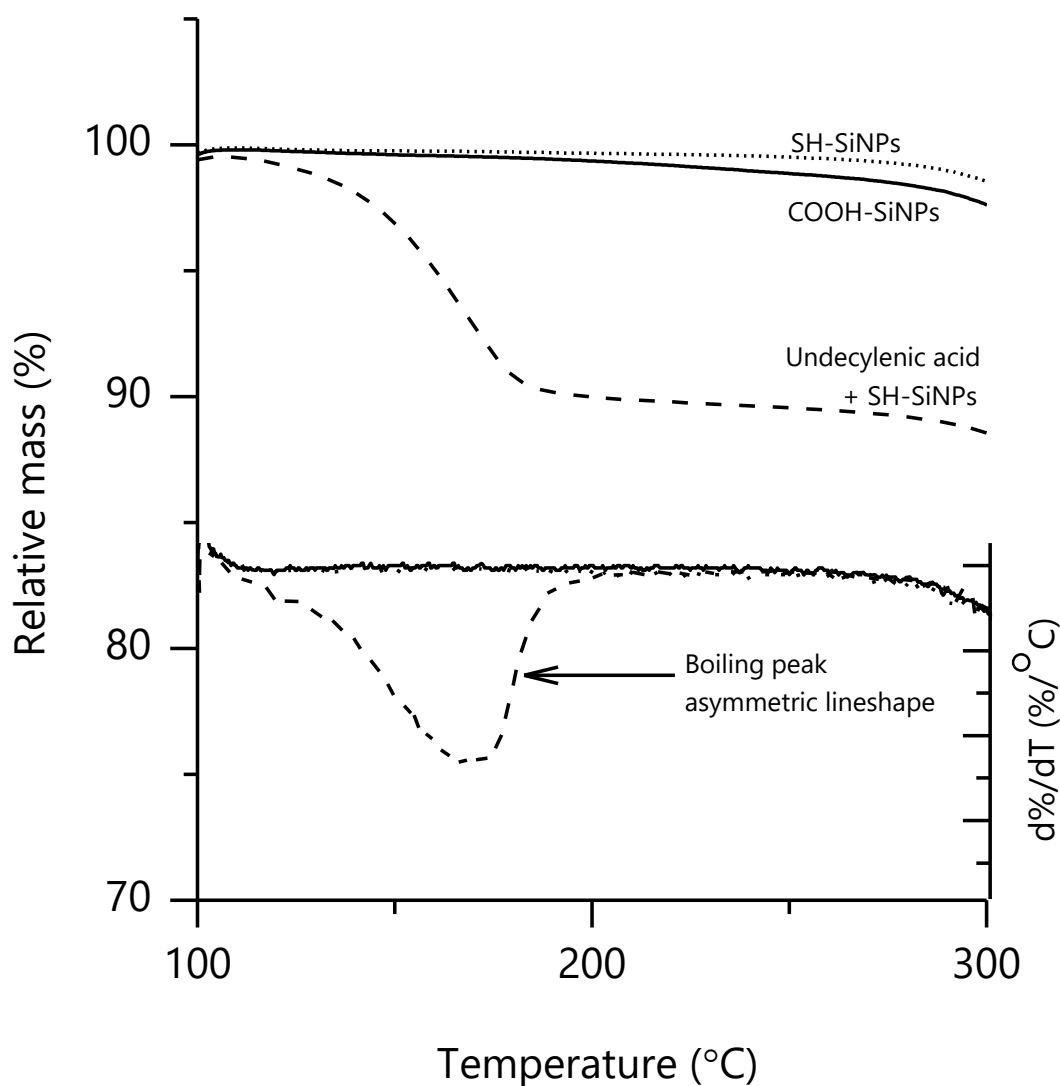
[203], which was notable in the derivative thermogram as a large asymmetric peak.Figure 4.1: Thermograms and derivative thermograms with respect to temperature of SH-SiNPs, COOH-SiNPs and unreacted SH-SiNPs with added undec-10-enoic acid

Functionalised COOH-SiNPs showed a slight degradation that was not present for thiol particles, but did not show the loss due to evaporation of unattached undec-10-enoic acid. The retention of the acid to the COOH-SiNPs at this temperature range indicated a more robust attachment had been achieved, specifically the successful attachment of moieties to the particle surface through thiol-ene click chemistry.

It can be seen in Figure 4.2 that the SH-SiNPs showed multiple overlapping weight loss events, making a clear identification of individual weight loss events and quantities more difficult. The degradation mechanisms did not show improved separation after changing the ramp rate of the

sample from 2.5 to 30 °C·min^{-1}. For the experiments to retain consistency, all further measurements were taken at 10°C.min^{-1} under nitrogen.
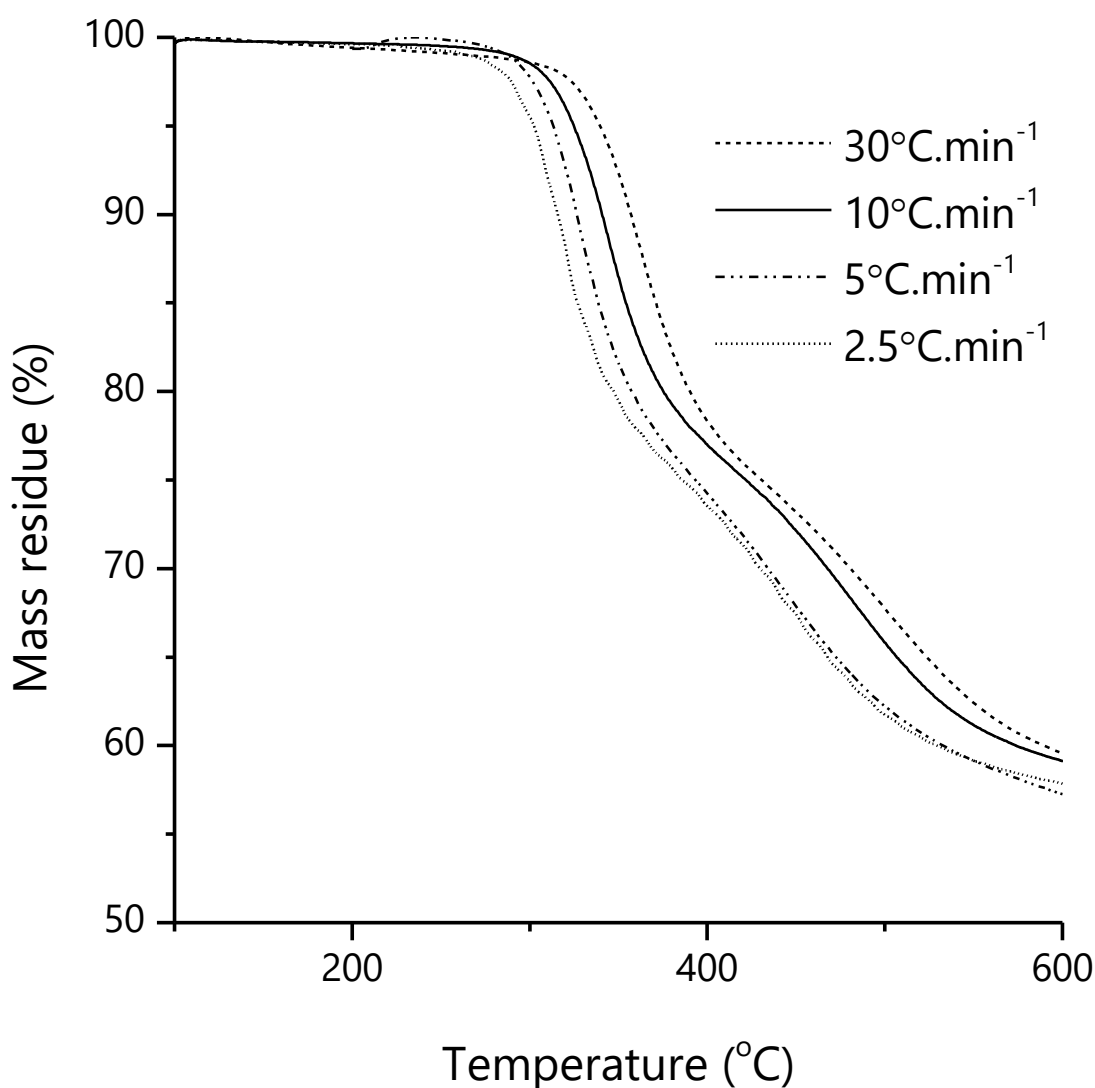
Figure 4.2: Thermograms of SH-SiNPs heated at indicated ramp rates under nitrogen atmosphere

Conventionally, the mass losses could be divided among three regions, based on the different rates of degradations. These regions, however, would not be directly related to the processes occurring, as they would not account for overlap of multiple peaks. This would reduce the accuracy of estimates of the mass losses due to specific processes. To more accurately measure and interpret the thermograms, the derivatives with respect to temperature were taken of each of the measurements.

The final masses attained for each of the samples did not match the expected degradation of all the organic components of hydrolysed and condensed MPTMS. The SH-SiNPs can be considered as polysilsesquioxanes with repeating molecular units of $SiO_{1.5}C_3H_6SH$. These

units have a molar mass of 127.2 g·mol^{-1}. Therefore, they were expected to show similar degradation patterns to other polysiloxanes.

During pyrolysis of polysiloxanes, a complex $Si_xO_yC_z$ glass will form, with the exact chemical composition being unknown and unpredictable [204, 205]. Introducing air at high temperatures allows the remaining carbonaceous material to be removed, and introduces additional oxygen enabling the formation of SiO_2 as the final residue. With a molar mass of 60.08 g·mol^{-1}, the theoretical residual mass would be 47.2 %. Across repeated degradations of different batches of SH-SiNPs, the average residual mass was found to be 47.0 ± 0.8 %, which agreed with the theoretical value.
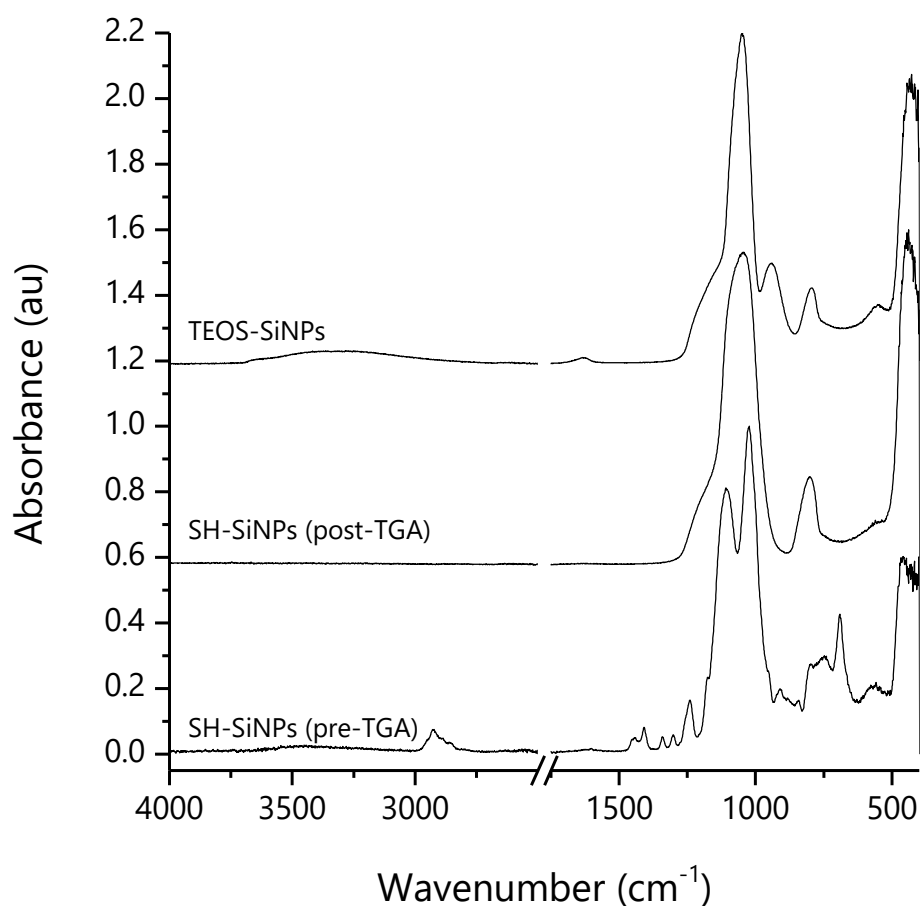
Figure 4.3: ATR-FTIR spectra of SH-SiNPs before and after thermal decomposition in TGA measurement, spectrum of TEOS-SiNPs for comparison

Figure 4.3 displays the ATR-FTIR spectra of SH-SiNPs taken before and after TGA measurements. A spectrum of TEOS-SiNPs was included for comparison. The SH-SiNPs after TGA measurement showed an ATR-FTIR spectrum similar to the TEOS-SiNPs, there were peaks due to the presence of Si-O-Si stretching at 1100cm^{-1} (with the broad shoulder at 1220

cm^{-1} indicating amorphous silicon [206]) and Si-O-Si bending at 800 cm^{-1}. The SH-SiNPs post-TGA showed no peaks that would indicate the presence of Si-OH peaks, no silanol groups are present as expected. The Si-C bond's characteristic peak at 1275 cm^{-1} was not present, indicating no silicon-carbon bonds were present, suggesting that the final product after the introduction of air was SiO$_2$.

Derivative thermograms with respect to temperature were taken to provide additional information about the degradation events occurring during pyrolysis of the nanoparticles. Curve fitting to the peaks present during the degradations was used to quantify the mass loss due to the event, without the overlapping mass losses of concurrent events.

Both asymmetric double sigmoidal (Equation 4.1) and Gaussian (Equation 4.2) curves were considered for curve fitting the temperature derivatives of the TGA thermograms, and the fits achieved for these peak shapes can be seen in Figure 4.4. The fit achieved by the asymmetric double sigmoidal peaks was observed to represent the data more closely during the degradation of the thiol peaks, and was capable of fitting the peak due to the evaporation of unbound undec-10-enoic acid. The Gaussian fit by comparison showed a poorer fit for the particle degradation events and as a symmetric peak, was unable to model the evaporation event of undec-10-enoic acid with accuracy. Thus for the curve fitting, asymmetric double sigmoidal curves were selected as the appropriate peak shape.
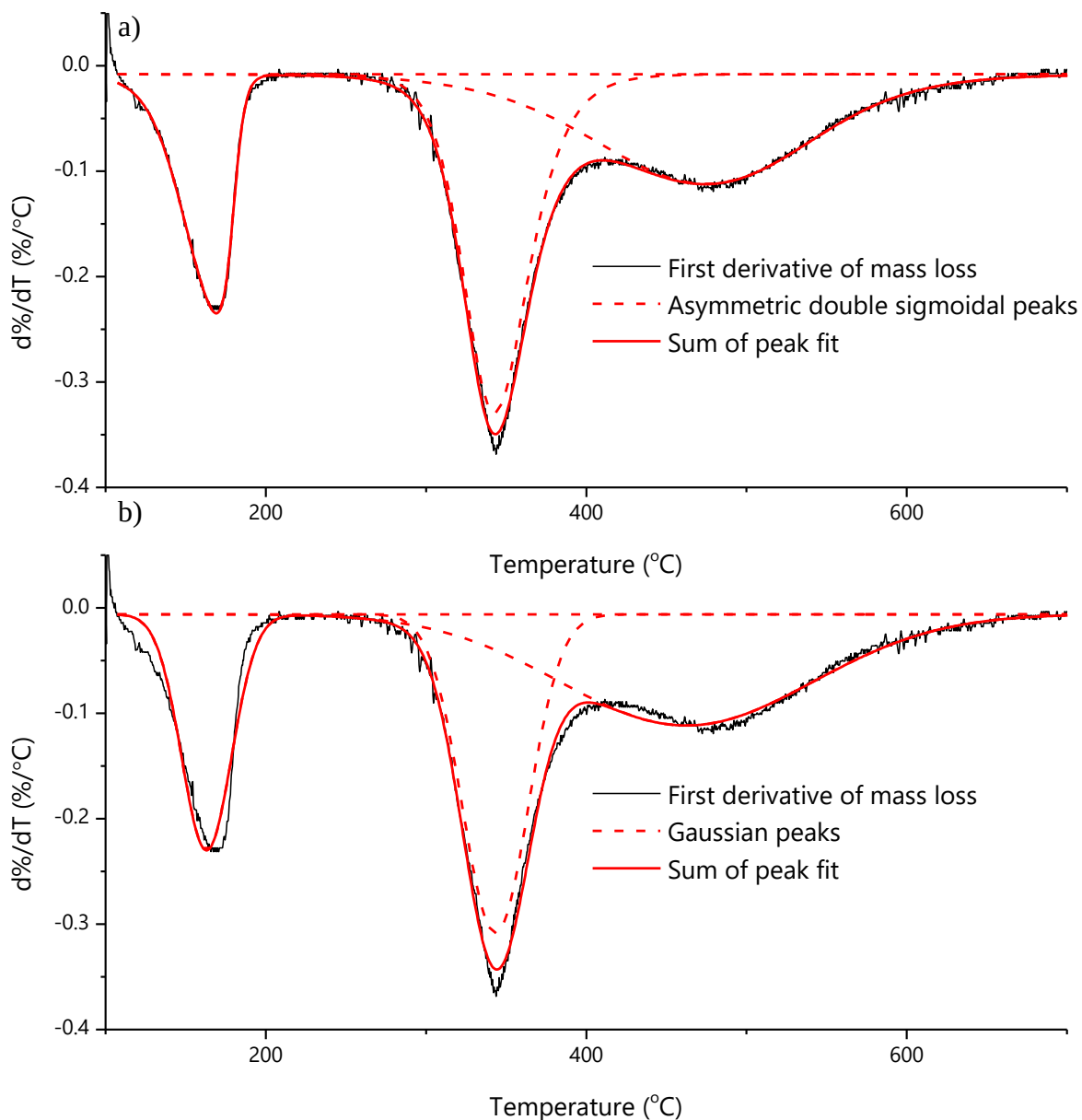
Figure 4.4: Derivative relative masses with respect to temperature of SH-SiNPs with unreacted undec-10-enoic acid added. Fit by a) Asymmetric double sigmoidal peaks and b) Gaussian peaks

Different sized SH-SiNPs showed slightly different degradation patterns, displayed in Figure 4.5. Both particles appeared to show a significant mass loss starting at 250°C, followed by a slower degradation. The larger particles then showed a small continuous mass loss starting at approximately 600°C that continued until air was introduced. Residue masses of the samples after switching the gas to air were similar, at 47.9 % and 46.7 % for the 80 nm and 170 nm particles respectively. These values showed reasonably good agreement with the theoretically expected value of 47.2 %.
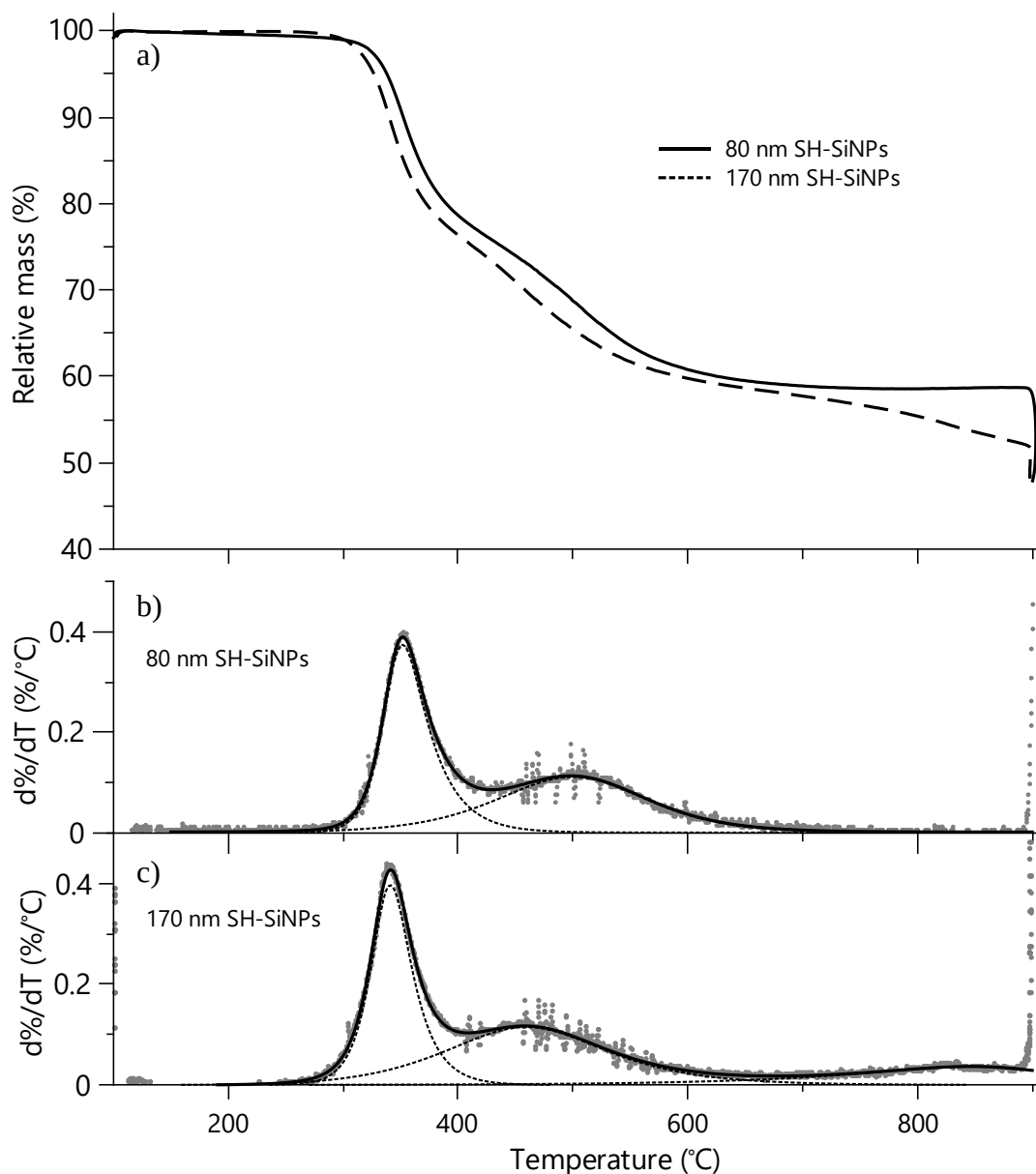
Figure 4.5: a) Relative masses of 80 and 170 nm diameter SH-SiNPs heated from 30-900°C, heating rate 10°C.min^{-1} under nitrogen, air was introduced at 900°C. b) Derivative relative mass losses with respect to temperature for 80 nm SH-SiNPs. c) Derivative relative masses with respect to temperature for 170 nm SH-SiNPs. Dotted lines are asymmetric double sigmoidal peaks fitted to the degradation events, solid lines are sums of fitted peaks

The dTGA results (Figure 4.5b and c) showed two peaks for the 80 nm particles, and three for the 170 nm particles, excluding the data for the final burn in air. The asymmetric double sigmoid peak parameters are listed in Table 4.1. The temperature recorded at the maximum rate of degradation (T_{Max}) was also reported. Slight differences in the curves were noted between the particle diameters. For larger particles, degradation events were found to happen at lower temperatures and the peaks overlapped across a greater temperature range. Curve

fitting of these peaks indicated similar peak areas between samples. An additional broad peak was present for the larger particles, with an onset estimated at 600°C.

Table 4.1: Asymmetric double sigmoidal peak fitting parameters and peak properties for derivative thermograms of SH-SiNPs of different diameters

80 nm	Area (%)	T_{Max} (°C)	x_c (°C)	A (%/°C)	w_1	w_2	w_3
Peak 1	18.7	352	343.4203	-0.01278771	0	8.902305	18.85105
Peak 2	22.2	497	517.8626	-0.004272874	0	61.90074	39.99397
170 nm							
Peak 1	18.6	341	337.057	-0.01493754	0	10.2237	14.43933
Peak 2	22.4	457	449.3624	-0.004591358	0	46.07212	51.43023
Peak 3	7.1	893	889.3478	-0.001172335	0	96.93755	32.32346

If an additional peak were incorporated into the peak fitting the curve could be replicated using multiple Gaussian or other curves, however, for the optimal fit, this would require multiple peaks that share the same maximum temperature, but with a higher onset temperature, and lower final temperature. This was judged as unlikely, and fits were confined to as few peaks as necessary to obtain a reasonable agreement with the data.

For each of the curve fits, the first peak corresponded to the range of 270-500°C. Peak onsets were in agreement with the expected temperature for the degradation of thiol groups [196]. The peak areas in both cases were approximately 18 %, according to the peak fits for both particle diameters. If all the sulfur were to be removed during this step as H_2S, this peak size would be insufficient, suggesting incomplete removal of the sulfur from the particles. By molecular mass, H_2S makes up 26.8 % of the particle, and so this event does not correspond to the total expected loss of H_2S from the original sample. This could indicate trapping of degradation products within the sample. Alternatively, owing to the complex degradation of mercapto-terminal organics, the residue produced may also have included high-sulfur content residues [207], affecting the molecular weight unless removed by oxidation.

The smaller particles showed a maximum degradation rate at approximately 15°C higher than the larger particles. This suggests the particle degradation was autocatalytic in nature, similar to many solid-state decompositions [208]. Groups degrading in larger particles would therefore be expected to take a greater amount of time to diffuse out compared to those in smaller

particles. This gives them a greater residence time and opportunity for autocatalytic degradation to occur. This has been found in polymeric particles previously, in which a linear relationship was found between the particle size and the degradation rate [209].

The second peak for each of the curve fits corresponded to 22-23 % of the mass loss. This step was attributed to the loss of shorter carbon chain groups from the surface, resulting in the formation of the $Si_xO_yC_z$ char expected. Carbon content was expected to remain at this step, as the area of the peak was unable to account for the complete loss of propyl groups from the sample. Further, when the TGA run was terminated before the introduction of air to the system, the residue formed at the end of this step was black or grey in colour, which indicated the presence of carbon. An earlier peak maximum was again found for the larger particles, showing a maximum degradation rate approximately 50°C lower than the smaller particles.

The third degradation for the larger silica particles was likely to be the loss of remaining carbon content from the particles. This may have been occurring at a lower temperature for the larger particles with similar reasoning to the previous two degradation steps. The increased size led to an increased residence time for the loss of the compounds, which autocatalysed the degradation, resulting in an increased rate of reaction. This reaction was not completed before the air was introduced. This would suggest that the smaller particles were capable of undergoing a similar degradation at higher temperatures than were analysed here.

The air degradation produced a mass loss of approximately 11 % for the 80 nm SH-SiNPs, and approximately 3 % for the 170 nm SH-SiNPs. This accounted for the remaining carbon residue in the sample. When the mass loss due to the third degradation was considered along with the air burn, the values for the remaining carbon residue for both agreed to within 1 % of the theoretically expected value.
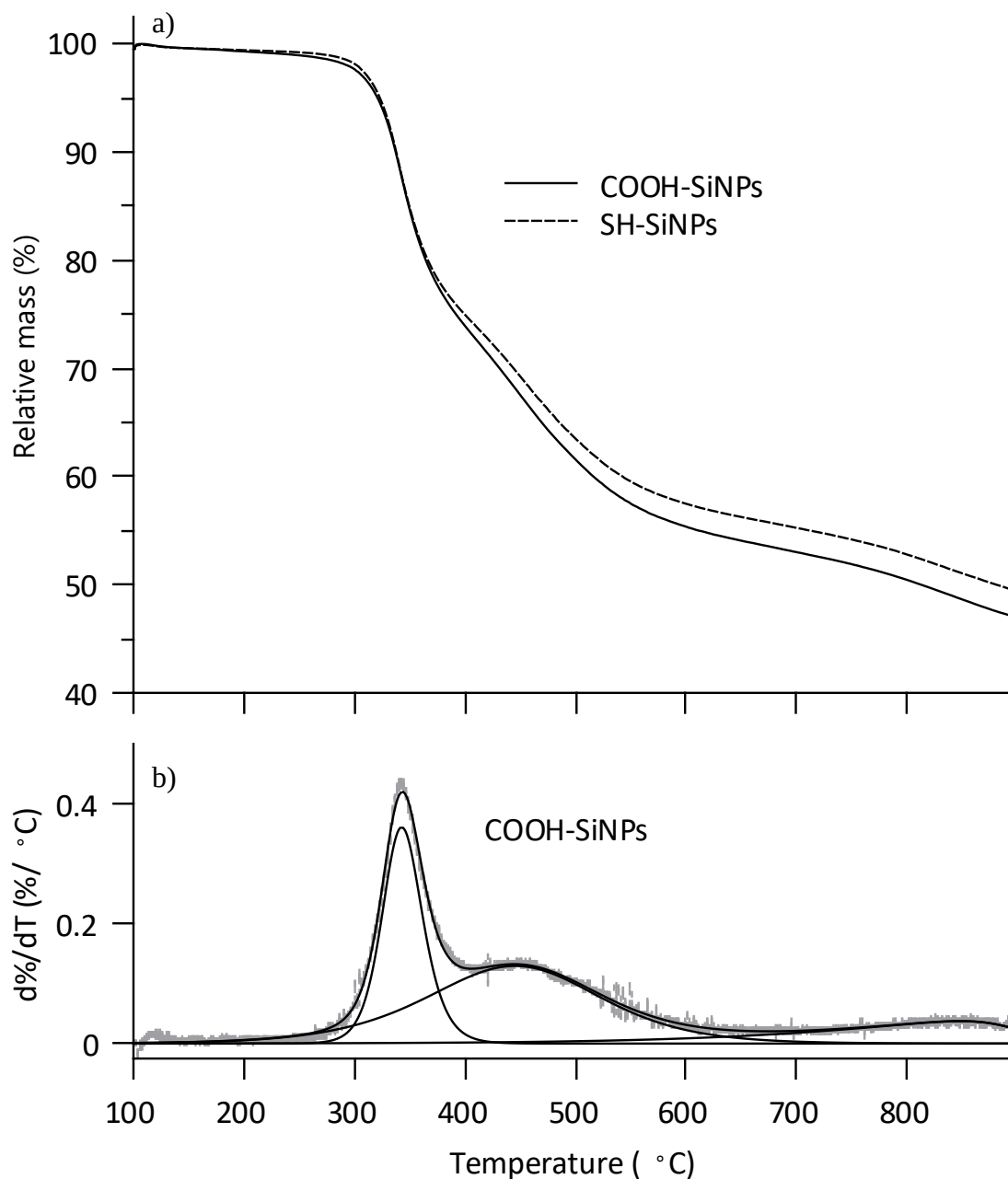
Figure 4.6: a) Thermogram of COOH-SiNPs and SH-SiNPs. b) First derivative of mass loss of COOH-SiNPs' thermogram with respect to temperature, grey points indicating measured data, dotted lines the fitted asymmetric double sigmoidal curves and solid line the sum of the fitted curve

Figure 4.6a) shows the thermograms for COOH-SiNPs and corresponding unreacted SH-SiNPs. Both showed a similar degradation pattern, however the COOH-SiNPs showed lower residual mass, with a difference of 1.9 %, which corresponded to the original sample containing 4.0 % by mass undec-10-enoic acid. This indicated an attachment density of 6.5 ± 0.7 groups·nm^{-2}, agreeing with the upper limit expected geometrically (Section 4.2.1). No peak was noted for the earlier degradation of acid than the SH-SiNPs, indicating attachment occurred.

85

Table 4.2: Mass losses for degradation events modelled in temperature-derivative thermogram of SH-SiNPs and COOH-SiNPs

Degradation event	Peak areas (%)		Event difference (%)
	SH-SiNPs	COOH-SiNPs	
Peak 1 (337 °C)	18.6	17.9	-0.8
Peak 2 (454°C)*	22.4	27.7	5.3
Peak 3 (850 °C)	7.1	6.4	0.7
Air burn	2.8	3.4	0.6
Total (dTGA)	51.0	55.4	4.5
	Mass residues (%)		
Residue (TGA)	46.7	44.8	-1.9

The derivative thermogram shown in Figure 4.6b) was taken, and asymmetric double sigmoidal peaks were fit. Peak areas are presented in Table 4.2, and compared the peak areas of the SH-SiNPs from which the particles were prepared. For each of the degradation events, the maximum rate of mass loss was within ±1 °C before and after the reaction. This suggests the additional moiety did not provide a weak point, or weak bond, where an initial degradation could occur.

The second degradation event showed a similar maximum point, but an increased peak area compared to the SH-SiNPs. This peak was associated with the major degradation of the alkane chain on the particle groups. Thus, the increased mass loss in this section was attributed to the degradation of the attached undec-10-enoic acid moiety, effectively delaying the degradation of the thioether bonds compared to the terminal thiols. If the thioether and thiol bonds were to degrade simultaneously, it would be expected that the entire moiety would be removed at the same time during the first degradation event. Due to the relative stability of the –COOH terminal functional group, for it to remain stable until approximately the same time as the –SH terminal groups is sensible.

Figure 4.7: a) Thermogram of Br-SiNPs and SH-SiNPs. b) First derivative of mass loss of Br-SiNPs' thermogram with respect to temperature, grey points indicating measured data, dotted lines the fitted asymmetric double sigmoidal curves and solid line the sum of the fitted curve

Br-SiNPs showed a final residue of 39.6 % (Figure 4.7a) and mass residues between the Br-SiNPs and SH-SiNPs differed by 6.4 %. Assuming the final product was SiO_2 after the addition of air, the residue indicates the SH-SiNPs consisted of 86 % of the original sample, indicating 14 % of the sample was the bromoundecene moiety, corresponding to 8.5 ± 1 groups·nm^{-1}, higher than the expected surface functional density of particles.

In the derivative thermogram, (Figure 4.7b), three degradation events were evident. The first event was named Peak Br, with the remaining two peaks denoted as Peak 1 and 2, for consistency with the peaks observed in all other functional particles. This peak occurred below the first peak due to the degradation of the thiol groups on the surface. The shape and position of the peak suggested the attachment of the bromoundecene occurred, rather than the association of physisorbed bromoundecene. Compared to the physisorbed undec-10-enoic acid

in Figure 4.1, the derivative TGA peak was more symmetric, and had a higher temperature of maximum mass loss rate. As 11-bromo-1-undecene has a lower boiling point that undec-10-enoic acid (149-150 °C compared to 275 °C) it was expected that even if the bromoundecene were physisorbed, it would show a mass loss feature at a lower temperature than it did.

Table 4.3: Mass losses for degradation events modelled in temperature-derivative thermogram of SH-SiNPs and Br-SiNPs

| Degradation event | Peak areas (%) | | Event difference (%) |
	SH-SiNPs	Br-SiNPs	
Peak Br (210 °C)	-	8.5	8.5
Peak 1 (350 °C/345 °C)*	19.9	22.1	2.2
Peak 2 (485 °C)	23.8	20.1	-3.7
Air burn	9.0	9.3	0.3
Total (dTGA)	52.7	60.1	7.3
	Mass residues (%)		
Residue (TGA)	45.8	39.6	-6.2

* After functionalisation the maximum mass loss for peak 2 shifted from 350 °C to 345 °C

Table 4.3 shows the areas, representing relative degradation quantities, for each of the peaks modelled in the dTGA measurements of the Br-SiNPs, and their underlying SH-SiNPs. The first step showed a maximum mass loss rate at 210 °C. This was attributed to the degradation of the bromoundecene attached to the surface through the loss of bromine as hydrogen bromide, followed by the degradation of the carbon chain. Curve fitting with an asymmetric double sigmoidal peak suggested the total degradation for this peak was 8.5 % by mass. Based on the residual mass the expected mass loss due to hydrogen bromide was 4.7 %, suggesting the first peak resulted from the loss of additional degradation products, but not from the loss of the entire bromoundecene moiety.

It is possible the increased peak area was due to the loss of the hydrogen bromide, destabilising the undecene and allowing the carbon degradation to occur at a lower temperature than those protected by the thiol group. Peak 1, identified in the SH-SiNPs as the degradation of the SH-terminal groups, had a maximum mass loss rate 5 °C lower, and shows an increased area. This suggests the additional carbon groups being lost from the undecene chain were being lost in this range, overlapping with the existing thiol peak. If the undecene groups had been completely lost prior to this degradation event, the peak area would be reduced due to the lesser relative quantity of thiol groups within the sample. This area reduction was found in peak 2,

identified as the degradation of the propyl arm of the MPTMS. The maximum mass loss rate for peak 2 was unchanged after functionalisation, suggesting the additional mass loss due to the bromoundecene was not occurring enough within this temperature range to affect the degradation.

Thus, the moiety was expected to decompose through the loss of the bromine first as hydrogen bromide, followed by the degradation of the carbon chain, rather than through direct breakage of the C-S bond of the thioether. In support of this mechanism was that the temperature found for the degradation agrees with that of bromine-containing polymers [210-212]. Additionally, this early degradation was not found in the cases where the particle was functionalised with a worse leaving group, such as in the cases of the OH-SiNPs, COOH-SiNPs and StS-SiNPs.

Loss of the attached moiety was followed by the loss of the thiol groups from the surface and loss of carbon containing units from the MPTMS, in the same fashion as the SH-SiNPs. Introduction of air to the heated Br-SiNPs removed 9.3 % of the particle mass, showing a similar loss to the underlying thiol particles in which 9.0 % was removed at the same point.
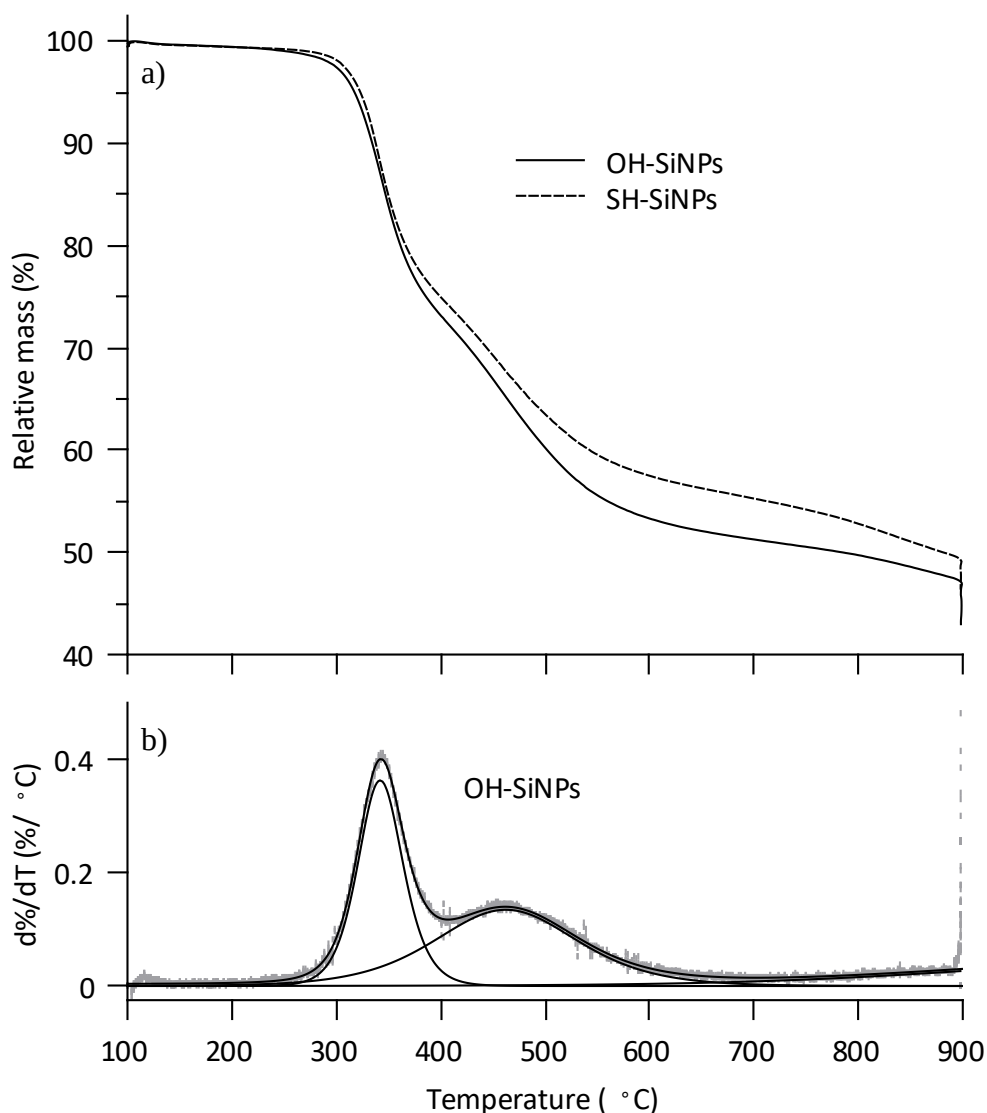
Figure 4.8: a) Thermogram of OH-SiNPs and SH-SiNPs. b) First derivative of mass loss of OH-SiNPs' thermogram with respect to temperature, grey points indicating measured data, dotted lines the fitted asymmetric double sigmoidal curves and solid line the sum of the fitted curves

Figure 4.8 shows the TGA and dTGA curves of OH-SiNPs. These particles showed large degradations at both 340 and 460 °C. Both OH-SiNPs and SH-SiNPs showed a slow degradation starting at approximately 600 °C which continued until the gas was exchanged with air. The final mass difference was found to be 3.7 %, this corresponds to 7.8 % of the original sample being the undecenol moiety, indicating 13.5 ± 3 groups·nm^{-2}, higher than expected by theory, and high in comparison to other functionalities observed. The lack of an evaporation peak suggested the large attachment density was a result of a strong interaction with the surface, rather than physisorption or association.

Table 4.4: Mass losses for degradation events modelled in temperature-derivative thermogram of SH-SiNPs and OH-SiNPs

Degradation event	Peak areas (%)		Event difference (%)
	SH-SiNPs	OH-SiNPs	
Peak 1 (337 °C/341 °C)	18.6	20.3	1.6
Peak 2 (454 °C/464 °C)*	22.4	26.9	4.5
Peak 3 (894 °C)	7.1	5.0	-2.1
Air burn	2.8	4.6	1.8
Total (dTGA)	51.0	56.8	5.9
	Mass residues (%)		
Residue (TGA)	46.7	43.0	-3.7

Table 4.4 shows the areas determined for each peak from the dTGA measurements of the OH-SiNPs and the SH-SiNPs from which they were made. It also indicates the relative difference in mass loss that occurs due to each degradation event. The first peak showed a maximum degradation rate at 341°C, close to the unreacted SH-SiNPs. The second peak showed a maximum degradation rate at 464°C, 10°C higher than the unreacted particles. Both peaks showed a slight increase in area compared to the unreacted particles. The slow degradation starting at approximately 600°C was smaller for the OH-SiNPs compared to the SH-SiNPs.

These observations suggest the moieties degraded at a similar temperature to the underlying thiol groups. This served to protect the carbon chain of the attached moiety due to the stability of the end group, and prevented the shifting of mass losses to lower temperatures. The undecenol moiety was expected to degrade at a similar temperature to the unreacted particles, based on the poor leaving group character of the hydroxyl group, which would be expected to degrade at a temperature similar to the thiol groups [213]. When the air was introduced, the OH-SiNPs showed an increased mass loss compared to the unreacted particles, offsetting the smaller degradation event immediately prior.
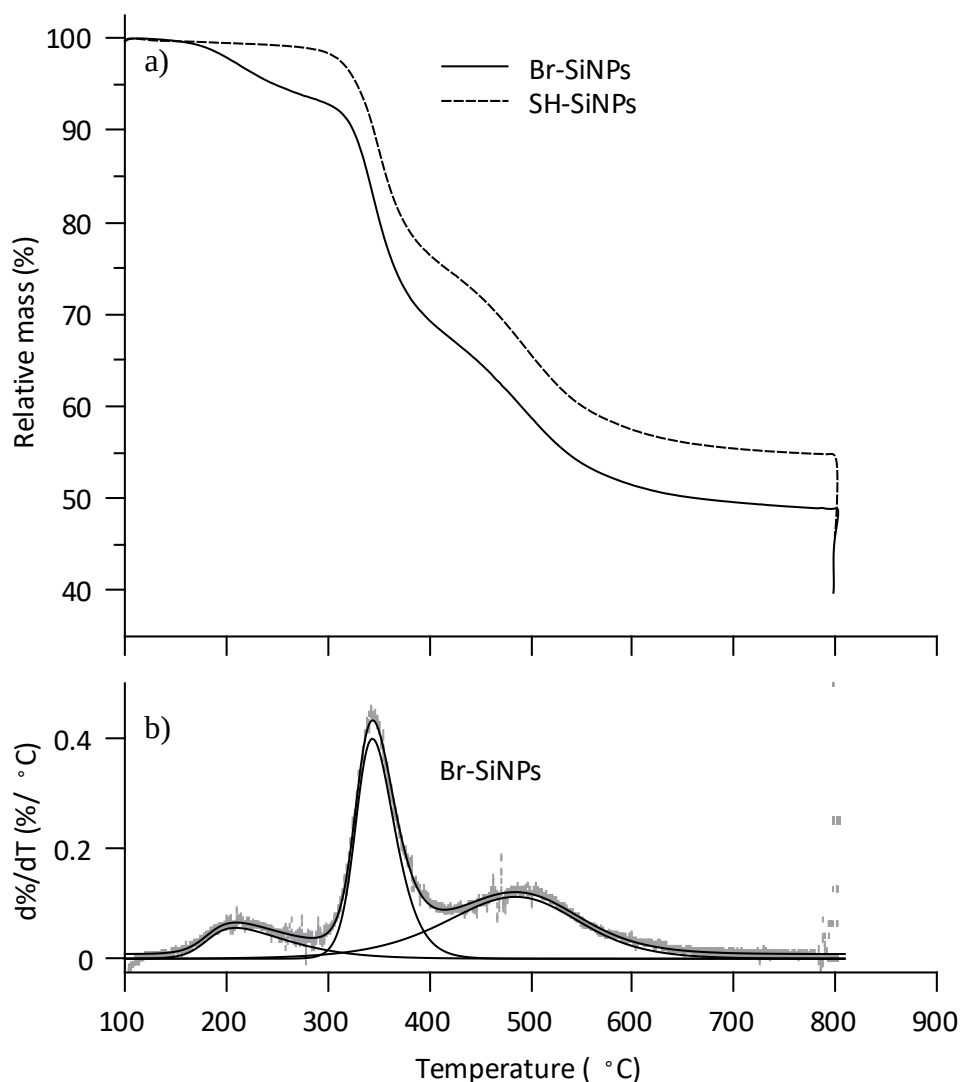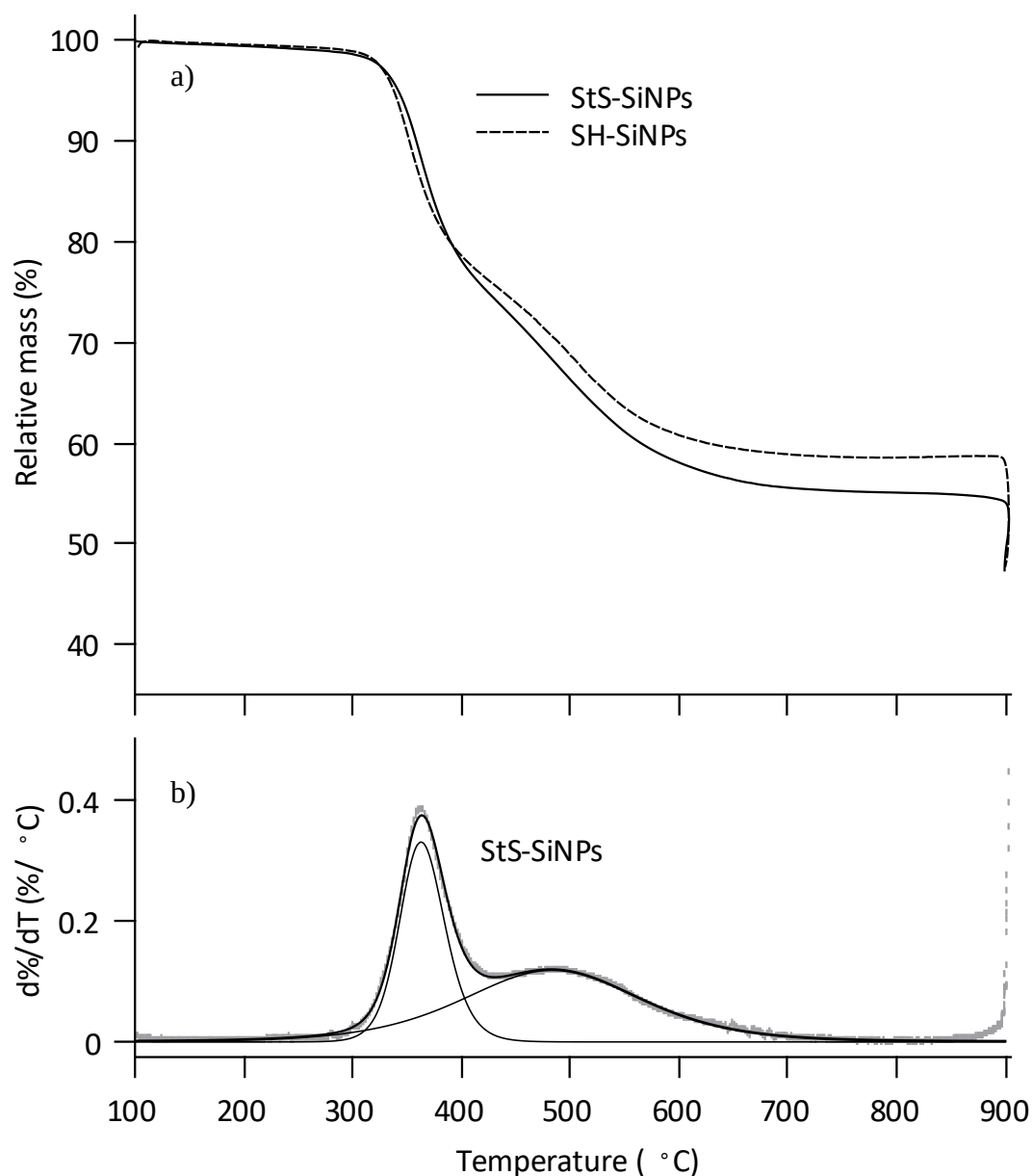
Figure 4.9: a) Thermogram of StS-SiNPs and SH-SiNPs. b) First derivative of mass loss of StS-SiNPs' thermogram with respect to temperature, grey points indicating measured data, dotted lines the fitted asymmetric double sigmoidal curves and solid line the sum of the fitted curves

In Figure 4.9, TGA and dTGA traces of StS-SiNPs are given. During degradation a large difference between the functionalised and non-functionalised particles was observed, however, the difference was reduced upon the introduction of air. StS-SiNPs showed a similar mass loss during the first degradation (363 °C max) however, during the second degradation (484 °C max) showed a larger mass loss. The increased area could have been due to the loss of SO_2 from the sample, as well as the loss of aromatic degradation products from the styrene group [214, 215].

Table 4.5: Mass losses for degradation events modelled in temperature-derivative thermogram of SH-SiNPs and StS-SiNPs

Degradation event	Peak areas (%)		Event difference (%)
	SH-SiNPs	StS-SiNPs	
Peak 1 (350 °C/363 °C)	18.7	18.3	0.3
Peak 2 (499 °C/484 °C)*	22.2	26.0	2.7
Air burn	11.0	6.9	-4.1
Total (dTGA)	51.9	51.2	-1.1
	Mass residues (%)		
Residue (TGA)	47.9	47.3	-0.6

The final relative masses of the StS-SiNPs and SH-SiNPs samples were similar with a difference of 0.6 %, within the range of uncertainty of the degradation of SH-SiNPs. One potential reason for this could have been the formation of non-SiO_2 degradation products from the attached moieties such as sodium sulfate [215]. This would reduce the difference noted in the residue. With this assumption, the original particle would consist of 1.9 %w/w of styrene sulfonate moiety, giving the attachment density for the styrene sulfonate particles as approximately 1.3 groups$\cdot$nm^{-2}, lower than that achieved for other functionalities. This could have been due to the relatively large attachment site required for the styrene sulfonate functionality in comparison to the other attachments made.

4.2.3 Surface attachment density determination – FTIR

If, such as in previous work [108], a calibration curve was prepared using the CH_3 absorbance to directly determine the surface functional density of the particles, it would only apply to particles of the same size. The calibration curves presented in this work are prepared for application to particles regardless of their relative size, giving results as a molar or mass percentage of the particle sample.

Due to the overlap between the absorbencies of the acid hydroxyl group and the alkane vibration absorbencies, the absorbance at 2926 cm^{-1} was not useful for analysis. An analogous method was used in which the absorbance of the carbonyl group was compared, and, as done in previous work, the silica absorbance signal used as an internal standard.

The absorbance method of the sample is based on the Beer-Lambert law for samples. By using the unchanged silica peak as an internal standard, the effect of differing path length and sample

contact with the ATR crystal was eliminated. ATR-FTIR, not being a surface-sensitive technique, produces absorbencies based on the concentration of the functional groups present in the sample. By using the silica signal as an internal standard, the measured quantity becomes proportional to the mixing ratio of the functional groups and the silica nanoparticles.

Table 4.6: Masses of undecylenic acid and SH-SiNPs used to create the carbonyl calibration curve

Diameter (nm)	m(SH-SiNPs) (mg)	m(Undecylenic acid) (mg)	Mass ratio (%w/w)
138	~10	0	0
	13.5	0.07	0.5
	14.7	0.15	1.0
	20.6	0.42	2.0
	15.4	0.47	3.0
	20.1	0.82	3.9
	10.4	0.50	4.5
	10.2	0.82	7.4
	16.5	1.52	8.4
203	~10	0	0
	19.1	0.22	1.1
	17.1	0.39	2.2
	16.6	0.57	3.3
	25.3	1.14	4.3
	19.4	1.13	5.5
	17.0	1.23	6.7

Two samples of SH-SiNPs were taken, having diameters of 203 nm and 138 nm respectively (measured by DLS). Known quantities of undec-10-enoic acid were added to the samples and used to prepare calibration curves of absorbance of the carbonyl signal against the mass concentration of undec-10-enoic acid in the samples. Table 4.6 shows the masses of undec-10-enoic acid and SH-SiNPs used in creating the curves, converted to mass ratios.

Figure 4.10 shows the ATR-FTIR spectra of the SH-SiNPs with undec-10-enoic acid added. The spectra showed a carbonyl signal in, ν(C=O), at 1720 cm^{-1}. The spectra for the SH-SiNPs were otherwise functionally identical, showing no notable difference between sample a) and

b), indicating that any surface effect from the smaller particles was not significant enough to affect the spectrum.
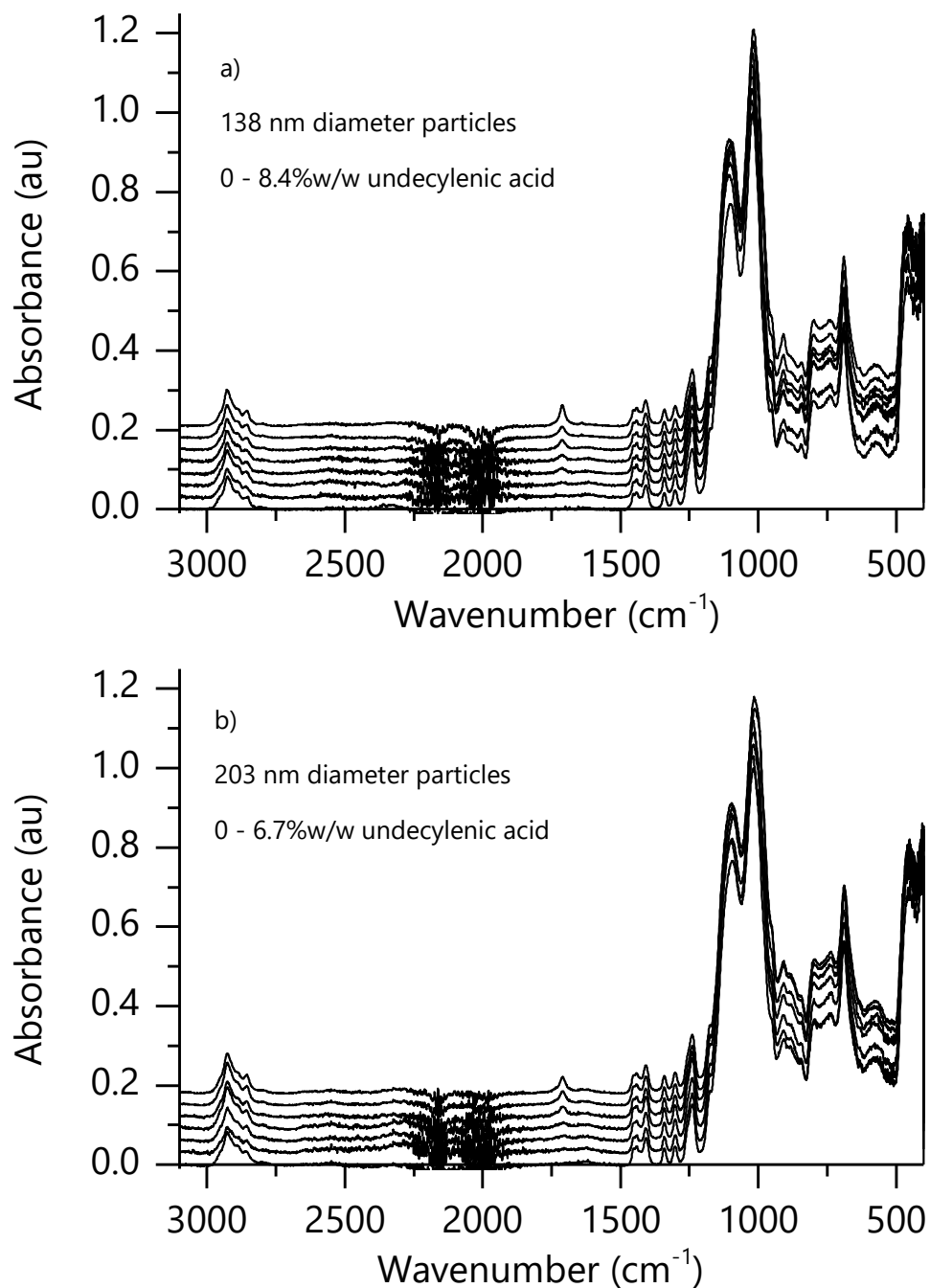
Figure 4.10: Offset ATR-FTIR spectra of SH-SiNPs with undec-10-enoic acid added in mass ratio indicated for a) 138 nm particles, b) 203 nm particles. Spectra normalised to Si-O-Si peak at 1070 cm^{-1}.

Figure 4.11 shows the measured absorbencies of the carbonyl signals for the two SiNP samples, and the calibration curve parameters determined. The curves produced were almost identical, falling completely within error of each other. This curve was thus applied to the COOH-SiNPs measured in this work. Surface functional groups for each sample were determined by

converting the relative mass concentration into surface functional density by using the specific surface area of the particles, measured as described in Section 3.5.2.

Diameter (nm)	Slope ($\times 10^{-3}$)	Intercept ($\times 10^{-3}$)	R^2
138	5.24±0.12	2.57±0.23	0.997
203	5.25±0.5	2.1±2.0	0.950
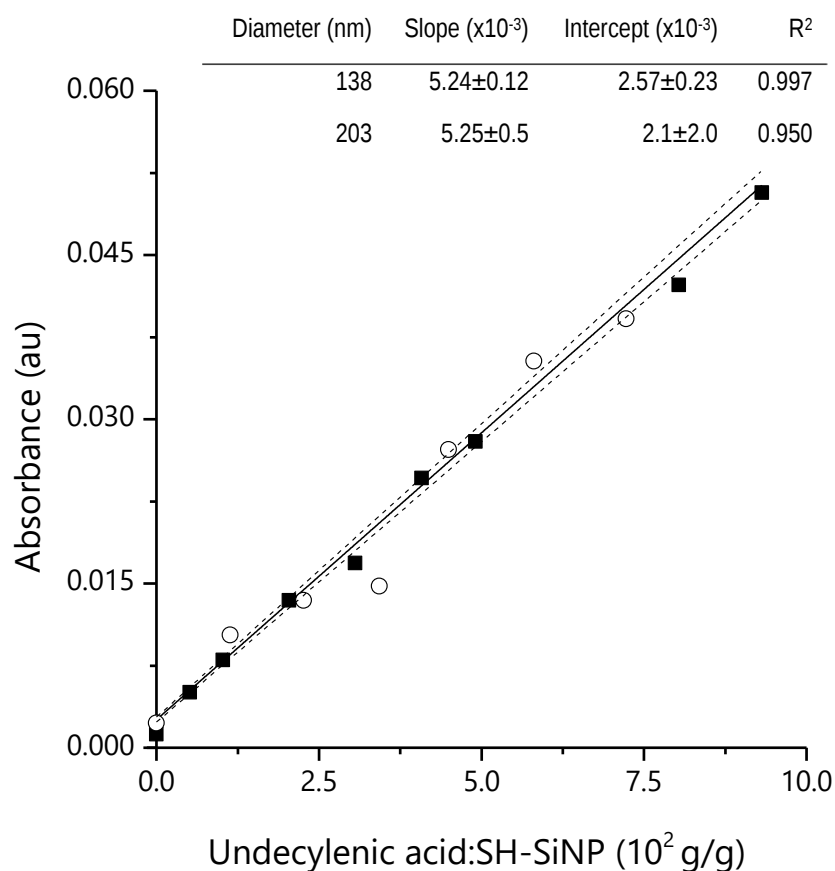
Figure 4.11: Calibration curve of carbonyl signal absorbance against relative mass of undecylenic acid in particle sample, with curve parameters inset. Solid symbols are 138 nm particles; open symbols are 203 nm particles. Solid line is curve based on 138 nm particles, dashed lines indicate upper and lower estimates of error based on calibration curve.

A similar curve was prepared using undecenol (Figure 4.12) to produce a calibration curve for the alkane absorbance, again normalised to the silica peak, to measure the surface functional density of the Br-SiNPs and OH-SiNPs. As undecenol and bromoundecene share the same number of carbon units in their structures, no converting factor for the absorbance was required. The x-axis in this case was converted to molar percent, to account for the different masses of the bromoundecene and undecenol.

$$y = 0.00599x + 0.06891$$
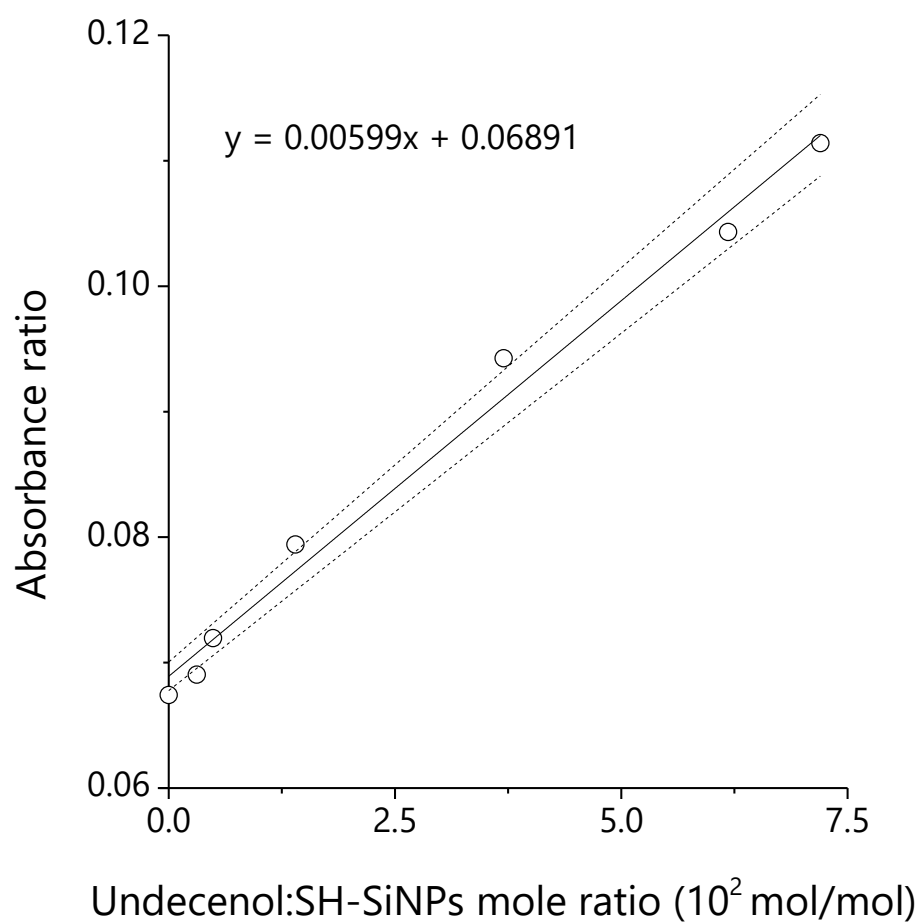
Figure 4.12: Calibration curve of absorbance of $v(CH_2)$ signal, normalised to Si-O-Si signal. Dashed lines indicate upper and lower estimates of error based on calibration curve.

Figure 4.13 shows the ATR-FTIR spectra for the unfunctionalised SH-SiNPs and functionalised COOH-, Br-, and OH- SiNPs. Slight differences were seen in the spectra of the functionalised particles. Common to all functionalised samples was an increase in the $v(CH_2)$ compared to the unfunctionalised SH-SiNPs. Additionally COOH-SiNPs showed a small peak at 1720 cm^{-1} due to the carbonyl functional group.
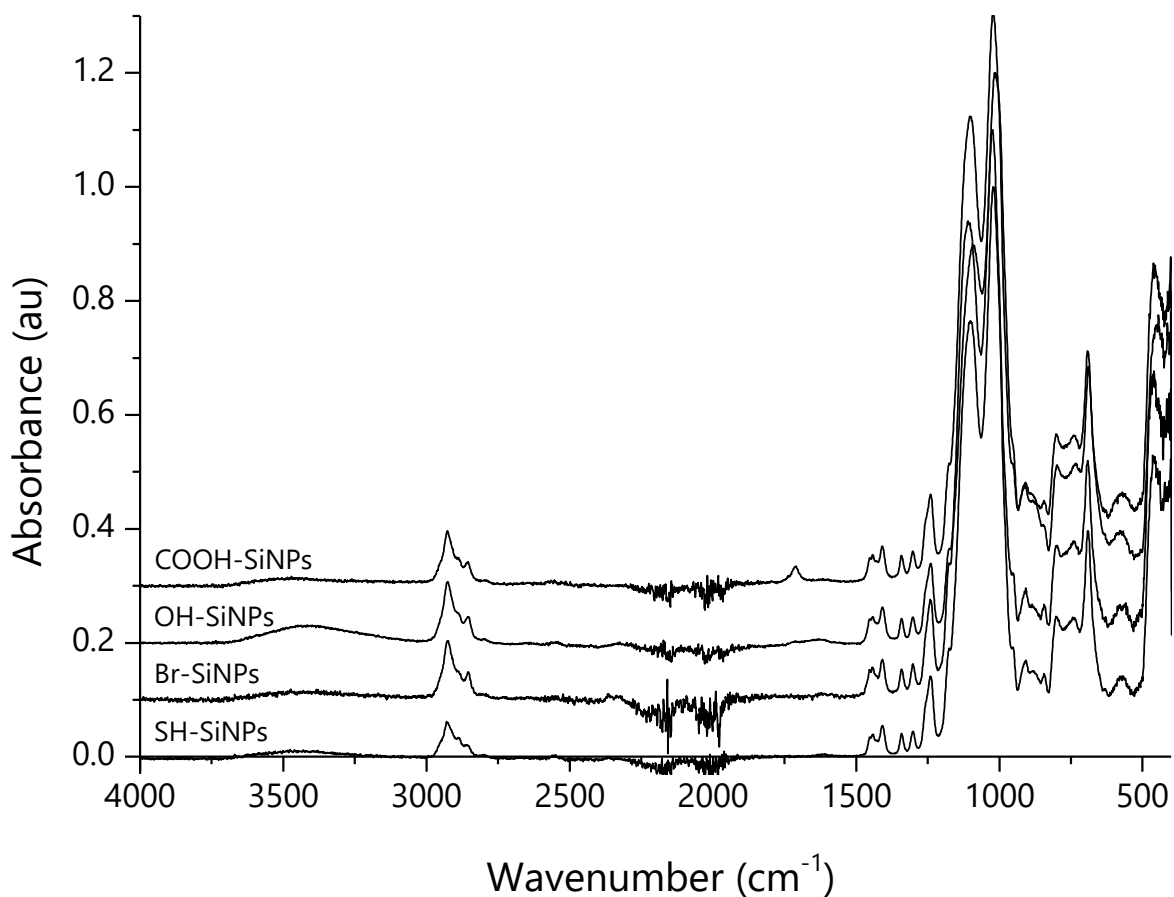
Figure 4.13: ATR-FTIR spectra of SH-, Br-, OH-, and COOH-SiNPs, normalised to the Si-O-Si signal, offset by 0.1 au

Table 4.7 shows the surface functional densities measured for the Br-, OH- and COOH-SiNPs. StS-SiNPs were not included as no result based on ATR-FTIR absorbance was determined. The ATR-FTIR measurements for each particle were found to be similar to the values determined for by TGA measurement of the samples.

Table 4.7: Surface functional group density determined by TGA and ATR-FTIR for SH-SiNPs functionalised with indicated group

Functional group	Surface groups, TGA (groups·nm^{-2})	Surface groups, ATR-FTIR (groups·nm^{-2})
Br	8.5 ± 1	7.5 ± 0.5
OH	13.5 ± 3	13.7 ± 1
COOH	6.5 ± 0.7	ν(C=O): 5.7 ± 1
		ν(CH$_2$): 5.4 ± 0.7

98

The OH-SiNPs were found by both techniques to show a surface functional density higher than was theoretically expected of the particles. ATR-FTIR measurements were taken of OH-SiNPs reacted for increasing lengths of time, from 1.5 hours, up to 3 days (Figure 4.14). It was found that the alkane absorbance peak increased with increasing reaction time, further above the theoretical value of 6.2 groups·nm^{-2}. Repeated and extensive washing of the particles after reaction resulted in no change to the ATR-FTIR spectrum, suggesting the additional undecenol was attached to the surface, rather than associated. Further, the ATR-FTIR spectrum did not show an alkene signal at 3080 cm^{-1}, which would be expected to be present if the excess undecenol were simply associated with the particle.
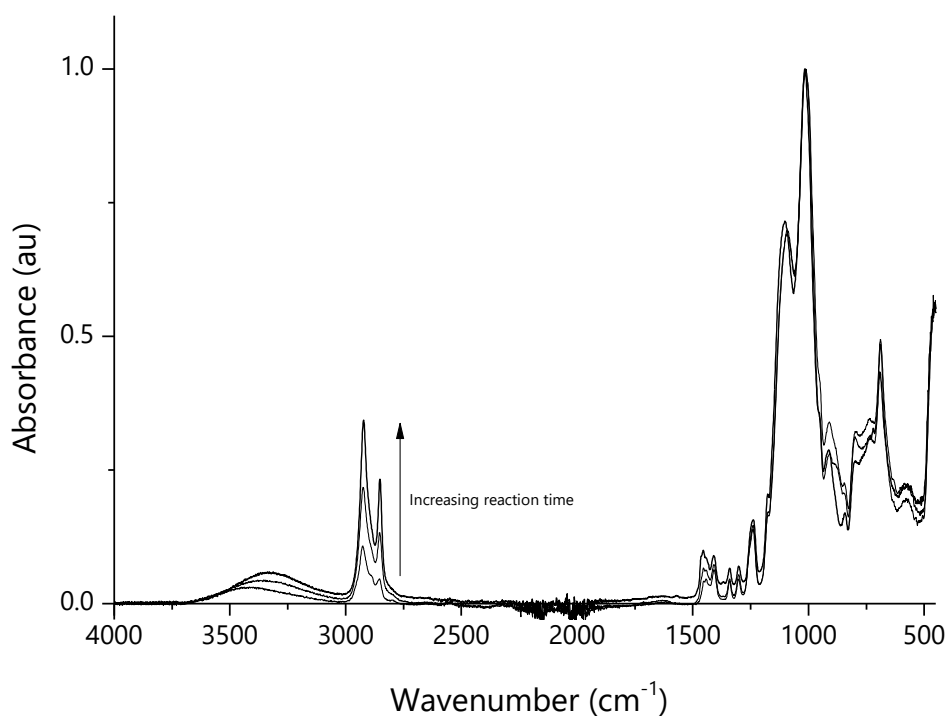
Figure 4.14: ATR-FTIR spectra of OH-SiNPs synthesised from SH-SiNPs under radical addition conditions for reaction periods ranging from 1.5 hours to 3 days

4.3 Conclusions

This chapter has described the functionalisation of SH-SiNPs, achieving high surface functional densities, with bromoundecene (8.5 groups$\cdot$nm^{-2}), undecenol (13.5 groups$\cdot$nm^{-2}) and undec-10-enoic acid (6.5 groups$\cdot$nm^{-2}). These values were similar to the theoretical maximum value for particles of this nature, as calculated geometrically. StS-SiNPs were found to show a lower attachment density (1.3 groups$\cdot$nm^{-2}) in comparison, and an explanation for this based on the effective area of the attachment unit was proposed.

Established analysis methods for TGA have been modified to provide additional insight into the degradation of the modified and unmodified SH-SiNPs. A more accurate method of determining mass loss during their degradation has been demonstrated. ATR-FTIR analysis of the particle samples has been expanded to produce calibration curves applicable to particle samples without requiring additional curves to be prepared for different particle sizes.

5 Effects of nanoparticle aggregation on rheological and solution properties of nanofluids

5.1 Overview

This chapter details the preparation and investigation of nanofluids prepared in concentrations ranging from 1-54 % w/w in water. Concentration dependent rheological effects, optical properties and aggregation properties were measured. The expected relationship showing increasing sample viscosity and shear thinning behaviour was found when the concentration was increased, coinciding with an increase in the average particle diameter, as measured by concentration dependent DLS measurements.

To determine the impact of aggregation, nanoparticles were functionalised using undec-10-enoic acid; a fatty acid terminated with a carboxylic acid. Thiol-ene click chemistry was used to produce acid terminal particles in the same manner as has been previously demonstrated with bromoundecene [108]. Undec-10-enoic acid is pH responsive, with a pKa of 5.38 [218]. Variance to this value is possible, as the exact pKa value of an organic acid may depend on the packing or self-association of the molecule in solution [219].

The pH of the solution was altered to assess the effect this has on the aggregation and solution stability of the nanoparticles and the resultant effect on the rheological behaviour of nanofluids from 1-54 %w/w. By changing the pH towards more basic, the aggregation of the particles in solution was minimised, due to the increased charge between them. This indicated a lack of compacting behaviour under high shear.

Herschel-Bulkley models were applied to the rheological profiles obtained for each of the solutions, and good agreement was found with the data. The changes in rheological behaviour were explained in this context and related to the aggregation state of the particles.

It is understood that when particle concentration in solution is increased, agglomerates of particles can form, acting as large particles in solution [216, 217]. This can affect solution rheological profiles [63]: the large agglomerates acting as individual particles in flow, and serving to reduce the effective concentration of the solution, i.e. a lower number of effective particles are dispersed in solution.

5.2 Solution properties of standard particles

Particle functionality was altered to change the agglomeration and the effects on the rheology of the solution were investigated.

5.2.1 AS40 – Standards
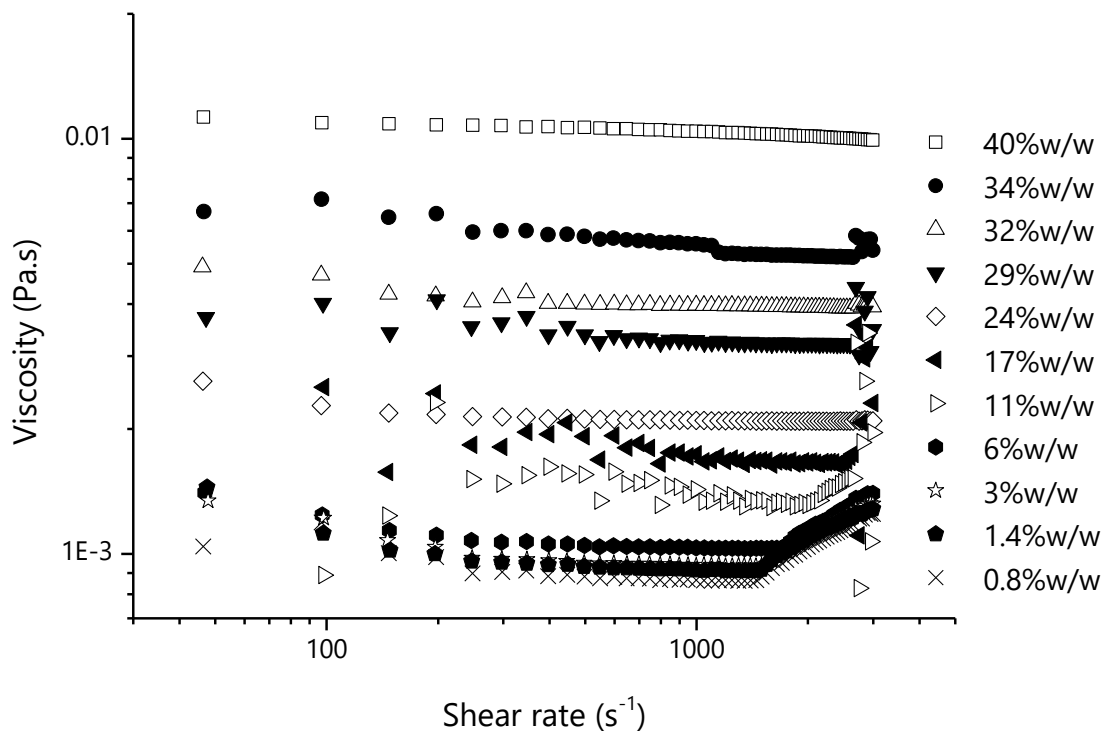
Figure 5.1: Rheological profiles of AS40 solutions diluted to specified w/w% using Milli-Q water

Figure 5.1 shows the rheological profiles obtained for AS40 samples at concentrations between 0.8 and 40 %w/w. The low viscosity samples in this concentration regime necessitated the use of a cup-and-bob rheometer to reduce sample noise. Throughout the shear rates measured, the samples displayed Newtonian behaviour. Sample viscosities were found to increase with concentration and were taken as the zero shear values for each sample.

The lower concentration samples, 0.8-11 %w/w showed increasing viscosity values at shear rates above approximately 1300 s^{-1}. This increase was not reflective of shear thickening of the sample, and was instead related to secondary flow and inertial effects [220]. A power law was fit to the data showing the apparent shear thickening behaviour, returning a flow index of 1.5.

This is characteristic of partially inertial flow [221], and thus the data showing this effect were not considered further.
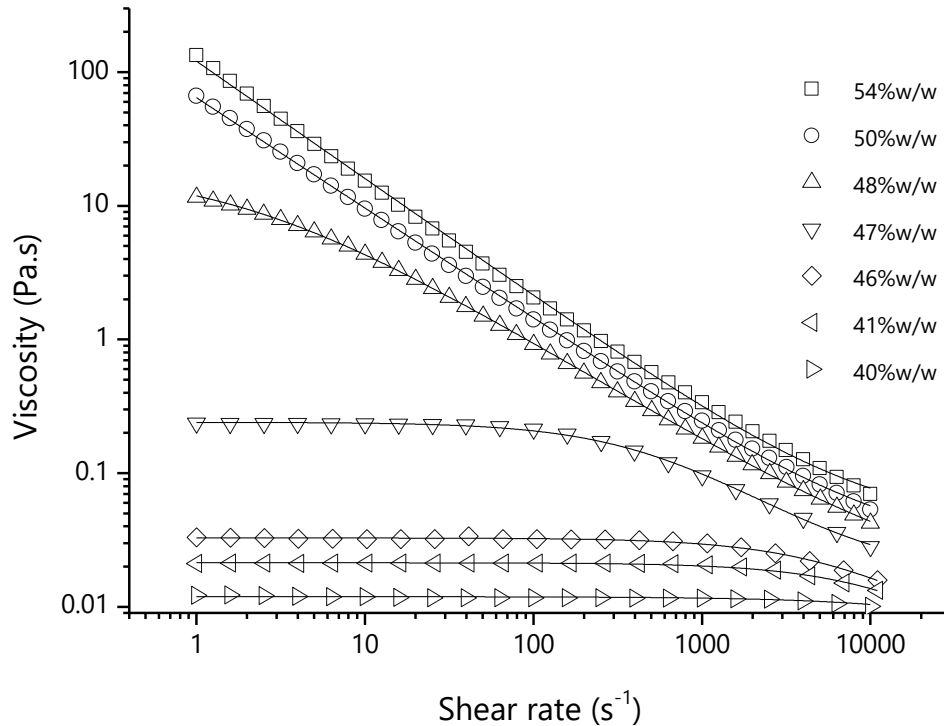
Figure 5.2: Rheological profiles of 20 nm silica nanofluids at specified weight concentrations, prepared from Ludox AS40 silica. Lines are Cross models fit to the data.

Higher concentration solutions (from 40-54 %w/w) showed non-Newtonian behaviour with increasing shear (Figure 5.2). The samples from 40-47 %w/w showed a Newtonian section at low shear rates, followed by a transition into shear-thinning behaviour at high shear rates. The transition point occurred at lower shear rates with increasing concentration. At 48 %w/w the transition point was slightly below the measured shear rate range, while at 50-54 %w/w the shear thinning behaviour occurs for the entire shear rate range measured.

For samples from 48-54 %w/w, the effective slope (that is, the slope of log(y) *vs* log(x)) decreased in magnitude at higher shear rates. This occurred at lower shear rates with increasing concentration, suggesting that the samples tended towards their infinite value at lower shear rates when they were at higher concentration. The lower concentration samples did not show this behaviour in the shear range measured.

Taking the zero shear rates of the samples for which a zero-shear plateau was visible in the studied range, the relationships between viscosity and concentration were quantified. It is well known that the viscosity of a colloidal sample can be related directly to its volume fraction [222], and many semi-empirical relationships exist to describe their behaviour. Figure 5.3 displays the zero-shear viscosity value measured for different concentration samples of AS40 nanofluids in which a low-shear viscosity plateau was clearly determinable. The curve fits are different viscosity equations relating the effective volume fraction against the relative viscosity, given by Equation 1.11, Equation 1.12, Equation 1.13, and Equation 1.14.

Volume fraction was first changed to the effective volume fraction in solution (determined by Equation 1.7) before curve fitting was undertaken. According to Equation 1.6, as the particle concentration increases, the value of κ^{-1} decreases, giving different effective volume fraction relationships at different concentrations. By calculating κ^{-1} for each point, the effect of concentration can be accounted for, instead of producing a single effective volume fraction relationship for all samples regardless of concentration. If, instead, the effective volume fraction were incorporated into the curve fitting equations, a single average value of κ^{-1} would be used, reducing the accuracy of the effective volume fractions determined.

The critical volume fractions determined by the equations for each sample were 0.51 using the Quemada function, 0.51 using the Mendoza function and 0.48 using the Krieger-Dougherty function. This showed excellent agreement with previous analyses conducted on smaller diameter LUDOX AS40 silica, which also determined a critical volume fraction of 0.51 [144]. Further, it showed that the effective volume fraction determined by the addition of the electrical double layer of the particles to the particle radius agreed with the observed data.

The inset, showing detail of the lower concentration fluids measured, shows that at the lower concentrations the Quemada curve slightly overestimated the relative viscosity of the samples, while the Krieger-Dougherty equation began to underestimate the data as the concentration increased. The modified Ward equation showed good agreement with the data, suggesting that adding the Debye length may be a good representation of the effective particle diameter. The modified Ward equation did show deviations from experimental data as the concentration increased, which was expected owing to the expected upper limit of applicability of $\phi_{eff} <$ 0.35 [154]. The Mendoza function showed good agreement with the measured data at low concentrations.
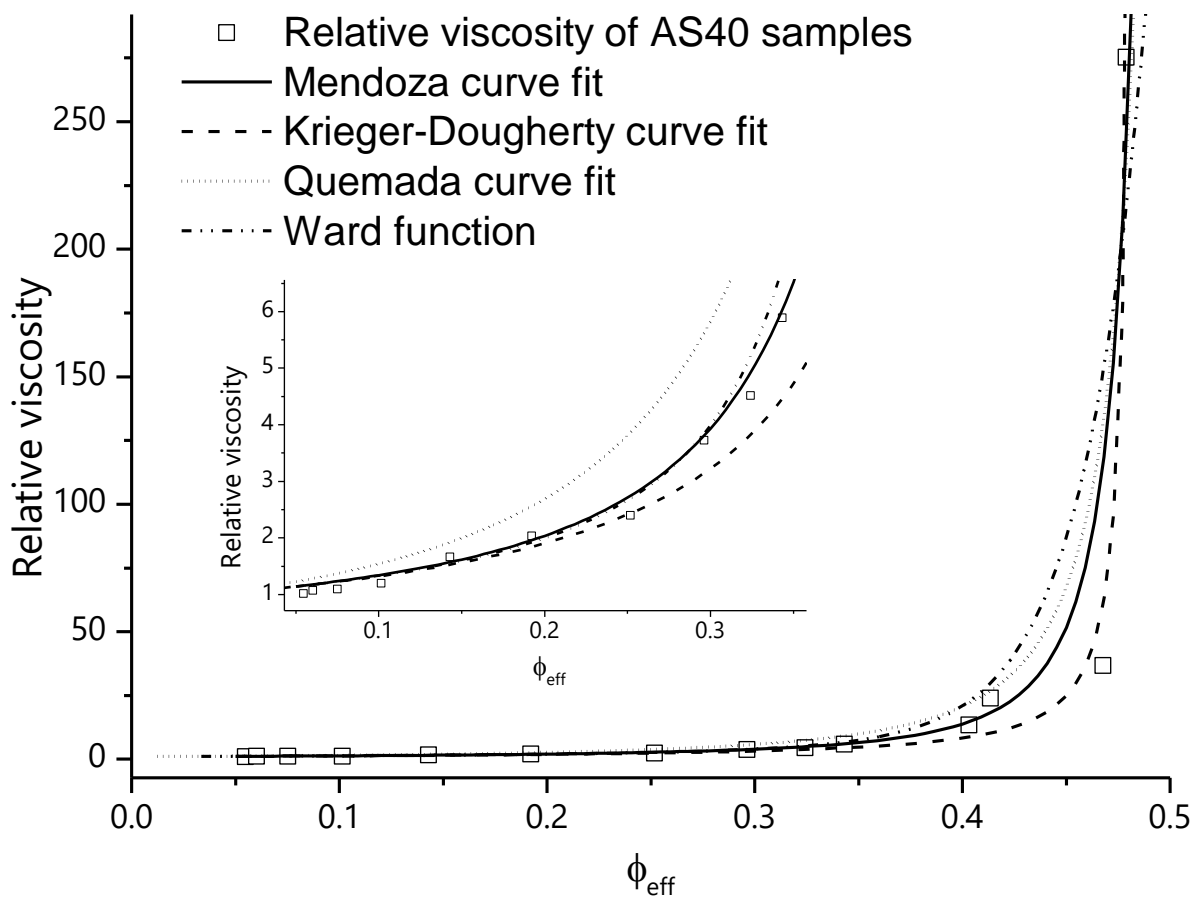
Figure 5.3: Relative viscosity of AS40 SiNP nanofluids against effective volume fraction of solution, lines are fitted functions of viscosity, inset is zoom-in of data below an effective volume fraction of 0.35.

Cross models (Equation 1.18) were fit to the high concentration solutions and are represented as lines in Figure 5.2. To fit the Cross model to the data the infinite value was estimated using the Mendoza equation (Equation 1.14). For the estimate, it was assumed that at infinite shear rate the critical volume fraction was 0.74. This assumption has been used conventionally for high shear measurements of particle: it considers that at infinite shear, all interparticle interactions that would result in a lower packing density are overwhelmed by the shear forces, allowing the particles to adopt the densest regular packing configuration samples [156]. The effective volume fractions used for this analysis were based on the effective volume fractions determined by calculating the Debye length of the particles and adding these values to the effective particle radii.

The Cross model parameters for the fluids are in Table 5.1, and show a number of trends. The inverse value of the Cross constant indicates the onset shear rate of shear thinning behaviour. The 50 and 54 %w/w samples had volume fractions equal to or greater than the critical volume fraction, thus the high zero-shear viscosities determined for these samples were considered as

arbitrarily high numbers, tending towards infinity. The onset of shear thinning for these was similarly arbitrarily close to zero. For the samples with an onset of shear thinning measurable within the tested range it was noted that increasing concentration led to a lower onset of shear thinning of the sample.

Table 5.1: Cross model parameters for AS40 silica nanofluids of specified concentrations

Concentration (%w/w)	ϕ	ϕ^*	Estimated η_∞ (Pa·s)	η_0 (Pa·s)	α_c (s)	m
40	0.22	0.40	0.0009	0.0119	1.1×10^{-5}	0.77
41	0.23	0.41	0.0039	0.0213	8.1×10^{-5}	1
46	0.27	0.47	0.0073	0.0326	1.7×10^{-4}	1
47	0.28	0.48	0.0170	0.240	1.7×10^{-3}	1
48	0.29	0.49	0.0142	18.9	0.50	0.76
50	0.30	0.51	0.0252	2.9×10^{11}	2.9×10^{11}	0.83
54	0.34	0.56	0.0406	8.8×10^{7}	4.9×10^{6}	0.88

Determining the flow index for the samples from 40-47 %w/w was difficult due to the relatively small section of the shear thinning profile visible. At the higher volume fractions, however, a large enough section of the shear thinning section of the profile was evident to determine the flow index for the samples. The samples measured showed similar flow indices, with a slight tendency towards increasing shear-thinning character with increasing concentration.

5.2.2 TEOS – Standards

TEOS-SiNPs were prepared as larger sized particle standards. Solutions of TEOS particles were hazy and clear at low concentrations (<1 %w/w) transitioning to an opaque white solution as the concentration increased. Above 54 %w/w the samples solidified, tending towards precipitation of white or translucent solids, and no longer flowed as a liquid.
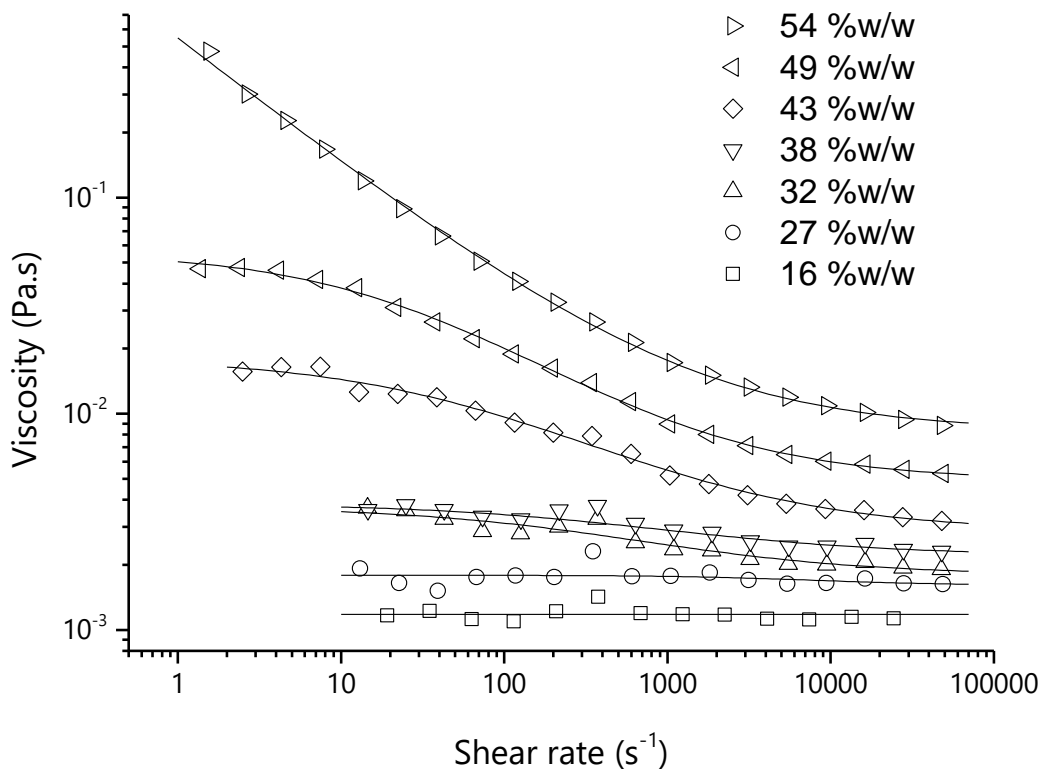
Figure 5.4: Rheological profiles of 120 nm silica nanofluids at specified weight concentrations, prepared from nanoparticles synthesised from TEOS. Lines are Cross models fit to the data.

Figure 5.4 shows the rheological profiles of nanofluids based on TEOS-SiNPs, which showed some similarity to the nanofluids prepared from the AS40 particles. At lower concentrations, the profile was near-Newtonian, with minimal shear thinning. As the volume fraction increased non-Newtonian behaviour became evident in the solutions, with shear thinning behaviour connecting two plateau values of viscosity. The shear thinning section of the 43 and 49 %w/w samples occurred over a smaller range of shear rates than the shear thinning behaviour observed for the AS40 particles.

For a sample of a given volume fraction, at any specified shear rate, the TEOS-SiNP nanofluids exhibited a lower viscosity than the comparable AS40 nanofluid. The effect of particle diameter on sample viscosity is an inconsistently reported phenomenon in literature with both increasing and decreasing viscosity with particle diameter reported for many different particle systems [3].The zero and infinite shear values of viscosity were visible for most samples, occurring within the range of the shear rates measured.

Apparent volume fractions of TEOS-SiNP nanofluids were measured by taking the effective diameter of the TEOS-SiNPs in solution, as that of the hydrodynamic diameter measured by DLS (153.6 nm), and the primary particle diameter as that measured by SEM (121.0 nm).

Table 5.2: Parameters of Cross models applied to rheological profiles of TEOS-SiNP based nanofluids

Concentration (%w/w)	η_∞ (Pa·s)	η_0 (Pa·s)	α_c (s)	m
54	0.0083	1000*	3.7×10^6	0.59
49	0.0049	0.056	3.9×10^{-2}	0.64
43	0.0028	0.018	1.5×10^{-2}	0.58
38	0.0022	0.0038	1.7×10^{-3}	0.59
32	0.0018	0.0037	0.0027	0.60
27	0.0016	0.0018	1.4×10^{-4}	0
16	0.0011	0.0012	1.8×10^{-4}	0

Table 5.2 displays the parameters derived from fitting Cross models to each of the profiles. The lower viscosity samples (27 and 38 %w/w) suggest flow indices of one, however, the relatively small difference in viscosity these samples exhibited suggest they would be more accurately modelled as Newtonian fluids.

For the concentrations between 43-54 %w/w, as found for the AS40 nanofluids, the zero and infinite shear viscosities increased with increasing volume fraction. The onset of the shear thinning behaviour also shifted to lower shear rates with increasing concentration. Unlike the AS40 profiles, the 43 & 49 %w/w samples showed the zero-shear viscosity plateau, the shear thinning section of the profile, and at least the beginning of the infinite shear viscosity plateau within the measured shear rate range. The range in which shear thinning occurs was smaller compared to that of the AS40 samples.

The flow indices were lower values than that of the AS40 samples, indicating the samples exhibited less shear thinning character. No notable trend was observed relating concentration to flow index. Using the Mendoza equation (Equation 1.14) to compare the zero and infinite shear viscosities against the concentration, critical shear values of 0.54 and 0.69 were obtained. Similar to the AS40 nanofluids, those made from TEOS-SiNPs showed a clear distinction of behaviours between dilute samples and those at high concentrations.

5.3 Measurement of pH-mediated particle and fluid properties

5.3.1 Effect of pH on particle properties

From the TGA results presented in Section 4.2.2, the COOH-SiNPs were determined to have a surface functional density of 6.5 groups·nm^{-2}. Dried COOH-SiNPs were characterised after treating them at different pH values, to investigate the impact of pH on the particle FTIR spectrum and particle thermal stability. The solution pH was adjusted using hydrochloric acid and sodium hydroxide respectively. When basified, COOH-SiNPs were referred to as COONa-SiNPs.

The ATR-FTIR spectra obtained for the acidified and basified particles were compared (Figure 5.5). These particles showed a small peak present at 1720 cm^{-1} assigned to the ν(C=O) group. When the pH was adjusted to 13 and the samples dried from this solution the peak at 1720 cm^{-1} disappeared, and a broader peak became apparent at 1560 cm^{-1}, characteristic of carboxylates, and thus was assigned to the ν(-C=OO^{-}) group. No other notable change was detected in the spectra, with the alkane peak remaining the same intensity in both measurements.
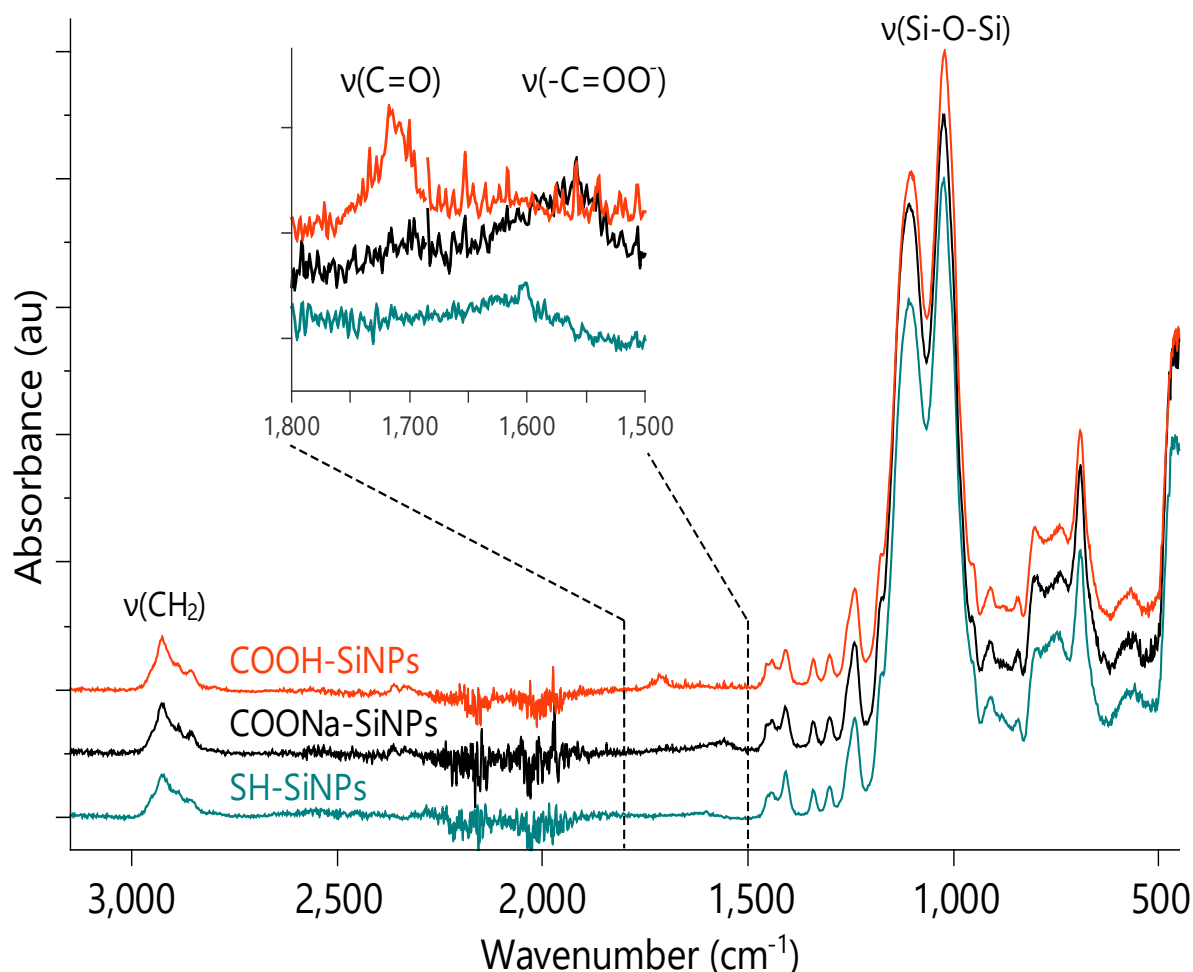
Figure 5.5: ATR-FTIR spectra of SH-SiNPs, COOH-SiNPs, & COONa-SiNPs, normalised to ν(Si-O-Si). Inset: Region of 1500-1800 cm^{-1} showing carbonyl and carboxylate signals

The presence of the carbonyl-carboxylate shift with pH indicated the attached acid moieties retained their acidic character, and had not been functionalised via side reaction to another chemistry. EDXS measurements of the COOH-SiNPs and COONa-SiNPs were taken (Figure 5.6) to check for the presence of sodium, indicating the acid-base reaction, or chlorine, to confirm the removal of all excess salt. The COOH-SiNPs showed peaks for silicon, carbon, oxygen and sulfur as expected, while the COONa-SiNPs showed the presence of sodium in addition. No chlorine peak was detectable in the COONa-SiNP measurements, indicating that the sodium was not present because of the brine wash, and instead due to the acid-base reaction of the particles.
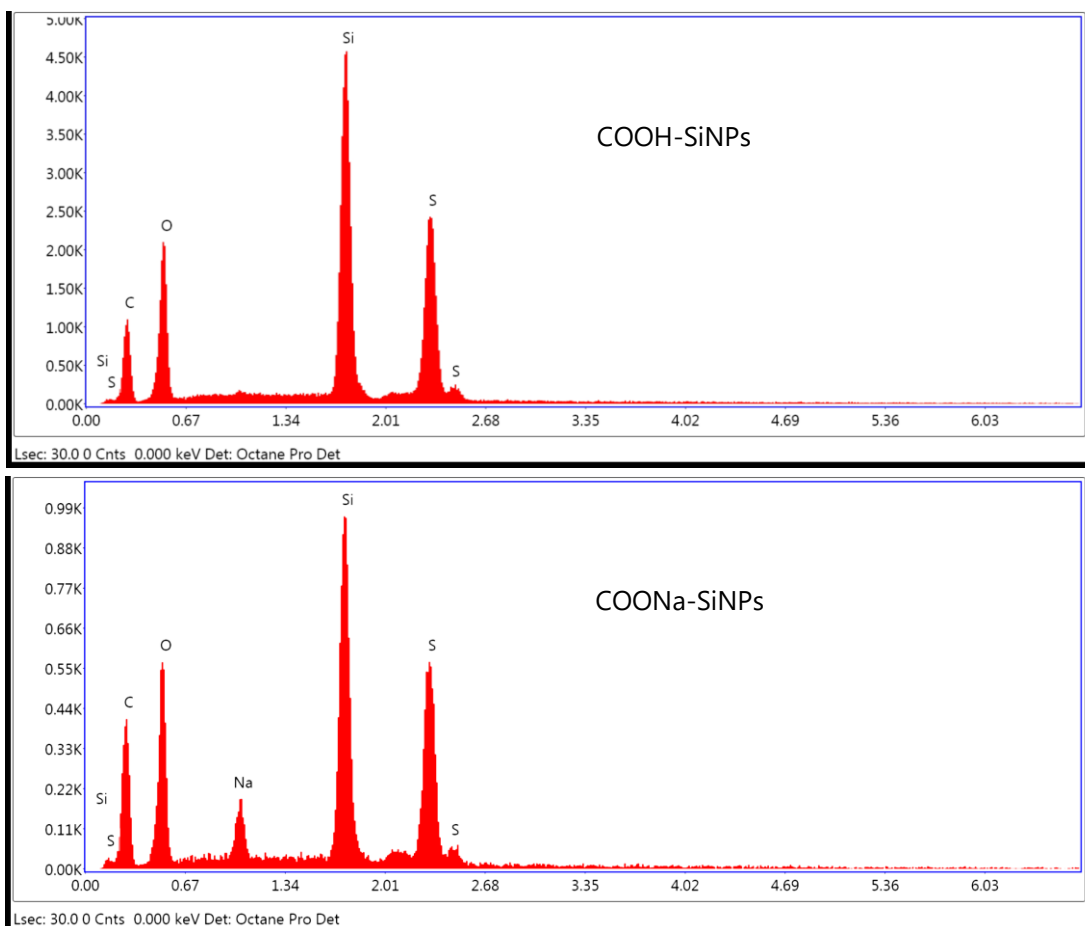
Figure 5.6: EDXS measurements of COOH-SiNPs and COONa-SiNPs

TGA profiles of the particles in acid form and base form were taken to investigate any differences between samples (Figure 5.7a). The derivative curves of relative mass (Figure 5.7b & c) showed two degradation events for each sample, with the same pattern: a sharper first peak, overlapping with a broader secondary peak. COONa-SiNPs (Figure 5.7c) showed later temperatures at which the maximum degradation rate occurred in both events. The events also occurred over a longer period, resulting in the broadening of the peaks.
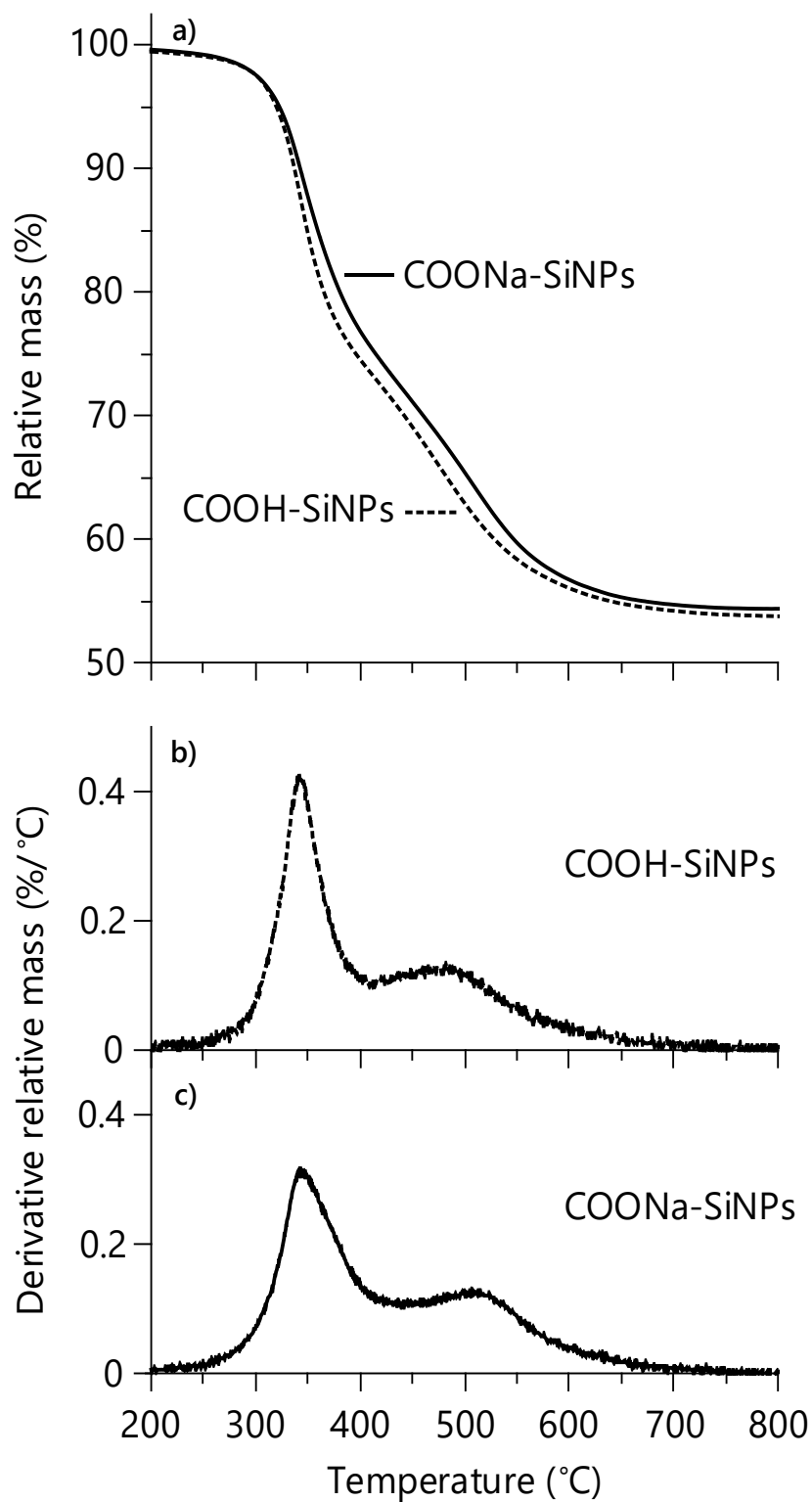
Figure 5.7: a) Relative mass remaining of COOH-SiNPs and COONa-SiNPs heating under nitrogen (20 mL.min-1) b) Derivative of relative mass with respect to temperature for COOH-SiNPs c) Derivative of relative mass with respect to temperature for COONa-SiNPs

COONa-SiNPs displayed a slightly increased mass across the temperature range, the inconsistent difference between the acid and salt forms indicating a difference in stability. Were the difference solely due to the presence of the additional sodium mass the sample degradation would be expected to be proportionately less across the entire range. During thermal degradation, organic salts may decompose, and the additional mass was theorised to be due to the formation of inorganic sodium salts.

To investigate the COOH-SiNP behaviour in solution small quantities of the particles were dispersed in water at different pH values, and qualitatively, a difference was immediately obvious. Figure 5.8 shows photographs taken of the COOH-SiNPs when water at of pH 4, 4.5, 5 & 6 was added, with and without physical agitation. It was seen that at pH 5 and above the particles immediately dispersed, though not throughout the entire volume available. Blue colouration due to light scattering effects was visible, indicating that the particles were well dispersed and were not agglomerated in solution. At pH 4.5 the particles did not disperse easily in solution, forming white flocs, sonication did not successfully disperse the particles. At pH 4 the particles formed solid pellets, which were only slightly broken apart during sonication.
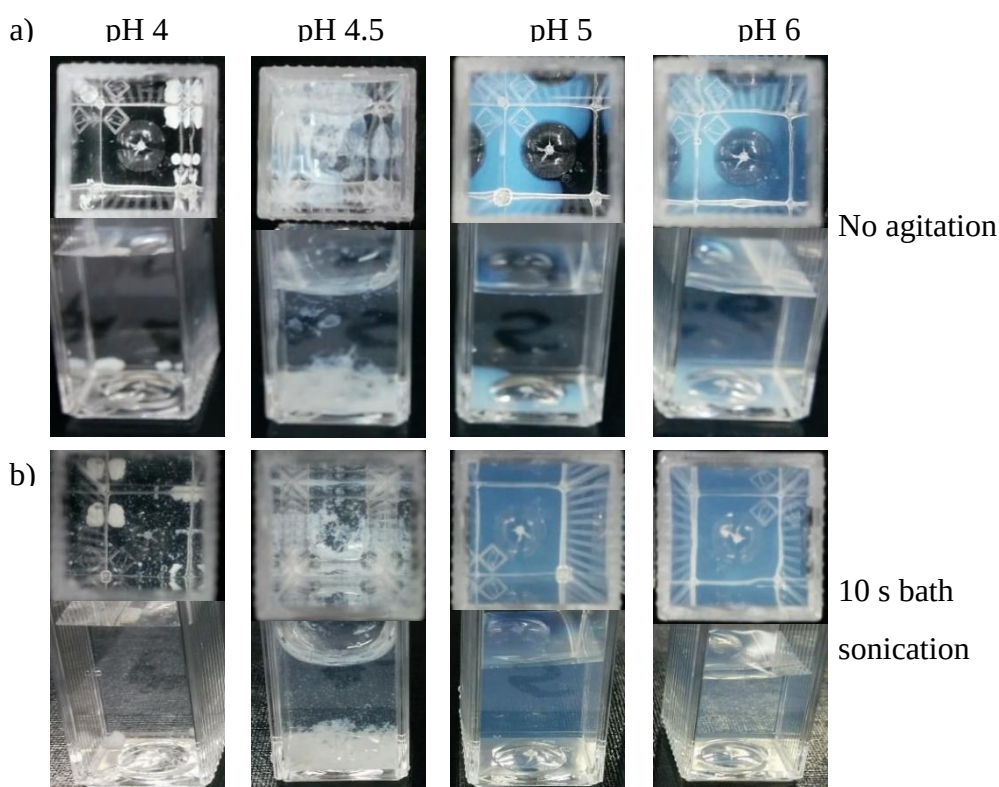
Figure 5.8: Photographs of top and side views of cuvettes containing COOH-SiNPs with water of controlled pH (left to right pH = 4, 4.5, 5, 6) a) are photos taken 1 minute after solvent addition with no sample agitation, b) are samples after bath sonication for 10 s
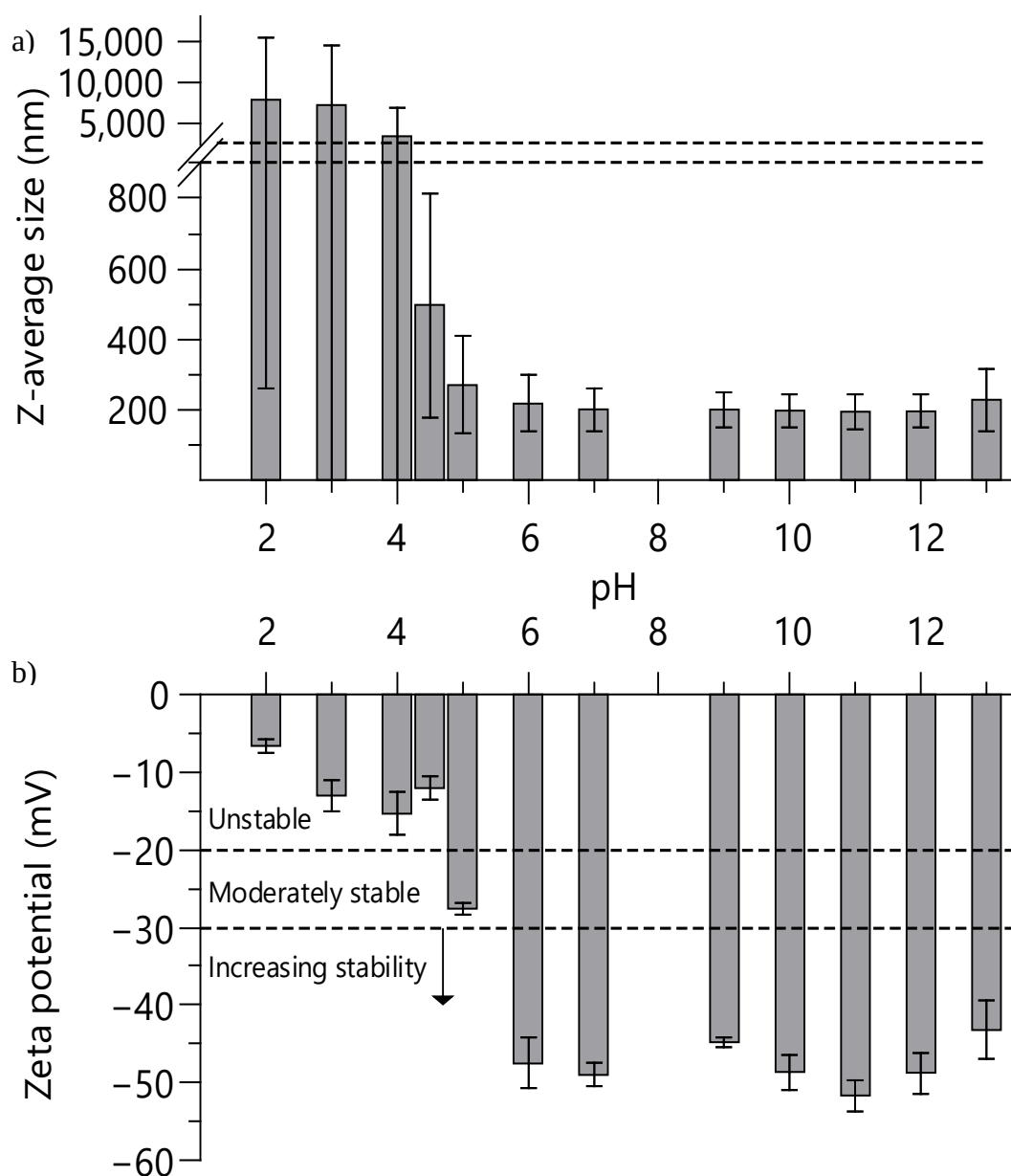
Figure 5.9: a) Z-average diameter of COOH-SiNPs measured by DLS. b) Zeta potential of COOH-SiNPs. All samples were in 10 mmol·L^{-1} sodium chloride solution with pH adjusted by addition of hydrochloric acid or sodium hydroxide as necessary. Error bars are ±1 standard deviation.

To investigate the solution-mediated properties of COOH-SiNPs, DLS and zeta potential measurements were undertaken on silica nanoparticles in 10 mmol·L^{-1} sodium chloride solution (Figure 5.9). Between pH 6 and 13 the nanofluid samples showed a similar, highly negative zeta potential. No visible aggregation was present, and DLS measurements indicated this: all Z-average diameters measured were similar and indicative of primary particles as the

dominant particle formation. Any formation of dimers, or trimers in solution would have been expected to increase the average diameter and PDI.

Undec-10-enoic acid has a pKa of 5.38, thus, between pH 6 and 13 the undec-10-enoic acid moieties on the particle surface would be mostly, or completely, deprotonated, enacting stabilisation through electrostatic repulsion.

At pH 5, the particles showed a zeta potential value of -27.6 mV, putting them into the region of moderate stability. This region is characterised by initially stable particles, which over time agglomerate in solution. It was noted that the DLS measurements of this sample indicated an increase in effective particle diameter and dispersity, suggesting the formation of agglomerates in solution. However, as the average particle diameter (269 ± 140 nm) remained below double the primary particle diameter (195 ± 50), the majority formation in solution was still primary particles. At this pH, close to the pKa value, it would be expected that the undec-10-enoic acid moieties would be partially protonated, reducing the repulsive interparticle interaction, promoting agglomerate formation.

Reducing the pH further, to pH 4.5 the solution became unstable. The Z-average diameter and dispersity increased, indicating the presence of large agglomerates. When the pH was reduced below pH 4, the zeta potential continued to trend towards zero. The reduction in the zeta potential was indicative of the loss of electrostatic stabilisation due to the protonation of the moieties, eliminating the electrostatic repulsion that stabilised the primary particles in solution.

COOH-SiNPs were used to prepare nanofluids at 12 %w/w, and their rheological profiles were recorded under increasing shear, from 5-50000 s-1 (Figure 5.10). Each run was repeated three times and an average profile constructed. Rheological profiles of the samples were found to remain similar across the pH range 5-13, showing good agreement with the zeta potential and DLS measurements at similar pH values. Cross models were applied to describe the data, however, due to the low values of viscosity obtained and the lack of non-Newtonian behaviour observed outside of the sample error, estimating Cross parameters was difficult. The parameters are included for completeness (Table 5.3); however, it should be noted that the pH 5, 6 and 13 samples were considered similar enough as to be indistinguishable. At pH 4, non-Newtonian behaviour was observed, however, only the shear thinning section of the profile was obtained during measurement. The infinite shear viscosity value should be similar to the values obtained for the other pH samples, due to the complete interparticle interaction breakdown expected at high shear, and this was supported by the fit of the data.

Particle aggregation can be an explanation for the rheological profiles found. The breakdown of agglomerates in solution has been proposed as a mechanism by which shear thinning can occur. At low shear rates, the large agglomerates in solution resist the flow in solution due to their greater inertia. This resistance to flow manifested as a higher viscosity. As the shear forces increase, agglomerate breakdown results in primary particle formation. These particles, smaller than the agglomerates, are more easily able to move in the direction of flow, resulting in a lower viscosity overall. This aggregation can be controlled by the pH of the solution, and so further investigation was done in determining the rheological properties of silica nanoparticle nanofluids at greater concentrations at different pH value. Concentration induced aggregation was investigated at pH 5.8 and pH 13.
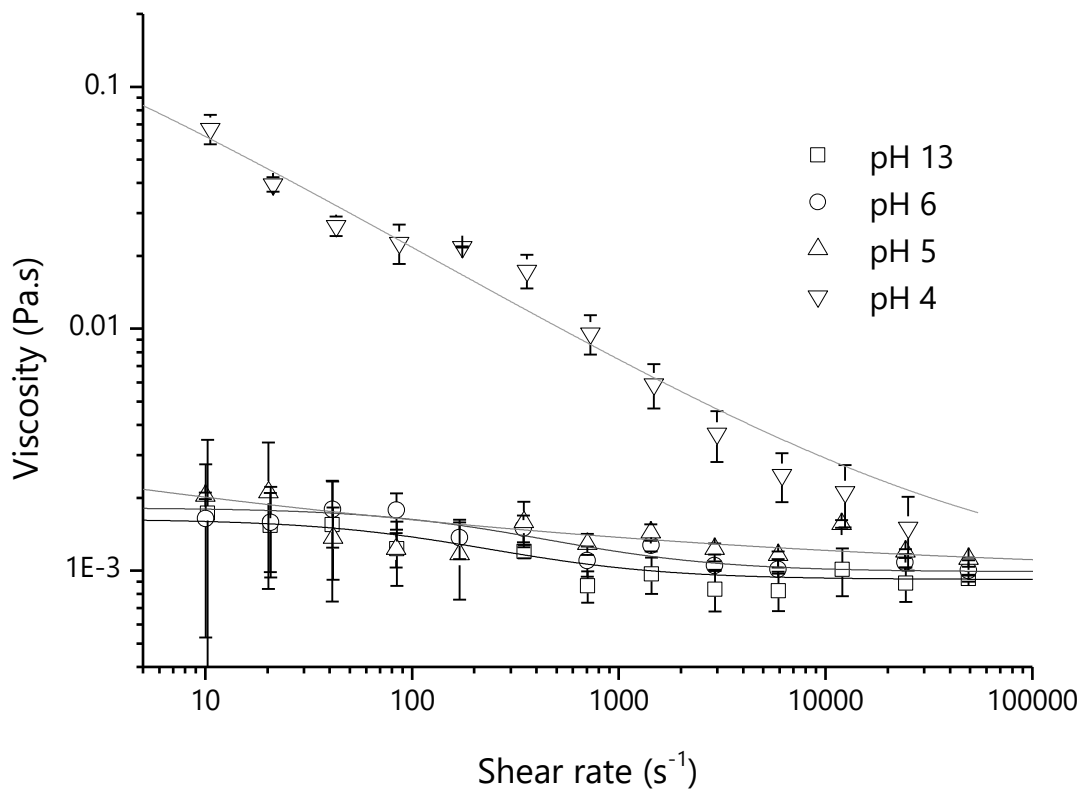
Figure 5.10: Rheological profiles of COOH-SiNP nanofluids at specified pH values. Concentration is ~12 % by weight. Points are averaged measurements across multiple runs with error bars being ± 1 standard deviation. Lines are Cross models fitted to each profile.

Table 5.3: Cross model parameters of models applied to rheological profiles of 12 %w/w COOH-SiNPs in water at specified pH values

pH	η_∞ (Pa·s)	η_0 (Pa·s)	α_c (s)	m
13	0.00092	0.0016	0.0056	1
6	0.00099	0.0018	0.003	1
5	0.00093	0.63	1.7×10^{13}	0.19
4	0.00089	0.43	3.2	0.52

5.3.2 Concentration controlled measurements of fluid properties

The two values selected for pH measurement, 5.8 and 13, were chosen to produce a broad range of potential behaviour. At pH 4, it would be expected that aggregation would dominate, rendering all solutions measured, regardless of concentration, similar in behaviour. The lower pH value was selected therefore to be close to, but above the expected pKa value of the undecanoic acid group, pH 5.38. This way, stabilisation due to charge could be expected but, due to the nature of organic acids, not as greatly as at pH 13. Higher pH values were not reasonably useable for measurement, as pH values above 13 dissolve organosilane particles.

At pH 5.8 (Figure 5.11) the fluids displayed significant increases in viscosity with increasing concentration. Shear thinning behaviour was present in the samples at higher concentration (34 %w/w and 47 %w/w), but did not appear measurably up to 10 %w/w. Of the samples that did show shear thinning behaviour, no zero-shear plateau viscosity value was visible.

Cross models were fitted to the data and the parameters are displayed in Table 5.4. The samples also showed a higher viscosity than the TEOS SiNPs at comparable concentrations. Infinite shear values of viscosity for each sample, however, showed similar values to the control TEOS-SiNP nanofluids at similar concentrations. This similarity was expected as for the COOH-SiNPs the electrostatic stabilisation (the main interparticle interaction expected) should have been completely overwhelmed by shear forces.

This behaviour was consistent with agglomerate breakdown: large agglomerates in solution experienced a resistance to flow under due to shear, but as the shear forces increased these agglomerates broke, producing smaller particle groups in solution. These were able to flow more easily in the direction of shear, reducing the viscosity. The minimum expected viscosity from this was the same as expected of primary particles in solution. Dispersions of solid particles often exhibit shear thickening at high shear rates. Commonly this is caused by

jamming, wherein the particles are unable to continue flowing, impeding solution flow. This viscosity increase was not observed even at shear rates as high as 50000 s^{-1}.
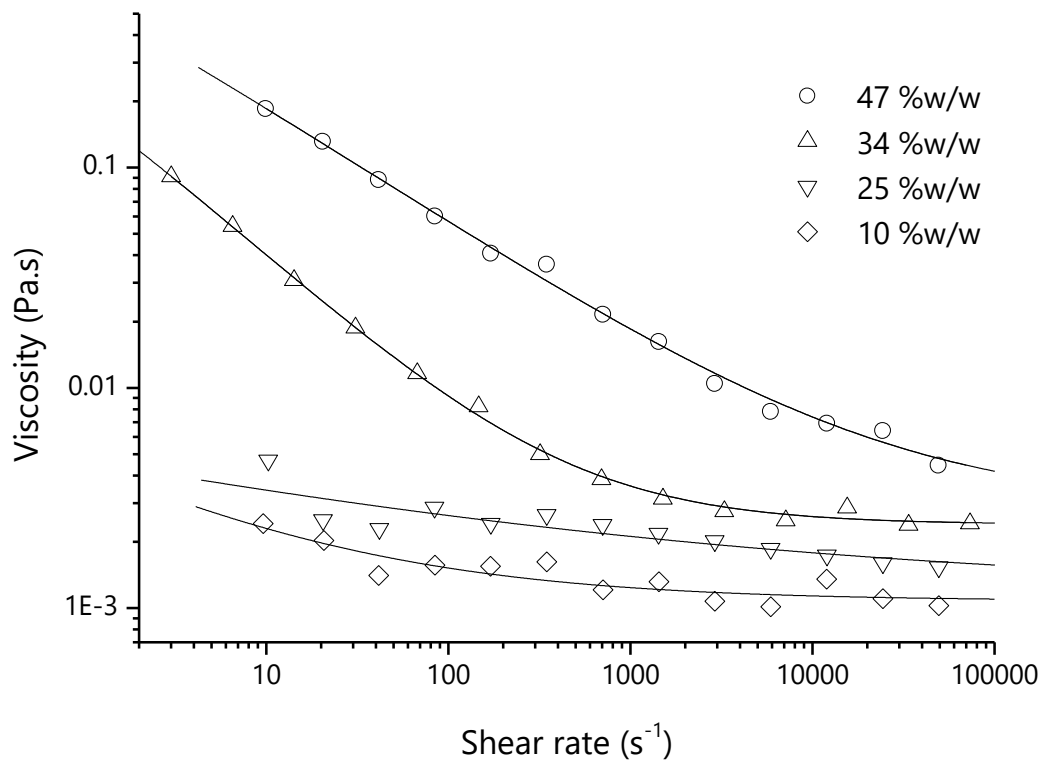
Figure 5.11: Rheological profile of pH 5.8 COOH-SiNP nanofluid, at indicated weight percent concentration, lines are Cross models fit to the data.

At pH 13 (Figure 5.12), the rheological profiles of all samples showed comparatively lower viscosities. At low shear rates (5-100 s^{-1}) and high concentrations (32 and 49 %w/w), some shear thinning behaviour was evident, however less than for the 47 %w/w sample at pH 5.8. Based on agglomerate breakdown, this was an expected relationship. From the DLS measurements at pH 13, the aggregation of the sample was minimal. This would imply no agglomerates were present, and thus that the solution was initially at its lowest viscosity. The small amount of shear thinning behaviour present at the higher shear rates may indicate the presence of agglomerates that were unavoidable, based on the high particle concentration in solution.
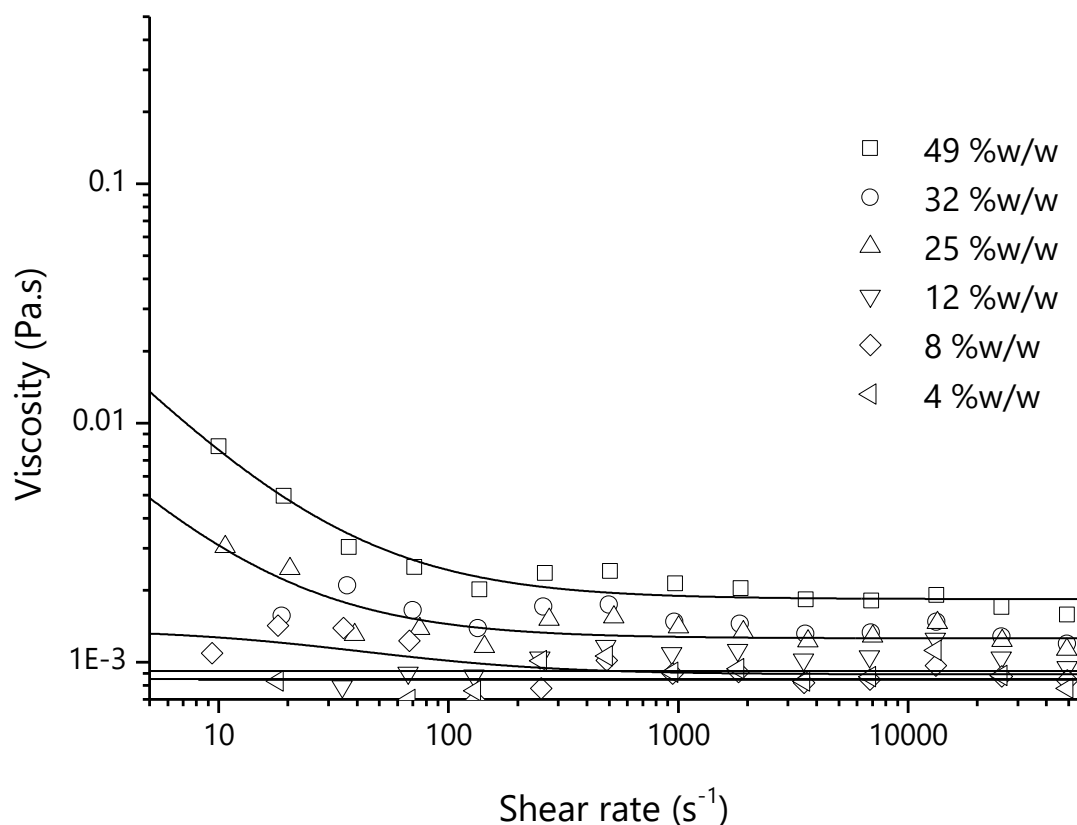
Figure 5.12: Rheological profile of pH 13 COOH-SiNP nanofluid, at indicated weight percent concentration.

Most of the samples showed no significant non-Newtonian behaviour, and, aside from the sample at 49 %w/w, any apparent behaviour was considered as due to instrumental artefacts and noise. Samples were modelled with the Cross equation (Equation 1.18), which reduces to a Newtonian equation (Equation 1.15) for samples that did not show shear thinning effects. The parameters determined for each fit are given in Table 5.4.

The samples at pH 13 remained similar in behaviour from 4-49 %w/w, with low viscosities, lower than the values obtained at lower pH, and lower than TEOS particles of the same concentration. This suggests that at pH 13 the effective volume fraction of the particles was sufficiently similar to that of the particle diameters themselves, that the effective critical volume was not significant elevated enough to reach the critical volume fraction.

Table 5.4: Cross model parameters for rheological profiles of nanofluids at specified concentrations and pH values

pH	Concentration (%w/w)	η_∞ (Pa·s)	η_0 (Pa·s)	α_c (s)	m
5.8	10	0.0011	190	6.2×10^{10}	0.44
	25	0.0012	2.7	1.6×10^{15}	0.19
	34	0.0024	0.94	6.5	0.76
	47	0.0029	3.4	19	0.54
13	4	0.00094	0.0009	-	0
	8	0.00089	0.0014	0.029	1
	12	0.00091	0.0009	-	0
	25	0.0013	0.15	7.9	1
	32	0.00089	0.0009	-	0
	49	0.0018	1.2	21	1

Due to the difficulty in fitting Cross parameters to the data, a simpler three-parameter equation of rheology, the Herschel-Bulkley model (Equation 1.17), was fit to the data, showing good agreement. The parameters determined for each fit are given in Table 5.5. At pH 5.8 the consistency index was noted to increase with increasing concentration, showing a large increase between 25 and 47 %w/w, modelling the increased viscosity noted in the higher concentration samples. Zero shear stress, even at the highest concentration was relatively small. The flow indices indicated near-Newtonian or effectively Newtonian behaviour at low concentrations, dropping at 47 %w/w, indicative of shear thinning character.

At pH 13, the profiles remained remarkably similar across the range of concentrations investigated. The consistency index showed a small increase across the concentration range, while the zero shear, stress remained low, and the flow indices indicated Newtonian behaviour in all samples.

Table 5.5: Herschel-Bulkley model parameters (consistency index, yield stress and flow index) for rheological profiles of nanofluids at specified concentrations and pH values

pH	Concentration (%)	k (mPa·s)	τ_0 (mPa)	n
5.8	10	1.3	0.5	0.93
	25	3.8	0	0.91
	47	103	574	0.71
13	4	1.1	7.2	1.0
	8	0.95	8.3	1.0
	12	1.2	0	0.99
	25	1.4	8.2	0.99
	32	2.0	4.5	0.95
	49	2.0	55	0.98

5.3.3 Sonication of nanofluids

Breaking agglomerate structures can occur with stabilisation through the surface charge (modifying the pH) or by shear force over time. The second one does not address the long-term stability of the nanofluids. The zeta potential measured still indicates an unstable solution. One method of disaggregating the particles without introducing a stabilising agent is through sonication.

A sample of COOH-SiNP nanofluid was measured under sequential increasing and decreasing shear rates (Figure 5.13) in order to establish a baseline of how these particles behave without immediate prior sonication, and thus with the presence of aggregates. The profiles observed in each case indicated a larger viscosity as the shear rate approached zero, decreasing with increasing shear. What appears to be a small increase in viscosity at the higher shear rates measured was an artefact: at high shear rates instabilities in solution create inconsistencies between the shear rate and the viscosity, due to wave effects in the sample. This caused an apparent increase in viscosity measured.
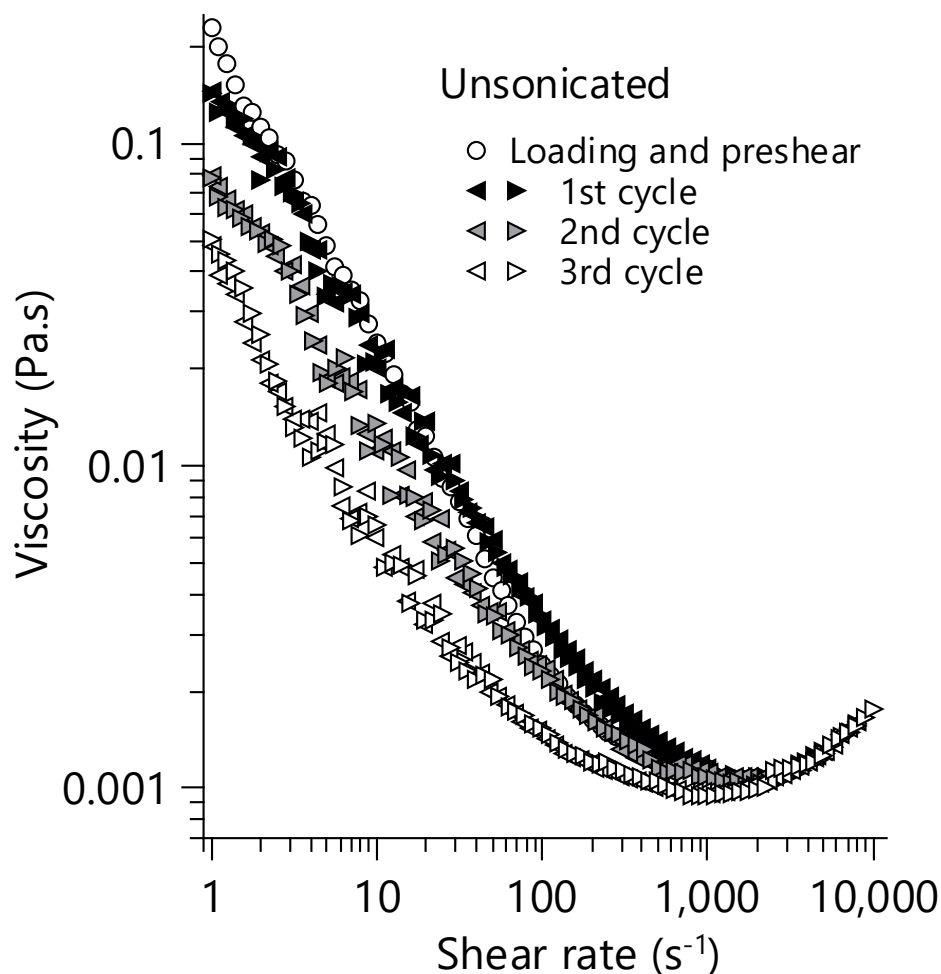
Figure 5.13: Rheological profiles of COOH-SiNPs at pH 5.8, direction of arrow indicates whether shear rate was increasing or decreasing. Loading and preshear cycle was increasing shear rate,

The viscosity of each profile was seen to decrease with each maximum shear rate reached. The samples showed consistent down and up profiles, but then show a lowered viscosity. This continues through the three runs measured. This was consistent with the shear breakdown of the sample. As indicated by the intermittent stability in the zeta potential values and the greater than primary particle diameters measured by DLS, the particles existed in solution as agglomerates. These agglomerates acted as larger particles in solution, resisting flow due to their greater inertia. This required greater force to move them in the direction of flow, which was measured as a higher viscosity. As the shear rate increased the agglomerates broke down under shear induced forces, resulting in smaller particles in solution. These smaller particles were more able to move in the direction of the flow, resulting in a smaller measured viscosity.
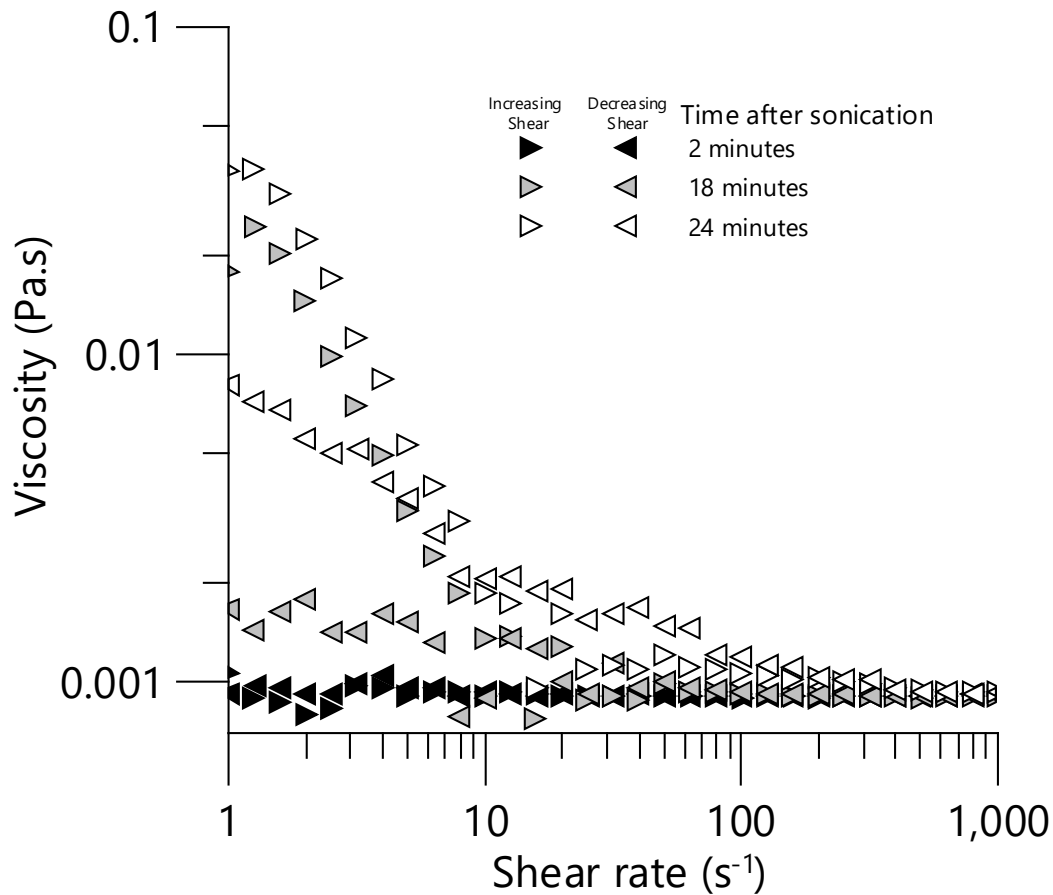
Figure 5.14: Rheological profiles of COOH-SiNP nanofluids after sonication, direction of arrows indicates increasing or decreasing shear rate

Figure 5.14 shows the rheological profiles of nanofluid samples after sonication under increasing and decreasing shear rates. After two minutes, the increasing and decreasing shear rate measurements indicated similar Newtonian profiles, with a viscosity approaching that of water, the base fluid. After 18 minutes, the sample showed shear thinning behaviour at low shear rates before returning to a low value similar to that of the base fluid. As the shear rate was lowered from this, a slight increase in viscosity was found, though to a much lower value than before. After 24 minutes, the shear thinning behaviour was evident again under increasing shear, taking longer to return to the lower value found. When the shear rate was decreased, a slight increase in viscosity was again noted, returning a final value lower than before the shearing at this step.

The final viscosity (i.e. the viscosity a low shear rates when the shear rate was being reduced) increased with time from sonication. This suggested the reformation of agglomerates was behind the increase in viscosity, which implies that this reformation happened on a timescale

of minutes. This was supported by the reduction in the viscosity of the solutions after shearing. As the samples did not return to a Newtonian profile the presence of some agglomerates was expected, and they may have been reformed during the experiment, however, this reformation was slow.

5.4 Conclusions

Particles functionalised with undec-10-enoic acid retained the capacity for acid-base chemistry, which affected their surface functionality and subsequent solution properties. COONa-SiNPs were found to be slightly more thermally stable than COOH-SiNPs, showing later thermal degradation events.

The aggregation of COOH-SiNPs in solution was controlled by pH. This aggregation was found to have significant effects on the rheological properties of the solution. Higher pH values allowed for higher concentrations of COOH-SiNPs to be incorporated into solution without negatively affecting the viscosity of the solution, or its rheological properties. When basified, solutions of up to 49 %w/w could be obtained, which showed near-Newtonian behaviour. Conversely, by reducing the pH, particle aggregation could be induced resulting in an increase in viscosity and shear thinning behaviour.

These properties were simulated by sonication of the solution, to break apart the agglomerates. Agglomerate breakdown in this fashion resulted in a lower value of viscosity and an elimination of shear thinning behaviour. The viscosity and shear thinning behaviour returned on a timescale of minutes after sonication.

6 Role of surface functionality on rheological behaviour

6.1 Overview

Particle interaction and aggregation has a significant effect on the rheological properties of a solution. Altering the surface chemistry changes the interparticle interaction and the particle-solvent interaction. This in turn has implications for the particle aggregation and solution effects and results in a change in rheological character of the solution.

The changes in particle functionality can be more significant, resulting in changes to stability of dispersions of the particles in various solvents and changing their interactions in aqueous solutions. As the particle volume fraction in solution increases, the interparticle interactions become dominant in determining the properties of the solution. In electrostatically stabilised solutions, interparticle repulsion occurs and at high concentrations, there is direct overlap between the particle electrical double layers, resulting in significant repulsion.

In the absence of stabilising forces large particle agglomerates can form, increasing in size with volume fraction. The size of agglomerates in solution results in a greater effective viscosity, as the larger agglomerates are more resistant to movement under shear forces [52, 155, 223]. Agglomerates can be broken down by shear forces, resulting in smaller effective particles in solution, lowering the viscosity [63]. This manifests itself as an apparent shear thinning behaviour, and can be reversible. Theoretically, this agglomerate breakdown can continue until the primary particles are reached.

Stabilised particles may also show shear-thinning effects as the concentration increases, as discussed in Section 5.2.1. Specifically, changed in rheological behaviour may occur with increasing concentration, with a general overview presented in Figure 6.1a. At low volume fractions, the particles are unlikely to have significant interparticle interaction, resulting in a Newtonian fluid. As the concentration increases the interparticle interaction becomes more significant, and the overall rheological behaviour approaches that of a generalised Newtonian fluid. Interparticle interaction acting in resistance to flow is overcome with shear rate, resulting in shear thinning. Above a critical concentration, the particles are effectively caged by the surrounding particles, resulting in the development of a yield stress. The three general viscosity curves expected for nanoparticle suspensions are displayed in Figure 6.1b.

a) [Fluid ⟷ Solid-like regions; y-axis $\log\left(\frac{\tau_0 r^3}{k_B T}\right)$]

Repulsive interparticle interactionor agglomeration

Ideal spheres ($\phi_c = \phi_G$)

0 $\quad \phi_c \quad\quad\quad \phi_G \quad \phi_{RCP} \quad \phi_{FCC} \quad 1$
$\phi \quad\quad = 0.58 \quad = 0.64 \quad = 0.74$

b) [y-axis η (Pa·s); x-axis $\dot{\gamma}$ (s^{-1})]

$\phi > \phi_c$

$\phi < \phi_c$

$\phi \rightarrow 0$
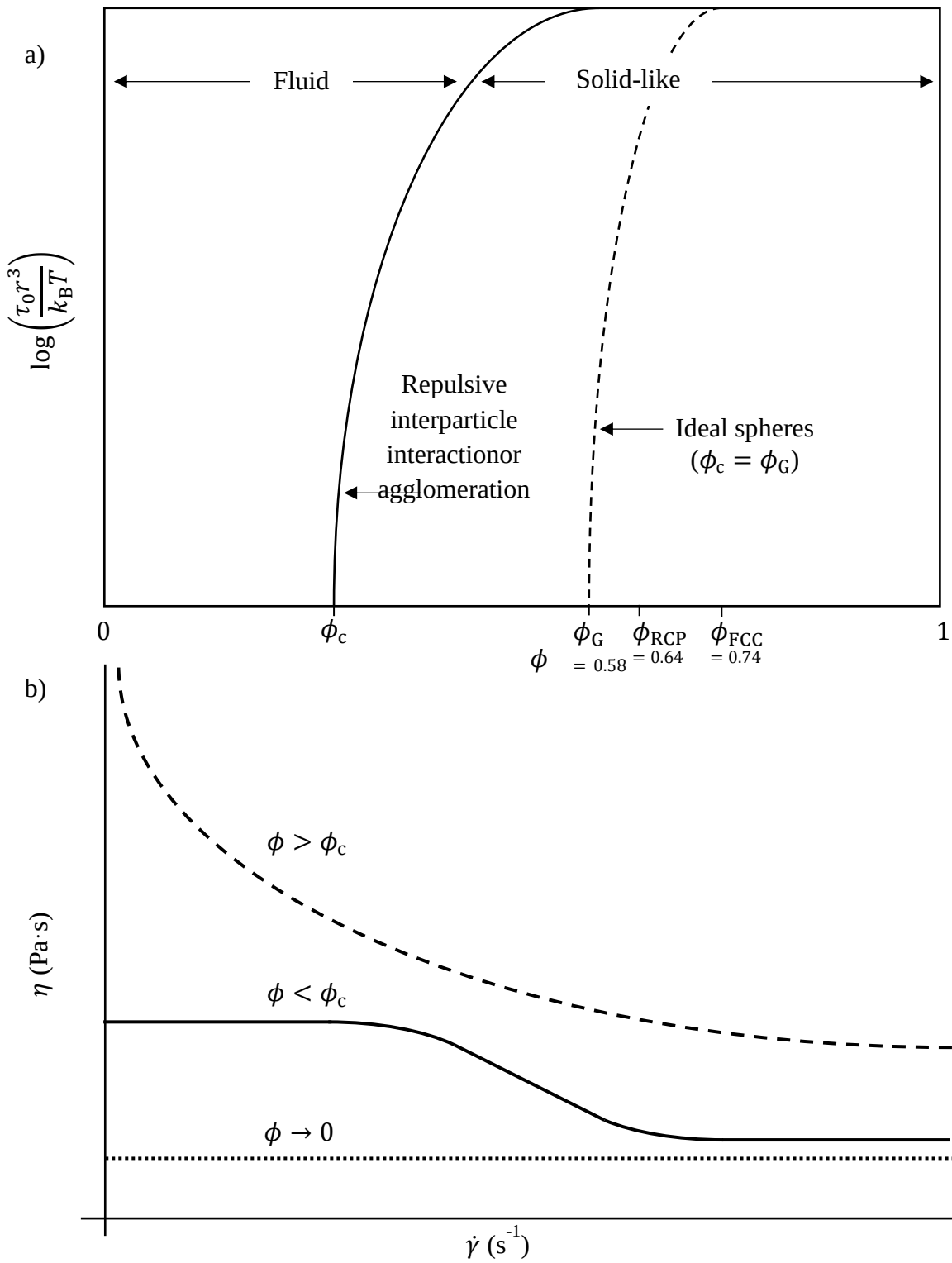
Figure 6.1: a) Representation of yield stress as a function of particle volume fraction, with cases indicated for repulsive interacting particles or agglomerated particles, and ideal spheres; b) General viscosity curves as a function of shear rate for samples with volume fractions falling within three separate regimes

Due to the incorporation of solvent into the agglomerate structure, the effective size of an agglomerate is greater than that of its constituent particles, resulting in a greater effective

volume fraction in solution. At high effective volume fractions, caging can occur, which happens at volume fractions significantly lower than in dispersions of stabilised particles. Caging of particles restricts their movement into a three-dimensional grid structure, resulting in particles being incapable of movement without disturbing the entire grid structure. This results in a yield stress, based on the energy required to destroy the grid like structure of the dispersion.

In Chapter 5 the effect of pH on particle interactions was investigated and in this chapter, particle functionality was systematically varied to understand interparticle interactions. Agglomeration and the effects on the rheology of the solution were investigated. Functional groups were selected that were intended to increase the dispersion stability of the particles in aqueous solution (OH-SiNPs and StS-SiNPs) and others were selected to make the particle-solvent interaction less favourable (Br-SiNPs and U-SiNPs).

6.2 Dispersion and dispersion stability of functionalised particles

Silica nanoparticles with different surface chemistries were prepared by surface modification of the SH-NPs based on the approach from Mangos *et al.* [108]. To produce OH-SiNPs, SH-SiNPs were reacted with undecenol. Similarly, Br-SiNPs were prepared using bromoundecene, U-SiNPs were prepared using undecene, and StS-SiNPs were prepared by reaction with sodium 4-vinylstyrenesulfonate.
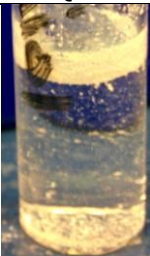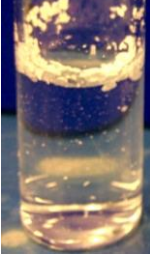
Functionalised particles had different dispersion properties. Table 6.1 shows images of attempts to redisperse these functionalised nanoparticles in water, with and without sonication, and with adjustment of the pH of the solution to pH 11 using sodium hydroxide.

When dry, SH-SiNPs loosely adhered to the glass of the vial. When Milli-Q water was added, they did not disperse in solution, floating on the surface. With sonication, the particles formed smaller agglomerates, however did not form a stable solution. With stirring at pH 11, greater solution stability was obtained, however large, visible agglomerates remained.

OH-SiNPs displayed a similar profile, not forming a stable solution in water with sonication or pH adjustment. All OH-SiNP solutions showed large agglomerates and collapsed over time. This solution, when filtered through a 0.45 µm filter became clear and colourless, indicating the white colouration was due to large agglomerates, rather than individually dispersed particles as expected. By comparison, filtration of samples of StS-SiNPs and COOH-SiNPs

dispersed under basic conditions retained white colouration after filtration, with SEM and DLS measurements confirming the presence of particles. Br-SiNPs in dry form displayed little adhesion to the glass vial. When water was added, Br-SiNPs did not form a stable dispersion, remaining as large agglomerates even with sonication and stirring. The particles remained on the surface of the solution.

Table 6.1: Redispersion of dried, functionalised particles in Milli-Q water, with sonication, and with sodium hydroxide to pH 11

Particle type	Dry	Milli-Q Water	Sonication	pH 11, stirring
SH-SiNPs				
OH-SiNPs				
Br-SiNPs				

Functionalisation reactions were performed on SH-SiNPs prepared from the same batch of particles to produce identically sized-particles, measured as 172±19 nm by SEM, with differing surface functionalities. These particles were measured by DLS to characterise the effective particle diameter in solution (Table 6.2).

Table 6.2: Z_{av} diameter measured by DLS of 172 nm average diameter particles, functionalised with specified terminal groups, italicised data indicate the particles showed obvious aggregation even at low concentration. DLS measurements (excluding the measurements in IPA) conducted in aqueous, 10 mM sodium chloride solution. * Indicates sample has been dried and redispersed.

Functionality (172±19 nm by SEM)	Z_{av} (nm)	PDI
SH-SiNPs	203.7	0.11
SH-SiNPs *	262.4	0.20
COOH-SiNPs	206.5	0.20
StS-SiNPs	193.3	0.02
Br-SiNPs	*276.7*	*0.25*
OH-SiNPs	*338.8*	*0.29*
OH-SiNPs (IPA)	190.7	0.03
OH-SiNPs (IPA) *	197.5	0.05

The DLS measurements of the same particles gave different average particle diameters, and polydispersity indices, with all samples showing an average diameter greater than that measured from SEM. This was expected, owing to the measurement by DLS of hydrodynamic radii, as well as the measurement of agglomerated structures in solution, as noted in Section 1.5.1.1.

Samples prepared from SH-SiNPs showed different values depending on the processing conditions of the SH-SiNPs. If the SH-SiNPs were cleaned and prepared as a low concentration dispersion without having dried previously, the Z_{av} diameter measured was approximately 30 nm higher than the SEM result, with a low PDI suggesting good dispersity. If, however, the measurement was made of a low concentration solution prepared from dried particles, the Z_{av} diameter increases significantly, along with an increase in PDI. This suggests the particles formed agglomerates when dried that were difficult to break apart to form a stable solution after drying. Measurements of the COOH-SiNPs showed a similar Z_{av} diameter as the unprocessed SH-SiNPs. As these samples were prepared in Milli-Q water without the addition of base, the stabilisation experienced by these particles in solution was lesser, though they were still capable of forming a stable dispersion, as well as forming dispersions easily after drying, as discussed previously in Section 5.3.1.

The StS-SiNPs showed a relatively low Z_{av} diameter and a low PDI, suggesting the particles exist primarily as stabilised primary particles in solution, without significant aggregation. This

would be expected due to the charged surface of the StS-SiNPs producing a strong electrostatic repulsion between particles, stabilising the dispersions.

The Br- and OH-SiNPs showed evident agglomeration, even at low concentration. The DLS results reflected this, showing large Z_{av} diameters and PDI values. It was expected that Br-SiNPs would be hydrophobic and thus prone to aggregation in water. The OH-SiNPs' hydrophobicity indicated the terminal hydroxyl functionality was not sufficiently capable of producing a stable dispersion, suggesting interparticle interaction was favoured over particle-solvent interaction in this case. When dispersed in isopropyl alcohol, OH-SiNPs showed a Z_{av} diameter that showed good agreement with the value measured for StS-SiNPs in water, indicating their improved dispersion within this solvent. Further, after drying and subsequent redispersion, OH-SiNPs were still capable of forming stable dispersions in IPA, with only minimal increase noted in the Z_{av} diameter and PDI. The Br-SiNPs were unable to disperse effectively in water, ethanol, isopropyl alcohol, hexane, anisole, toluene, chloroform, dichloromethane or chlorobenzene, with large white agglomerates present in all cases. It was noted that in organic solvents the Br-SiNPs did not float on the surface of the sample, instead forming large poorly suspended agglomerates that rapidly settled to the base of the vial.

It should be noted, that whilst the DLS measurement may not give the actual particle diameter as determined by SEM, it does provide critical information for rheological applications. The effective particle diameter in solution has a significant effect on the final properties of a suspension, more so than the actual particle diameter [224]. Thus monitoring of the hydrodynamic radii of particles was critical to understanding the solution properties.

SEM images of functionalised nanoparticles (Figure 6.2) cannot directly show the impact of surface functionality on the aggregation effects in solution. However, they did provide some qualitative information on the interparticle interactions of functionalised particles based on how they dried. For unprocessed SH-SiNPs (see Figure 3.2) and StS-SiNPs, the SEM images showed significantly greater ordering of nanoparticles when dried, with patterning observable for drop-cast samples. The Br-SiNPs and OH-SiNPs showed no ordering, drying in large, random agglomerates, consistent with the DLS measurements of the particles. As the evaporation process was not expected to be capable of breaking apart agglomerates of particles, this was considered sensible. Particle-solvent interaction is known to be a critical parameter in the drying patterns of particles. The "coffee-ring" effect is a commonly observed behaviour of dried colloidal particles [225], and can be attributed to the balance of interparticle, particle-

solvent and particle-substrate forces against the force of the outward flow due to evaporation. The rate of evaporation is of particular importance in this case, for stabilised particles it has been conjectured that a higher rate of drying results in a more ordered, but more cracked surface, while a slower rate results in lower rates of cracking, but with greater disorder due to the increased propensity towards agglomerate formation during drying [226].

Br-SiNPs

StS-SiNPs
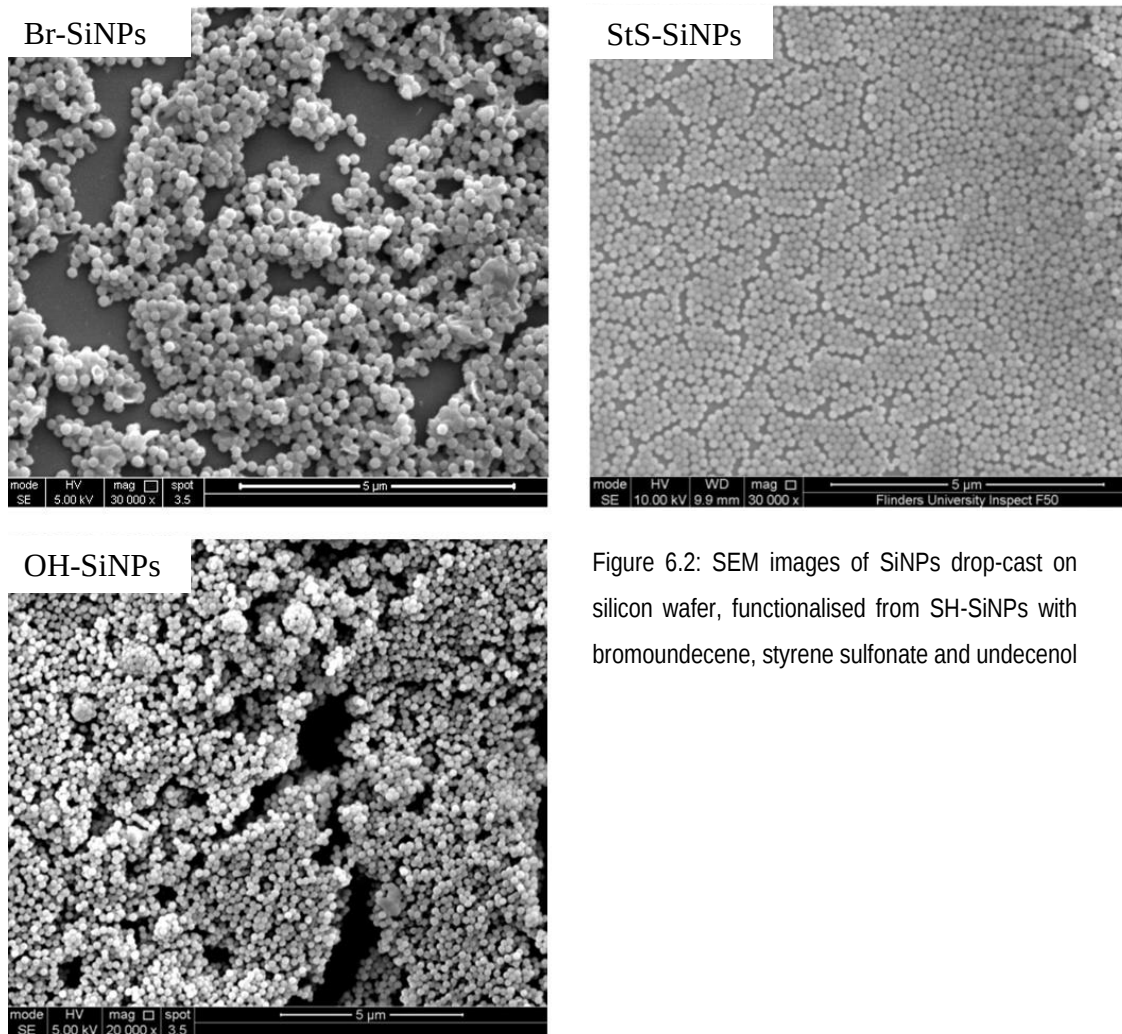
OH-SiNPs

Figure 6.2: SEM images of SiNPs drop-cast on silicon wafer, functionalised from SH-SiNPs with bromoundecene, styrene sulfonate and undecenol

Table 6.3: Z-average diameter and PDI measured by DLS measurements of SH-SiNPs in aqueous solutions at indicated pH

pH	Z-average diameter (nm)	PDI
1	294.3	0.36
2	208.9	0.33
4	215.9	0.36
7	244.3	0.34
8	220.6	0.34
9	236.1	0.34
10	222.4	0.36
11	239.0	0.34
13	231.7	0.35

Table 6.4: Z-average diameter and PDI measured by DLS measurements of StS-SiNPs in aqueous solutions at indicated pH

pH	Z-average diameter (nm)	PDI
1	149.0	0.071
3	149.1	0.15
7	159.3	0.11
11	147.8	0.088
13	147.7	0.12

The unreacted particles were significantly less capable of forming solutions than the TEOS SiNP standards, as well as the COOH-SiNPs when under basic conditions. Changes to pH were not capable of producing significant particle stabilisation or reduction of the effective particle diameter in solution (Table 6.3). The average hydrodynamic diameters measured for the particles were larger than the original particles (138.3 nm), and were not significantly different based on the pH of the solution, nor did any pH tested result in an improved dispersion. As the pKa value of propylmercaptan groups are ~10.6 [227] electrostatic stabilisation would not be expected until high pH values.

The pH stability of the StS-SiNPs was investigated by adjusting the pH of the StS-SiNP solutions (Table 6.4). StS-SiNPs showed Z-average diameters greater than the diameter known by SEM of 109.6 nm), with similar variances in particle diameters compared across the entire range. This was compared to the prior measurements made of the COOH-SiNPs (Section 5.3.1), which showed a significant increase in average diameter and variation as the solution pH reached the pKa of undecylenic acid. As the Z-average diameter and distribution of the particles did not change, the StS-SiNP nanofluids were determined to be stable from pH 1-13.

134

6.3 Rheological properties of nanofluids prepared from unmodified SH-SiNPs

Nanofluids of SH-SiNPs were prepared and their rheological properties measured at different concentrations. At low concentrations, SH-SiNP nanofluids in water were white and opaque. In ethanol or 10:90 ethanol:water mixtures, low concentration solutions were white in colour, however, displayed blue colouration characteristic of light scattering. If left in water at neutral pH, SH-SiNPs samples sedimented out of solution within 24 hours. When concentrated by centrifugation the pellets produced were white and opaque, however thin sections formed translucent solids showing blue or blue-green colour.

SH-SiNPs showed reasonable stability in solution, DLS measurements indicated the apparent particle diameter in solution was significantly larger than that measured by SEM (279 nm by DLS and 152 nm by SEM) indicative of aggregation in solution. The larger agglomerates would act as effective "particles", which has implications for the solution stability and the rheological properties of the dispersion.

Agglomerates formed of poorly stabilised particles in solution can be broken apart by shear forces, resulting in smaller agglomerates [228]. This can continue until no agglomerates remain, with only individual particles present in solution at infinite shear rate. Recalling Equation 1.10 the effective volume fraction in the solution can be related to the effective diameter of agglomerates in solution, which can be approximated by the diameter measured by DLS. This gives an overall higher volume fraction, and thus a higher viscosity. With shear breakdown of the agglomerates, this effective volume fraction decreases and, based on the relationship between apparent viscosity and the volume fraction, the apparent viscosity decreases.

All SH-SiNP nanofluids investigated showed significant shear thinning behaviour, even at low concentrations (Figure 6.3). At low concentrations (below 16 %w/w) an infinite-shear viscosity plateau was observable, however at high concentrations (20 %w/w and above) only the shear-thinning section of the rheograms were observed, as seen in Figure 6.3. No SH-SiNP nanofluid sample showed a visible zero-shear viscosity plateau. Samples at 20 %w/w and above were no longer flowing liquid dispersions, instead behaving as pastes: samples did not flow when tilted and could be loaded onto the rheometer lower plate by spatula. Extreme sample failure was found for the 65 %w/w sample that was not found in the case of the lower concentration

samples. At high shear rates (approaching 1000 s^{-1}), the sample was ejected from the measuring apparatus, resulting in an uncontrolled reduction in the measured apparent viscosity.
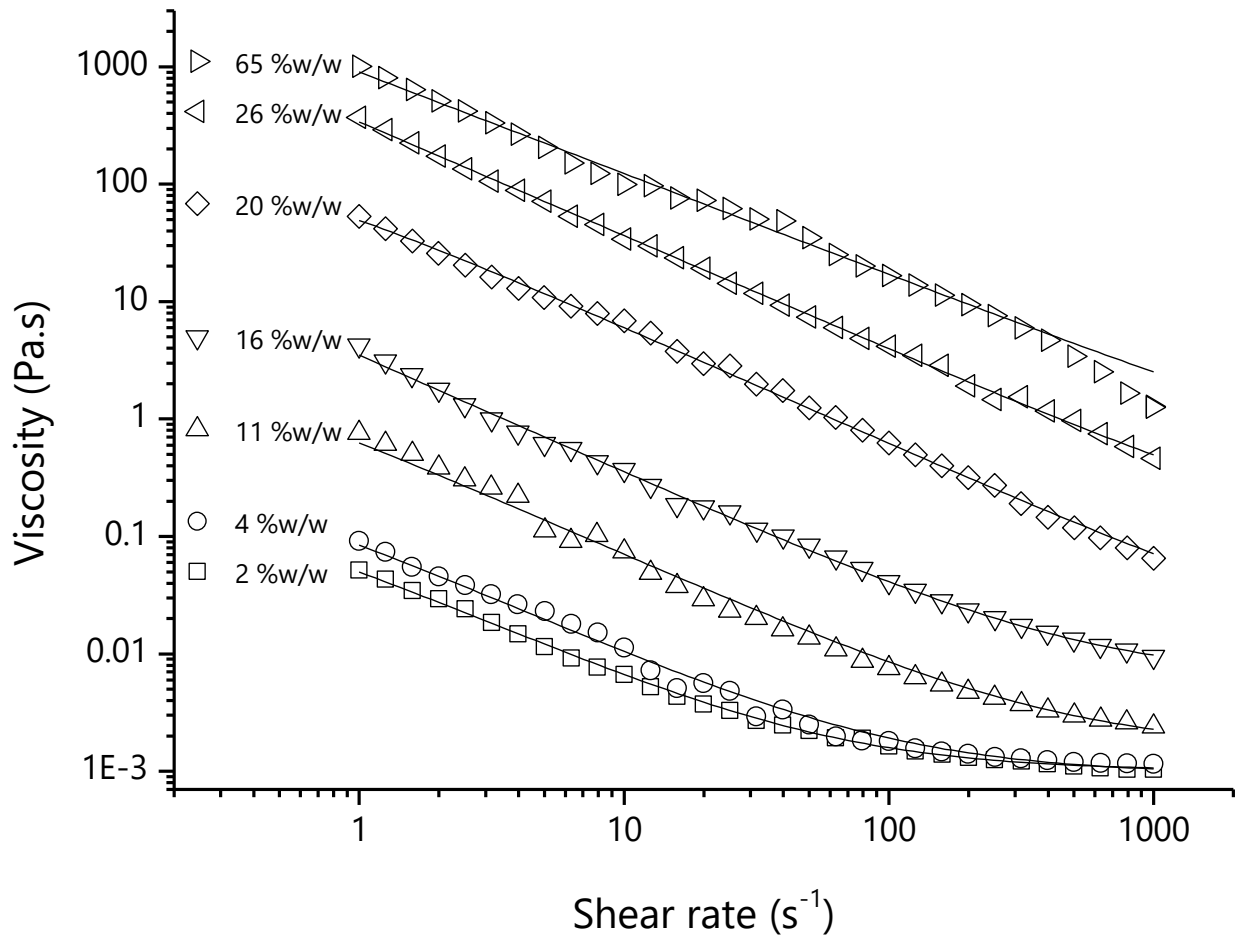
Figure 6.3: Viscosity rheograms of SH-SiNPs at specified weight concentrations in solution. Lines are Cross models of rheological profiles.

Table 6.5: Parameters of Cross models applied to rheological profiles of SH-SiNP based nanofluids with calculated values of apparent yield stress determined from each model

Concentration (%w/w)	η_0 (Pa.s)	η_∞ (Pa.s)	α_c (s)	m	τ^* (Pa)
2	0.30656	0.00101	5.28846	1	0.058
4	0.60511	0.000951	6.24544	1	0.097
12	5.97544	0.00158	8.55496	1	0.70
16	5.03x10^{16}	0.00626	1.44x10^{16}	1	3.5
20	250.6675	0.01	4.09063	1	61
26	2.59x10^9	0.07765	12442800	0.97	210
65	1.78x10^9	0.2082	19357500	0.86397	92

Cross models were applied to the SH-SiNP nanofluids (Table 6.5), however it should be noted that fitting a four-parameter viscosity model was made significantly more difficult when only small sections of the profile were visible. The models showed flow indices approaching or achieving a value of $m = 1$, which is the upper limit in the Cross model, with samples showing increasing shear thinning behaviour as m approached one. Despite the limited section of the profile observable, this suggests highly shear-thinning character was evident.

A value for an apparent yield stress can be extracted from the Cross model, representing the stress at which a large reduction in the sample viscosity occurs [171]. This value was given by $\tau^* = \frac{\eta_0}{\alpha_c}$, included in the list of parameters for the Cross models, in Table 6.5. This value increased with sample volume fraction, experiencing a large increase in samples above 20 %w/w. The sample measured at 65 %w/w showed an apparent decrease compared to the 26 %w/w sample, however this may have been due to the difficulty in fitting values for the Cross model to the rheogram.

Fitting the Quemada equation (Equation 1.12) to the infinite shear viscosity and the volume fraction, gave a critical volume fraction of 0.18, a very low value compared to the equivalent volume fraction for non-interacting spheres (0.74). This suggested the particles continued to show significant interparticle interaction even when strongly sheared, with agglomerates remaining in solution under high shear conditions, increasing the effective volume fraction. The poor ability of the shear force to break apart the agglomerates was reflective of the inability of the SH-SiNPs to be redispersed under aqueous conditions once dried, as found in Section 6.2.

An independent estimate of the apparent yield stress was obtained by plotting the data on a stress-shear rate plot and fitting Herschel-Bulkley models to the measurements (Figure 6.4). The Herschel-Bulkley model fits the data using sample yield stress as an independent parameter, being the stress value extrapolated to a shear rate of zero. The Herschel-Bulkley model gave good agreement with all samples measured up to 26 %w/w, the model was unable to fit the sample at 65 %w/w effectively. As it was expected that the sample by this mass concentration has ceased behaving as a dispersion in the same fashion, and instead behaving as a thick slurry, this poor fit was expected.
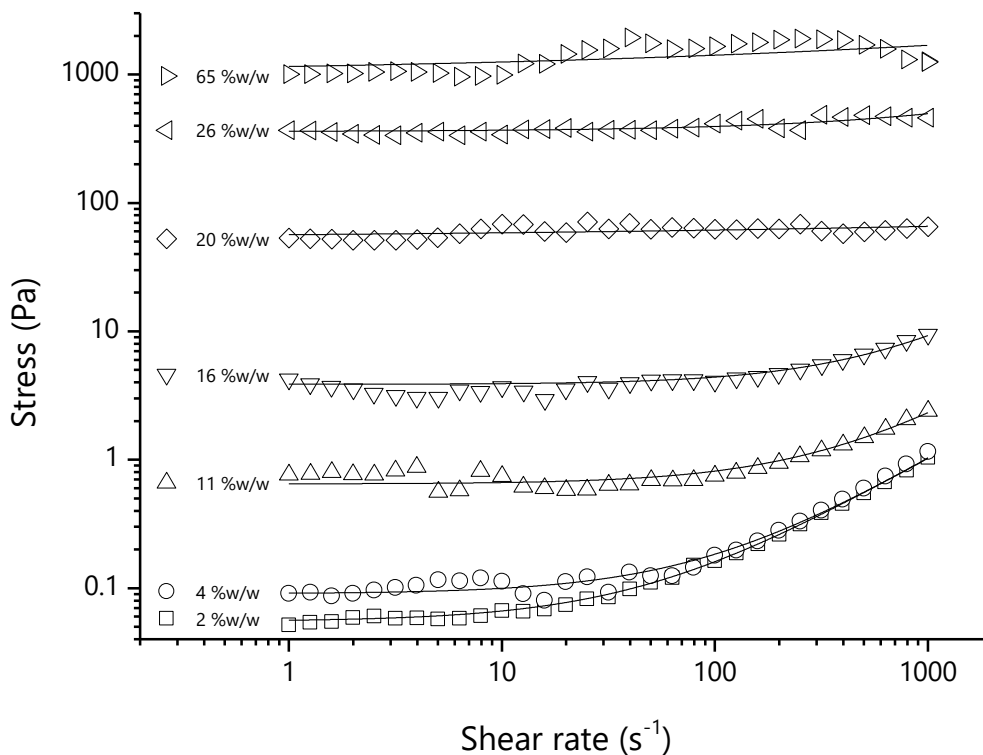
Figure 6.4: Stress-shear rate plots of SH-SiNPs at indicated mass concentrations. Solid lines are Herschel-Bulkley models fit to the data.

Table 6.6 shows the fitting parameters used for the Herschel-Bulkley models of the SH-SiNP nanofluids from Figure 6.4. The fitting models suggested the samples showed an increasing yield stress with concentration, showing a large increase at 20 %w/w and above. It was also noted that the yield stress values found showed reasonable agreement with the values determined from the Cross model, which are representative of similar, but not identical concepts of yield behaviour [171]. Similarly, the consistency index was found to increase significantly past 20 %w/w. The flow indices measured for each of the samples were close to one for the lower concentration samples, which in the Herschel-Bulkley model suggests near Newtonian behaviour at high shear rates. This differs from the Cross model as the models use different assumptions as to which section was representative of the power-law behaviour section of the nanofluid. In this model, the assumption was that the yield stress occurs because of particle agglomerate breakup at a critical stress value, causing the yielding behaviour, with the dispersion of smaller or primary particles resulting from this behaving in a Newtonian fashion.

Table 6.6: Herschel-Bulkley parameters for SH-SiNP nanofluids displayed in Figure 6.4, also included are apparent yield stresses from Table 6.5 determined from Cross models fit to the data

Mass fraction (%w/w)	K (Pa.s)	n	τ_0 (Pa)	τ^* (Pa)
2	0.00136	0.95127	0.0527	0.058
4	0.000468	1.12218	0.09355	0.097
12	0.00403	0.91012	0.72017	0.70
16	0.01059	0.91925	3.43453	3.5
20	2.58037	0.20534	54.73	61
26	11.29498	0.37783	333.9012	210
65	32.90979	0	1288.74	92

Figure 6.5 shows the storage and loss moduli measured for the high concentration SH-SiNP nanofluids, showing that under increasing strain, the samples behaved as viscoelastic solids. The crossover point for the 26 %w/w sample was at a strain of approximately 5 %, which was significantly above that expected for an electrostatically stabilised sample. This suggests the linear viscoelastic region of the sample was due to the caging of the SH-SiNPs in solution at low strain. The yield stress in the sample in this case can be interpreted as the required force to cause the interparticle structure to fail [229].

If the particles existed as primary particles in solution, at these concentrations they would not be caged by their neighbouring particles, however, the formation of agglomerates in solution increases the effective volume fraction of the particles (recalling Equation 1.10). These agglomerates are present in solution above a critical volume fraction that effectively cages them between their neighbours, which results in the network structure. The yield stress in this case can be interpreted as the critical stress required to disrupt this network structure, and enable the agglomerates to flow. As the strain increases, the sample agglomerates are broken into smaller groups, allowing them to flow more easily, resulting in the shear thinning behaviour observed, and leading the sample to behave as a viscous liquid.
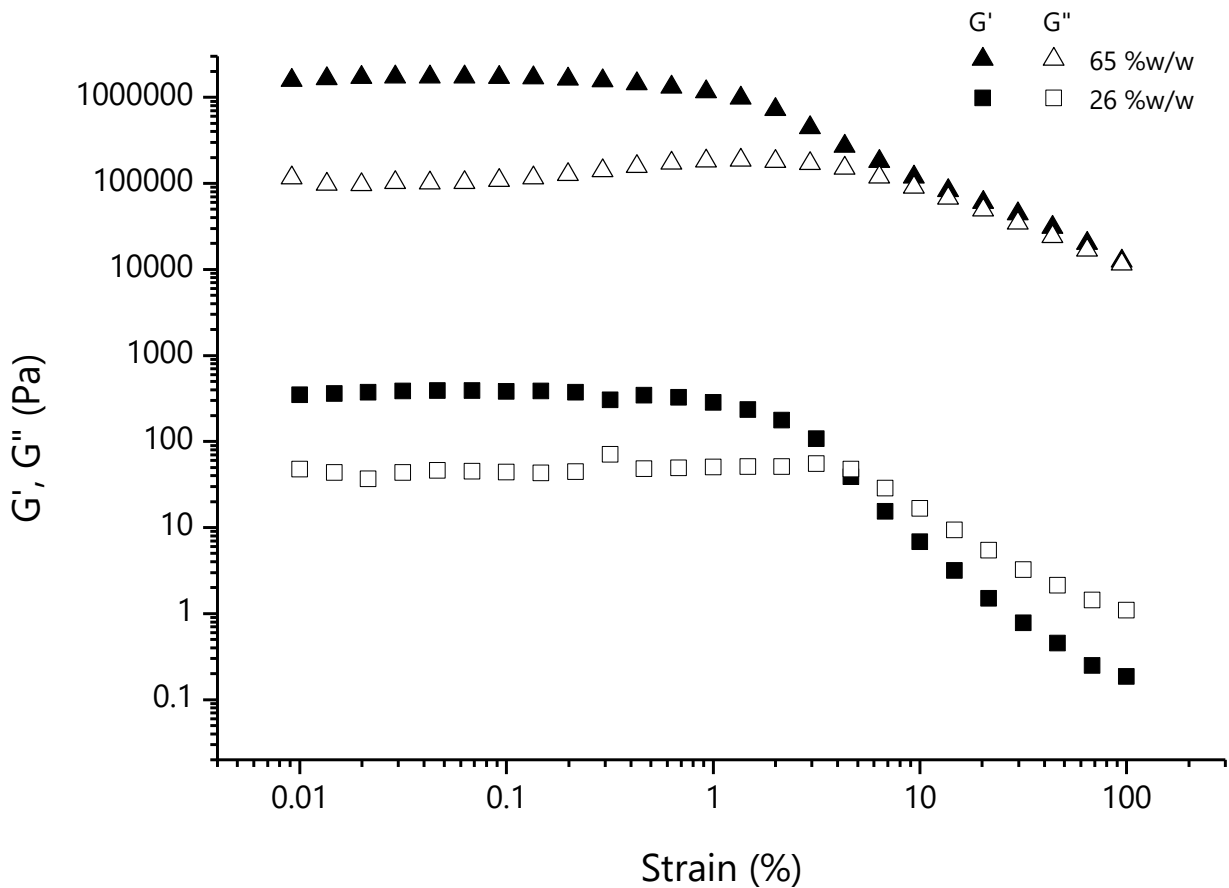
Figure 6.5: Storage and loss moduli measured under increasing strain, of high concentration SH-SiNP nanofluids

6.4 Nanofluids prepared from particles with different surface chemistry

The fluids produced from these particles showed significant shear thinning character due to the breakdown of large agglomerates. Despite their theoretically greater affinity for water than either the Br-SiNPs or the U-SiNPs, solutions of OH-SiNPs showed significant immediate aggregation even at low concentrations, similar to the non-polar analogues, as was noted in Table 6.1.

Figure 6.6 shows viscosity a rheogram obtained for a nanofluid prepared from U-SiNPs at a concentration of 2 %w/w. The nanofluid showed shear thinning behaviour, transitioning at about 1000 s^{-1} to a Newtonian plateau. A zero-shear viscosity plateau was not visible in the measured range, and for the Cross model this value was set as $\eta_0 = 10000\eta_\infty$. Higher concentration solutions of OH-, Br- and U-SiNPs could not be produced, forming inhomogeneous solutions with large visible agglomerates.
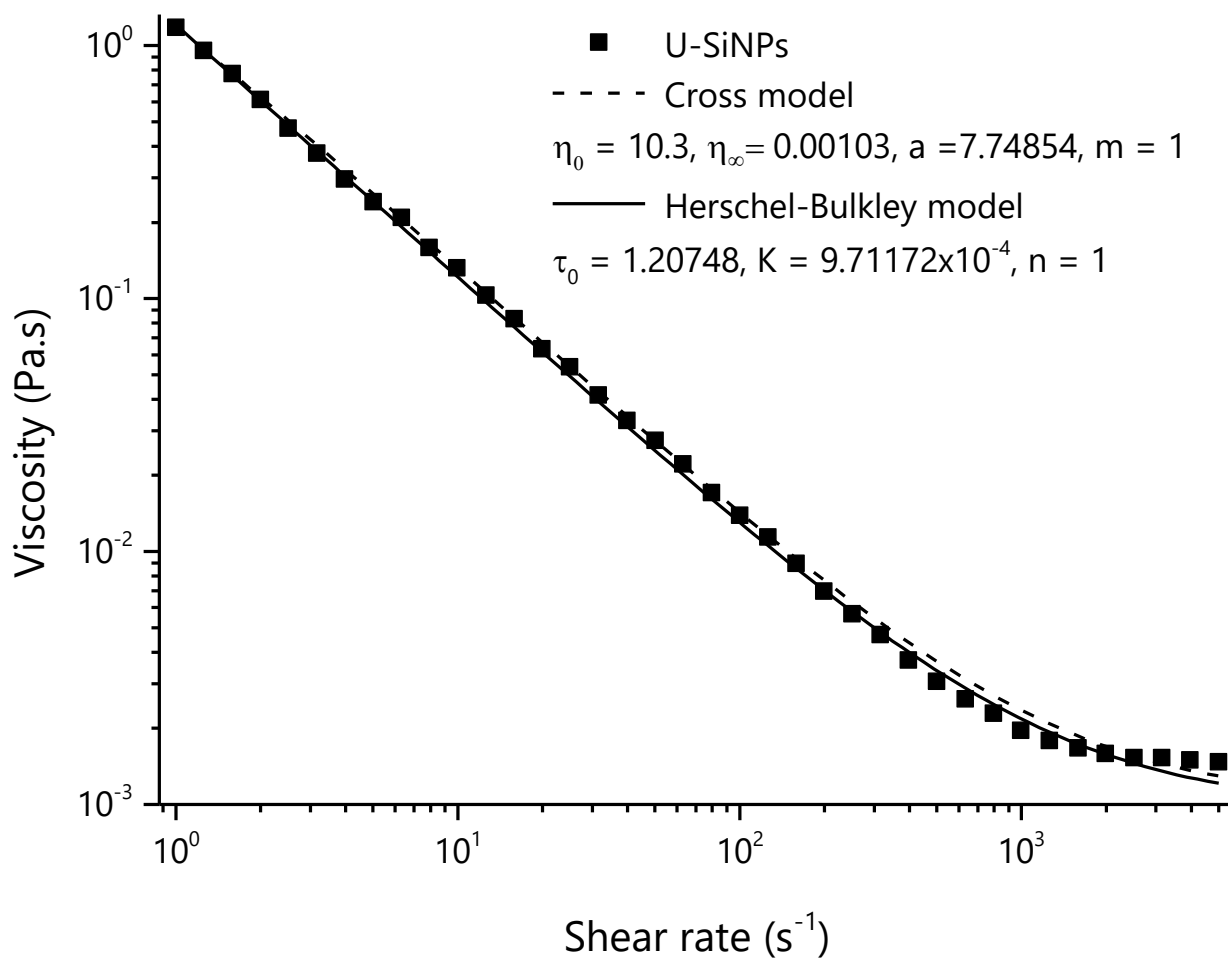
Figure 6.6: Rheogram of U-SiNPs at 2 %w/w in solution. Lines are Cross model and Herschel-Bulkley model of rheological profiles.

For these samples, it would be expected that the shear thinning behaviour occured due to the breakdown of the agglomerate structures in solution by the application of shear force. The agglomerate structures broke down into smaller units that were less massive, and thus more capable of moving in the direction of flow, producing less resistance in solution. This manifested as a lower viscosity. The infinite-shear viscosity plateau in this case represented the breakdown of the agglomerated in solution has producing units that can flow smoothly with the applied force. When the shear force was ceased, the nanoparticles remained as large, visible agglomerates in solution. This agreed with the observation that the particles were unable to be physically dispersed in solution with any degree of stability.

6.5 Rheological and solution properties of nanofluids prepared from charged particles
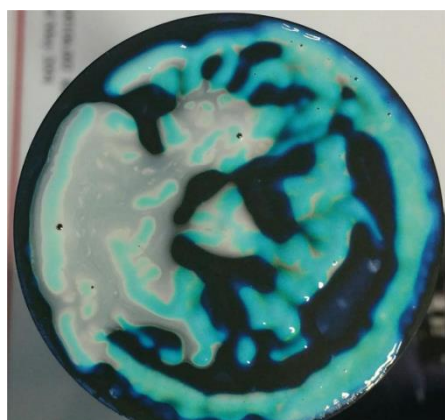
Figure 6.7: StS-SiNP solution on rheometer plate geometry, hazy section due to additional water added
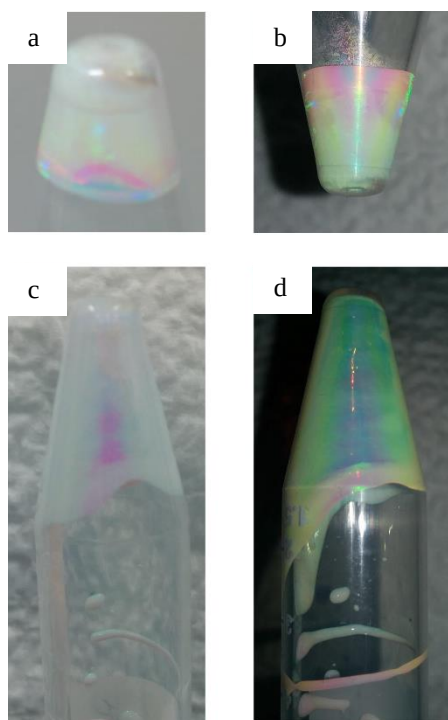
Figure 6.8: Pellets of StS-SiNPs obtained from centrifugation a) under ambient light without agitation, b) under directed light with agitation, c) under ambient light after agitation, d) under directed light after agitation

Samples of StS-SiNPs showed the blue colouration characteristic of light scattering at low concentrations. As the concentration of the solutions increased they became white and opaque, but blue when thin layers of them were formed. The colouration remained present after shearing (Figure 6.7). This behaviour reflected that observed for concentrated dispersions of charge-stabilised latex [230]. Monodisperse latexes have been found to show this type of light scattering, attributed to Bragg reflection of light, based on the ordering of particles into planes [231]. This light scattering confirmed the monodispersity of the samples visually, as polydisperse samples would be incapable of forming the ordered structure necessary to scatter light in this manner, further it indicated there was no significant flocculation or agglomeration in solution, which would serve to disrupt this order and prevent the iridescence from occurring [231].
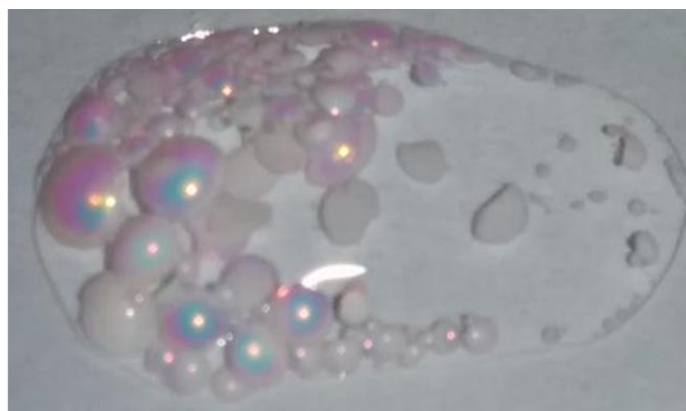
Figure 6.9: Concentrated pellets of StS-SiNPs dropped onto glass slide, with MiliQ water dropped over sample under directed illumination.

At high concentrations, samples were white and opaque, with opalescent colour (Figure 6.8). The highly concentrated pellet solution could be manipulated by pipette, and poured, retaining the colouration during flow and when left at rest. Under directed light, more blue and green colouration was evident. Unlike the lower concentration solutions, when additional water was placed on the pellet, the particles did not immediately disperse or form a more dilute solution (Figure 6.9). This was potentially due to the increased density and viscosity of the pellets resulting in a stratified solution. The samples did not show signs of mixing, indicated by haziness or white colouration of the additional water before the sample dried.
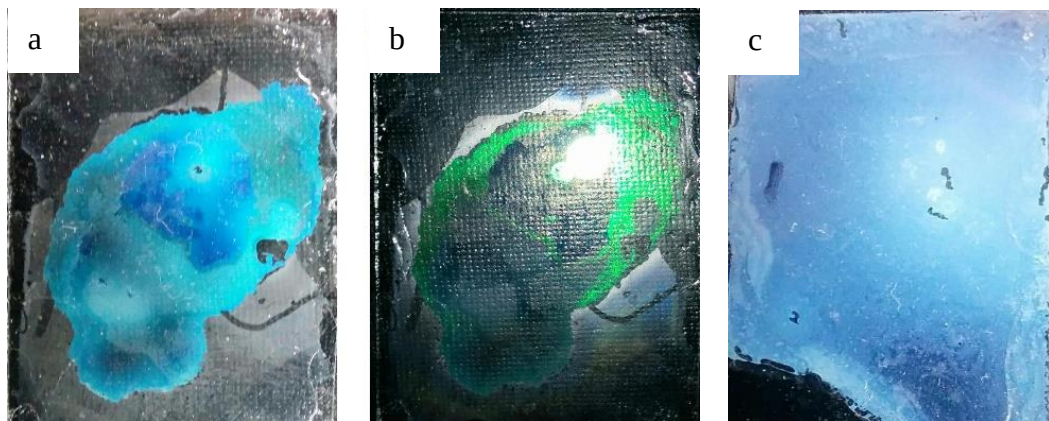
Figure 6.10: Thin film of StS-SiNP nanofluid droplets pressed between glass slides. Sealed with superglue under a) ambient light, and b) directed light. c) Sample of StS-SiNPs dropped and pressed between two glass slides and sealed with superglue after drying.

A thin film of the nanofluid showed an intense blue colouration under ambient light conditions, and green opalescence under directed light (Figure 6.10). The intense colouration was noted to disappear as the particle dried, becoming white with minimal blue colouration. As the underlying silica nanoparticles are white, the colouration of the final dried product will remain milky-white with only pale colouration. Other studies have concluded that the addition of black particles, such as carbon black, can reduce the light scattering and result in more intense colours when dried, however, this was not investigated. This structural colour is characteristic of opals [83, 84], which have a similar structure, made of regular, ordered silica micro- or nanoparticles. Synthetic opals have been prepared from various nanoparticles previously, including silica [84, 86, 183] and polymer spheres [87, 232]. Thin films can be prepared and a great deal of work is now being undertaken on using nanoparticle samples to generate coloured surfaces and objects [233]. These nanoparticles would be suitable as a medium for generating structural colour in these methods.
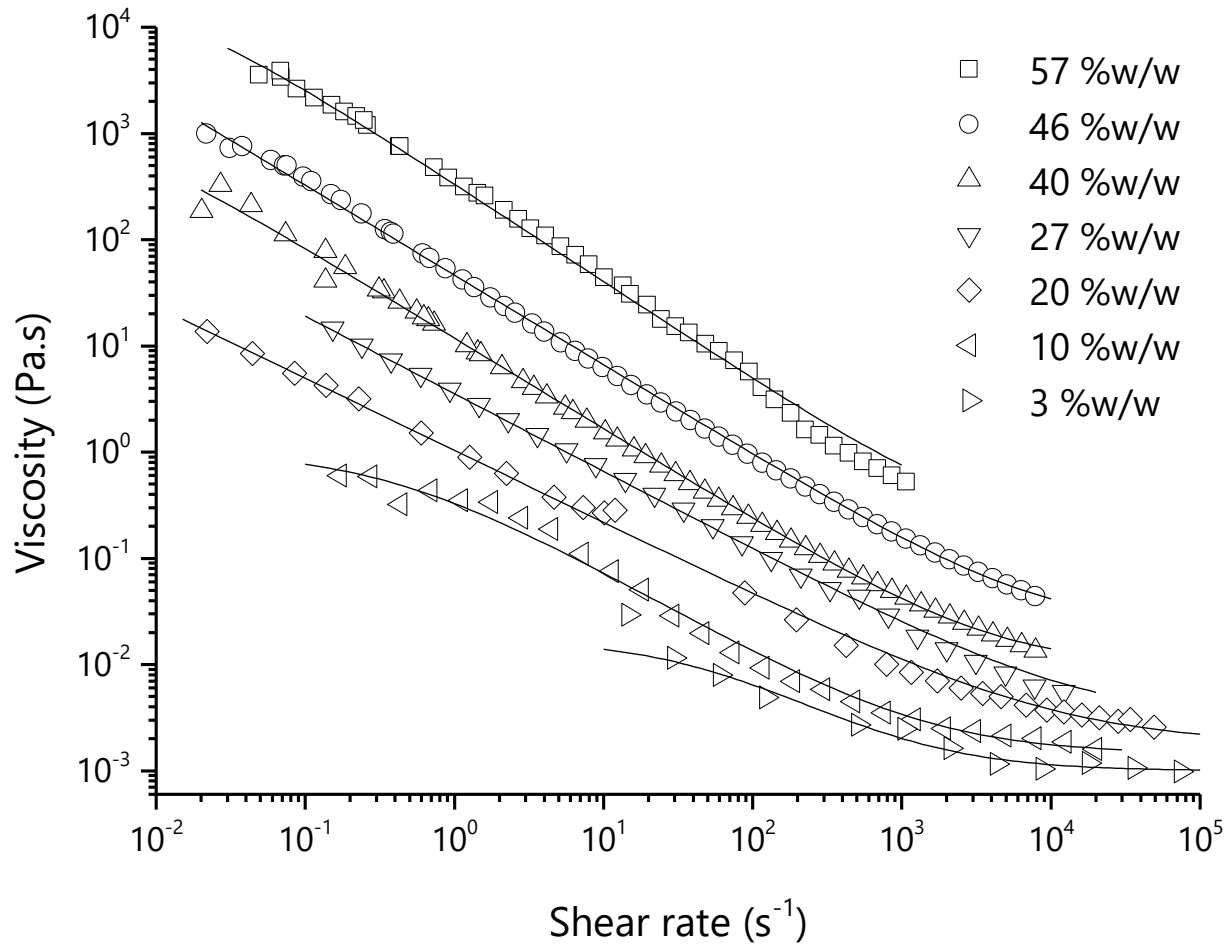
Figure 6.11: Rheological profiles of StS-SiNPs at specified weight concentrations in solution. Lines are Cross models of rheological profiles.

Table 6.7: Parameters of Cross models applied to rheological profiles of StS-SiNP based nanofluids, with values of apparent yield stress determined from each model

Concentration (%w/w)	η_∞ (Pa.s)	η_0 (Pa.s)	α_c (s)	m	τ^* (Pa)
57	0.08397	10357.80179	33.72665	0.93202	310
46	0.03021	5738.59248	234.22813	0.87264	24
40	0.01014	1599.65198	288.90561	0.86263	5.5
27	0.00357	54.74164	27.47561	0.7766	2.0
20	0.0023	32.44247	87.74811	0.7345	0.37
10	0.00145	1.03145	2.62779	0.7964	0.39
3	9.03551×10^{-4}	0.09113	0.73711	0.6566	0.12

The rheological profiles of StS-SiNPs (Figure 6.11) showed some similarities to the nanofluids prepared from SH-SiNPs. The apparent viscosities measured for the StS-SiNPs were lower at lower concentrations compared to similar concentration SH-SiNP nanofluids. However, the samples of 40-57 %w/w showed comparable viscosity values to the higher concentration solutions of SH-SiNPs. It was noted, however, that the StS-SiNPs remained able to flow until 46 %w/w, only forming a paste at 57 %w/w. This contrasted with the SH-SiNPs that formed pastes above 20 %w/w.

Cross models (Table 6.7) were found to show good agreement with the data measured for the nanofluids, apart from the 57 %w/w sample, which was better fit by a power-law function. Lower concentrations (3-10 %w/w) of the StS-SiNPs showed an initial plateau value of viscosity at low shear, followed by shear thinning as the shear rate increased.

Samples from 20-57 %w/w showed increasing flow indices with increasing concentration, however, did not reach one, as was the case for the SH-SiNP nanofluids. The two lowest concentrations, 3 and 10 %w/w showed higher flow indices than would be expected by this trend, however, the overall degree of shear thinning of these samples was significantly less, rendering fitting the four-parameter Cross equation more difficult. The increase in the flow index with increasing concentration could have been indicative of increasing shear-thinning character of the sample.

The infinite shear viscosity was compared against the volume fraction, and curve fit using Equation 1.11, Equation 1.12, and Equation 1.13. Critical volume fractions for these samples were determined to be 0.32, 0.38 and 0.35 respectively. Incorporating Equation 1.7 into the curves, and taking the critical volume fraction as 0.74, the effective particle diameters were estimated, found as 192.0, 193.9 and 190.4 nm respectively, which compare favourably with the value determined for the particles at infinite dilution, by DLS, of 192.2 nm.

Shear-thinning onset occured at a lower shear rate than was measured for all samples above 10 %w/w. The apparent yield stresses calculated from the Cross models increased with increasing concentration, remaining lower than similar yield stresses found for the SH-SiNPs at the same concentration. This suggested that any internal structure formed was more easily broken apart by the shear forces in solution, allowing the samples to flow, reflected by the observation that the samples remained able to flow without agitation until high volume fractions.
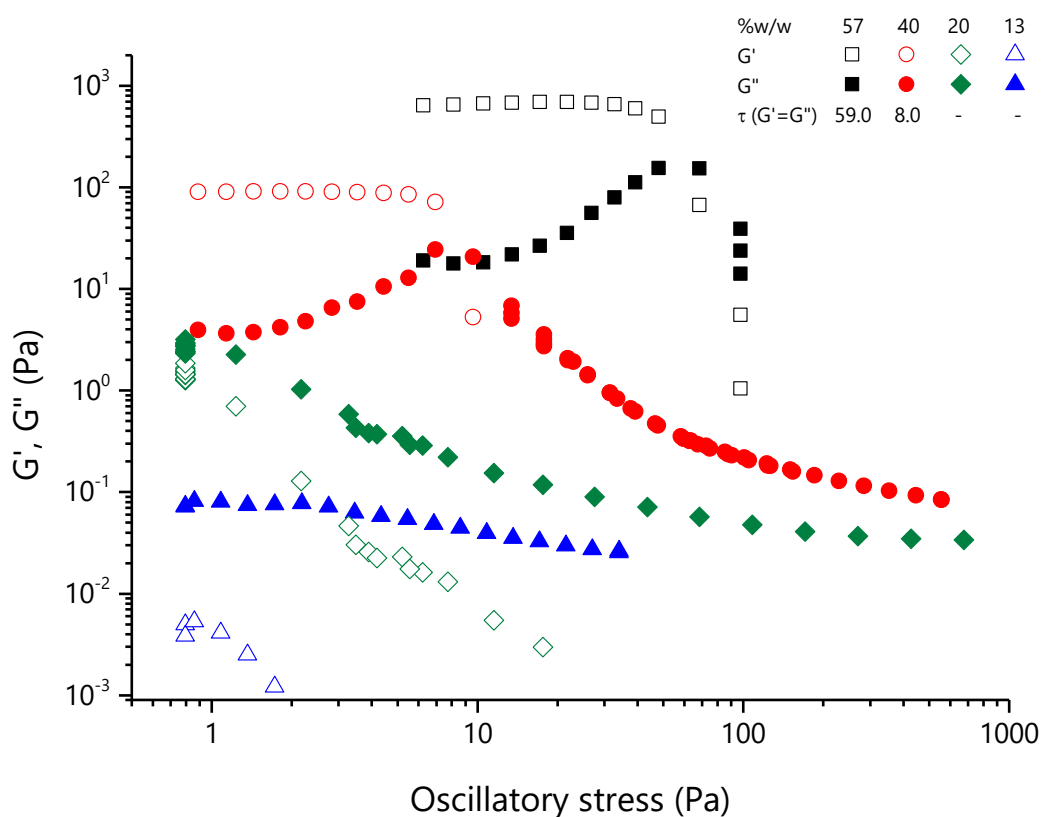
Figure 6.12: Oscillatory stress sweep plot showing storage and loss moduli of StS-SiNP nanofluids of specified concentration. Crossover points are identified by the stress value at which in the legend

StS-SiNP nanofluid viscoelastic properties were further characterised by dynamic oscillatory stress measurements (Figure 6.12). Lower concentration nanofluids did not show a yield point within the measured range, with G' > G" at all stresses measured. This suggested these solutions behave as a viscoelastic liquid.

Higher concentration samples behaved as a viscoelastic solid, with the linear viscoelastic region moving to higher oscillatory stress values with increasing concentration. The crossover points similarly increased with increasing concentration.

At low concentrations, the StS-SiNPs showed similar flow profiles under both increasing and decreasing shear rates. At 32 %w/w, a hysteresis in the flow rheogram was observed (Figure 6.13). Under decreasing shear, the flow plot was found to shift towards higher shear stresses. Higher stress values under decreasing shear indicated that the restructuring of the fluid occurs at a faster rate when a shear rate was applied, compared to when no force at all was applied. This suggested that at higher concentrations the StS-SiNP nanofluids exhibited rheopexy.
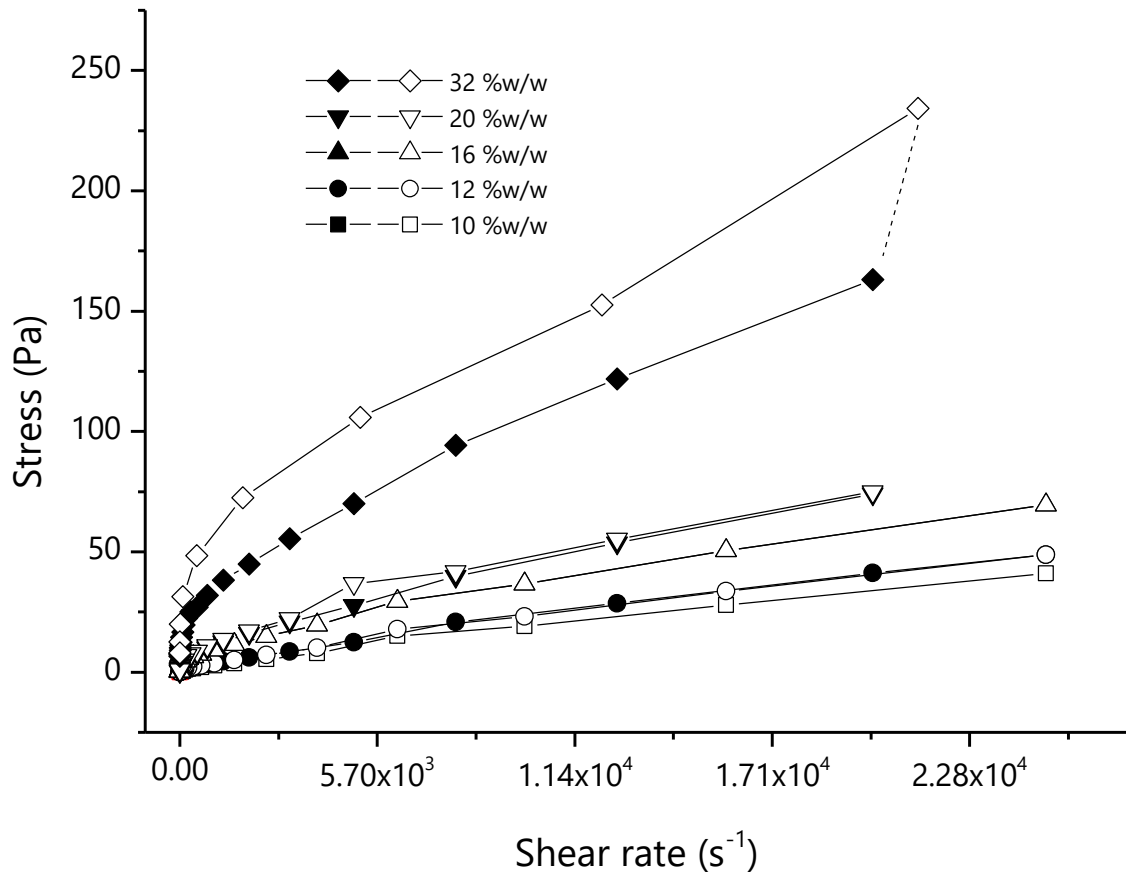
Figure 6.13: Stress vs shear rate for nanofluids prepared from StS-SiNPs at specified weight fraction, black points indicate increasing shear rate, white points indicate decreasing shear rate.

Collating the flow parameters for each of the nanofluids prepared and plotting them against the volume fraction of the nanoparticles, as displayed in Figure 6.14, a number of specific behaviours were observed, reflective of the behaviour of the particles when dispersed. For the poorly water-dispersible particles a high flow index was found, indicating shear thinning behaviour was observed even at low concentrations. The SH-SiNPs showed a small decrease in the flow index as the concentration increased, however, this decrease was small and likely due to the difficulty in fitting the curves to the sample. The high flow indices for these samples were reflective of the shear thinning occurring due to the breakdown of agglomerate structures in solution, enabling easier flow as the units broke down. The flow indices remained high

147

across the concentration range as the interparticle forces causing the aggregation were not highly concentration dependent.

The COOH-SiNPs showed a different behaviour based on the pH of the sample, at high pH the flow index remained at zero (or effectively zero due to the difficulty in fitting a Cross model to a Newtonian section of a rheogram). At pH 5.8 the sample showed an increase in flow index at higher volume fractions, while at pH 4 the samples showed a high flow index at low volume fraction. This was reflective of the increased stabilisation of the particles with increasing pH, the lower particles showed a lesser degree of interparticle repulsion and were more prone to aggregation. The highly repulsive particles at pH 13 existed primarily as individual particles and do not show significant agglomerate breakdown, which would result in shear thinning effects.

The TEOS-SiNPs showed a flow index of zero until a critical concentration at approximately $\phi = 0.18$, at which point the flow index increased, remaining at about 0.6. The LUDOX AS40 nanofluids showed a slight increase in flow index with concentration, below this value the shear thinning section of the rheological profile was not sufficiently within the range of the viscosity rheogram to provide an accurate estimate. However, at low concentration the value for the flow parameter effectively became zero, suggesting a behaviour similar to that observed for the TEOS-SiNPs in which a critical concentration occured, resulting in a sharp increase in flow curve. This critical concentration was determined by the effective particle diameter in solution, which acts to increase the volume fraction of the particles, causing them to become caged at lower concentrations than would be expected from hard spheres.

Flow indices of StS-SiNP nanofluids showed a generally increasing trend as volume fraction increased, however the flow index remains relatively high at all volume fractions studied. This suggests for these that an interparticle ordering was formed, which was further suggested by the apparent colouration of the particles. It was capable of forming even at low volume fractions due to the relatively long range of the electrostatic interactions of the particles. The flow indices increased with increasing concentration due to the increasing strength of this interparticle interaction. The repulsion between particles became more pronounced as the interparticle spacing reduced, due to the increased volume fraction. Breakage of this ordering was associated with the shear thinning character modelled of the samples.
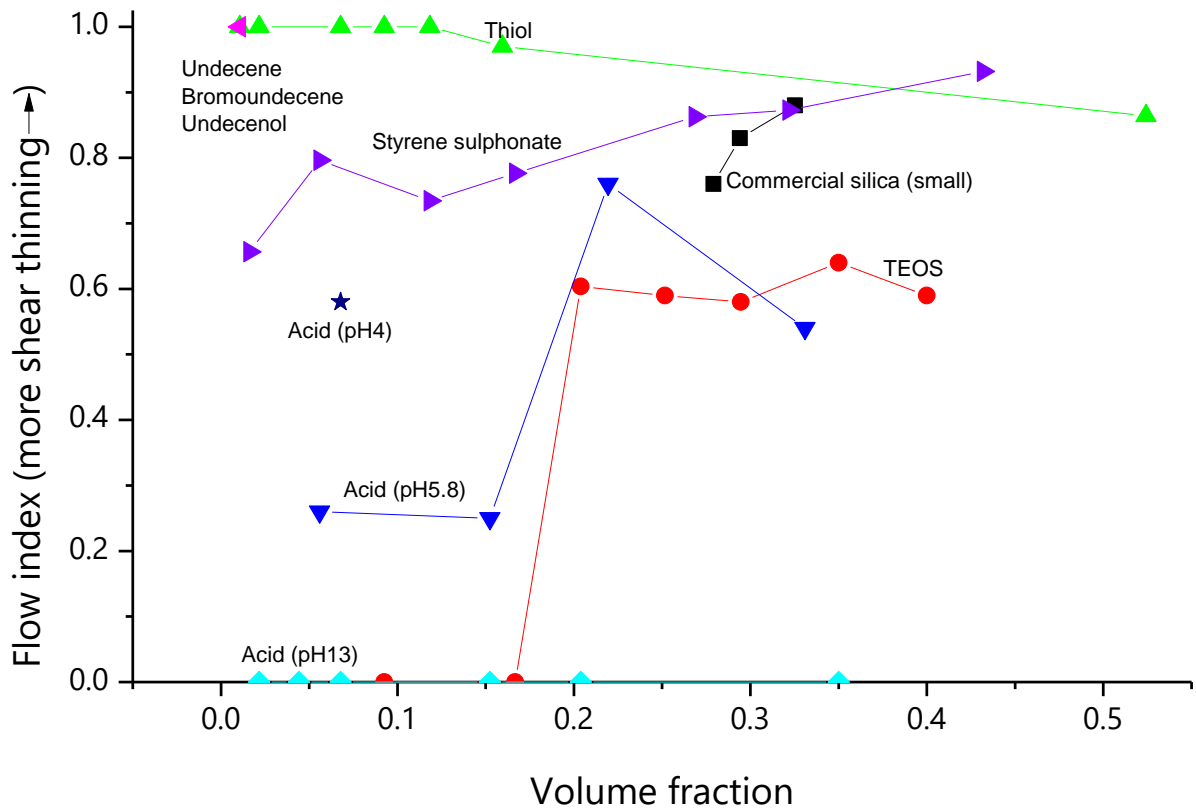
Figure 6.14: Flow indices of nanofluids prepared from different terminal functional groups, as modelled by the Cross equation, against volume fraction of nanoparticles. ■LUDOX AS40 ●TEOS-SiNPs ▲ SH-SiNPs ▶ StS-SiNPs ★COOH-SiNPs (pH 4) ▼ COOH-SiNPs (pH 5.8) ◆COOH-SiNPs (pH 13) ◀ U-SiNPs, Br-SiNPs, OH-SiNPs

6.6 Conclusions

SH-SiNPs were poorly dispersible in water, only capable of forming low concentration dispersions that exhibited shear thinning behaviour even as low as 2 %w/w. High concentration samples formed pastes. All concentration samples, when modelled by the Cross equation showed flow indices approaching one, indicating shear thinning behaviour, in contrast to the previously measured AS40 and TEOS-SiNP nanofluids. The effective yield stress calculated, indicated that at volume fractions greater than 0.18 the SH-SiNPs formed a network like structure from caged particle agglomerates, which was capable of being broken apart under shear force. High concentration solutions were white in colour, suggesting uniform light scattering, characteristic of large agglomerates.

Functionalisation of SH-SiNPs with undecenol, bromoundecene or undecene formed samples that were not readily dispersible in water, resulting in large agglomerates regardless of the concentration. DLS analysis of these samples indicated the formation of large, polydisperse

agglomerates in solution compared to the primary particle diameter, resulting in solutions that showed significant shear thinning behaviour even at low concentrations. High concentration solutions were unable to be produced.

StS-SiNPs could be formed into high concentration solutions without significant agglomeration or sedimentation. The DLS measurements of these particles showed significant solution stability, with effective solution diameters indicating individual charge-stabilised particles as the primary component of the solution, compared to large aggregates. Solutions produced displayed rheological profiles able to be represented by the Cross model of non-Newtonian behaviour. The StS-SiNPs behaved more similarly to the AS40 nanofluids that used a stabilising agent, compared to the SH-SiNPs from which they were made. Higher concentration samples also showed the solution structural colouration of a charged latex.

High concentration solutions showed behaviour characteristic of a viscoelastic solid, which suggested a microstructure existed in solution, with a critical concentration determined at a volume fraction of 0.38. Above this volume fraction an apparent yield stress developed, calculated from the Cross model parameters fit to the viscosity profiles. The disruption of this microstructure by a critical shear stress was the onset of flow in the sample, and the cause of the shear thinning behaviour, rather than the breakage of agglomerate structures such as in the dispersions of SH-SiNPs. Shear rate-shear stress plots of StS-SiNP nanofluids showed hysteresis, which could be accounted for by a rheopectic effect, where the shear force assisted in the rebuilding of the dispersion microstructure.

7 Conclusions and future directions

7.1 Conclusions

Improvements to the scale and quantity of particles producible by single-silane precursor synthesis of SH-SiNPs were made, allowing multi-litre scale particle syntheses to be conducted, with improved particle uniformity. Particle specific surface area was determined by BET surface area measurement to be 39.0±0.7 m$^2 \cdot$g^{-1} for 84 nm diameter particles. The particles were confirmed by these measurements to be non-porous. By incorporating the particle distribution, determined from SEM measurement of the particles, in the calculation of the specific surface area the surface area was calculable directly as 38.6 nm$^2 \cdot$g^{-1}, within the range measured by BET.

Geometric calculations of the particle surfaces produced an estimate of 6.25 groups$\cdot$nm^{-2} of surface functionality, and high attachment densities of 5.4-13.7 groups$\cdot$nm^{-2} were found for undec-10-enoic acid, undecenol and bromoundecene attachments. Through analysis of dTGA data additional insight into the degradation of modified and unmodified SH-SiNPs was provided, and shown to be dependent in part on particle diameter. A modified calibration method for ATR-FTIR data analysis was proposed that was independent of particle diameter.

After functionalisation, the effect of pH was investigated on dispersions of COOH-SiNPs, with particular attention to the effect of pH on the aggregation state. Excellent dispersion stability was found when the pH of the dispersion was sufficient to deprotonate the acid functional groups, and the particle concentration of the solution was increased up to 49 %w/w with only minor non-Newtonian behaviour evident. Lowering the pH was found to increase the agglomerate diameter in solution. The concentration at which non-Newtonian behaviour was evident lowered with lowering pH. Sonication could break down the agglomerates temporarily, however, at neutral to acidic pH the agglomerate structure was recovered quickly.

Br-SiNPs, U-SiNPs and OH-SiNPs were found to show similar, poorly water-dispersible behaviour, showing shear-thinning character at all concentrations tested. Unfunctionalised SH-SiNPs were also poorly dispersible in solution, giving severe shear thinning effects at all concentrations. For SH-SiNPs a critical volume fraction of particles being determined as $\phi = 0.18$, indicative of poor dispersion in solution.

It was found that StS-SiNPs could be made into high concentration solutions without visibly aggregating or precipitating out of solution, behaving similarly to AS40 nanofluids. Significant shear thinning effects were found, with the degree of shear thinning increasing with increasing

concentration, as determined from Cross models fitted to the obtained profiles. These solutions also showed significant light scattering effects, with opalescent colouration evident. High concentration solutions of StS-SiNPs showed viscoelastic solid behaviour, which indicated the existence of a microstructure in solution. Shear rate-shear stress plots suggested there was a thixotropic hysteresis assisting the rebuilding a dispersion microstructure.

7.2 Future directions

Synthesis of 3-MPTMS particles follows a similar method to TEOS-SiNPs; however, the reaction time for the synthesis is longer, on the order of days compared with minutes. Development of the method to enable faster particle production would be useful for increasing the throughput of the functionalised particles. Monitoring the particle growth with real-time DLS and zeta potential measurements would provide valuable information into the growth mechanism of the SH-SiNPs, and how it differs from the much-studied TEOS-SiNPs.

Analysis of the particles via the TGA-dTGA comparison method could be expanded by introducing additional characterisation during the degradation. By connecting the output of the TGA to a FTIR spectrophotometer gas phase flow cell, real time measurement of the chemical identity of the species lost from TGA could be undertaken.

StS-SiNPs show colouration in sample, which retains the colouration before and after shearing. Investigating the dispersion structure with simultaneous small-angle X-ray scattering and rheology at an appropriate beamline setup, would provide insight into the microstructure of the solutions as well as providing real-time data on the possible thixotropic reformation of the microstructure, and would be an interesting extension to the work presented here.

The stability of the StS-SiNPs and their opalescent colour under aqueous conditions, suggests their potential future application in generation of structural coloured surfaces and objects, such as fabrics. Deposition of thin films of the StS-SiNPs onto flexible surfaces and fibres could be investigated as an inexpensive, simple means of producing opalescent materials with an underlying support structures with desirable mechanical properties. Further work in surface modification of the SiNPs also provides an avenue for further research, high concentration values are obtainable with a variety of functional groups, and significant changes to the particle properties are evident with the functional groups presented in this work. The COOH-SiNPs, owing to their ability to redisperse with minimal agitation under high pH conditions, can be investigated for their long-term storage use. One critical problem with large-scale nanoparticle

production is the strength of the association between particles when aggregated during drying. This is often overcome through the usage of strong sonication with the addition of dispersing agents; however, the COOH-SiNPs are able to overcome this. Continuing this, the addition of functional groups with switchable properties based on pH, light or another trigger would be of interest to particle properties, particularly those in which the switch results in a conformal change to the moiety structure, and how this responds to high surface functional density.

8   References

1. Nguyen, C., et al., *Temperature and particle-size dependent viscosity data for water-based nanofluids–hysteresis phenomenon.* International Journal of Heat and Fluid Flow, 2007. **28**(6): p. 1492-1506.
2. Lu, K. and C. Kessler, *Colloidal dispersion and rheology study of nanoparticles.* Journal of Materials Science, 2006. **41**(17): p. 5613-5618.
3. Koca, H.D., et al., *Effect of particle size on the viscosity of nanofluids: A review.* Renewable and Sustainable Energy Reviews, 2017.
4. Buongiorno, J., et al., *A benchmark study on the thermal conductivity of nanofluids.* Journal of Applied Physics, 2009. **106**(9).
5. Murshed, S.M.S., K.C. Leong, and C. Yang, *Enhanced thermal conductivity of TiO₂ -water based nanofluids.* International Journal of Thermal Sciences, 2005. **44**(4): p. 367-373.
6. Wang, J.J., et al., *Heat conduction mechanisms in nanofluids and suspensions.* Nano Today, 2012. **7**(2): p. 124-136.
7. Ponmani, S., et al., *Formation and characterization of thermal and electrical properties of CuO and ZnO nanofluids in xanthan gum.* Colloids and Surfaces a-Physicochemical and Engineering Aspects, 2014. **443**: p. 37-43.
8. Taylor, R., et al., *Small particles, big impacts: A review of the diverse applications of nanofluids.* Journal of Applied Physics, 2013. **113**(1).
9. Herranz, T., et al., *Reactivity of Au nanoparticles supported over SiO₂ and TiO₂ studied by ambient pressure photoelectron spectroscopy.* Catalysis Today, 2009. **143**(1-2): p. 158-166.
10. Lopez, N. and J.K. Norskov, *Catalytic CO oxidation by a gold nanoparticle: a density functional study.* J Am Chem Soc, 2002. **124**(38): p. 11262-3.
11. Narayanan, R. and M.A. El-Sayed, *Shape-dependent catalytic activity of platinum nanoparticles in colloidal solution.* Nano Letters, 2004. **4**(7): p. 1343-1348.
12. Panigrahi, S., et al., *Synthesis and size-selective catalysis by supported gold nanoparticles: Study on heterogeneous and homogeneous catalytic process.* Journal of Physical Chemistry C, 2007. **111**(12): p. 4596-4605.
13. Eustis, S. and M.A. El-Sayed, *Why gold nanoparticles are more precious than pretty gold: noble metal surface plasmon resonance and its enhancement of the radiative and nonradiative properties of nanocrystals of different shapes.* Chemical society reviews, 2006. **35**(3): p. 209-217.
14. Ansar, S.M., S. Chakraborty, and C.L. Kitchens, *pH-Responsive mercaptoundecanoic acid functionalized gold nanoparticles and applications in catalysis.* Nanomaterials, 2018. **8**(5): p. 339.
15. Tokonami, S., et al., *Novel synthesis, structure, and oxidation catalysis of Ag/Au bimetallic nanoparticles.* Journal of Physical Chemistry C, 2010. **114**(23): p. 10336-10341.
16. Haruta, M., *Size- and support-dependency in the catalysis of gold.* Catalysis Today, 1997. **36**(1): p. 153-166.
17. Vert, M., et al., *Terminology for biorelated polymers and applications (IUPAC Recommendations 2012).* Pure and Applied Chemistry, 2012. **84**(2): p. 377-410.
18. Klaessig, F., M. Marrapese, and S. Abe, *Current perspectives in nanotechnology terminology and nomenclature,* in *Nanotechnology Standards.* 2011, Springer. p. 21-52.

19.   Shin, D.H. and D. Banerjee, *Enhanced specific heat of silica nanofluid.* Journal of Heat Transfer-Transactions of the Asme, 2011. **133**(2).

20.   Chung, S.J., et al., *Characterization of ZnO nanoparticle suspension in water: Effectiveness of ultrasonic dispersion.* Powder Technology, 2009. **194**(1-2): p. 75-80.

21.   Jesumathy, S., M. Udayakumar, and S. Suresh, *Experimental study of enhanced heat transfer by addition of CuO nanoparticle.* Heat and Mass Transfer, 2012. **48**(6): p. 965-978.

22.   Barbes, B., et al., *Thermal conductivity and specific heat capacity measurements of Al_2O_3 nanofluids.* Journal of Thermal Analysis and Calorimetry, 2013. **111**(2): p. 1615-1625.

23.   Yu, W., et al., *Heat transfer to a silicon carbide/water nanofluid.* International Journal of Heat and Mass Transfer, 2009. **52**(15-16): p. 3606-3612.

24.   Yu, W., et al., *Experimental investigation on thermal conductivity and viscosity of aluminum nitride nanofluid.* Particuology, 2011. **9**(2): p. 187-191.

25.   Hu, P., et al., *Thermal Conductivity of AlN-Ethanol Nanofluids.* International Journal of Thermophysics, 2008. **29**(6): p. 1968-1973.

26.   Sidik, N.A.C., M.N.A.W.M. Yazid, and S. Samion, *A review on the use of carbon nanotubes nanofluid for energy harvesting system.* International Journal of Heat and Mass Transfer, 2017. **111**: p. 782-794.

27.   Li, S.B., et al., *Effect of surface modification and medium on the rheological properties of silica nanoparticle suspensions.* Ceramics International, 2016. **42**(6): p. 7767-7773.

28.   Hotta, Y., et al., *Effect of oligosaccharide alcohol addition to alumina slurry and translucent alumina produced by slip casting.* Journal of the American Ceramic Society, 2003. **86**(5): p. 755-760.

29.   Kadosh, T., et al., *In situ characterization of spinel nanoceramic suspensions.* Journal of the American Ceramic Society, 2012. **95**(10): p. 3103-3108.

30.   Żyła, G., M. Cholewa, and A. Witek, *Dependence of viscosity of suspensions of ceramic nanopowders in ethyl alcohol on concentration and temperature.* Nanoscale research letters, 2012. **7**(1): p. 412.

31.   Trisaksri, V. and S. Wongwises, *Critical review of heat transfer characteristics of nanofluids.* Renewable and Sustainable Energy Reviews, 2007. **11**(3): p. 512-523.

32.   Wang, X. and A. Mujumdar, *Heat transfer characteristics of nanofluids: a review.* J Therm Sci, 2007. **46**: p. 1 - 19.

33.   Choi, S. and J. Eastman, *Enhancing thermal conductivity of fluids with nanoparticles.* ASME-Publications-Fed, 1995. **231**: p. 99-106.

34.   Kakac, S. and A. Pramuanjaroenkij, *Review of convective heat transfer enhancement with nanofluids.* International Journal of Heat and Mass Transfer, 2009. **52**(13-14): p. 3187-3196.

35.   Wu, J.M. and J.Y. Zhao, *A review of nanofluid heat transfer and critical heat flux enhancement-Research gap to engineering application.* Progress in Nuclear Energy, 2013. **66**: p. 13-24.

36.   Wen, D.S., et al., *Review of nanofluids for heat transfer applications.* Particuology, 2009. **7**(2): p. 141-150.

37.   Xie, H., et al., *Thermal conductivity of suspensions containing nanosized SiC particles.* International Journal of Thermophysics, 2002. **23**(2): p. 571-580.

38.   Li, F.C., et al., *Experimental study on the characteristics of thermal conductivity and shear viscosity of viscoelastic-fluid-based nanofluids containing multiwalled carbon nanotubes.* Thermochimica Acta, 2013. **556**: p. 47-53.

39.   Wu, S.Y., et al., *Thermal energy storage behavior of Al_2O_3-H_2O nanofluids.* Thermochimica Acta, 2009. **483**(1-2): p. 73-77.

40.   Starace, A.K., et al., *Nanofluid heat capacities.* Journal of Applied Physics, 2011. **110**(12).

41.   Putnam, S.A., et al., *Thermal conductivity of nanoparticle suspensions.* Journal of Applied Physics, 2006. **99**(8): p. -.

42.   Patel, H.E., et al., *Thermal conductivities of naked and monolayer protected metal nanoparticle based nanofluids: Manifestation of anomalous enhancement and chemical effects.* Applied Physics Letters, 2003. **83**(14): p. 2931-2933.

43.   Nguyen, C.T., et al., *Heat transfer enhancement using Al₂O₃-water nanofluid for an electronic liquid cooling system.* Applied Thermal Engineering, 2007. **27**(8-9): p. 1501-1506.

44.   Wang, X.W., X.F. Xu, and S.U.S. Choi, *Thermal conductivity of nanoparticle-fluid mixture.* Journal of Thermophysics and Heat Transfer, 1999. **13**(4): p. 474-480.

45.   Sridhara, V. and L.N. Satapathy, *Al₂O₃-based nanofluids: a review.* Nanoscale Res Lett, 2011. **6**(1): p. 456.

46.   Xie, H.Q., et al., *Thermal conductivity enhancement of suspensions containing nanosized alumina particles.* Journal of Applied Physics, 2002. **91**(7): p. 4568-4572.

47.   Duangthongsuk, W. and S. Wongwises, *Measurement of temperature-dependent thermal conductivity and viscosity of TiO₂ -water nanofluids.* Exp Therm Fluid Sci, 2009. **33**(4): p. 706 - 714.

48.   Hakim, L.F., et al., *Nanoparticle coating for advanced optical, mechanical and rheological properties.* Advanced Functional Materials, 2007. **17**(16): p. 3175-3181.

49.   Mahbubul, I.M., et al., *Rheological behavior of Al₂O₃/R141b nanorefrigerant.* International Journal of Heat and Mass Transfer, 2014. **73**(0): p. 118-123.

50.   Lyckfeldt, O., L. Palmpist, and E. Carlstrom, *Stabilization of alumina with polyelectrolyte and comb copolymer in solvent mixtures of water and alcohols.* Journal of the European Ceramic Society, 2009. **29**(6): p. 1069-1076.

51.   Ghadimi, A., R. Saidur, and H.S.C. Metselaar, *A review of nanofluid stability properties and characterization in stationary conditions.* International Journal of Heat and Mass Transfer, 2011. **54**(17-18): p. 4051-4068.

52.   Srivastava, S., *Effect of aggregation on thermal conductivity and viscosity of nanofluids.* Applied Nanoscience, 2012. **2**(3): p. 325-331.

53.   Birdi, K.S., *Handbook of surface and colloid chemistry, fourth edition*. 2015: CRC Press.

54.   Murshed, S., K. Leong, and C. Yang, *Thermophysical and electrokinetic properties of nanofluids–a critical review.* Applied Thermal Engineering, 2008. **28**(17-18): p. 2109-2125.

55.   Slomkowski, S., et al., *Terminology of polymers and polymerization processes in dispersed systems (IUPAC Recommendations 2011).* Pure and Applied Chemistry, 2011. **83**(12): p. 2229-2259.

56.   Sokolov, S.V., et al., *Reversible or not? Distinguishing agglomeration and aggregation at the nanoscale.* Analytical chemistry, 2015. **87**(19): p. 10033-10039.

57.   Batchelor, G.K., *The effect of Brownian motion on the bulk stress in a suspension of spherical particles.* Journal of Fluid Mechanics, 1977. **83**(1): p. 97-117.

58.   Einstein, A., *Investigations on the theory of the Brownian movement*. 1956: Courier Corporation.

59.   Sperling, R.A. and W.J. Parak, *Surface modification, functionalization and bioconjugation of colloidal inorganic nanoparticles.* Philos Trans A Math Phys Eng Sci, 2010. **368**(1915): p. 1333-83.

60.   Liang, Y., et al., *Interaction forces between colloidal particles in liquid: Theory and experiment*, in *Advances in Colloid and Interface Science*. 2007. p. 151-166.

61.   Ninhama, B.W., *On progress in forces since the DLVO theory.* Advances in Colloid and Interface Science, 1999. **83**: p. 1-17.

62.   Trefalt, G. and M. Borkovec, *Overview of DLVO Theory.* Laboratory of Colloid and Surface Chemistry, University of Genebra, 2014: p. 1-10.

63.   Metin, C.O., et al., *Aggregation kinetics and shear rheology of aqueous silica suspensions.* Applied Nanoscience, 2014. **4**(2): p. 169-178.

64.   Keblinski, P., J.A. Eastman, and D.G. Cahill, *Nanofluids for thermal transport.* Materials today, 2005. **8**(6): p. 36-44.

65.   Sato, T. and R. Ruch, *Stabilization of colloidal dispersions by polymer adsorption.* 1980: Dekker.

66.   Grasso, D., et al., *A review of non-DLVO interactions in environmental colloidal systems.* Re/Views in Environmental Science & BioTechnology, 2002. **1**: p. 17-38.

67.   Gurav, P., et al., *Stable colloidal copper nanoparticles for a nanofluid: Production and application.* Colloids and Surfaces a-Physicochemical and Engineering Aspects, 2014. **441**: p. 589-597.

68.   Kobayashi, M., et al., *Aggregation and charging of colloidal silica particles: effect of particle size.* Langmuir, 2005. **21**(13): p. 5761-9.

69.   Velegol, D., J.L. Anderson, and S. Garoff, *Determining the forces between polystyrene latex spheres using differential electrophoresis.* Langmuir, 1996. **12**(17): p. 4103-4110.

70.   Grządka, E., *Stability of manganese dioxide by guar gum in the absence or presence of surfactants.* Cellulose, 2014. **21**(3): p. 1641-1654.

71.   Trefalt, G., et al., *Electrokinetics and colloid behavior.* Laboratory of Colloid and Surface Chemistry, University of Genebra, 2014: p. 1-10.

72.   Israelachvili, J.N., *Intermolecular and surface forces*. 2011: Academic press.

73.   Van der Hoeven, P.C. and J. Lyklema, *Electrostatic stabilization in non-aqueous media.* Advances in Colloid and Interface Science, 1992. **42**: p. 205-277.

74.   Hsu, M.F., E.R. Dufresne, and D.A. Weitz, *Charge stabilization in nonpolar solvents.* Langmuir, 2005. **21**(11): p. 4881-4887.

75.   Zhang, Z., et al., *A modified method to calculate critical coagulation concentration based on DLVO theory.* Mathematical Problems in Engineering, 2015. **2015**.

76.   Napper, D.H., *Polymeric stabilization of colloidal dispersions*. Vol. 3. 1983: Academic Pr.

77.   Brown, M.A., A. Goel, and Z. Abbas, *Effect of electrolyte concentration on the stern layer thickness at a charged interface.* Angewandte Chemie International Edition, 2016. **55**(11): p. 3790-3794.

78.   Boon, N., et al., *Effective charges and virial pressure of concentrated macroion solutions.* Proceedings of the National Academy of Sciences, 2015. **112**(30): p. 9242-9246.

79.   Laaksonen, T., et al., *Stability and electrostatics of mercaptoundecanoic acid‑capped gold nanoparticles with varying counterion size.* ChemPhysChem, 2006. **7**(10): p. 2143-2149.

80.   Rodriguez-Arco, L., et al., *Steric repulsion as a way to achieve the required stability for the preparation of ionic liquid-based ferrofluids.* J Colloid Interface Sci, 2011. **357**(1): p. 252-4.

81.   Armstrong, G., L. Johnson, and A. Parker, *Effect of polymeric steric stabilizers on the settling of alumina.* Journal of applied polymer science, 1994. **52**(7): p. 997-1004.

82.   Rosen, M.J. and J.T. Kunjappu, *Surfactants and interfacial phenomena*. 2012: John Wiley & Sons.

83.   Darragh, P.J., et al., *Origin of precious opal.* Nature, 1966. **209**(5018): p. 13.

84.   Gao, W., M. Rigout, and H. Owens, *The structural coloration of textile materials using self-assembled silica nanoparticles.* J Nanopart Res, 2017. **19**(9): p. 303.

85.   Armstrong, E. and C. O'Dwyer, *Artificial opal photonic crystals and inverse opal structures - fundamentals and applications from optics to energy storage.* Journal of Materials Chemistry C, 2015. **3**(24): p. 6109-6143.

86.   Landon, P.B. and R. Glosser, *Self-assembly of spherical colloidal silica along the [100] direction of the FCC lattice and geometric control of crystallite formation.* Journal of Colloid and Interface Science, 2004. **276**(1): p. 92-96.

87.   Ruhl, T., P. Spahn, and G.P. Hellmann, *Artificial opals prepared by melt compression.* Polymer, 2003. **44**(25): p. 7625-7634.

88.   Haddad, Z., et al., *A review on how the researchers prepare their nanofluids.* International Journal of Thermal Sciences, 2014. **76**: p. 168-189.

89.   Taylor, R., et al., *Small particles, big impacts: A review of the diverse applications of nanofluids.* Journal of Applied Physics, 2013. **113**(1): p. 011301.

90.   Wang, B., et al., *Gold-ionic liquid nanofluids with preferably tribological properties and thermal conductivity.* Nanoscale Res Lett, 2011. **6**(1): p. 259.

91.   Kumaresan, V., et al., *Phase change material-based nanofluids for heat transfer enhancement in latent heat thermal energy storage system.* International Journal of Green Nanotechnology: Biomedicine, 2012. **4**(4): p. 541-546.

92.   Bobbo, S., et al., *Viscosity of water based SWCNH and TiO$_2$ nanofluids.* Experimental Thermal and Fluid Science, 2012. **36**: p. 65-71.

93.   Wang, F., et al., *Surfactant-free ionic liquid-based nanofluids with remarkable thermal conductivity enhancement at very low loading of graphene.* Nanoscale Res Lett, 2012. **7**(1): p. 314.

94.   Li, Q., Y. Xuan, and J. Wang, *Measurement of the viscosity of dilute magnetic fluids.* International journal of thermophysics, 2006. **27**(1): p. 103-113.

95.   Chen, L., et al., *Nanofluids containing carbon nanotubes treated by mechanochemical reaction.* Thermochimica Acta, 2008. **477**(1-2): p. 21-24.

96.   Chougule, S.S. and S. Sahu, *Thermal performance of automobile radiator using carbon nanotube-water nanofluid—experimental study.* Journal of Thermal Science and Engineering Applications, 2014. **6**(4): p. 041009.

97.   Nguyen, C., et al., *Viscosity data for Al$_2$O$_3$–water nanofluid—hysteresis: is heat transfer enhancement using nanofluids reliable?* International Journal of Thermal Sciences, 2008. **47**(2): p. 103-111.

98.   Jung, H.S., D.S. Moon, and J.K. Lee, *Quantitative analysis and efficient surface modification of silica nanoparticles.* Journal of Nanomaterials, 2012. **2012**: p. 8.

99.   Babu, K. and R. Dhamodharan, *Synthesis of polymer grafted magnetite nanoparticle with the highest grafting density via controlled radical polymerization.* Nanoscale Res Lett, 2009. **4**(9): p. 1090-102.

100.   Zoppe, J.O., et al., *Surface-initiated controlled radical polymerization: State-of-the-art, opportunities, and challenges in surface and interface engineering with polymer brushes.* Chemical Reviews, 2017. **117**(3): p. 1105-1318.

101.   Stöber, W., A. Fink, and E. Bohn, *Controlled growth of monodisperse silica spheres in the micron size range.* Journal of colloid and interface science, 1968. **26**(1): p. 62-69.

102.   Fox, J.R., et al., *Steric stabilization of Stöber silica dispersions using organosilanes.* Journal of materials science, 1987. **22**(12): p. 4528-4531.

103.   Deng, G., et al., *Control of surface expression of functional groups on silica particles.* Materials Science & Engineering C-Biomimetic and Supramolecular Systems, 2000. **11**(2): p. 165-172.

104. Finocchio, E., et al., *Adsorption of trimethoxysilane and of 3-mercaptopropyltrimethoxysilane on silica and on silicon wafers from vapor phase: an IR study.* Langmuir, 2007. **23**(5): p. 2505-9.

105. Ji, T., et al., *Organosilane grafted silica: Quantitative correlation of microscopic surface characters and macroscopic surface properties.* Applied Surface Science, 2017. **399**: p. 565-572.

106. Riccio, D.A., J.L. Nugent, and M.H. Schoenfisch, *Stöber synthesis of nitric oxide-releasing S-nitrosothiol-modified silica particles.* Chemistry of Materials, 2011. **23**(7): p. 1727-1735.

107. Nakamura, M. and K. Ishimura, *One-pot synthesis and characterization of three kinds of thiol-organosilica nanoparticles.* Langmuir, 2008. **24**(9): p. 5099-108.

108. Mangos, D.N., T. Nakanishi, and D.A. Lewis, *A simple method for the quantification of molecular decorations on silica particles.* Science and Technology of Advanced Materials, 2014. **15**(1): p. 015002.

109. Han, Y., et al., *Unraveling the growth mechanism of silica particles in the Stöber method: In situ seeded growth model.* Langmuir, 2017. **33**(23): p. 5879-5890.

110. Hyde, E.D., et al., *Colloidal silica particle synthesis and future industrial manufacturing pathways: a review.* Industrial & Engineering Chemistry Research, 2016. **55**(33): p. 8891-8913.

111. Belton, D.J., O. Deschaume, and C.C. Perry, *An overview of the fundamentals of the chemistry of silica with relevance to biosilicification and technological advances.* The FEBS journal, 2012. **279**(10): p. 1710-1720.

112. Nakamura, M., et al., *One-pot synthesis and characterization of dual fluorescent thiol-organosilica nanoparticles as non-photoblinking quantum dots and their applications for biological imaging.* Journal of Materials Chemistry, 2011. **21**(12): p. 4689-4695.

113. Brinker, C.J., *Hydrolysis and condensation of silicates: effects on structure.* Journal of Non-Crystalline Solids, 1988. **100**(1-3): p. 31-50.

114. LaMer, V.K. and R.H. Dinegar, *Theory, production and mechanism of formation of monodispersed hydrosols.* Journal of the American Chemical Society, 1950. **72**(11): p. 4847-4854.

115. Degen, I.A., *Detection of the methoxyl group by infrared spectroscopy.* Applied Spectroscopy, 1968. **22**(3): p. 164-166.

116. Masalov, V., et al., *Mechanism of formation and nanostructure of Stöber silica particles.* Nanotechnology, 2011. **22**(27): p. 275718.

117. Green, D., et al., *Size, volume fraction, and nucleation of Stober silica nanoparticles.* Journal of colloid and interface science, 2003. **266**(2): p. 346-358.

118. Bhakta, S., et al., *Sodium hydroxide catalyzed monodispersed high surface area silica nanoparticles.* Mater Res Express, 2016. **3**(7): p. 075025.

119. Jafarzadeh, M., I. Ab Rahman, and C. Sipaut, *Synthesis of silica nanoparticles by modified sol-gel process: The effect of mixing modes of the reactants and drying techniques.* Vol. 50. 2009. 328-336.

120. Yuan, L., et al., *In situ measurement of surface functional groups on silica nanoparticles using solvent relaxation nuclear magnetic resonance.* Langmuir, 2017. **33**(35): p. 8724-8729.

121. Cauda, V., C. Argyo, and T. Bein, *Impact of different PEGylation patterns on the long-term bio-stability of colloidal mesoporous silica nanoparticles.* Journal of Materials Chemistry, 2010. **20**(39): p. 8693-8699.

122. Sui, T., et al., *Bifunctional hairy silica nanoparticles as high-performance additives for lubricant.* Scientific Reports, 2016. **6**: p. 22696.

123. Northrop, B.H. and R.N. Coffey, *Thiol–ene click chemistry: computational and kinetic analysis of the influence of alkene functionality.* Journal of the American Chemical Society, 2012. **134**(33): p. 13804-13817.

124. Hoyle, C.E., A.B. Lowe, and C.N. Bowman, *Thiol-click chemistry: a multifaceted toolbox for small molecule and polymer synthesis.* Chem Soc Rev, 2010. **39**(4): p. 1355-87.

125. Killops, K.L., L.M. Campos, and C.J. Hawker, *Robust, efficient, and orthogonal synthesis of dendrimers via thiol-ene "click" chemistry.* J Am Chem Soc, 2008. **130**(15): p. 5062-4.

126. Hoyle, C.E. and C.N. Bowman, *Thiol–ene click chemistry.* Angewandte Chemie International Edition, 2010. **49**(9): p. 1540-1573.

127. Stetefeld, J., S.A. McKenna, and T.R. Patel, *Dynamic light scattering: a practical guide and applications in biomedical sciences.* Biophysical reviews, 2016. **8**(4): p. 409-427.

128. Pecora, R., *Dynamic light scattering: applications of photon correlation spectroscopy.* 2013: Springer Science & Business Media.

129. Anderson, W., et al., *A comparative study of submicron particle sizing platforms: accuracy, precision and resolution analysis of polydisperse particle size distributions.* J Colloid Interface Sci, 2013. **405**: p. 322-30.

130. Kestens, V., et al., *Challenges in the size analysis of a silica nanoparticle mixture as candidate certified reference material.* Journal of Nanoparticle Research, 2016. **18**(6): p. 171.

131. Vernon-Parry, K., *Scanning electron microscopy: an introduction.* III-Vs Review, 2000. **13**(4): p. 40-44.

132. Humphreys, J., R. Beanland, and P.J. Goodhew, *Electron microscopy and analysis.* 2014: CRC Press.

133. Brunauer, S., et al., *On a theory of the van der Waals adsorption of gases.* Journal of the American Chemical Society, 1940. **62**(7): p. 1723-1732.

134. Xu, X., et al., *Effect of sodium oleate adsorption on the colloidal stability and zeta potential of detonation synthesized diamond particles in aqueous solutions.* Diamond and related materials, 2005. **14**(2): p. 206-212.

135. Socrates, G., *Infrared and Raman characteristic group frequencies: tables and charts.* 2004: John Wiley & Sons.

136. Skoog, D.A., F.J. Holler, and S.R. Crouch, *Principles of instrumental analysis.* 2017: Cengage learning.

137. Chen, C., et al., *Thermogravimetric pyrolysis kinetics of bamboo waste via Asymmetric Double Sigmoidal (Asym2sig) function deconvolution.* Bioresource technology, 2017. **225**: p. 48-57.

138. Mueller, R., et al., *OH surface density of SiO_2 and TiO_2 by thermogravimetric analysis.* Langmuir, 2003. **19**(1): p. 160-165.

139. Xi, Y., et al., *Thermogravimetric analysis of organoclays intercalated with the surfactant octadecyltrimethylammonium bromide.* Journal of Thermal Analysis and Calorimetry, 2005. **81**(1): p. 91-97.

140. Price, D.M., D.J. Hourston, and F. Dumont, *Thermogravimetry of polymers.* Encyclopedia of analytical chemistry, 2000: p. 8094-8105.

141. Dai, C.L., et al., *The first study of surface modified silica nanoparticles in pressure-decreasing application.* Rsc Advances, 2015. **5**(76): p. 61838-61845.

142. Pastor, E., et al., *Physical adsorption vs. chemical binding of undecylenic acid on porous silicon surface: a comparative study of differently functionalized materials.* Physica Status Solidi C - Current Topics in Solid State Physics, Vol 6, No 7, 2009. **6**(7): p. 1704-+.

143. Staff, B.S.I., B.S. Institution, and BSI., *Glossary of rheological terms*. 1975: B S I Standards.

144. Di Giuseppe, E., et al., *Rheological and mechanical properties of silica colloids: from Newtonian liquid to brittle behaviour.* Rheologica acta, 2012. **51**(5): p. 451-465.

145. Hasanzadeh, M., V. Mottaghitalab, and M. Rezaei, *Rheological and viscoelastic behavior of concentrated colloidal suspensions of silica nanoparticles: A response surface methodology approach.* Advanced Powder Technology, 2015. **26**(6): p. 1570-1577.

146. Mueller, S., E.W. Llewellin, and H.M. Mader, *The rheology of suspensions of solid particles.* Proceedings of the Royal Society a-Mathematical Physical and Engineering Sciences, 2010. **466**(2116): p. 1201-1228.

147. Frankel, N. and A. Acrivos, *On the viscosity of a concentrated suspension of solid spheres.* Chemical Engineering Science, 1967. **22**(6): p. 847-853.

148. Hoffmann, A. and J. Kevelam, *Model for the interparticle surface separation in concentrated mono-and polydisperse suspensions.* AIChE journal, 1999. **45**(2): p. 285-290.

149. Quemada, D. and C. Berli, *Energy of interaction in colloids and its implications in rheological modeling.* Advances in colloid and interface science, 2002. **98**(1): p. 51-85.

150. Wen, Y.H., J.L. Schaefer, and L.A. Archer, *Dynamics and rheology of soft colloidal glasses.* ACS Macro Letters, 2015. **4**(1): p. 119-123.

151. van der Vaart, K., et al., *Rheology of concentrated soft and hard-sphere suspensions.* Journal of Rheology, 2013. **57**(4): p. 1195-1209.

152. Desmond, K.W. and E.R. Weeks, *Influence of particle size distribution on random close packing of spheres.* Physical Review E, 2014. **90**(2): p. 022204.

153. Yu, W. and S. Choi, *The role of interfacial layers in the enhanced thermal conductivity of nanofluids: a renovated Maxwell model.* Journal of nanoparticle research, 2003. **5**(1-2): p. 167-171.

154. Avsec, J. and M. Oblak, *The calculation of thermal conductivity, viscosity and thermodynamic properties for nanofluids on the basis of statistical nanomechanics.* International Journal of Heat and Mass Transfer, 2007. **50**(21-22): p. 4331-4341.

155. Genovese, D.B., *Shear rheology of hard-sphere, dispersed, and aggregated suspensions, and filler-matrix composites.* Advances in colloid and interface science, 2012. **171**: p. 1-16.

156. Mendoza, C.I. and I. Santamaria-Holek, *The rheology of hard sphere suspensions at arbitrary volume fractions: An improved differential viscosity model.* The Journal of chemical physics, 2009. **130**(4): p. 044904.

157. Poon, W.C. and M. Haw, *Mesoscopic structure formation in colloidal aggregation and gelation.* Advances in Colloid and Interface Science, 1997. **73**: p. 71-126.

158. Einstein, A., *A new determination of molecular dimensions.* Ann. phys, 1906. **19**(2): p. 289-306.

159. Oliver, D. and S.G. Ward, *Relationship between relative viscosity and volume concentration of stable suspensions of spherical particles.* Nature, 1953. **171**(4348): p. 396.

160. Krieger, I.M. and T.J. Dougherty, *A mechanism for non-Newtonian flow in suspensions of rigid spheres.* Transactions of the Society of Rheology, 1959. **3**(1): p. 137-152.

161. Pabst, W., *Fundamental considerations on suspension rheology.* CERAMICS SILIKATY., 2004. **48**(1): p. 6-13.

162. Deepak Selvakumar, R. and S. Dhinakaran, *Effective viscosity of nanofluids — A modified Krieger–Dougherty model based on particle size distribution (PSD) analysis.* Journal of Molecular Liquids, 2017. **225**: p. 20-27.

163.   Quemada, D., *Rheological modelling of complex fluids. I. The concept of effective volume fraction revisited.* The European Physical Journal-Applied Physics, 1998. **1**(1): p. 119-127.

164.   IUPAC., *Compendium of chemical terminology, 2nd ed. (the "Gold Book").* Compiled by A. D. McNaught and A. Wilkinson. Blackwell Scientific Publications, Oxford (1997). XML on-line corrected version: http://goldbook.iupac.org (2006-) created by M. Nic, J. Jirat, B. Kosata; updates compiled by A. Jenkins. ISBN 0-9678550-9-8. https://doi.org/10.1351/goldbook.

165.   Hackley, V.A. and C.F. Ferraris, *Guide to rheological nomenclature: Measurements in ceramic particulate systems.* 2001: National Institute of Standards and Technology Gaithersburg.

166.   Barnes, H. and K. Walters, *The yield stress myth?* Rheologica acta, 1985. **24**(4): p. 323-326.

167.   Barnes, H.A., *The yield stress—a review or 'παντα ρει'—everything flows?* Journal of Non-Newtonian Fluid Mechanics, 1999. **81**(1-2): p. 133-178.

168.   Dinkgreve, M., et al., *On different ways of measuring "the" yield stress.* Journal of Non-Newtonian Fluid Mechanics, 2016. **238**: p. 233-241.

169.   Møller, P.C., J. Mewis, and D. Bonn, *Yield stress and thixotropy: on the difficulty of measuring yield stresses in practice.* Soft matter, 2006. **2**(4): p. 274-283.

170.   Moller, P., et al., *An attempt to categorize yield stress fluid behaviour.* Philosophical Transactions of the Royal Society of London A: Mathematical, Physical and Engineering Sciences, 2009. **367**(1909): p. 5139-5155.

171.   Dimitriou, C.J., G.H. McKinley, and R. Venkatesan, *Rheo-PIV analysis of the yielding and flow of model waxy crude oils.* Energy & Fuels, 2011. **25**(7): p. 3040-3052.

172.   Irgens, F., *Generalized Newtonian fluids*, in *Rheology and Non-Newtonian Fluids.* 2014, Springer. p. 113-124.

173.   Rao, M.A., *Flow and functional models for rheological properties of fluid foods*, in *Rheology of Fluid, Semisolid, and Solid Foods.* 2014, Springer. p. 27-61.

174.   Herschel, W.H. and R. Bulkley, *Konsistenzmessungen von Gummi-Benzollösungen.* Kolloid-Zeitschrift, 1926. **39**(4): p. 291-300.

175.   Cross, M.M., *Rheology of non-Newtonian fluids: A new flow equation for pseudoplastic systems.* Journal of Colloid Science, 1965. **20**(5): p. 417-437.

176.   Carreau, P.J., *Rheological equations from molecular network theories.* Transactions of the Society of Rheology, 1972. **16**(1): p. 99-127.

177.   Rahman, I.A., M. Jafarzadeh, and C.S. Sipaut, *Physical and optical properties of organo-modified silica nanoparticles prepared by sol-gel.* Journal of Sol-Gel Science and Technology, 2011. **59**(1): p. 63-72.

178.   Takeda, Y., et al., *Capillary electrochromatography using monoamine- and triamine-bonded silica nanoparticles as pseudostationary phases.* J Chromatogr A, 2016. **1427**: p. 170-6.

179.   Huang, C., et al., *Impact of ATRP initiator spacer length on grafting poly(methyl methacrylate) from silica nanoparticles.* Langmuir, 2009. **25**(23): p. 13351-60.

180.   Zhuravlev, L.T., *The surface chemistry of amorphous silica. Zhuravlev model.* Vol. 173. 2000. 1-38.

181.   Ya. Davydov, V., A. V. Kiselev, and L. T. Zhuravlev, *Surface and bulk hydroxyl groups of silica by infrared spectra and D_2O-exchange.* Vol. 60. 1964. 2254-2264.

182.   Kawamura, A., et al., *Full-color biomimetic photonic materials with iridescent and non-iridescent structural colors.* Sci Rep, 2016. **6**: p. 33984.

183.   Takeoka, Y., et al., *Structurally coloured secondary particles composed of black and white colloidal particles.* Sci Rep, 2013. **3**(1): p. 2371.

184. Pang, C.W., J.Y. Jung, and Y.T. Kang, *Thermal conductivity enhancement of Al$_2$O$_3$ nanofluids based on the mixtures of aqueous NaCl solution and CH$_3$OH.* International Journal of Heat and Mass Transfer, 2013. **56**(1-2): p. 94-100.

185. Ahmed, G.S., et al., *FTIR analysis of silane grafted high density polyethylene.* Plastics Rubber and Composites, 2009. **38**(1): p. 13-20.

186. Beganskienė, A., et al., *FTIR, TEM and NMR investigations of Stöber silica nanoparticles.* Vol. 10. 2004.

187. Tejedor-Tejedor, M.I., L. Paredes, and M.A. Anderson, *Evaluation of ATR−FTIR spectroscopy as an "in situ" tool for following the hydrolysis and condensation of alkoxysilanes under rich H$_2$O conditions.* Chemistry of Materials, 1998. **10**(11): p. 3410-3421.

188. Li, Y.S., et al., *Vibrational spectroscopic studies of vinyltriethoxysilane sol-gel and its coating.* Spectrochim Acta A Mol Biomol Spectrosc, 2004. **60**(12): p. 2759-66.

189. Okabayashi, H., et al., *Surface structure of silica gel reacted with 3-mercaptopropyltriethoxysilane and 3-aminopropyltriethoxysilane: formation of the S-S bridge structure and its characterization by Raman scattering and diffuse reflectance Fourier transform spectroscopic studies.* Colloid and Polymer Science, 2002. **280**(2): p. 135-145.

190. Shih, P.T.K. and J.L. Koenig, *Raman studies of silane coupling agents.* Materials Science and Engineering, 1975. **20**: p. 145-154.

191. Li, Y.S., et al., *Preparation and characterization of silica coated iron oxide magnetic nano-particles.* Spectrochim Acta A Mol Biomol Spectrosc, 2010. **76**(5): p. 484-9.

192. *Geometric properties: Size and shape*, in *Food Physics*. 2007, Springer Berlin Heidelberg: Berlin, Heidelberg. p. 73-115.

193. Thommes, M., et al., *Physisorption of gases, with special reference to the evaluation of surface area and pore size distribution (IUPAC Technical Report).* Pure and Applied Chemistry, 2015. **87**(9-10): p. 1051-1069.

194. Alothman, Z., *A review: Fundamental aspects of silicate mesoporous materials.* Vol. 5. 2012. 2874-2902.

195. Sideridou, I.D. and M.M. Karabela, *Effect of the amount of 3-methacyloxypropyltrimethoxysilane coupling agent on physical properties of dental resin nanocomposites.* Dent Mater, 2009. **25**(11): p. 1315-24.

196. Loof, D., et al., *Quantitative and qualitative analysis of surface modified cellulose utilizing TGA-MS.* Materials, 2016. **9**(6): p. 415.

197. Kao, H.M., et al., *Highly carboxylic-acid-functionalized ethane-bridged periodic mesoporous organosilicas: synthesis, characterization, and adsorption properties.* Chem Asian J, 2012. **7**(9): p. 2111-7.

198. Heidarzadeh, N., et al., *Thermal degradation of random copolyesters based on 1,4-butanediol, terepthalic acid and different aliphatic dicarboxylic acids.* Thermochimica Acta, 2017. **654**: p. 101-111.

199. Perejón, A., et al., *Kinetic analysis of complex solid-state reactions. A new deconvolution procedure.* The Journal of Physical Chemistry B, 2011. **115**(8): p. 1780-1791.

200. Stankovic, B., J. Jovanovic, and B. Adnadjevic, *Application of the Suzuki–Fraser function in modelling the non-isothermal dehydroxylation kinetics of fullerol.* Reaction Kinetics, Mechanisms and Catalysis, 2018. **123**(2): p. 421-438.

201. Zhuravlev, L.T., *Concentration of hydroxyl-groups on the surface of amorphous silicas.* Langmuir, 1987. **3**(3): p. 316-318.

202. Ramanath, G., et al., *Self-assembled subnanolayers as interfacial adhesion enhancers and diffusion barriers for integrated circuits.* Applied Physics Letters, 2003. **83**(2): p. 383-385.

203. Gabbott, P., *Principles and applications of thermal analysis.* 2008: John Wiley & Sons.

204. Schiavon, M.A., et al., *Investigation on kinetics of thermal decomposition in polysiloxane networks used as precursors of silicon oxycarbide glasses.* Journal of Non-Crystalline Solids, 2002. **304**(1): p. 92-100.

205. Greil, P., *Active-filler-controlled pyrolysis of preceramic polymers.* Journal of the American Ceramic Society, 1995. **78**(4): p. 835-848.

206. Launer, P. and B. Arkles, *Silicon Compounds: Silanes & Silicones.* Inc.: Morrisville, PA, USA, 2013.

207. Taylor, H.A. and E.T. Layng, *The thermal decomposition of propyl mercaptan.* The Journal of Chemical Physics, 1933. **1**(11): p. 798-808.

208. Benoit, P., R. Ferrillo, and A. Granzow, *Kinetic applications of thermal analysis - a comparison of dynamic and isothermal methods.* Journal of thermal analysis, 1985. **30**(4): p. 869-877.

209. Dunne, M., O. Corrigan, and Z. Ramtoola, *Influence of particle size and dissolution conditions on the degradation properties of polylactide-co-glycolide particles.* Biomaterials, 2000. **21**(16): p. 1659-1668.

210. Boz, E., et al., *Precision ethylene/vinyl bromide polymers.* Advanced Synthesis & Catalysis, 2007. **349**(1-2): p. 137-141.

211. Boz, E., et al., *Synthesis and crystallization of precision ADMET polyolefins containing halogens.* Macromolecules, 2006. **39**(13): p. 4437-4447.

212. Mehl, M., et al., *A kinetic modeling study of the thermal degradation of halogenated polymers.* Journal of Analytical and applied pyrolysis, 2004. **72**(2): p. 253-272.

213. Yang, H., et al., *Thermal decomposition behavior of poly (vinyl alcohol) with different hydroxyl content.* Journal of Macromolecular Science, Part B, 2012. **51**(3): p. 464-480.

214. Yao, Q. and C.A. Wilkie, *Thermal degradation of blends of polystyrene and poly (sodium 4-styrenesulfonate) and the copolymer, poly (styrene-co-sodium 4-styrenesulfonate).* Polymer degradation and stability, 1999. **66**(3): p. 379-384.

215. Jiang, D.D., et al., *TGA/FTIR studies on the thermal degradation of some polymeric sulfonic and phosphonic acids and their sodium salts.* Polymer degradation and stability, 1999. **63**(3): p. 423-434.

216. Kretzschmar, R., H. Holthoff, and H. Sticher, *Influence of pH and humic acid on coagulation kinetics of kaolinite: A dynamic light scattering study.* Journal of Colloid and Interface Science, 1998. **202**(1): p. 95-103.

217. Izak-Nau, E., et al., *Altered characteristics of silica nanoparticles in bovine and human serum: The importance of nanomaterial characterization prior to its toxicological evaluation.* Vol. 10. 2013. 56.

218. Rodriguez, J.L., P.C. Schulz, and J.E. Puig, *Low-concentration aqueous solutions of undecenoic acid and sodium undecenoate.* Colloid and Polymer Science, 1999. **277**(11): p. 1072-1078.

219. Cistola, D.P., et al., *Ionization and phase behavior of fatty acids in water: application of the Gibbs phase rule.* Biochemistry, 1988. **27**(6): p. 1881-8.

220. Ewoldt, R.H., M.T. Johnston, and L.M. Caretta, *Experimental challenges of shear rheology: How to avoid bad data*, in *Complex Fluids in Biological Systems: Experiment, Theory, and Computation*, S.E. Spagnolie, Editor. 2015, Springer New York: New York, NY. p. 207-241.

221. Brown, E. and H.M. Jaeger, *The role of dilation and confining stresses in shear thickening of dense suspensions.* Journal of Rheology, 2012. **56**(4): p. 875-923.

222. Dörr, A., A. Sadiki, and A. Mehdizadeh, *A discrete model for the apparent viscosity of polydisperse suspensions including maximum packing fraction.* Journal of Rheology, 2013. **57**(3): p. 743-765.

223. Behzadfar, E., et al., *Effect of solid loading and aggregate size on the rheological behavior of PDMS/calcium carbonate suspensions.* Brazilian Journal of Chemical Engineering, 2009. **26**(4): p. 713-721.

224. Wang, T., et al., *Viscosity and aggregation structure of nanocolloidal dispersions.* Chinese Science Bulletin, 2012. **57**(27): p. 3644-3651.

225. Bhardwaj, R., et al., *Self-assembly of colloidal particles from evaporating droplets: role of DLVO interactions and proposition of a phase diagram.* Langmuir, 2010. **26**(11): p. 7833-7842.

226. Piroird, K., et al., *Role of evaporation rate on the particle organization and crack patterns obtained by drying a colloidal layer.* EPL (Europhysics Letters), 2016. **113**(3): p. 38002.

227. Yabroff, D., *Extraction of mercaptans with alkaline solutions.* Industrial & Engineering Chemistry, 1940. **32**(2): p. 257-262.

228. Tolpekin, V., et al., *Aggregation and breakup of colloidal particle aggregates in shear flow, studied with video microscopy.* Langmuir, 2004. **20**(7): p. 2614-2627.

229. Yang, H.-G., et al., *Rheological behavior of titanium dioxide suspensions.* Journal of colloid and interface science, 2001. **236**(1): p. 96-103.

230. Bagchi, P., B. Gray, and S. Birnbaum, *Poly (vinyl toluene) Model Latices*, in *Polymer Colloids II*. 1980, Springer. p. 225-263.

231. Krumrine, P. and J. Vanderhoff, *Applicability of DLVO theory to the formation of ordered arrays of monodisperse latex particles*, in *Polymer Colloids II*. 1980, Springer. p. 289-312.

232. Spahn, P., et al., *Modification of the refractive-index contrast in polymer opal films.* Journal of Materials Chemistry, 2011. **21**(24): p. 8893-8897.

233. Gao, W., M. Rigout, and H. Owens, *Facile control of silica nanoparticles using a novel solvent varying method for the fabrication of artificial opal photonic crystals.* Journal of Nanoparticle Research, 2016. **18**(12): p. 387.